



HAL
open science

Une méthode d'optimisation topologique multi-échelle CAO-compatible

Giulia Bertolino

► **To cite this version:**

Giulia Bertolino. Une méthode d'optimisation topologique multi-échelle CAO-compatible. Eco-conception. HESAM Université, 2022. Français. NNT : 2022HESAE035 . tel-03741356

HAL Id: tel-03741356

<https://pastel.hal.science/tel-03741356v1>

Submitted on 1 Aug 2022

HAL is a multi-disciplinary open access archive for the deposit and dissemination of scientific research documents, whether they are published or not. The documents may come from teaching and research institutions in France or abroad, or from public or private research centers.

L'archive ouverte pluridisciplinaire **HAL**, est destinée au dépôt et à la diffusion de documents scientifiques de niveau recherche, publiés ou non, émanant des établissements d'enseignement et de recherche français ou étrangers, des laboratoires publics ou privés.

ÉCOLE DOCTORALE SCIENCES DES MÉTIERS DE L'INGÉNIEUR
Institut de Mécanique et d'Ingénierie I2M – Campus de Bordeaux

THÈSE

présentée par : **Giulia BERTOLINO**

soutenue le : **30 Juin 2022**

pour obtenir le grade de : **Docteur d'HESAM Université**

préparée à : **École Nationale Supérieure d'Arts et Métiers**

Spécialité : **Mécanique**

MULTI-SCALE TOPOLOGY OPTIMISATION IN A CAD COMPATIBLE FRAMEWORK

THÈSE dirigée par :
M. MONTEMURRO Marco

et co-encadrée par :
M. PERRY Nicolas
M. POURROY Franck

Jury

M. Alain BERNARD, Professeur, École Centrale de Nantes, LS2N
M. François-Xavier IRISARRI, Ingénieur de recherche HDR, ONERA, DMSC
M. Francois JOUVE, Professeur, Université Paris Cité, LJLL
Mme Sonia CAFIERI, Professeure, École Nationale de l'Aviation Civile, ENAC
M. Jean-Philippe PERNOT, Professeur, Arts et Métiers Sciences et Technologies, LISPEN
M. Marco MONTEMURRO, Professeur, Arts et Métiers Sciences et Technologies, I2M
M. Nicolas PERRY, Professeur, Arts et Métiers Sciences et Technologies, I2M
M. Franck POURROY, Maître de conférences, Université Grenoble Alpes, G-SCOP

Président
Rapporteur
Rapporteur
Examinatrice
Examinateur
Examinateur
Examinateur
Examinateur

**T
H
È
S
E**

Contents

Contents	2
List of Figures	6
List of Tables	10
Acknowledgements	17
Funding	19
Résumé étendu de la thèse	21
1 Introduction	39
1.1 The COFFA project context	39
1.2 The Thesis objectives	41
1.3 Outline of the work	42
2 State of the Art	45
2.1 Introduction to the state of the art	45
2.2 On the topology optimisation methods	45
2.2.1 Density-based TO methods	46
2.2.2 Level-set method	50
2.2.3 The ESO and BESO methods	54
2.3 On the integration of multi-scale analysis in topology optimisation	56
2.3.1 Multi-scale topology optimisation by considering topological variables at lower scale	57
2.3.2 Multi-scale topology optimisation by considering topological variables at all scales	59
2.3.3 Experimental validation of the multi-scale topology optimisation through three-point bending tests	60
2.4 On the surface reconstruction methods	62

2.4.1	Parametrisation techniques	64
2.4.2	Surface fitting	66
2.5	Conclusion	68
3	The SANTO algorithm	71
3.1	Fundamentals of non-uniform rational basis spline hyper-surfaces	71
3.2	The NURBS-based SIMP method for single-scale problems .	73
3.2.1	Design variables	73
3.2.2	Objective function	76
3.2.3	Constraint functions	79
3.2.4	Problem formulation	81
3.3	The SANTO structure	81
3.4	Numerical results	85
3.4.1	The 2D benchmark problem	86
3.4.2	The 3D benchmark	88
3.5	Conclusion	91
4	Multi-scale topology optimisation I	95
4.1	The strain energy homogenisation method	96
4.2	The multi-scale NURBS-based SIMP method	99
4.3	Numerical results	106
4.3.1	2D benchmark problem	107
4.3.1.1	Sensitivity of the RVE topology to the NURBS entity integer parameters	108
4.3.1.2	Sensitivity of the RVE topology to the initial guess	111
4.3.1.3	Sensitivity of the RVE topology to the macroscopic loading condition	113
4.3.2	3D benchmark problem	115
4.4	Conclusions and prospects	118
5	Multi-scale topology optimisation II	121
5.1	Multi-scale topology optimisation of ACM in the NURBS-based SIMP framework	122
5.1.1	Design variables	124
5.1.2	Objective function	126
5.1.3	Constraint functions	128
5.1.4	Problem formulation	131
5.2	Results	132
5.2.1	2D Benchmark problems	133

5.2.1.1	Sensitivity of the optimised solution to the mass/volume constraint fraction	136
5.2.1.2	Sensitivity of the optimised solution to the starting guess at the lower scale	138
5.2.1.3	Sensitivity of the optimised solution to the anisotropy of the RVE and to the macroscopic loads	143
5.2.1.4	Sensitivity of the optimised topology to mixed non-zero boundary conditions	146
5.2.2	3D benchmark problems	155
5.2.2.1	Sensitivity of the optimised solution to the constraint type imposed at the macroscale	157
5.2.2.2	Sensitivity of the optimised solution to the scale separation requirement	160
5.2.2.3	Sensitivity of the optimised topology to mixed non-zero boundary conditions	161
5.3	Conclusions and prospects	166
6	Experimental validation of the multi-scale topology optimisation method	169
6.1	Problem description	170
6.2	Characterisation of the bulk material properties	171
6.2.1	Tensile behaviour of rigid resin 4000	171
6.2.2	Flexural behaviour of rigid resin 4000	174
6.3	Topology optimisation of 3PB-like specimen in the NURBS-based SIMP framework	177
6.3.1	Design variables	178
6.3.2	Objective function and optimisation constraints	179
6.3.3	Problem formulation	180
6.4	Numerical results	181
6.4.1	2D results	182
6.4.2	3D results	187
6.5	Validation of the optimised topologies through three-point bending tests	190
6.6	Conclusions and prospects	196
7	An Efficient Hybrid Optimization Strategy for Surface Reconstruction	199
7.1	Fundamentals of the shape preserving method	200
7.2	Surface Fitting of Genus zero Open Surfaces	202
7.2.1	Design Variables	202

7.2.2	Problem Formulation and Numerical Strategy	206
7.2.2.1	The Meta-Heuristic Exploration Phase . . .	207
7.2.2.2	The Deterministic Optimisation Phase . . .	210
7.3	General Strategy for Genus G Surfaces (Open and Closed) .	212
7.4	Studied Cases and Results	216
7.5	Comparison with Surface Reconstruction Methods from the Literature	233
7.6	Conclusions and prospects	235
8	Conclusions and prospects	241
8.1	General conclusions	241
8.2	Prospects	244
	Bibliography	247
A	Gradient of the work of the internal forces	265
B	Computational cost of SEHM	269
C	Surface fitting - Gradient of the objective function	271
	Scientific production	277

List of Figures

0.1	Influence du nombre de points de contrôle et des degrés sur la topologie optimale du VER pour un problème 2D	27
0.2	Influence de la condition de chargement sur la topologie optimale du VER pour un problème 3D : (a)-(b) solution B-spline, (c)-(d) solution NURBS.	27
0.3	Influence du déplacement imposé sur la topologie optimale aux échelles inférieure et supérieure pour un problème 2D	31
0.4	Influence de la contrainte sur la séparation d'échelle sur la topologie optimale aux échelles inférieure et supérieure pour un problème 3D	32
0.5	Méthode de reconstruction appliquée à la <i>Ear Surface</i> : a) points cibles, b) surface NURBS, c) paramétrisation de la surface NURBS.	37
0.6	Méthode de reconstruction appliquée à la <i>Kettle Surface</i> : a) points cibles, b) surface NURBS.	38
2.1	General flowchart of the SIMP algorithm.	49
2.2	Level-set function example for 2D TO problems.	52
2.3	Diagram of the parametrisation and fitting phase constituting the surface reconstruction procedure.	63
3.1	The effect of the degree value (a)-(b), and of the CPs number (a)-(c) on the local support.	74
3.2	The effect of the CPs value (a)-(b), and of the weights value (a)-(c) on the shape of the surface.	75
3.3	Flow-chart of the SANTO algorithm.	82
3.4	Geometry and boundary conditions of the 2D benchmark of a cantilever beam.	87
3.5	Benchmark problem 2D-BK: influence of the degrees and CPs number on the optimised topology for B-spline solutions.	88
3.6	Benchmark problem 2D-BK: influence of the degrees and CPs number on the optimised topology for NURBS solutions.	89

3.7	Benchmark 2D-BK - Optimal value of the compliance vs. the number of CPs for different degrees.	90
3.8	Geometry and boundary conditions of the 3D benchmark structure.	91
3.9	Benchmark problem 3D-BK: influence of the degrees and CPs number on the optimised topology for (a) B-spline and (b) NURBS solutions.	92
4.1	Characteristic scales of the multi-scale topology optimisation problem: (a) the macroscopic (upper) scale of the structure and (b) the lower (i.e., mesoscopic or microscopic) scale of the lattice RVE	100
4.2	Geometry and boundary conditions of the benchmark problem 2D-BK	108
4.3	Benchmark problem 2D-BK: sensitivity of the optimised topology to CP numbers and basis functions degrees, B-spline solutions	109
4.4	Benchmark problem 2D-BK: sensitivity of the optimised topology to CP numbers and basis functions degrees, NURBS solutions	110
4.5	Benchmark problem 2D-BK: compliance vs. CPs number and degrees for B-spline and NURBS solutions	110
4.6	Benchmark problem 2D-BK: CAD model of the RVE optimised topology for a NURBS surface with $p_1 = p_2 = 2$ and $n_{CP} = 1225$	112
4.7	Benchmark problem 2D-BK: influence of the initial guess on the optimised topology for (a)-(b) B-spline and (c)-(d) NURBS solutions with $p_1 = p_2 = 2$ and $n_{CP} = 1225$	113
4.8	Benchmark problem 2D-BK: influence of the macroscopic loading condition on the RVE optimised topology for (a)-(c) B-spline and (d)-(e) NURBS solutions with $p_1 = p_2 = 3$ and $n_{CP} = 1225$	114
4.9	Geometry and boundary conditions of the benchmark problem 3D-BK: (a) only axial forces are applied at the macroscopic scale, (b) axial and shear forces are applied at the macroscopic scale .	116
4.10	Benchmark problem 3D-BK: influence of the loading condition at the macroscopic scale on the RVE optimised topology for (a)-(b) B-spline and (c)-(d) NURBS solutions with $p_1 = p_2 = p_3 = 3$ and $n_{CP} = 5832$	117
5.1	Characteristic scales of the two-scale topology optimisation problem: (a) the upper (macroscopic) scale of the structure and (b) the lower (i.e., mesoscopic or microscopic) scale of the representative volume element of the architected cellular material .	124

5.2	Finite element model of the representative volume element of the architected cellular material with its characteristic size for 2D problems.	134
5.3	Finite element model, geometrical parameters and applied boundary conditions of benchmark problems (a) BK1-2D and (b) BK2-2D.	135
5.4	Finite element model, geometrical parameters and applied boundary conditions of benchmark problems (a) BK3-2Da and (b) BK3-2Db.	136
5.5	BK3-2Da: Macroscopic compliance vs. applied displacement for optimised topologies resulting from two-scale topology optimisation. Solutions obtained by employing NURBS entities, with $n_{mCP} = 25 \times 25$ and $n_{MCP} = 31 \times 17$ and $p_{\chi i} = 3$, ($i = 1, 2$, $\chi = m, M$).	149
5.6	BK3-2Da: Macroscopic compliance vs. applied displacement for optimised topologies, resulting from single-scale topology optimisation, made of a) isotropic material and b) transversely isotropic material. Solutions obtained by employing NURBS entities, with $n_{MCP} = 31 \times 17$ and $p_{Mi} = 3$, ($i = 1, 2$).	153
5.7	BK3-2Db: Macroscopic compliance vs. applied displacement for optimised topologies resulting from two-scale topology optimisation. Solutions obtained by employing NURBS entities, with $n_{mCP} = 25 \times 25$ and $n_{MCP} = 31 \times 17$ and $p_{\chi i} = 3$, ($i = 1, 2$, $\chi = m, M$).	156
5.8	Finite element model of the representative volume element of the architected cellular material with its characteristic size for 3D problems.	157
5.9	Finite element model, geometrical parameters and applied boundary conditions of benchmark problems (a) BK1-3D, (b) BK2-3D and (c) BK3-3D.	158
6.1	Workflow of the design methodology for specimens subject to 3PBT-like loading conditions	172
6.2	Schematic representation of the tensile dog-bone-like specimens with the related geometric parameters.	173
6.3	σ - ε curves obtained from the tensile tests.	173
6.4	σ - ε curve of the average tensile material behaviour.	174
6.5	Schematic representation of the 3PBT apparatus with the related geometric parameters	175
6.6	σ - ε curves obtained from 3PBT.	176
6.7	σ - ε curve of the average flexural material behaviour.	177

6.8	Finite element model of the representative volume element with its characteristic size for 2D problems.	183
6.9	Finite element model of the macroscopic scale problem with its characteristic size for 2D problems.	184
6.10	2D test case: influence of the problem formulation on the optimised topology: a) optimised solution of DC1 (upper scale), b) optimised solution of DC2 (lower scale), c) optimised solution of DC3 (lower scale), d) optimised solution of DC3 (upper scale).	186
6.11	Finite element model of the representative volume element of the with its characteristic size for 3D problems.	188
6.12	Finite element model of the macroscopic scale with its characteristic size for 3D problems.	189
6.13	3D test case: influence of the problem formulation on the optimised topology: a) optimised solution of DC1 (upper scale), b) optimised solution of DC2 (lower scale), c) optimised solution of DC3 (lower scale), d) optimised solution of DC3 (upper scale).	191
6.14	CAD model of the optimised topology for design case (a) DC1, (b) DC2 and (c) DC3.	192
6.15	Orientation and position of the sample during printing for design cases (a) DC1, (b) DC2 and (c) DC3	193
6.16	Experimental set-up of the three-point bending test for the optimised 2D topologies for each design case.	193
6.17	Force vs. displacement curve obtained from three-point bending test on the optimised sample of each design case.	194
6.18	Finite element model and boundary conditions for the non-linear analysis conducted a posteriori on the optimised samples (for each design case).	195
6.19	Force vs. displacement curves for each design case by considering different material behaviours for the rigid resin 4000.	196
7.1	Mapping of the triangulated surface on the parametric domain.	200
7.2	Calculation of the weights of the SPM.	202
7.3	Flowchart of the the hybrid surface fitting strategy.	207
7.4	Individual's genotype.	210
7.5	Manual segmentation.	213
7.6	C0 and C1 connectivity conditions.	214
7.7	Design variables inheritance among patches (red stars denote the parameters u_1 and u_2 resulting from the SPM for each patch).	217
7.8	The Carpet-like Surface (BK1)	223
7.9	The Ear Surface (BK2)	224
7.10	The Face Surface (BK3)	225

7.11	The thigh-bone surface (BK4) - parametrisation through the SPM	226
7.12	The thigh-bone surface (BK4)	227
7.13	A genus $g = 1$ open surface (BK5) - parametrisation through the SPM, case $n_p = 2$.	228
7.14	A genus $g = 1$ open surface (BK5) - parametrisation through the SPM, case $n_p = 4$.	229
7.15	A genus $g = 1$ open surface (BK5), case $n_p = 2$.	230
7.16	A genus $g = 1$ open surface (BK5), case $n_p = 4$.	231
7.17	The Kettle surface (BK6) - parametrisation through the SPM	232
7.18	The Kettle surface (BK6)	233
7.19	The Fan Disk surface (BK7) - parametrisation through the SPM	236
7.20	The Fan Disk surface (BK7)	237
7.21	The Club surface (BK8) - parametrisation through the SPM	238
7.22	The Club surface (BK8)	239

List of Tables

3.1	GCMMA algorithm parameters	85
3.2	2D-BK: compliance and volume for the optimised topologies in the three configurations of B-spline/NURBS parameters.	87
3.3	3D-BK: compliance and volume for the optimised topologies defined via the B-spline/NURBS entities.	91
4.1	MMA algorithm parameters	106
4.2	2D-BK: elastic constants for the optimised topologies in the case $p_1 = p_2 = 3$, $n_{CP} = 1225$ for each loading condition	115
4.3	3D-BK: elastic constants for the optimised topologies in the case $p_1 = p_2 = p_3 = 3$ and $n_{CP} = 5832$ for each load case	118
5.1	GCMMA algorithm parameters.	132
5.2	BK1-2D: optimised topologies at both scales, when the mass fraction is set as $\gamma_{Mm} = 0.35$. Solutions obtained by employing B-spline entities, with $n_{mCP} = 25 \times 25$ and $n_{MCP} = 29 \times 15$ and $p_{\chi i} = 3$, ($i = 1, 2$, $\chi = m, M$).	139

5.3	BK1-2D: optimised topologies at both scales, when the mass fraction is set as $\gamma_{Mm} = 0.45$. Solutions obtained by employing B-spline entities, with $n_{mCP} = 25 \times 25$ and $n_{MCP} = 23 \times 14$ and $p_{\chi i} = 3$, ($i = 1, 2$, $\chi = m, M$).	140
5.4	Optimisation results related to the problems listed in Tables 5.2 - 5.3 in terms of reference and optimal compliance and geometrical constraints values.	141
5.5	BK1-2D: optimised topologies at both scales for different starting topologies at the RVE scale. Solutions obtained by employing B-spline entities, with $n_{mCP} = 25 \times 25$ and $n_{MCP} = 29 \times 15$ and $p_{\chi i} = 3$, ($i = 1, 2$, $\chi = m, M$).	143
5.6	BK1-2D: optimised topologies at both scales for different starting topologies at the RVE scale. Solutions obtained by employing NURBS entities, with $n_{mCP} = 25 \times 25$ and $n_{MCP} = 29 \times 15$ and $p_{\chi i} = 3$, ($i = 1, 2$, $\chi = m, M$).	144
5.7	Optimisation results related to the problems listed in Tables 5.5 - 5.6 in terms of reference and optimal compliance and geometrical constraints values.	145
5.8	BK1-2D: optimised topologies at both scales by considering an RVE with orthotropic and anisotropic behaviour. Solutions obtained by employing NURBS entities, with $n_{mCP} = 25 \times 25$ and $n_{MCP} = 29 \times 15$ and $p_{\chi i} = 3$, ($i = 1, 2$, $\chi = m, M$).	146
5.9	BK2-2D: optimised topologies at both scales by considering an RVE with orthotropic and anisotropic behaviour. Solutions obtained by employing NURBS entities, with $n_{mCP} = 25 \times 25$ and $n_{MCP} = 29 \times 15$ and $p_{\chi i} = 3$, ($i = 1, 2$, $\chi = m, M$).	147
5.10	Optimisation results related to the problems listed in Tables 5.8 - 5.9 in terms of reference and optimal compliance and geometrical constraints values.	147
5.11	BK3-2Da: optimised topologies at both scales under mixed non-zero BCs. Solutions obtained by employing NURBS entities, with $n_{mCP} = 25 \times 25$ and $n_{MCP} = 31 \times 17$ and $p_{\chi i} = 3$, ($i = 1, 2$, $\chi = m, M$).	150
5.12	BK3-2Da: optimised topologies at the macroscopic scale under mixed non-zero BCs when the bulk material is considered isotropic or transversely isotropic. Solutions obtained by employing NURBS entities, with $n_{MCP} = 31 \times 17$ and $p_{Mi} = 3$, ($i = 1, 2$).	151
5.13	Optimisation results related to the problems listed in Table 5.11 in terms of reference and optimal compliance and geometrical constraints values.	152

5.14	Optimisation results related to the problems listed in Table 5.12 in terms of optimal compliance and geometrical constraints values.	152
5.15	BK3-2Db: optimised topologies at both scales under mixed non-zero BCs. Solutions obtained by employing NURBS entities, with $n_{mCP} = 25 \times 25$ and $n_{MCP} = 31 \times 17$ and $p_{\chi i} = 3$, ($i = 1, 2$, $\chi = m, M$).	154
5.16	Optimisation results related to the problems listed in Table 5.15 in terms of reference and optimal compliance and geometrical constraints values.	155
5.17	BK1-3D: optimised topologies at both scales for different macroscopic constraints. Solutions obtained by employing NURBS entities, with $n_{mCP} = 11 \times 11 \times 11$, $n_{MCP} = 27 \times 15 \times 10$ and $p_{\chi i} = 3$, ($i = 1, 2, 3$, $\chi = m, M$).	159
5.18	BK2-3D: optimised topologies at both scales for different macroscopic constraints. Solutions obtained by employing NURBS entities, with $n_{mCP} = 11 \times 11 \times 11$, $n_{MCP} = 15 \times 12 \times 15$ and $p_{\chi i} = 3$, ($i = 1, 2, 3$, $\chi = m, M$).	160
5.19	BK1-3D: influence of the scales separation requirement on the optimised topology (at both scales). Solutions obtained by employing NURBS entities, with $n_{mCP} = 11 \times 11 \times 11$, $n_{MCP} = 35 \times 25 \times 15$ (first case) or $n_{MCP} = 27 \times 15 \times 10$ (second case) and $p_{\chi i} = 3$, ($i = 1, 2, 3$, $\chi = m, M$).	162
5.20	BK2-3D: influence of the scales separation requirement on the optimised topology (at both scales). Solutions obtained by employing NURBS entities, with $n_{mCP} = 11 \times 11 \times 11$, $n_{MCP} = 23 \times 17 \times 23$ (first case) or $n_{MCP} = 15 \times 12 \times 15$ (second case) and $p_{\chi i} = 3$, ($i = 1, 2, 3$, $\chi = m, M$).	163
5.21	Optimisation results related to the problems listed in Tables 5.17 - 5.18 in terms of reference and optimal compliance and geometrical constraints values.	164
5.22	Optimisation results related to the problems listed in Tables 5.19 - 5.20 in terms of reference and optimal compliance and geometrical constraints values.	164
5.23	BK3-3D: optimised topologies at both scales under mixed non-zero BCs. Solutions obtained by employing NURBS hyper-surfaces, with $n_{mCP} = 11 \times 11 \times 11$, $n_{MCP} = 27 \times 15 \times 10$ and $p_{\chi i} = 3$, ($i = 1, 2, 3$, $\chi = m, M$).	165
5.24	Optimisation results related to the problems listed in Table 5.23 in terms of reference and optimal optimal compliance and geometrical constraints values.	166

6.1	Actual values of W and T of the dog-bone samples.	172
6.2	Tensile yield stress σ_{yt} and tensile Young's modulus E_t values extrapolated from the results in Fig. 6.3.	174
6.3	Actual dimensions of the samples used for 3PBT.	175
6.4	Results of the 3PBT.	176
6.5	GCMMA algorithm parameters.	182
6.6	Elasticity matrix of the optimised topologies illustrated in Fig. 6.10	185
6.7	Elasticity matrix of the optimised topologies illustrated in Fig. 6.13	190
6.8	Printing parameters of the samples for each design case.	193
7.1	Number of TPs for each benchmark.	217
7.2	Design variables bounds.	217
7.3	Genetic parameters of the ERASMUS algorithm	218
7.4	<i>Active-set</i> algorithm parameters	218
7.5	MEP: numerical results.	220
7.6	DOP: numerical results.	221
7.7	MEP and DOP: computational time [s].	222
7.8	Comparison of DOP results with state of the art algorithms.	235

Acronyms

3PBT	three-point bending test
ACM	architected cellular material
AHM	asymptotic homogenisation method
BC	boundary condition
BESO	bidirectional evolutionary structural optimisation
BF	basis function
CNLPP	constrained non-linear programming problem
CP	control point
DLP	digital light processing
DOF	degree of freedom
DOP	deterministic optimisation phase
DR	design requirement
ESO	evolutionary structural optimisation
FE	finite element
GA	genetic algorithm
GCMMA	globally convergent method of moving asymptotes
HJ	Hamilton-Jacobi
IGA	isogeometric analysis
KV	knot vector
LIT	lattice infill technique
LSF	level-set function
LSM	level-set method
MEP	meta-heuristic exploration phase
MMA	method of moving asymptotes
ND	Newmann-Dirichlet

NURBS non-uniform rational basis spline
PBC periodic boundary condition
PEEK polyetheretherketone
PLA polylactic acid
RBF radial basis function
RVE representative volume element
SANTO SIMP and NURBS for topology optimisation
SC-BCC simple cubic and body centered cubic
SEHM strain energy-based homogenisation method
SIMP solid isotropic material with penalisation
SLM selective laser melting
SPM shape preserving method
SPONS shape-preserving and poly-NURBS surface reconstruction
TO topology optimisation
TP target point
TPE total potential energy
TPSE thin-plate spline energy
TV topological variable

Acknowledgements

First and foremost, I would like to thank my supervisors Marco Montemurro, Nicolas Perry and Franck Pourroy, for their willingness to help me during the work and for providing me with the opportunity to increase my engineering background and to understand the fascinating dynamics of the research world.

My sincerest thanks go to the I2M and the G-SCOP Laboratories, that thanks to the ANR agency supported the COFFA research project. I am particularly thankful to Philippe Marin, Frédéric Vignat for their time and their interest in my work.

A big thank you goes to my parents, who always encouraged me to get involved in the difficulties, for their great and constant support (not only moral) and for teaching me by their example how to face life with grit and passion. I would also like to thank my brother Enrico and Tiziana who showed me what it means to carry out a project together with perseverance and love to achieve great satisfaction.

I would also like to express my gratitude to my family in Bordeaux: my friends. Thanks to Carlos, JuanJo, Alexandre, Giulio, Michele, Adele, Lorenzo, Enrico, Alberto, Giulia, Thibaut, Thomas, Marco x2, all colleagues of the I2M lab, who were always available for discussion and sharing and thanks to whom Bordeaux will always occupy a special place in my memories.

I want to thank Carolina and Chiara, new or long-time friends, who through their wisdom and light-heartedness toward life have been an example and a point of reference in life. Thank you for the time spent in meaningful discussions that have been indispensable in making me grow as a person.

I would also like to thank Monica and Martina who have been understanding and joking friends at the same time. They showed me how to play down and not take ourself seriously, to be able to face difficulties always with a smile.

Finally, I would like to thank Davide, who has been able to stand by

me throughout the whole journey with sensitivity and intelligence. He supported me in the darkest moments and laughed with me in the light one, believed in me when I did not believe and loved me without borders. There are no words to express how grateful I am to you and how much love I feel for you. You are my life partner, I want to continue to deserve you.

Funding

This Thesis has been funded by the French National Research Agency through the research project COFFA (“Conception et Optimisation de Forme pour la Fabrication Additive”) ANR-17-CE10-0008. The candidate is profoundly grateful for the support.

Résumé étendu de la thèse

Le contexte et le projet COFFA

Pendant ces dernières années, les procédés ALM ((de l'anglais *additive layer manufacturing*) ont été de plus en plus employés dans divers secteurs industriels (aéronautique, automobile, énergétique, biomédical, etc.). Ceci est dû à la demande croissante de composants personnalisés avec des géométries complexes et des performances (mécanique, thermique, légèreté, etc.) accrues.

Contrairement aux techniques de fabrication conventionnelles (dites soustractives), comme, par exemple, l'usinage et l'estampage, les technologies ALM créent la forme finale par superposition de couches. Par conséquent, ces technologies ont la capacité d'utiliser la matière première de manière efficace, en minimisant l'énergie et les déchets. En outre, la technologie ALM permet de dépasser les contraintes de conception liées aux procédés traditionnels, offrant ainsi un nouvel espace de possibilités pour les concepteurs. L'ALM permet la création de géométries complexes, de structures résistantes et de nouvelles solutions technologiques comme les matériaux et structures architecturés à gradient de propriétés. L'ALM permet également de réaliser des pièces multi-matériaux de manière continue (dits aussi FGM, de l'anglais *functionally graded materials*) ou discontinue (empilement de zones mono-matériaux). Le gain potentiel en coût, masse, performances fonctionnelles et réalisation est considérable par rapport aux possibilités offertes par les procédés soustractifs classiques.

Néanmoins, l'utilisation de ces technologies comporte un certain nombre d'inconvénients. Tout d'abord, de nombreux défauts (état de surface, porosités, défauts de forme, etc.) peuvent apparaître sur les pièces fabriquées par les différents procédés ALM; de plus, il n'existe pas une procédure standard pour qualifier les performances mécaniques des pièces fabriquées dans le domaine de la résistance (robustesse) ainsi que l'endurance (résistance à la fatigue, durabilité, vieillissement, etc.).

L'objectif de la conception est de définir un produit qui répond aux dif-

férentes exigences résultant des besoins du client et de la nécessité d'être fabriqué à un coût raisonnable. Dans le processus de conception, les concepteurs alternent les phases de synthèse au cours desquelles ils proposeront et modéliseront des formes qui, selon eux, répondent aux exigences, et les phases d'analyse au cours desquelles ils vérifieront cette adéquation. Dans le cas de la fabrication additive, la conception d'un produit nécessite des connaissances et des méthodes qui pourraient exploiter la liberté donnée par les procédés ALM tout en répondant aux contraintes imposées par les phénomènes physiques mis en jeu par la technologie. Par conséquent, les outils et les méthodes qui devraient être élaborés pour aider les concepteurs doivent permettre de réaliser à la fois les phases de synthèse et d'analyse.

Au cours des dernières années, les codes commerciaux de conception et de simulation ont évolué, leur offre a essayé de couvrir ce besoin. Cependant, les concepteurs peuvent éprouver des difficultés face à des offres logicielles complexes (optimisation topologique, simulation numérique) et, d'autre part, ils doivent faire face à une évolution indispensable des méthodologies de conception autour de ces outils. En effet, l'optimisation des structures doit prendre en compte, dès la phase de conception préliminaire, les contraintes technologiques des technologies ALM et traiter des aspects multi-physique et multi-échelle pouvant influencer le comportement de certains produits (p. ex., structures en treillis, matériaux architecturés, etc.).

Pour pallier ces inconvénients, le projet COFFA, financé par l'agence ANR et réalisé dans le cadre d'une collaboration entre deux laboratoires de recherche, à savoir le laboratoire I2M à Bordeaux et le laboratoire G-SCOP à Grenoble, a été conçu pour intégrer les connaissances sur les procédés ALM et les phénomènes physiques connexes afin de faciliter le travail du concepteur au cours des différentes étapes de la chaîne numérique ALM, et ainsi réduire le temps requis pour chaque étape. Les différents objectifs du projet peuvent être repris comme suit:

- **Aide au concepteur.** La mise en œuvre d'une méthodologie de conception appropriée (et des outils connexes) visant à intégrer le concepteur (son expertise et son point de vue) pendant toute phase de la chaîne numérique ALM.
- **Une représentation appropriée de la topologie du produit.** Le développement d'un descripteur topologique approprié, basé sur des entités géométriques pures qui peuvent être facilement interfacées avec l'algorithme d'optimisation topologique développé au laboratoire I2M ainsi qu'avec un logiciel de conception assisté par ordinateur (CAO) commercial et qui donne (avec un bon niveau de précision et de confiance) la réponse physique (mécanique, thermique, etc.) de la structure.

- **L'intégration de solutions optimisées dans l'environnement de CAO.** Le développement d'une nouvelle représentation mathématique de formes complexes (correctement paramétrées directement dans l'environnement CAO) qui sera interfacée avec l'outil d'optimisation topologique.
- **L'outil de reconstruction de surface.** L'intégration d'un outil de reconstruction de surface automatique (ou semi-automatique) pour minimiser le temps passé sur cette étape.
- **Contraintes de fabrication.** L'intégration des contraintes de fabrication liées au processus ALM spécifique dans la formulation du problème d'optimisation de la topologie depuis la phase de conception préliminaire.
- **L'intégration d'analyses multi-échelles dans le processus d'optimisation.** L'intégration d'analyses multi-échelles et la prise en compte des difficultés liées à l'hétérogénéité et à l'anisotropie de matériaux complexes dans le processus d'optimisation sont des enjeux majeurs. Aujourd'hui, ces aspects ne sont pas intégrés dans les logiciels d'OT du commerce (Hyperworks[®], ANSYS[®], ABAQUS[®], etc.). L'intégration des spécificités des analyses multi-échelle dans un logiciel d'OT n'est pas une tâche anodine. Plusieurs défis scientifiques relatifs à cette tâche peuvent être évoqués : quelle est la méthode d'homogénéisation adaptée (vis-à-vis des temps de calcul et de la précision de calcul) à un processus d'OT ? Comment prendre en compte le couplage faible et fort entre les échelles du problème lorsque les descripteurs topologiques sont définis à chaque échelle ? Comment assurer le respect de la conditions sur la séparation entre échelles et, donc, la validité des résultats de la méthode d'homogénéisation et du processus d'OT ? Comment calculer le gradient des réponses physiques à chaque échelle en cas de couplage faible / fort ? Les réponses à ces questions trouvent un réel intérêt dans le cadre de la conception de matériaux et structures architecturés dans divers domaines (biomédical, aéronautique, automobile, énergétique, etc.).

Les défis scientifiques relevés dans la thèse

Compte tenu des enjeux décrits ci-dessus, cette thèse se focalise sur la prise en compte des spécificités des analyses multi-échelles dans l'OT et sur le développement d'un outil de reconstruction de surface semi-automatique pour le post-traitement des frontières de topologies optimisées déterminées

à l'aide d'un logiciel d'OT original développé au laboratoire I2M. Plus en détail, les sujets abordés dans ce manuscrit sont les suivants.

1. La formulation (et l'intégration) de problèmes multi-échelle au sein de la méthode d'optimisation topologique basée sur les hypersurfaces NURBS (de l'anglais *non-uniform rational basis spline*) et sur l'approche SIMP (de l'anglais *solid isotropic material with penalisation*) développée au laboratoire I2M est abordée. Le nouvel algorithme qui en résulte permet d'obtenir des composants optimisés en termes de topologie et d'anisotropie (à toute échelle pertinente du problème). En particulier, l'approche proposée est appliquée à la conception multi-échelle de matériaux cellulaires architecturés (MCA). La topologie du MCA est optimisée à chaque échelle impliquée dans la formulation du problème, notamment l'échelle du volume élémentaire représentatif (VER) et l'échelle macroscopique du produit en tenant compte du couplage faible entre les échelles. Dans ce manuscrit, le terme "couplage faible" entre échelles doit être interprété comme suit : au cours du processus d'optimisation, la variable topologique introduite à l'échelle du VER (aussi appelée échelle inférieure) affecte les réponses structurelles définies aux échelles inférieure et supérieure, tandis que la variable topologique définie à l'échelle supérieure (c'est-à-dire l'échelle macroscopique) n'affecte que les réponses structurelles macroscopiques. L'efficacité de l'approche proposée est testée à la fois sur des problèmes de référence 2D et 3D tirés de la littérature et validée via des essais effectués sur des éprouvettes optimisées réalisées au laboratoire I2M.
2. Un outil de reconstruction de surface semi-automatique a été développé pour manipuler les résultats des problèmes 3D afin d'obtenir une représentation CAO-compatible des surfaces complexes constituant la frontière des topologies optimisées. En effet, dans le cadre de la méthode SIMP basée sur les hypersurfaces NURBS, à la fin du processus d'optimisation, la frontière de la topologie optimisée est obtenue à la suite d'une opération de seuillage effectuée sur une hyper-surface NURBS 4D. Par conséquent, bien que la topologie soit décrite, à chaque itération, par une entité NURBS explicite, la frontière de la topologie optimisée est disponible sous forme d'une surface implicite (qui n'est pas compatible avec les logiciels CAO). Grâce à un logiciel commercial (par exemple, ParaView®), on peut obtenir la frontière du composant optimisé. Cette surface est représentée via un format de langage de tessellation standard natif (STL), qui est composé d'un ensemble de facettes triangulaires, avec leur vecteur nor-

mal relatif. Néanmoins, bien qu'un fichier STL dérivée d'une entité NURBS 4D ait de bonnes caractéristiques en termes de représentation des surfaces composant la frontière de la topologie optimisée (aucun triangle dégénéré ou manquant n'est présent dans le format STL), il ne peut pas fournir une représentation explicite de la frontière de la topologie optimisée et, par conséquent, il n'est pas compatible avec les logiciels CAO. La notion de compatibilité CAO utilisée ci-dessus est liée à la possibilité de modifier les propriétés d'une surface continue par des opérations simples (disponibles dans n'importe quel logiciel CAO) en termes de continuité locale ou de genre (cette dernière notion est liée au nombre de trous dans la surface). L'efficacité de l'outil de reconstruction semi-automatique développé dans cette thèse est testée sur certaines surfaces complexes tirées de la littérature et comparée aux résultats trouvés via d'autres méthodes.

La structure du manuscrit et le contenu des Chapitres

Afin d'aborder correctement les défis décrits dans la section précédente, le manuscrit (qui est rédigé en anglais) est articulé autour de 8 Chapitres.

Le premier Chapitre porte sur la description du contexte scientifique, de la problématique clé abordée dans le cadre du projet COFFA et des enjeux scientifiques associés. L'étude bibliographique sur laquelle repose la thèse est présentée au Chapitre 2. Trois thèmes principaux sont abordés dans l'état de l'art : 1) les principales méthodes d'OT disponibles dans la littérature ; 2) l'intégration des analyses multi-échelle dans les méthodes d'OT ; 3) les méthodes numériques traitant du problème de la reconstruction de surface. En ce qui concerne l'intégration des analyses multi-échelle dans les stratégies d'OT, l'étude bibliographique aborde les approches disponibles dans la littérature concernant la d'OT à l'échelle inférieure seulement et aux échelles inférieure et supérieure simultanément. Les questions théoriques / numériques liées à l'intégration des techniques générales d'homogénéisation numérique dans les problèmes d'OT multi-échelle et la nature du couplage entre les échelles (faible ou forte) sont discutées en profondeur. Des études numériques/expérimentales très récentes visant à démontrer l'efficacité des approches d'OT multi-échelles sont également présentées.

Concernant l'état de l'art sur les méthodes traitant du problème de reconstruction de surface, les méthodes manuelles et semi-automatiques sont présentées. En particulier, il est montré que les problèmes de reconstruc-

tion de surface peuvent être divisés en deux sous-problèmes : le premier porte sur la détermination d'une paramétrisation appropriée de la surface triangulaire initiale, tandis que le second se concentre sur la résolution d'un problème d'approximation de surface, dont le but est de trouver la meilleure surface paramétrique explicite approximant la surface triangulaire (cible).

Le Chapitre 3 présente les fondements de la méthode SIMP basée sur les hypersurfaces NURBS développée au laboratoire I2M et les principales caractéristiques du code SANTO (de l'anglais *SIMP and NURBS for topology optimisation*).

Dans le Chapitre 4, les principales caractéristiques de l'approche d'OT multi-échelle sont présentées. En particulier, dans ce Chapitre, le descripteur topologique n'est défini qu'à l'échelle du VER et la formulation du problème comprend des réponses structurelles définies aussi bien à l'échelle inférieure qu'à l'échelle supérieure. L'accent est mis sur l'influence du type de symétrie élastique du VER et des contraintes technologiques de fabrication (par exemple la contrainte sur l'épaisseur minimale imprimable) sur la topologie optimisée du VER. En outre, l'importance du choix d'une méthode d'homogénéisation appropriée est également discutée en mettant en évidence certains aspects liés aux coûts de calcul.

L'approche proposée dans ce Chapitre tient compte de la variable topologique définie uniquement à l'échelle du VER, tandis que les réponses physiques peuvent être définies à chaque échelle du problème, selon les critères introduits dans la formulation du problème d'optimisation. L'approche proposée est basée sur les hyper-surfaces NURBS, sur la méthode aux éléments finis standard et sur la méthode d'homogénéisation SEHM (de l'anglais *strain energy homogenisation method*), à savoir une stratégie d'homogénéisation numérique basée sur l'équivalence de l'énergie de déformation entre milieu hétérogène et homogène équivalente pour effectuer la transition d'échelle.

La méthode a été testée sur des structures benchmark 2D et 3D tirées de la littérature: certaines solutions optimales sont représentées (à titre illustratif) dans les figures 4.5 et 4.10 (plus de détails sont données dans le Chapitre 4).

Les résultats trouvés sont encourageants et certaines caractéristiques de l'approche proposée méritent d'être soulignées.

1. Trois principaux avantages du formalisme NURBS peuvent être clairement identifiés : (a) contrairement à l'approche SIMP classique, pour réduire l'effet damier et la dépendance de la topologie optimisée de la finesse du maillage, il n'est pas nécessaire de définir un filtre, car la propriété de support local des entités NURBS établit une relation im-

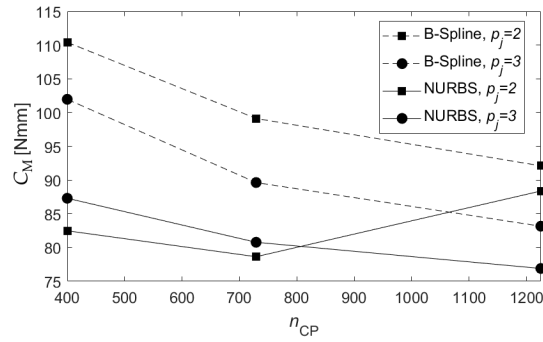


Figure 0.1 – Influence du nombre de points de contrôle et des degrés sur la topologie optimale du VER pour un problème 2D

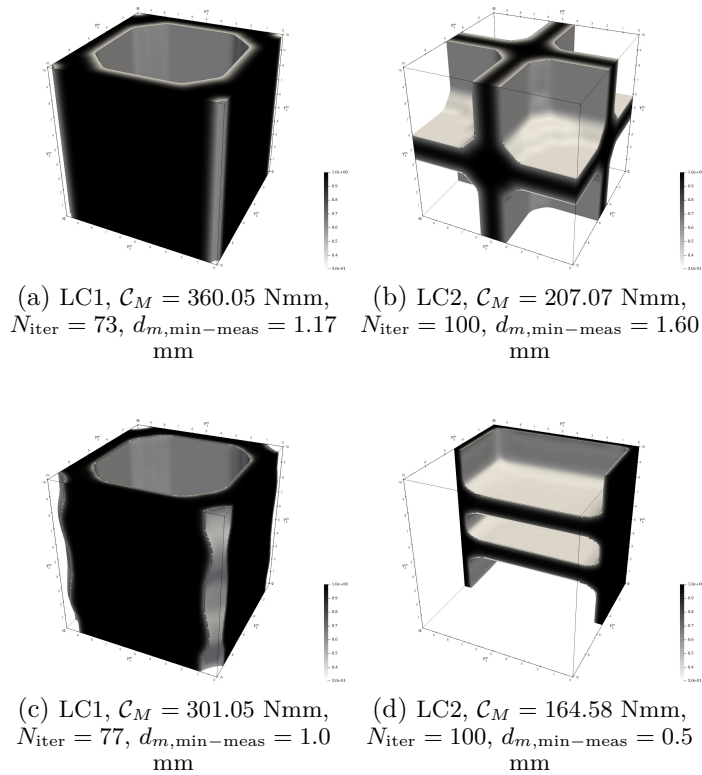


Figure 0.2 – Influence de la condition de chargement sur la topologie optimale du VER pour un problème 3D : (a)-(b) solution B-spline, (c)-(d) solution NURBS.

plicité entre la pseudo-densité des éléments contigus, (b) par rapport à l'approche SIMP classique, le nombre de variables de conception est réduit et (c) la phase de reconstruction CAO est simplifiée grâce à l'utilisation des NURBS.

2. Une analyse de sensibilité de la topologie optimisée du VER aux paramètres entiers de l'entité NURBS a été effectuée. Contrairement au problème classique de la minimisation de la souplesse soumise à une contrainte sur la fraction volumique pour des problèmes mono-échelle, lorsque des entités B-spline sont employées pour décrire le champ de pseudo-densité du VER, plus le nombre de points de contrôle est élevé (pour un degré donné) ou plus le degré des polynômes de Bernstein est élevé (pour un nombre donné de points de contrôle) plus la valeur de la fonction objective est petite. Inversement, lorsque des entités NURBS sont utilisées pour décrire la variable topologique VER, aucune règle générale ne peut être définie et les résultats semblent satisfaire approximativement la tendance globale observée dans les travaux précédents (c.-à-d. plus le degré est petit ou plus le nombre de points de contrôle est élevé, plus la valeur de la fonction objective est faible). De plus, un excellent compromis entre les coûts de calcul et les performances de la solution finale peut être réalisé en utilisant un nombre de points de contrôle égal aux trois quarts du nombre d'éléments de maillage.
3. L'influence des poids de l'entité NURBS sur la topologie optimisée a été évalué. En particulier, en considérant le même nombre de points de contrôle et de degrés, la fonction objectif de la solution NURBS est inférieure à celle B-spline, et la frontière de la solution NURBS est plus lisse que celle de la solution B-spline.
4. L'influence de la solution initiale a été prise en compte. En particulier, les problèmes d'OT multi-échelles sont fortement non-convexes et se caractérisent par plusieurs minima locaux. Par conséquent, un soin particulier doit être mis dans le choix de la topologie initiale et des calculs d'optimisation multiples (en utilisant différents points de départ) doivent être effectués afin de trouver un minimum local efficace.
5. Le cas de chargement à l'échelle macroscopique influence fortement la topologie optimisée du VER. En particulier, afin de satisfaire les exigences du problème en question et de résister aux charges appliquées, la topologie du VER évolue vers une configuration optimisant la réponse élastique macroscopique du continuum.

6. La contrainte technologique sur l'épaisseur minimale est correctement prise en compte, sans introduire de contrainte d'optimisation explicite, en définissant correctement les paramètres entiers de l'entité NURBS.
7. Les meilleures performances, en termes de coûts de calcul lorsqu'elles sont utilisées dans le cadre d'OT multi-échelle, de la méthode SEHM basée sur l'énergie de déformation des éléments par rapport à la méthode SEHM basée sur les contraintes moyennes des éléments ont été rigoureusement éprouvées.

En ce qui concerne les perspectives de l'étude présentée au Chapitre 4, ce travail est loin d'être exhaustif sur le thème des analyses multi-échelle et de la conception des matériaux architecturés au moyen de l'OT. Premièrement, la méthodologie proposée devrait être étendue au cas des problèmes de l'OT multi-échelle où les variables topologiques sont définies à différentes échelles (cet aspect sera abordé dans le Chapitre 5). À cette fin, dans le cadre de la méthode SIMP basée sur les hypersurfaces NURBS, le nombre d'entités NURBS devrait être égal, au moins, au nombre d'échelles impliquées dans la formulation du problème. Les relations existant entre ces entités (c'est-à-dire les variables topologiques définies à différentes échelles) devraient être soigneusement déterminées afin d'énoncer correctement le problème d'optimisation et de satisfaire les hypothèses à la base de la méthode SEHM. Deuxièmement, les contraintes technologiques, liées au procédé de fabrication additive, devraient être intégrées dans la formulation du problème d'OT multi-échelle, en particulier en termes de caractéristiques géométriques du VER, par exemple, angle de surplomb, courbure admissible, etc. Enfin, des critères de tenue appropriés devraient être formulés pour le matériau anisotrope homogène à l'échelle macroscopique et intégrés dans la formulation du problème d'OT multi-échelle. En outre, afin d'identifier les régions les plus critiques à l'échelle macroscopique et de transférer le champ de contrainte/déformation local au VER, une méthode d'homogénéisation adaptée prenant en compte le couplage fort entre les échelles devrait être développée et intégrée dans le processus d'OT.

Dans le Chapitre 5, la formulation des problèmes d'OT multi-échelle est étendue au cas plus général où le descripteur topologique est défini aux échelles inférieure et supérieure. L'importance d'une formulation appropriée de certains critères, comme la condition de séparation entre échelles, la contrainte technologique sur l'épaisseur minimale imprimable à l'échelle inférieure, la contrainte de masse/volume aux deux échelles est discutée en détail. En outre, l'effet des conditions limites mixtes non nulles du type Neumann-Dirichlet et l'influence du type de symétrie élastique du VER sur la topologie optimisée aux échelles inférieure et supérieure sont étudiés.

Dans ce Chapitre, une approche pour l'optimisation simultanée des propriétés du matériau et de la topologie de matériaux architecturés a été présentée. Plus précisément, le problème de conception multi-échelle d'un matériau architecturé est formulé comme un problème d'OT à deux échelles. Dans ce contexte, deux variables topologiques ont été introduites : la première est définie à l'échelle du VER (qui peut être l'échelle microscopique ou mésoscopique, selon les longueurs caractéristiques du problème), tandis que la deuxième est définie à l'échelle macroscopique. Un couplage faible entre les échelles inférieure et supérieure a été considéré dans la formulation du problème. En effet, les réponses structurelles à l'échelle supérieure dépendent à la fois du descripteur topologique défini à cette échelle et de celui introduit à l'échelle inférieure par le calcul de la matrice d'élasticité équivalente du matériau homogène fictif, qui remplace le VER à l'échelle supérieure. Dans ce contexte, la variable topologique à chaque échelle est représentée par le champ de pseudo-densité de la méthode SIMP, qui est décrite au moyen d'une hypersurface NURBS et la transition d'échelle est correctement définie à travers la méthode SEHM basée sur l'énergie de déformation. Les entités NURBS sont exploitées efficacement pour dériver la relation entre les variables topologiques définies à différentes échelles et aussi pour déterminer l'expression analytique du gradient des réponses physiques impliquées à toute échelle.

La méthode a été testée sur des structures benchmark 2D et 3D tirées de la littérature. Des exemples de topologies optimisées sont fournies (à titre illustratif) dans les Figures 5.7 et 0.4, pour des cas 2D et 3D, respectivement.

Les résultats trouvés (détaillés dans le Chapitre 5) ont permis de mettre en avant certaines caractéristiques de la méthodologie proposée. Tout d'abord, certains avantages du formalisme NURBS peuvent être clairement identifiés : (a) puisque le descripteur topologique est représenté par le champ de pseudo-densité sous la forme d'une entité NURBS, la topologie optimisée ne dépend pas de la finesse du maillage du modèle aux éléments finis, contrairement à la méthode classique SIMP ; b) contrairement à l'approche classique SIMP, il n'est pas nécessaire de définir un filtre pour réduire la dépendance de la topologie de la qualité du maillage, puisque la propriété de support local de l'hypersurface NURBS établit une relation implicite entre les éléments contigus; c) par rapport à l'approche classique SIMP, le nombre de variables de conception est réduit; d) puisque la topologie est décrite par une entité NURBS, la frontière de la topologie est disponible à chaque itération du processus d'optimisation, donc l'intégration des contraintes de nature géométrique (par exemple, sur la courbure locale de la frontière, sur la direction locale du vecteur tangent à la frontière, l'épaisseur maximale des branches topologiques, etc.) dans la formulation du problème

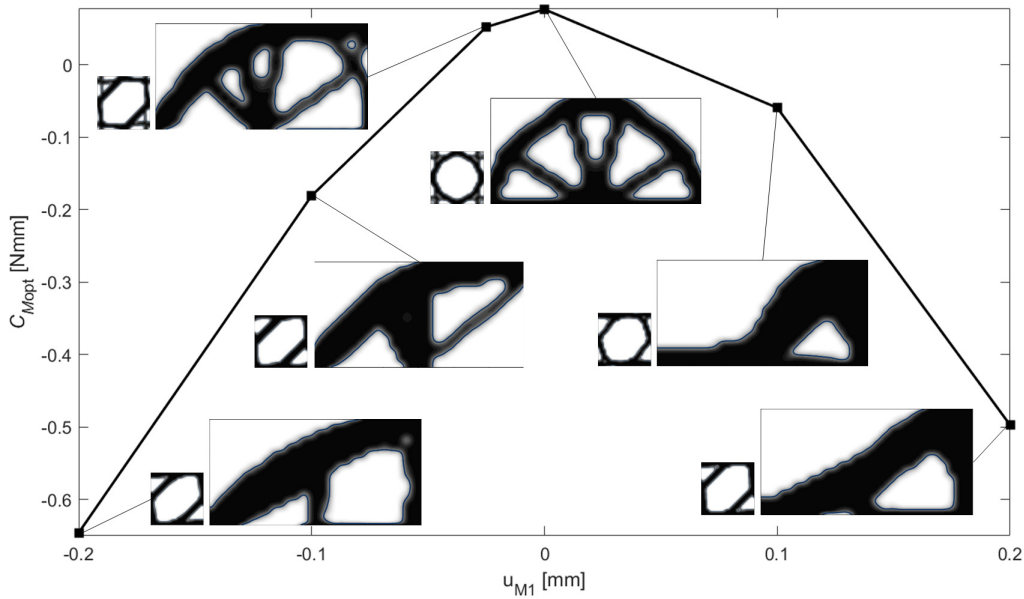


Figure 0.3 – Influence du déplacement imposé sur la topologie optimale aux échelles inférieure et supérieure pour un problème 2D

et la phase de reconstruction CAO de la frontière de la topologie optimisée deviennent des tâches relativement simples.

Bien entendu, comme dans le cas des résultats obtenus pour les problèmes d'OT mono-échelle avec la méthode SIMP basée sur les NURBS [108, 110], la topologie optimisée dépend des paramètres entiers de l'hypersurface NURBS, qui ont un impact direct sur la taille du support local. Deuxièmement, il a été démontré que, selon la formulation du problème, les valeurs de la fraction de volume/masse macroscopique et de la fraction de volume VER comme prévu, ont une forte influence à chaque échelle : une attention particulière doit être portée au choix de la combinaison de ces contraintes pour éviter des topologies "bizarres". Troisièmement, l'influence du groupe de symétrie élastique du VER sur la topologie finale, aux deux échelles, a été considérée. Les résultats mettent en évidence que, selon le problème étudié, forcer une symétrie élastique prédéfinie (orthotropie, isotropie transversale, etc.) pourrait se révéler un mauvais choix car des solutions complètement anisotropes caractérisées par des performances équivalentes ou meilleures peuvent exister. Par analogie avec l'optimisation multi-échelle des matériaux et structures composites, cela est dû à la non-convexité du problème d'optimisation et à l'existence de minima locaux équivalents caractérisés par des propriétés très différentes. Quatrièmement, l'influence de la solu-

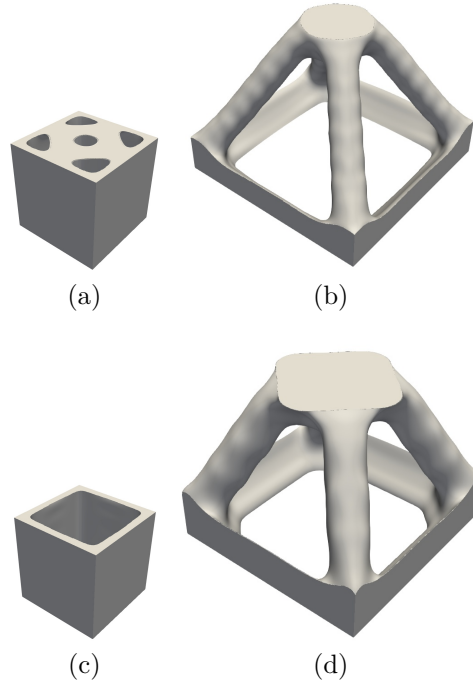


Figure 0.4 – Influence de la contrainte sur la séparation d'échelle sur la topologie optimale aux échelles inférieure et supérieure pour un problème 3D

tion initiale sur les topologies optimisées aux deux échelles a été prise en compte. Comme prévu, les résultats obtenus représentent une confirmation d'un fait bien établi : les problèmes d'OT multi-échelle des matériaux architecturés sont non-convexes; par conséquent, le choix de la topologie de départ du VER est d'une importance primordiale et a une forte influence sur la topologie optimisée aussi bien du VER que de la structure.

En outre, l'influence des conditions aux limites mixtes non-nulles du type Neumann-Dirichlet BCs sur la topologie optimisée a été étudiée. Les résultats obtenus mettent en évidence que, pour satisfaire les exigences du problème en cause et résister aux charges appliquées, la topologie du VER et la topologie macroscopique évoluent vers une configuration optimisant la réponse élastique macroscopique du matériau homogène équivalent, ainsi que la distribution de ce matériau à l'échelle supérieure.

Enfin, l'effet de la contrainte sur l'épaisseur minimale à chaque échelle du problème sur les topologies optimisées est correctement pris en compte, sans qu'il soit nécessaire d'introduire une contrainte d'optimisation explicite. En effet, cette contrainte peut être facilement satisfaite en définissant correcte-

ment les paramètres entiers de l'entité NURBS représentant la variable topologique à chaque échelle.

En ce qui concerne les perspectives sur ce sujet, plusieurs défis restent à relever. Tout d'abord, un ensemble de contraintes technologiques pertinentes, liées au processus de fabrication additive, devrait être intégré dans la formulation du problème d'OT multi-échelle, par exemple, angle de surplomb, courbure admissible, etc. Deuxièmement, afin de concevoir des matériaux architecturés optimisés en termes de tenue mécanique, une procédure d'homogénéisation appropriée avec un couplage fort entre les échelles devrait être développée et intégrée dans le processus d'optimisation. Enfin, des critères de défaillance appropriés aux échelles supérieure et inférieure devraient être dérivés et intégrés dans la formulation du problème d'OT multi-échelle pour le matériau anisotrope homogène à l'échelle macroscopique et pour le matériau à l'échelle du VER.

Le Chapitre 6 porte sur la validation expérimentale de l'approche d'OT multi-échelles présentée dans le Chapitre 5 à travers un test de flexion à trois points sur des topologies optimisées imprimées par le procédé de stéréolithographie en utilisant une résine thermoplastique. Dans ce Chapitre, les solutions optimisées déterminées par la méthode SIMP basée sur les NURBS, en considérant différentes formulations de problèmes, ont été validées expérimentalement. En particulier, trois cas d'études sont considérés : dans le premier cas, le descripteur topologique est défini uniquement à l'échelle macroscopique; dans le second cas, la variable topologique est introduite exclusivement à l'échelle du VER; dans le dernier cas, le descripteur topologique est introduit aux deux échelles simultanément. Pour chaque formulation du problème, l'objectif est de maximiser la rigidité de flexion en considérant des contraintes sur la légèreté, sur l'épaisseur minimale imprimable, et, lorsque le descripteur topologique est défini simultanément à l'échelle du VER et à l'échelle macroscopique, deux autres exigences sont prises en compte : la condition de séparation d'échelle (pour assurer la validité des résultats de la méthode SEHM) et une contrainte sur la fraction volumique de la phase solide composant le VER. Dans chaque cas, les conditions limites imposées à l'échelle macroscopique sont celles qui caractérisent l'essai de flexion à trois points : de cette façon, les topologies optimisées obtenues à la fin du processus peuvent être facilement fabriquées et validées expérimentalement.

Les topologies optimisées résultant des trois cas d'études ont été imprimées via d'études et validées par un essai de flexion à trois points. Bien entendu, une campagne expérimentale préliminaire d'essais a été menée pour caractériser le comportement (en traction et en flexion) de la résine thermoplastique constituant le matériau constitutif des éprouvettes optimisées.

Il est à noter que, bien que l'optimisation de la topologie ait été réalisée en supposant un comportement élastique linéaire du matériau composant l'échantillon et sous l'hypothèse de petits déplacements et de déformations, la comparaison entre les résultats numériques et expérimentaux est effectuée a posteriori par une analyse numérique non-linéaire sur les topologies optimisées reconstruites (c.-à-d., après reconstruction de leur frontière). Certaines points de la méthodologie proposée méritent d'être soulignées après une analyse minutieuse des résultats numériques. Premièrement, les meilleures performances, en termes de rigidité de flexion, sont obtenues dans le premier cas de conception où le descripteur topologique n'est introduit qu'à l'échelle macroscopique. Cela signifie que, en ce qui concerne l'essai de flexion en trois points, la topologie optimisée est caractérisée par un matériau isotrope remplissant l'ensemble du VER et distribué de manière optimale à l'échelle macroscopique. Cela est confirmé également par les résultats des deuxième et troisième cas de conception, qui montrent que, pour satisfaire aux contraintes du problème d'optimisation et de résister aux charges appliquées, la topologie du VER et celle de la structure évoluent vers une configuration optimisant la réponse élastique macroscopique du VER (modélisé à l'échelle macroscopique comme un matériau homogène équivalent), ainsi que la distribution du matériau à l'échelle supérieure, mais puisque la contraintes sur la légèreté et celle sur la fraction volumique de la phase solide sont introduites, la topologie optimisée à l'échelle du VER ne peut pas converger vers la solution isotrope. Bien entendu, lorsqu'on considère la formulation la plus générale du problème, c'est-à-dire celle impliquant le descripteur topologique aux deux échelles, lorsque la contrainte sur la fraction volumique de la phase solide à l'échelle du VER est supprimée et que seule celle sur la masse globale de la structure est conservée, la solution optimisée coïncide avec celle du premier cas de conception (dans lequel le descripteur topologique est défini uniquement à l'échelle supérieure). En ce qui concerne la comparaison entre les résultats numériques et expérimentaux obtenus sur les topologies optimisées (pour chaque cas d'étude), en termes de courbe force-déplacement, l'utilisation d'une loi constitutive non-linéaire de la résine thermoplastique ainsi que la modélisation des régions de contact entre l'éprouvette et les supports de la machine permettent d'obtenir un bon accord entre les courbes numériques et expérimentales seulement lorsque une courbe σ - ε décrivant le comportement de flexion de la résine est utilisée. Néanmoins, certaines différences entre les résultats numériques et expérimentaux peuvent être observées pour certaines valeurs du déplacement appliqué. Pour obtenir des résultats meilleurs (et plus cohérents), la courbe de compression-traction complète décrivant le comportement réel de la résine rigide devrait être modélisée au moyen d'une

routine définie par l'utilisateur, mais cette tâche ne rentre pas dans le cadre du présent travail et pourrait constituer une perspective de cette étude.

Une autre perspective de ce travail concerne l'intégration du comportement non-linéaire du matériau constitutif dans le processus d'optimisation topologique, en développant également une stratégie d'homogénéisation non linéaire appropriée (en ce qui concerne les deuxième et troisième cas d'étude). Enfin, des critères de défaillance appropriés aux échelles supérieure et inférieure devraient être dérivés et intégrés dans la formulation du problème d'OT multi-échelle pour le matériau anisotrope homogène à l'échelle macroscopique et pour le matériau constitutif à l'échelle du VER afin d'optimiser non seulement la rigidité de la structure, mais aussi sa résistance.

Enfin, le Chapitre 7 est centré sur la description de la méthode de reconstruction de surface semi-automatique développée dans cette thèse; l'efficacité de la stratégie est prouvée sur plusieurs problèmes de référence tirés de la littérature. Dans ce Chapitre, une stratégie efficace et générale de reconstruction des surfaces ouvertes et fermées de genre supérieur ou égal à zéro a été présentée. Cette stratégie est, en effet, capable d'approximer des ensembles convexes et non convexes de points cibles et s'articule en deux phases : la phase de *mapping* et la phase de *fitting*. L'approche proposée repose sur les caractéristiques suivantes.

- La phase de mapping utilise la méthode SPM (de l'anglais *shape preserving method*) pour récupérer un paramétrage correct de chaque sous-domaine composant le nuage de points.
- La phase de fitting est formulée au sens le plus général, c'est-à-dire sans introduire d'hypothèses ou de règles simplificatrices sur l'ensemble des paramètres régissant la forme de la surface NURBS, qui est utilisée comme entité paramétrique pour approximer l'ensemble des points cibles. À cet effet, une nouvelle expression de la fonction objectif (tenant compte à la fois des variables entières et continues régissant la forme de l'entité NURBS), ainsi qu'une contrainte appropriée sur la non-singularité de la matrice des fonctions de base de la surface NURBS, a été introduite. De plus, le problème est présenté comme un problème d'optimisation sous contraintes spécial, où le nombre d'inconnues est inclus parmi les variables de conception. En fait, lorsque des paramètres entiers (c.-à-d. degrés et nombre de nœuds le long de chaque direction paramétrique) sont inclus, ainsi que les paramètres continus (c.-à-d. les valeurs de nœuds et les poids), parmi les variables de conception, le problème d'optimisation résultant est défini sur un espace de dimension variable, ce qui nécessite un algorithme d'optimisation adapté pour

- trouver une solution optimale faisable.
- La non-convexité du problème et le fait que l'espace de conception a une dimension variable sont les deux principales raisons à la base de l'utilisation de stratégies numériques avancées pour résoudre le problème d'optimisation connexe. A cet effet, la recherche de la solution du problème d'approximation de surface est effectuée à travers un outil d'optimisation hybride composé par l'union de l'algorithme génétique ERASMUS couplé à un algorithme déterministe. La stratégie d'optimisation est divisée en deux étapes. Pendant la première phase, où l'algorithme ERASMUS est utilisé pour déterminer, simultanément, la valeur optimale des variables de conception entières et continues. Grâce à une stratégie darwinienne à deux niveaux (permettant l'évolution simultanée des espèces et des individus), cet algorithme est capable de trouver une solution pour un problème d'optimisation défini sur un espace de dimension variable (avec un nombre variable de variables de conception). L'objectif du problème pendant cette phase est de fournir une solution pseudo-optimale de départ pour la deuxième phase d'optimisation (résolue via un algorithme déterministe) où seules les variables continues sont optimisées, tandis que les variables entières sont maintenues constantes.
 - La phase d'approximation (et la formulation du problème d'optimisation associé) a également été généralisée au cas de surfaces ouvertes et fermées de genre supérieur à zéro où un assemblage de surfaces NURBS (appelé entité poly-NURBS), correctement connectées, est utilisé pour approximer l'ensemble non-convexe des points cibles.

L'efficacité de l'approche proposée a été testée sur des benchmarks tirés de la littérature : les résultats obtenus grâce à la méthode proposée montrent des performances supérieures, en termes de précision, à ceux disponibles dans la littérature ; des exemples sont illustrés dans les Figures 7.9 et 7.18 pour des surfaces de genre 0 et 1, respectivement.

En ce qui concerne les perspectives de ce travail, deux défis restent à relever. Le premier est le développement d'une stratégie de segmentation complètement automatique pour définir les patchs qui composent la tessellation. L'objectif de cette stratégie est de réduire les décisions arbitraires de l'utilisateur qui pourraient affecter la forme des patchs (et, par conséquent, le résultat de la phase de mapping et la qualité de la surface approximante). Le deuxième défi consiste à formuler le problème de segmentation en tant que problème d'optimisation sous contraintes. En particulier, quelle est la meilleure stratégie pour diviser une tessellation donnée ? Quel est le nom-

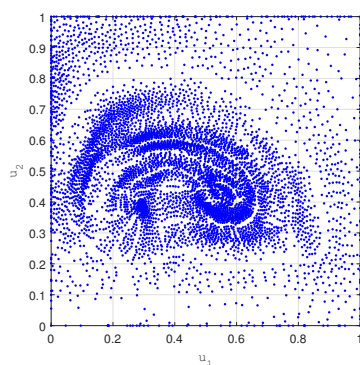
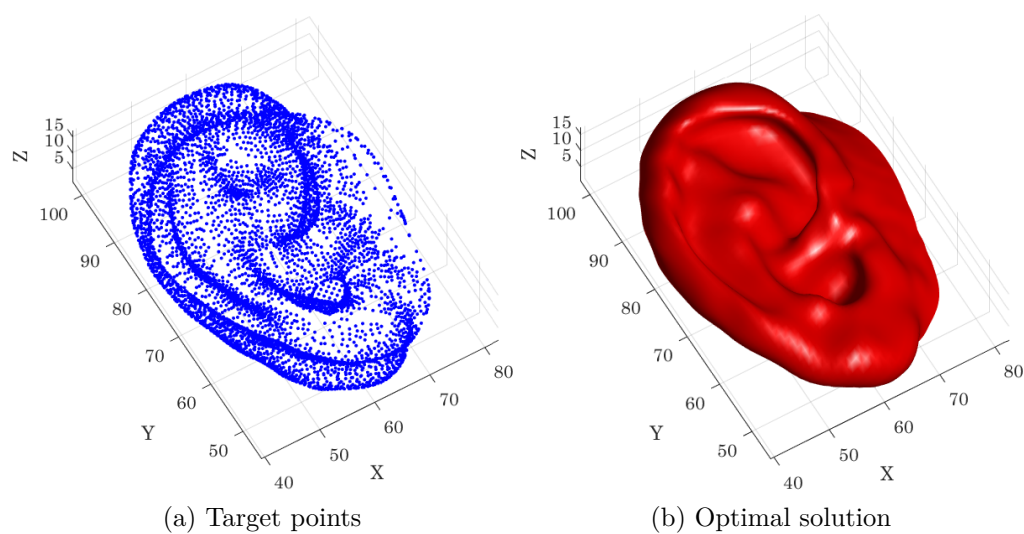


Figure 0.5 – Méthode de reconstruction appliquée à la *Ear Surface* : a) points cibles, b) surface NURBS, c) paramétrisation de la surface NURBS.

bre optimal de patches assurant une paramétrisation correcte de l'ensemble de la tessellation ? Quelle est la stratégie de segmentation optimale pour minimiser la distorsion et l'erreur de la surface d'ajustement finale ? Des recherches sont en cours sur ces aspects.

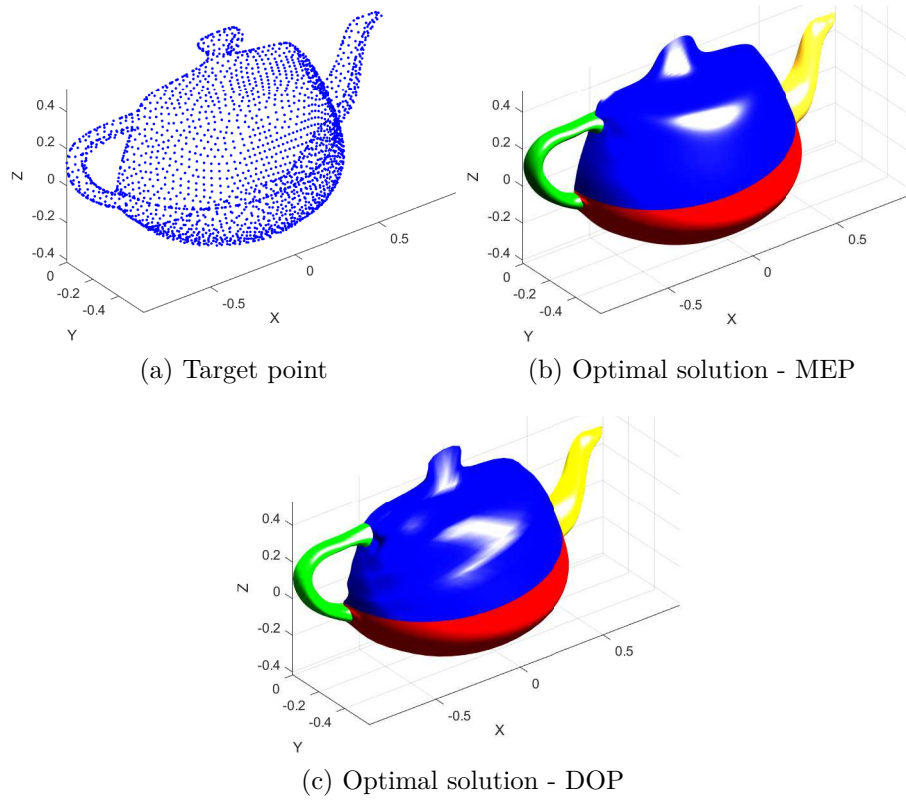


Figure 0.6 – Méthode de reconstruction appliquée à la *Kettle Surface* : a) points cibles, b) surface NURBS.

Chapter 1

Introduction

1.1 The COFFA project context

In the recent years, the Additive Layer Manufacturing (ALM) technology has become one of the most common production methods of the engineering industry. This increase in importance is due to respond to the growing demand of industries to produce customised components with complex geometries.

Unlike conventional manufacturing techniques, such as machining and stamping, that fabricate products by removing materials from a larger block or sheet, ALM creates the final shape by adding material. Therefore, these technologies have the ability of using the raw material in an efficient way, by minimising the energy and the material waste. In addition ALM can eliminate the design constraints linked to the traditional processes, hence offering a new space of possibilities for designers. ALM allows the creation of complex geometries, resistant structures and multi-scale structural patterns (i.e., lattice-like structure). ALM also allows realising multi-material parts either in a continuous way (gradient property materials) or in a discontinuous way (stacking of mono-material zones). For these reasons, the potential gain in cost, mass, functional performance and realization is considerable when compared to the possibilities offered by the classical subtractive processes.

Nevertheless, there are a number of disadvantages associated with the use of these technologies. Firstly, many defects (surface condition, porosities, shape defects, etc.) can appear on the parts manufactured through the different ALM processes, and there is no standard procedure to qualify the mechanical performance of the manufactured parts in the field of strength (robustness) as well as endurance (fatigue strength, durability, aging, etc.).

The objective of the design is to propose a product that meets the different requirements resulting from the customer's need and the need to be manufactured at a reasonable cost. In the actual design process, the designers alternate phases of synthesis during which they will propose and model shapes that they think meet the requirements, and phases of analysis during which they will verify this adequacy. In the case of additive manufacturing, the design of a product requires knowledge and methods that could exploit the freedom given by the ALM processes and could satisfy the constraints imposed by the physical phenomena employed by the technology. Therefore, the tools and the methods that should be developed to help designers must support both the synthesis and analysis phases.

Over the last few years, design and simulation commercial codes have evolved their offer trying, thus to cover this need. However, designers can experience difficulties when faced with complex software offers (topological optimization, numerical simulation), and, on the other hand, they have to deal with an indispensable evolution of design methodologies around these tools. Indeed, the optimization of structures must take into account, from the preliminary design phase, the technological constraints related to the ALM process and deal with multi-physics and multi-scale aspects that can influence the behavior of certain products (e.g., lattice structures).

To overcome these drawbacks, the COFFA project, funded by the ANR agency and carried out in the framework of a collaboration between two research laboratories, i.e., the I2M laboratory in Bordeaux and the G-SCOP laboratory in Grenoble, has been conceived to integrate the knowledge about the ALM manufacturing processes and the related physical phenomena to facilitate the work of the designer during the different stages of the ALM digital chain, and thus reduce the time required for each stage. The different objectives of the project can be resumed as follows:

- Aid to the designer. The implementation of a proper design methodology (and the related tools) aiming at integrating the designer (his expertise and his point of view) during any phase of the ALM numerical chain.
- A suitable and computationally-cheap representation of the product topology. The development of a suitable topological descriptor, based on pure geometric entities that can be easily interfaced with the topological optimization algorithm developed at the I2M laboratory as well as with commercial CAD software and that gives (with a good level of accuracy and confidence) the physical response (mechanical, thermal, etc.) of the structure.
- The integration of optimised solutions within the computer-aided design (CAD) environment. The development of a new mathemat-

ical representation of complex shapes (appropriately parameterized directly in the CAD environment) which will be interfaced with the topological optimization tool.

- The surface reconstruction tool. The integration of an automatic (or semi-automatic) surface reconstruction tool to minimize the time spent on this step.
- Manufacturability constraints. The integration of manufacturability constraints related to the specific ALM process in the formulation of the topology optimization problem since the preliminary design phase.
- The integration of multi-scale analyses into the design process. The integration of multi-scale analyses and of the difficulties related to the heterogeneity and anisotropy of complex materials in the design process is of capital importance. These aspects have been integrated in the topological optimization strategy based on non-uniform rational basis spline (NURBS) hyper-surfaces and on the solid isotropic material with penalisation (SIMP) method developed at the I2M laboratory.

1.2 The Thesis objectives

In the light of the aspects discussed above, this PhD thesis focuses on the consideration of multi-scale analyses in topological optimization and on the introduction of a semi-automatic surface reconstruction tool to be coupled with the topology optimisation (TO) software developed at the I2M laboratory. More in detail, the topics covered in this manuscript are the following ones.

1. The formulation (and the related integration) of multi-scale analyses within the topology optimisation method based on NURBS hyper-surfaces and on the SIMP approach developed at the I2M laboratory is faced. This task allows obtaining optimised components in terms of topology and anisotropy (at all relevant scales of the problem at hand). In particular, the proposed approach is applied to the multi-scale design of architected cellular materials (ACM). The topology of the ACM is optimised at each scale involved in the problem formulation, i.e., typically the scale of the representative volume element (RVE) and the macroscopic scale of the product by taking into account the weak coupling among scales. In this manuscript, the term "weak coupling" between scales must be interpreted as follows: during the optimisation process the topological variable introduced at

the RVE scale (also referred to as lower scale) affects the structural responses defined at both lower and upper scales, whilst the topological variable defined at the upper scale (i.e., the macroscopic scale) affects only the macroscopic structural responses. The effectiveness of the proposed approach is tested both on numerical benchmark problems taken from the literature and on experimental tests performed on optimised specimens carried out at the I2M laboratory.

2. A semi-automatic surface reconstruction tool has been developed to manipulate the results of 3D TO problems to obtain a CAD-compatible representation of complex surfaces constituting the boundary of the optimised topologies. In fact, in the framework of the NURBS-based SIMP method, at the end of the optimisation process, the boundary of the optimised topology is obtained as a result of a threshold operation on a NURBS hyper-surface. Therefore, although the topology is described, at each iteration, through a pure geometric explicit NURBS entity, the boundary of the optimised solution is available in implicit form. Through a commercial software (e.g., ParaView®), one can obtain the boundary of the optimised component. This latter is described by means of a triangulated surface, through a native standard tessellation language (STL) format, which is composed of a set of triangular facets, with their relative normal vector. Nevertheless, although an STL file has good characteristics in terms of representation of the surfaces composing the boundary of the optimised topology (no degenerate or missing triangles are present in the STL format), it cannot provide a continuous explicit parametrisation of the boundary and, accordingly, it is not compatible with CAD software. The notion of CAD-compatibility used above is related to the possibility of modifying the properties of a continuous surface through simple operations (available in any CAD software) in terms of its local continuity or in terms of its genus. The effectiveness of the semi-automatic reconstruction tool developed in this thesis is tested on some complex surfaces taken from the literature.

1.3 Outline of the work

The Thesis structure is conceived to provide an answer to each of the aforementioned goals. The Thesis outline is summarised here below.:

1. The bibliographic study on which the Thesis relies is presented in Chapter 2. Three main topics are addressed in the state of the art: 1) the main TO methods available in the literature; 2) the integration

of multi-scale analyses within TO methods; 3) the numerical methods dealing with the problem of surface reconstruction. As far as the integration of multi-scale analyses in TO strategies is concerned, a survey is proposed on the approaches available in the literature regarding both TO at the lower scale only and at the lower and upper scales concurrently. The theoretical / numerical issues related to the integration of general numerical homogenisation techniques in multi-scale TO problems and the nature of the coupling among scales (weak or strong) are deeply discussed. Very recent numerical/experimental studies aiming at showing the effectiveness on multi-scale TO approaches are discussed.

Regarding the literature survey on methods dealing with the surface reconstruction problem both manual and semi-automatic methods are presented. In particular, it will be shown that the surface reconstruction problems can be divided in two sub-problems: the first one deals with the determination of a suitable parametrisation of the initial triangulated surface, whilst the second one focuses on the resolution of a surface fitting problem, whose goal is to find the best parametric (i.e., explicit) surface approximating the triangulated (target) surface. The survey proposes different approaches available in the literature to deal with both sub-problems.

2. Chapter 3 introduces the fundamental of the NURBS-based SIMP method developed at the I2M laboratory and the main features of the SANTO (SIMP and NURBS for topology optimisation) code.
3. In Chapter 4, the main features of the multi-scale TO approach are presented. In particular, in this Chapter, the topological descriptor is defined only at the RVE scale and the problem formulation includes both lower and upper scales structural responses. The accent is put on the influence of the elastic symmetry type of the RVE and on the manufacturing requirements on the minimum printable size on the optimised topology of the RVE. Moreover, the importance of the choice of a suitable homogenisation method is also discussed by highlighting some aspects related to computational costs.
4. In Chapter 5, the multi-scale TO problem formulation is extended to the more general case wherein the topological descriptor is defined at both lower and upper scales. The importance of a proper formulation of some requirements, like the scale separation condition, the minimum member size constraint at the lower scale, mass/volume constraint at both scales are deeply discussed. Moreover, the effect of mixed non-zero boundary conditions of the Neumann-Dirichlet

type and of the elastic symmetry type of the RVE on the optimised topology at both lower and upper scales is investigated.

5. Chapter 6 deals with the experimental validation of the proposed multi-scale TO approach through a three point bending like test on optimised topologies printed by ALM processes for polymers.
6. Finally, Chapter 7 deals with the description of the semi-automatic surface reconstruction method developed in this Thesis; the effectiveness of the strategy is proven on several benchmark problems taken from the literature.

Chapter 2

State of the Art

2.1 Introduction to the state of the art

This Chapter aims at providing a non exhaustive state of the art about the three main topics discussed in this Ph.D. Thesis.

Firstly, the main topology optimisation (TO) methods and algorithms available in the literature are described, by highlighting advantages and shortcomings of each technique.

Secondly, a state of the art about the integration of multi-scale analyses in TO problems is presented. This part of the literature survey focuses essentially on the application of multi-scale TO methods to the design of architected cellular materials.

Finally, the last part of the Chapter focuses on a brief literature survey of the surface reconstruction methods available in the literature: the focus is put on parametrisation and surface fitting techniques to recover the explicit form of complex surfaces from a set of target points.

2.2 On the topology optimisation methods

In recent decades, TO has become a powerful design method in various fields of engineering, thanks to its ability of defining, iteratively, the distribution of one or more material phases in the volume of the component to satisfy the user-defined requirements and, simultaneously, reduce the mass of the part. Usually, the problem at hand is formulated as a constrained non-linear programming problem CNLPP, with the goal of minimising a given merit function by satisfying the set of imposed design requirements. In this literature review, the density-based methods, the level-set method (LSM), as well as the Evolutionary Structural Optimisation (ESO) and the

Bi-directional Evolutionary Structural Optimisation (BESO) methods are considered.

2.2.1 Density-based TO methods

In the context of density-based TO methods the topological descriptor is represented by a pseudo-density field which is projected over the mesh of the finite element (FE) model representing the discretisation of the continuum. A fictitious density function, which takes values in the interval $[0, 1]$, is then affected (through a pertinent penalty scheme) to the characteristic tensors of each element describing the physical phenomena of the problem at hand, e.g., elasticity tensor for structural mechanics, conductivity tensor for thermal problems, etc. Lower and upper bounds of the density function correspond to “void” and “solid” phases, respectively. Inasmuch as a physically meaningful, solid-void design is sought, “gray” elements, characterised by intermediate values of the density function, are allowed but penalised during optimisation. The physical properties of each element are computed (and penalised) according to the local pseudo-density value. The Solid Isotropic Material with Penalisation (SIMP) scheme is the most widespread penalty approach used for TO [1]. The success of the SIMP method is due to its efficiency and compactness [2].

A short explanation of the mathematical formulation of the SIMP strategy is presented below. Let $\Omega \subset \mathbb{R}^3$ be the design domain defined in the Euclidean 3D space, wherein a Cartesian orthogonal frame $O(x_1; x_2; x_3)$ is defined. Consider the classical problem of finding the optimal distribution of a solid isotropic heterogeneous material in the domain Ω with the goal of minimising the virtual work made by the external forces applied to the structure is minimised by satisfying, simultaneously, a volume equality constraint. The optimal material distribution Ω_{mat} in the design domain Ω is found defining a fictitious density function in all the domain Ω . As mentioned above, the stiffness tensor values, defined over the domain Ω , are penalised according to the following formula:

$$E_{ijkl}(\rho(x_1, x_2, x_3)) = \rho(x_1, x_2, x_3)^\alpha E_{ijkl}^0, \quad i, j, k, l = 1, 2, 3, \quad (2.1)$$

where E_{ijkl}^0 is the stiffness tensor of the bulk isotropic material and $\alpha > 1$ is a suitable parameter used to penalise the solution having intermediate densities. In the FE formulation of an equilibrium problem for a linear static analysis, let $\mathbf{u} \in \mathbb{R}^{N_{\text{DOF}}}$ be the vector of the full set of nodal displacements and rotations (called *degrees of freedom* (DOFs)), whose number is N_{DOF} and $\mathbf{f} \in \mathbb{R}^{N_{\text{DOF}}}$ be the vector of nodal external forces, the relation between

these two quantities is described by the equilibrium equation (static case under homogeneous Dirichlet's boundary conditions (BCs)) as follows:

$$\mathbf{K}\mathbf{u} = \mathbf{f}, \quad (2.2)$$

where $\mathbf{K} \in \mathbb{R}^{N_{\text{DOF}} \times N_{\text{DOF}}}$ is the global stiffness matrix of the structure, which can be expressed as:

$$\mathbf{K} = \sum_{e=1}^{N_e} \rho_e^\alpha \mathbf{L}_e^T \mathbf{K}_{0e} \mathbf{L}_e, \quad (2.3)$$

where $\mathbf{K}_{0e} \in \mathbb{R}^{N_{\text{DOF},e} \times N_{\text{DOF},e}}$ is the unpenalised element stiffness matrix expressed in the global reference frame (the number of DOFs of the element is $N_{\text{DOF},e}$), $\mathbf{L}_e \in \mathbb{R}^{N_{\text{DOF},e} \times N_{\text{DOF}}}$ is the connectivity matrix of element e , ρ_e is the value of the fictitious density at the generic element centroid and α is the penalisation coefficient (usually $\alpha = 3$). The work of external forces (which equals the one of internal forces) of the whole structure is computed as:

$$\mathcal{W} = \mathbf{u}^T \mathbf{f} = \mathbf{u}^T \mathbf{K}\mathbf{u}, \quad (2.4)$$

The problem of minimising the work of external forces subject to a constraint on the volume could be formulated as:

$$\begin{aligned} \min_{\rho_e} \quad & \frac{\mathcal{W}}{\mathcal{W}_{\text{ref}}} \\ \text{subject to :} \quad & \begin{cases} \mathbf{K}\mathbf{u} = \mathbf{f}, \\ \frac{V(\rho_e)}{V_{\text{ref}}} = \frac{\sum_{e=1}^{N_e} \rho_e V_e}{V_{\text{ref}}} = \gamma, \\ \rho_{\min} \leq \rho_e \leq 1, \quad e = 1, \dots, N_e, \end{cases} \end{aligned} \quad (2.5)$$

where \mathcal{W}_{ref} and V_{ref} are the reference values of the work of external forces and of the volume, respectively, V is the volume of the material domain, V_e is the volume of the generic element (the number of elements is N_e), while γ is the predefined volume fraction and ρ_{\min} is the lower bound imposed on the density field to prevent singularity in the resolution of the FE analysis. Therefore, the design variables in the SIMP method are the pseudo-density values evaluated at the elements centroids, and consequently the number of variables is equal to N_e . The classical SIMP problem is ill-posed; the optimised topology depends on the mesh size. To overcome this limitation some approaches [3] introduce a control of the structure perimeter, e.g., a restriction on the number of holes, or on the spatial gradient of the density

function. Nevertheless, the most common techniques rely on reducing the mesh dependency through a filtering operation [4]. Filters introduce dependency among adjacent elements to avoid/reduce the occurrence of checkerboard patterns on the pseudo-density field. TO optimisation strategies can be local, e.g., the ones exploiting the gradient of objective and constraint function to update the design variables at each iteration, or global, e.g., based on meta-heuristics algorithms allowing for a better exploration of the design domain. Since the TO problems are generally non-convex, the second approach can lead to a global optimum. However, their use is not advisable because of the high computational cost related to the high number of design variables. The advantage of using mathematical programming is the possibility to exploit the information of the objective and constraint function derivatives with respect to the whole set of design variables. In the case of the problem 2.5, the derivatives of the work of the external forces and of the volume are reported here below. The partial derivative of the work of external forces, reads:

$$\frac{\partial \mathcal{W}}{\partial \rho_e} = -\alpha \rho_e^{\alpha-1} \mathbf{u}^T \mathbf{K}_e^0 \mathbf{u}, \quad e = 1, \dots, N_e. \quad (2.6)$$

If the work of external forces of a single element is introduced as:

$$\mathcal{W}_e = \rho_e^\alpha \mathbf{u}^T \mathbf{K}_e^0 \mathbf{u}, \quad (2.7)$$

Eq. 2.6 can be simplified as:

$$\frac{\partial \mathcal{W}}{\partial \rho_e} = -\alpha \rho_e^{\alpha-1} \mathcal{W}_e, \quad e = 1, \dots, N_e. \quad (2.8)$$

The volume partial derivative reads:

$$\frac{\partial V}{\partial \rho_e} = V_e, \quad e = 1, \dots, N_e. \quad (2.9)$$

In TO, the computation of the derivatives is referred to as sensitivity analysis. An overview of the classical density-based TO algorithm based on the SIMP penalisation scheme is presented in Fig. 2.1. An alternative to the mathematical programming procedure is represented by the optimality condition. The main idea is to exploit the information about the conditions of optimality in order to develop an efficient heuristic updating scheme for element densities. The drawbacks of this method rely on the lack of generality, since it is necessary to develop *ad hoc* rules for problem formulation. Indeed, developing optimality heuristic criteria is anything but trivial for structural

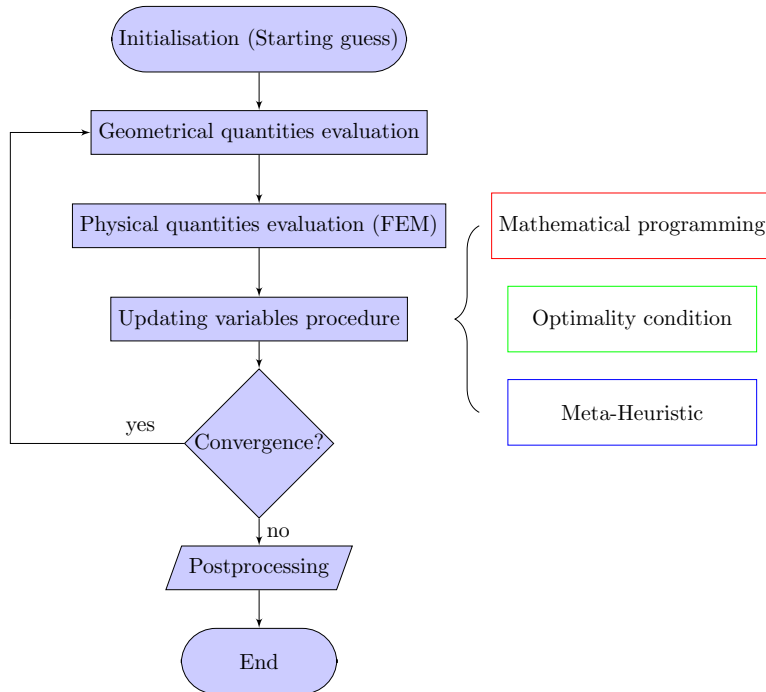


Figure 2.1 – General flowchart of the SIMP algorithm.

responses more complex than the work of external forces. Among the several gradient-based optimisation algorithms, the most exploited are the well known method of moving asymptotes (MMA) [5] and the enhanced globally convergent version of MMA (GCMMA) [6]. These methods replace the original objective function with an artificial convex or quasi-convex form approximating the original problem and iteratively updated according to the gradient information at the current point.

A summary of advantages and drawbacks of the density-based TO methods is provided here below.

Advantages

- Density-based methods are relatively easy to understand and can be coded in very compact scripts [7].
- The robustness of density-based methods has been widely tested in the literature. Indeed, they are very efficient and versatile for different problem formulations involving both local and global structural responses.
- Density-based methods are, today, available in well-established soft-

ware packages (Altair OptiStruct [8], TOSCA [9]), which constitute the reference for TO in the industrial field.

Drawbacks

- Since the pioneering works on TO, different strategies were proposed during the years to overcome classic TO drawbacks, like the checkerboard effect and the mesh dependence. Projection methods were proposed in [10] to mitigate these issues. In these methods, the design variables are the values of the fictitious density function at the nodes of the mesh, whilst the density at the element centroid is obtained through a Heaviside step function-based projection. Such a projection can be chosen in such a way to get a minimum length scale. However, the well-posedness of the problem is subject to an artificial choice (the filter size, the filter type, the projection method, etc.).
- Although their relative simplicity, density-based TO algorithms provide a FE-based description of the final geometry and a dedicated postprocessing phase must be carried out to obtain a smooth CAD-compatible design. This shortcoming involves both the mathematical nature and the lack of effective tools to interpret the final design in terms of CAD entities.
- In classical density-based TO algorithms is not possible to control of the boundary of the current topology during optimisation. This issue is related to the lack of a purely geometric entity describing the pseudo-density field (i.e., the topological descriptor).

2.2.2 Level-set method

The LSM applied in the TO framework [11–13] represents a valid alternative and a response to the limitations presented by density-based methods.

In the context of the the LSM, the topology is described through a suitable level-set function (LSF). This function defines, in an implicit form, the material phase or void zones, while the zero value represents the boundary of the topology at the current iteration. Let Ω be the material domain of the problem at hand, whose boundary is $\partial\Omega$. As usual, the material domain is embedded in the computational domain D . In this context, the structural boundary $\partial\Omega$ is represented implicitly by the zero-level of the LSF ϕ , which

is conventionally expressed as:

$$\begin{cases} \phi(\mathbf{x}) > 0 \Leftrightarrow \mathbf{x} \in \Omega \setminus \partial\Omega \\ \phi(\mathbf{x}) = 0 \Leftrightarrow \mathbf{x} \in \partial\Omega \\ \phi(\mathbf{x}) < 0 \Leftrightarrow \mathbf{x} \in D \setminus (\Omega \cap \partial\Omega). \end{cases} \quad (2.10)$$

An example of LSF for 2D TO problems is illustrated in Fig. 2.2.2. One can immediately infer that for a TO problem of dimension M a LSF function of dimension $M + 1$ is required to describe the topology of the continuum.

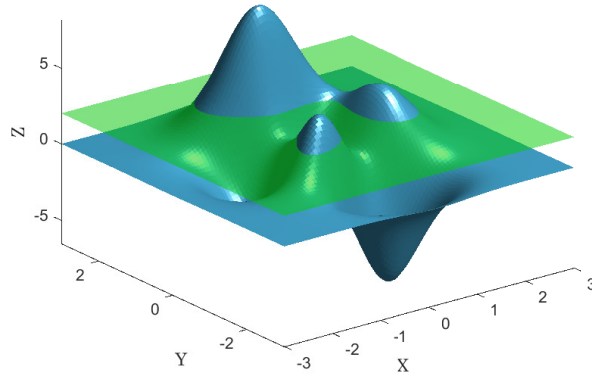
The flowchart of the LSM, described in the following is composed of six steps.

- 1- **LSF Parametrisation.** The first phase consists of the definition of the LSF function, which affects the nature of the TO problem in terms of non-linearity and convexity.

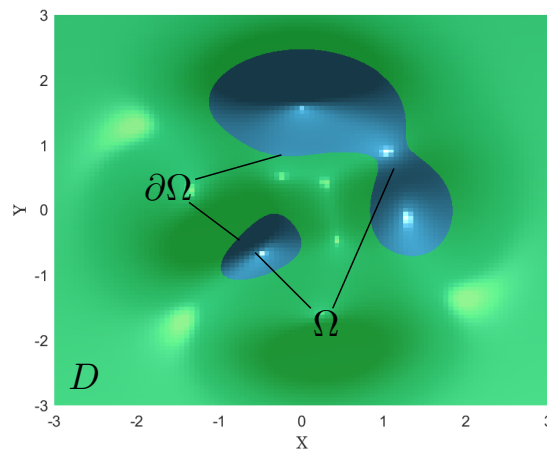
$$\Phi(\mathbf{x}, s) = \sum_i^n \Phi_i(\mathbf{x}, s) = \sum_i^n B_i(\mathbf{x}) s_i, \quad (2.11)$$

where $B_i(\mathbf{x})$ are the basis functions (BFs) depending on the coordinates, while s_i is the vector of parameters defining the LSF, which can be taken into account in the formula in different ways, e.g., as weighting factors. There are different ways to classify the nature of the LSF function, for example the size of the support domain, wherein the BF is not null. Starting from the local basis function, passing by the one with a midrange support size to finish with the global basis function one has an increase in the sensitivity of the responses to the LSF parameters, which corresponds to a faster evolution of the design. Another classification method concerns the type of BF. The radial BFs (RBFs) are the most commonly used, thanks to their simplicity, but they are commonly defined all over the design domain. However their mathematical formulation can be changed to pass from the global support to a compact one. Other possible choices are the FE BFs and the Fourier series. The FE BFs have the great advantage of defining the LSF evolution in the same way as the structural one. However, the RBFs functions guarantee a smoother gradient definition, thanks to the steepness of the LSF gradient at the boundary.

- 2- **Geometry mapping.** In the second step the transfer of information from the LSF to the underlying mesh is performed, by exploiting different methods. The conforming discretisation, which is a Lagrangian approach, considers just the material domain with a clear definition



(a) 3D representation of the LSF function for 2D TO problems.



(b) LSF contour plot: material (Ω), boundary ($\partial\Omega$) and void zones.

Figure 2.2 – Level-set function example for 2D TO problems.

of the boundary. It is well suited when local quantities are requested; however, it is time-consuming and sometimes difficult to perform, since a non structured mesh has to be generated at each iteration. A second possibility is represented by the density based mapping, which is an Eulerian approach. It consists in generate a regular mesh in all the design domain and affect the mechanical properties by defining a pseudo-density field, like in the SIMP method. This approach is more robust in terms of convergence and computational time, but it is affected by the same drawbacks of the SIMP method.

- 3- **Structural model.** After the geometry mapping the FE analysis is carried out to obtain the physical responses, which will be in the following step treated to evaluate the sensitivity to the objective/constraints functions with respect to the design variables.
- 4- **Sensitivity.** In this step, the sensitivity of the objective/constraints functions with respect to the design variables is evaluated. This task can be done in different ways. Surely, the most common method relies on the well-known updating procedure that use the Hamilton-Jacobi (HJ) partial different equation [14]

$$\frac{\partial \phi(\mathbf{x}, t)}{\partial t} + V_n(\mathbf{x}, t) |\nabla \phi(\mathbf{x}, t)| = 0, \quad \mathbf{x} \in D, \quad (2.12)$$

where $V_n(\mathbf{x}, t)$ is the component velocity field normal to the boundary related to its evolution, or, more precisely, to the shape derivatives of the Lagrangian functional. Moreover the shape derivatives do not allow for the generation of new holes, hence a sound alternative is represented by the topological derivatives, which allow assessing the sensitivity of the physical responses to the insertion of a infinitesimal hole in the structure [15]. Other methods to evaluate the sensitivity are based on mathematical programming, i.e., parameter shape derivatives, which exploit the link between the LSF gradient and the infinitesimal variation of the design variable, via the pseudo density field [16].

- 5- **Updating procedure.** As previously introduced the two fundamental methods to update the current topology are the solution to the HJ equation and the evaluation of the descent direction in the framework of mathematical programming algorithms. The solution of the HJ equation is not trivial. In fact it should be considered that the velocity field evaluation, which is meaningful just at the boundary of the domain, should be extended to a strip around the boundary for regularisation purposes. Secondly, the viscous term $\beta \Delta \phi(\mathbf{x}, t)$ should

be added to the right hand side of Eq. (2.12) to avoid singularities and obtain a smooth solution. Moreover, if the topological derivatives are introduced to enable hole generation mechanism, it should be considered that the HJ equation must be modified by adding a reaction term. The generalised HJ equation considers both the viscous and the reaction terms.

- 6- **Regularisation.** The convergence of the LSM is not so easy to achieve, so several regularisation techniques should be taken into account. It has been observed that to avoid convergence issues and strong variation of the LSF gradient along the boundary, the LSF can be re-initialised to a signed distance function, whose gradient norm is constant and equal to 1. This procedure is beneficial for the resolution of the HJ equation, but the zero-level contour is not maintained, which can lead to inconsistencies in the optimisation process. Other regularisation schemes consist of penalising the gradient of the LSF. As for the SIMP method, a perimeter constraint can stabilise the solution and make the result more robust with respect to the numerical artefacts. For example, using the Tichonov regularisation the gradient of the LSF can be related to an energetic term and can be summed to the objective function. However results will depend on this new parameter. Some regularisation techniques can be adopted during the geometry mapping phase with the integration of dedicated techniques, e.g., projecting the LSF on the pseudo-density field via an approximated Heaviside function can increase the region of influence of the boundary and the sensitivity will be smoother with an improvement on the convergence.

2.2.3 The ESO and BESO methods

Among the TO methods available in the literature, the ESO method and its extension, i.e., the BESO method, represent sound alternatives to face structural optimisation problems.

The ESO method is based on the combination of a metaheuristic algorithm and the Finite Element (FE) method [17]. The idea of introducing evolutionary algorithms to find the optimal topology, instead of using mathematical programming, came out from the observation of the behaviour of natural structures like shells, bones and trees. Hence, ESO exploits the combination between the results of the FE analysis, in terms of stress distribution, with an appropriate rejection criterion, which eliminates the elements characterised by lower values of the pseudo-density field and, thus, by

lower values of stresses. For isotropic materials, the ESO algorithm makes use of the rejection criterion based on the equivalent Von Mises stress, for which an element rejection occurs if the ratio of the local Von Mises stress to its maximum value over the structure is lower than a prescribed threshold value. The same ratio of rejection is maintained until a steady state in the FE analysis is reached, it means that the topology is accepted as intermediate result, afterwards the rejection ratio is increased by a fixed amount, i.e., the evolutionary rate, until a new state of equilibrium is achieved. During the evolutionary process the mesh is always kept unchanged, while a null stiffness tensor is assigned to rejected elements, which are excluded from the global stiffness matrix assembling. The convergence is met when a user-defined stop criterion is met. Examples of applications of the ESO method can be found in [18], regarding structural stiffness maximisation, or in [19] about modal analyses.

Unlike the ESO method, the BESO approach [20], allows for both removal and addition of elements, so that the influence of the optimised topology to the initial guess is drastically reduced (or avoided, depending on the problem at hand). In [20] a sensitivity number is introduced to indicate the contribution of an element removal or addition to the mean compliance, hence an element will be removed if its sensitivity number is the smallest and, conversely, it will be added if this number is the largest. Therefore, the BESO strategy differs from the ESO method, in terms of the criterion to update the stiffness tensor of each element: instead of using the stress state as indicator of rejection, the displacement field is used. The method has been reformulated in [21, 22], by adding features to obtain mesh-independent results, without checker-board pattern and by introducing a sensitivity number averaging method to speed up convergence. The works on ESO and BESO methods mentioned above make use of the so-called *hard-kill* technique to remove/add elements. Further developments have enabled the BESO hard-kill method to evolve into the BESO *soft-kill* method. The soft kill technique uses the SIMP penalisation scheme to penalise the element stiffness tensor rather than removing/adding elements. Convergence to optimised solutions is improved through this approach. A filter based on the minimum allowable radius of the geometry is used to avoid the dependence of the solution to the mesh [23, 24]. The effectiveness of this method has been shown on several benchmark problems [25, 26]. However, the parameters tuning the behaviour of the heuristics behind the BESO method have a strong influence on the final result. Finally, in [27], the LSM is coupled with the BESO algorithmic scheme to reduce the dependency of the solution to the mesh of the FE model.

2.3 On the integration of multi-scale analysis in topology optimisation

In the last decades, architected cellular materials (ACMs) became of great interest in different engineering fields, like aerospace, automotive and biomedical industries or in the energetic and chemical fields, due to the possibility of designing the material architecture at different scales. In this way it is possible to obtain very specific properties and performances according to the requirements of the problem at hand, e.g., high stiffness-to-weight and strength-to-weight ratios, high permeability, energy absorption and thermal insulation. Nowadays, an increasing amount of research works is devoted to the development of multi-scale design approaches for ACMs. The goal is to develop a general design approach by reducing the number of (unnecessary) simplifying hypotheses and by integrating into the problem formulation the design variables involved at different scales. The design variables can be either the parameters describing the structure topology at the macroscopic scale (also referred to as upper scale in the following) or those describing the topology of the representative volume element (RVE) of the ACM at the lower scale (i.e., mesoscopic or microscopic scale depending on the problem characteristic size). To this end, the scientific community is developing different approaches to optimise ACMs: parametric optimisation of the geometrical variables of predefined RVE topologies [28, 29], TO of the RVE to satisfy a given macroscopic elastic behaviour [30–39] and TO of the ACM at multiple scales [36, 40–55].

As a matter of fact, TO is identified as the most promising approach to carry out the concurrent topology and material optimisation (from a macroscopic scale perspective) since it allows for a total freedom in the choice of the material properties at the macroscopic scale, which depend upon the topology of the RVE at the lower scale. Moreover, when the problem is stated in the most general way, the optimisation of the topology of the ACM at multiple scales allows for avoiding the introduction of predefined RVE geometries, thus a wider design space can be explored and solutions more efficient than conventional ones can be found.

The basic idea behind the multi-scale TO of an ACM is that the material is iteratively removed from the design domain (at each scale) and redistributed in order to minimise a prescribed merit function by satisfying the set of design requirements (DRs). Different TO methods have been proposed in the literature to carry out the multi-scale TO of ACMs, like, for instance, the LSM [56–58], density-based TO method making use of the SIMP approach [31, 34, 59–61] or the BESO method [62]. The above

strategies can be applied, simultaneously, at the macroscopic scale of the structure and at the RVE scale, or just at this latter, with the aim of finding the optimal RVE topology showing a prescribed macroscopic behaviour, e.g., prescribed stiffness with the least mass as proposed in [63], maximum shear stiffness with a prescribed volume [64], or unconventional properties, like negative Poisson's ratio with a prescribed volume [35].

In this literature review, the approaches involving the design variables defined at both scales are discussed.

2.3.1 Multi-scale topology optimisation by considering topological variables at lower scale

As far as the strategies dedicated to the multi-scale design of ACMs are concerned, one of the most promising methods to perform multi-scale optimisation of ACMs is certainly TO. Indeed, through the use of modern TO algorithms, it is possible to add more freedom in the design process without using predefined RVE topologies [65–71].

In the literature, different multi-scale TO methods for designing ACMs are available: they are based on (a) the homogenisation method [72, 73], (b) the LSM [57, 58, 74–77], (c) the SIMP approach [61, 78–81] or (d) the BESO method [82]. These strategies are often applied at the scale of the ACM RVE to find the optimal topology satisfying the requirements of the problem at hand. Typical design requirements are RVE stiffness and relative density [63], RVE shear stiffness [64], or specific conditions related to auxetic ACMs [35, 83].

For example, Gao *et al.* [58] make use of the LSM to determine the optimal topology of the ACM RVE maximising the bulk modulus and the shear modulus subject to constraints on the volume of the RVE. Conversely, Guest and Prévost [61] adopt a different approach in order to maximise the effective elastic stiffness and the fluid permeability of ACMs. The TO problem is formulated in the SIMP framework and the homogenisation is performed numerically using the FE method, by enforcing periodic boundary conditions PBCs on the RVE.

In [81], the TO of the RVE of metamaterials with extreme properties subject to a single constraint on the material volume fraction is carried out. The merit function includes requirements on the components of the equivalent elasticity tensor of the homogenised material at the macroscopic scale, like prescribed values of the bulk modulus, of the shear modulus and of the Poisson's ratio. The TO is conducted in the SIMP framework.

In [84], the lattice infill technique (LIT) is used to post-process the op-

timised topologies provided by the SIMP approach. In this background, the optimal pseudo-density field resulting from the SIMP method, which describes the distribution of the equivalent homogeneous material at the macroscopic scale, is replaced by an ACM (of a given topology) characterised by a variable relative density, which matches, locally, the optimal pseudo-density field. The LIT is based on a predefined surrogate mechanical model of the lattice material, trained via ACM unit sampling and polynomial curve fitting.

When dealing with multi-scale TO problems, a fundamental step is the homogenisation method, which represents the link between the problem scales. Thanks to the homogenisation phase, the real ACM can be replaced by an equivalent homogeneous anisotropic medium at the macroscopic scale. Of course, the homogenisation technique can be applied only if (a) the RVE has a periodic distribution within the structure domain and (b) scales separation occurs.

In the majority of the existing works, the asymptotic homogenisation method AHM is used to perform the scale transition. For example, in [56], the equivalent elastic properties of the ACM at the macroscopic scale are computed by using an approximation of the displacement field via Taylor expansion. Similarly, in [35, 60, 85] the AHM is coupled to the Isogeometric analysis IGA, wherein the physical fields are evaluated by means of basis spline (B-spline) entities and where the boundary conditions (BCs) can be applied directly to the control points (CPs) of the B-spline entity.

A different homogenisation scheme is the so-called strain energy-based homogenisation method (SEHM), which is exploited in different works [58, 59, 61, 64, 80, 81]. It represents a sound alternative to the AHM, due to its straightforward numerical implementation and direct coupling with the SIMP approach. The SEHM is based on the equivalence between the strain energy of the heterogeneous ACM RVE and that of the corresponding volume of the equivalent homogenised anisotropic medium. The difference between the variants of the SEHM available in the literature is in the post-processing of the outcomes of the SEHM to assess the macroscopic elasticity tensor of the ACM. Indeed, one can retrieve either the averaged elements stresses inside the RVE [61] (in this case the resulting homogenisation scheme is called volume-averaged stress-based SEHM) or the elements strain energy [58].

2.3.2 Multi-scale topology optimisation by considering topological variables at all scales

As far as TO of ACMs at multiple scales is concerned, many research works are available in the literature: an exhaustive review on this topic can be found in [86]. For instance, Sivapuram *et al.* [56] make use of both the LSM and the shape sensitivity to optimise, at the same time, the topology of the ACM at both RVE and structure scales in order to minimise the macroscopic compliance subject to constraint on the volume fraction at each problem scale. The scale transition is ensured via the AHM. A different approach is proposed by Wang *et al.* [60]: firstly, the RVE topology is chosen from a database of predefined architectures; secondly, equivalent material properties at the macroscopic scale are assessed via AHM as a function of the RVE relative density; finally, the TO is performed at the macroscopic scale via the SIMP approach to minimise the macroscopic compliance subject to a constraint on the volume fraction. Another strategy, based on the lattice infill technique, is proposed by Yu *et al.* [84]. It consists of replacing the fictitious macroscopic heterogeneous material with a graded lattice material of a predefined topology characterised by a relative density equal to the local value of the pseudo-density field used to penalise the macroscopic stiffness tensor. To reduce the discrepancy between the results of the macroscopic TO and the structural responses evaluated after performing the lattice infill phase, a surrogate model of the ACM is developed and the penalisation scheme to be used at the macroscopic scale (during TO) is assessed *a priori* via lattice unit sampling and polynomial curve fitting. Finally, the TO problem is formulated by considering the volume as cost function to be minimised subject to a constraint on the Tsai-Hill failure criterion assessed on the lattice core. Xia *et al.* [62] proposed an approach for the concurrent optimisation of the material properties and of the macroscopic topology of a structure based on the bidirectional ESO method and finite element square technique to set the strong coupling between problem scales accounting for the non-linear behaviour of the material at the RVE scale and for stress redistribution at the macroscopic one. Li *et al.* [50] proposed a multi-scale TO of ACMs wherein the RVE characteristic size can change locally over the structure. Zhang *et al.* [75] proposed a method to optimise simultaneously the macroscopic design variables representing the distribution of different lattice materials and the microscopic design variables defining the topologies of different RVEs taking into consideration for the possibility of designing graded microstructures.

In all the aforementioned works, the key step is represented by the homogenisation method, which is needed to set the link between the scales

of the problem at hand, i.e., the microscopic (or mesoscopic) scale of the ACM RVE and the macroscopic scale of the structure. Thanks to the homogenisation method, at the macroscopic scale the ACM RVE is modelled as an equivalent homogeneous anisotropic material, allowing, in this way, the concurrent optimisation of the macroscopic topology and material properties (through the TO of the RVE) without increasing the computational effort. In the majority of the existing works the homogenisation approach is based either on the AHM (e.g., in [35, 60, 85], the AHM is coupled with the isogeometric analysis to carry out the multi-scale TO of ACMs) or on the SEHM, by considering either the variant making use of the stresses inside the RVE [61, 62] or the one making use of elements strain energy [38, 58].

2.3.3 Experimental validation of the multi-scale topology optimisation through three-point bending tests

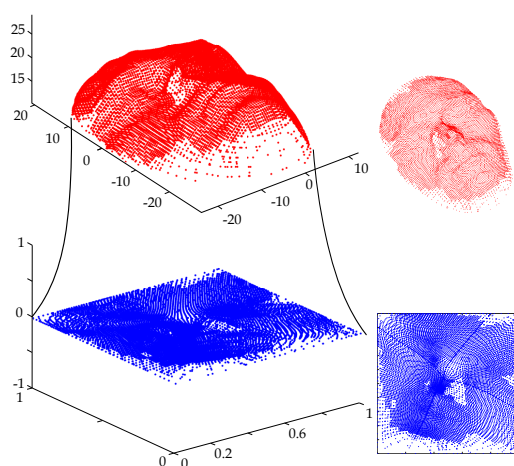
Regardless of the adopted approach, the assessment of the effectiveness of multi-scale TO algorithms can be done either numerically on meaningful benchmarks or experimentally by means of dedicated tests. In the following of this section, a brief survey about the experimental validation of optimised solutions obtained through TO methods available in the literature is presented. In particular, the discussion is limited to the well-known three-point bending test (3PBT) which is used to assess the effectiveness of some 2D and 3D benchmark problems subject to the same BCs of the 3PBT. In [87], a numerical design procedure and its corresponding experimental validation is presented to show how the constraint on the minimum printable feature can be taken into account in the optimization procedure, carried out through a density-based TO making use of the SIMP penalisation scheme, according to the resolutions of the chosen fabrication process. The compliance minimisation problem of a design domain subject to three-point bending loading is considered with a constraint on the volume fraction of the solid phase. The topological variables are defined only at the macroscopic scale and a manufacturability constraint is applied *a posteriori* to the optimised topology to eliminate the elements belonging to those topological branches whose thickness is smaller than the one prescribed by the minimum printable size related to the chosen AM technique. Conversely, Rashid *et al.* [88] employ the BESO method to optimise the topology of the RVE of a simple beam subject to three-point bending loading. The optimization problem is formulated in terms of compliance minimization with constraints on the volume, and experimental tests were performed on

two beams for which two different RVE topologies were used. The optimised specimens were fabricated through selective laser melting (SLM). The experimental tests were conducted to compare the mechanical response of solid specimens with the ones composed of optimised RVEs, in terms of load vs. displacements curves. Moreover, the obtained configurations were also investigated in terms of energy absorption capability. In [89], a comparison between the as-manufactured and as-designed lattice structure made of octet-truss RVE is presented. Tensile and flexural tests are performed on ACM specimens of different size and with a different number of RVE along the three axes. This comparison aims at pointing out the difference in mechanical performances between manufactured parts, which are strongly dependent on the process-induced defects, and the nominal ones. The numerical analysis is carried out by the well-known finite cell method. The experimental results shows a discrepancy between the nominal bending stiffness of the specimen obtained numerically and the one resulting from 3PBT. Moreover, reduced beam models are used to predict the bending behaviour of the lattice and validate classical strain gradient theory. In [90], a structural design of sandwich-like structures, wherein the core is composed of repetitive dome units filled with micro-lattice, is performed to maximise stiffness and energy absorption capability. The goal of the design/optimisation process is to find the optimal density distributions of the micro-lattice that can minimise the total compliance, with a constraint on the volume. The asymptotic homogenization technique is exploited to replace the equivalent elastic properties of the ACM material at the component scale. Numerical and experimental results are compared for different types of structures: completely solid dome components, dome with high density and low density RVE, same RVE or RVEs of variable topology within the structure. The experimental data show that the maximal energy absorption in the three point bending tests is reached by the graded large density dome micro-lattice structures. Zhang *et al.* [75] propose a method where the beam subjected to three-point bending test is optimized at the macroscopic scale while at the lower scale a predefined pattern of RVE is considered. To decrease the computational costs, the macroscopic mechanical properties of the RVE are assessed through the homogenization technique. In fact, the equivalent homogeneous behaviour of the RVE is modelled via polynomial functions depending on the relative density of the RVE. The problem is formulated in terms of compliance minimization with a constraint on the volume fraction. The predefined RVE topologies considered in this study are: simple cubic and body centered cubic (SC-BCC) as well as simple cubic and face centered cubic plate-lattices characterised by a cubic symmetry behaviour. Experimental tests are conducted on polyactic

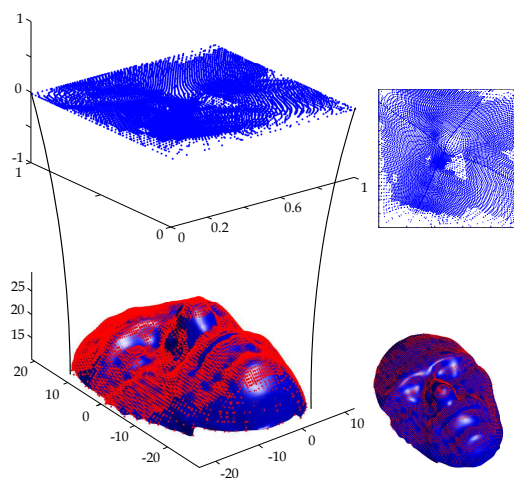
acid (PLA) specimens of the different models, and the best performances in terms of maximal bending stiffness are observed on the optimised SC-FCC structures. Kim and Park [91] make use of the SIMP method to perform different optimisation analyses at multiple scales. At the macroscopic scale the analysis is performed to achieve the compliance minimisation subject to a volume fraction constraint. At the microscopic scale the goal is to optimise the struts diameters with a constraint on the RVE volume with the implementation of a smoothing operation between struts to avoid stress concentration. Finally, at the macroscopic scale the optimised topology is filled by the graded lattice material, where the strut diameters is varied in order to met the local value of the optimised pseudo-density field at the upper scale. 3PBT is conducted on the optimised specimens fabricated in acrylic photo-polymer and fabricated by digital light processing (DLP). The analysis of the force vs. displacement curves outlined that the best configuration in terms of structural stiffness is the one where the topology at both scales is optimised. Moreover, the energy absorption capability is also improved compared to the behaviour of the configuration wherein the topology was optimised only at the macroscopic scale.

2.4 On the surface reconstruction methods

Surface reconstruction methods are widely exploited in the domain of reverse engineering and geometrical modelling. It consists of the approximation of a non-degenerate points cloud/tessellation, called target points (TP) through geometrical CAD-compatible entities, e.g., NURBS parametric surfaces, as schematically illustrated in Fig. 2.3. The TPs in the surface approximation problem are usually the vertices of the triangulation embedded in the description of an STL file, where the information about the connectivity and the surface normals of each external face is stocked. In general, the surface reconstruction strategy can be divided into two different phases: *parametrisation* and *fitting*, as shown in Fig. 2.3. The first step aims to define the set of parameters in a 2D Euclidean space linked to the vertices of the surface triangulation. The parametrisation should preserve the information about the three-dimensional shape of the tessellation to ensure a smooth surface approximation. Conversely, the fitting phase includes all the mathematical procedures used to solve the approximation problem, stated as least-square constrained or unconstrained minimisation problem. In the following sections a brief state of the art about the parametrisation and fitting methodologies is presented, without any ambition of exhaustiveness.



(a) Mapping of the TPs on the parametric domain.



(b) Approximation with a NURBS surface the original TPs.

Figure 2.3 – Diagram of the parametrisation and fitting phase constituting the surface reconstruction procedure.

2.4.1 Parametrisation techniques

Parametrisation techniques are founded on the assumption that, given any two surfaces with a similar topology, there exists a bijective mapping between them [92]. Therefore, if the surface to be mapped consists in a discrete triangulation, the mapping operation could be named *parametrisation* and its resulting surface the *parametrisation domain*.

Among the different parametrisation methods, four different approaches are presented in the following, in order to compare their features, advantages and drawbacks.

- **Projection method:** the preliminary hypothesis of this method [93] is that only unfolded surfaces are eligible. The goal of the point projection strategy is to find the set of pairs (u_1, u_2) parameters of the parametric surface $\mathbf{s}(u_1, u_2)$ with $\mathbf{s} \in \mathbb{R}^3$ corresponding to the projection of the N TPs $\text{OQ}_k = (x_k, y_k, z_k) \in \mathbb{R}^3$, $(k = 1, \dots, N)$ on the surface $\mathbf{s}(u_1, u_2)$, assuming that the projection of a triangulated surface leads to a unique solution. The set of parameters can be obtained by applying the point inversion strategy if the degree of the parametric surface is $p_i \leq 4, i = 1, 2$. If this condition is not met, the point projection strategy is articulated in three phases:

1. The distance between the TPs and the related position on the parametric surface is defined as: $\mathbf{r}(u_1, u_2) := \mathbf{s}(u_1, u_2) - \text{OQ}_k$.
2. To define the minimisation problem in terms of point projection, two scalar equations are employed:

$$\begin{cases} f(u_1, u_2) = \mathbf{r}^T \frac{\partial \mathbf{s}}{\partial u_1} = 0, \\ g(u_1, u_2) = \mathbf{r}^T \frac{\partial \mathbf{s}}{\partial u_2} = 0, \end{cases} \quad (2.13)$$

3. The Newton-Raphson method is applied to found the optimal couple of parameters (u_1, u_2) .

- **Mercator's mapping:** the method proposed by Sahand Jamal and Kim [94] has as objective to map a genus 0¹ closed surface to the external surface of a sphere. Hence, a pair of parameters (e.g., latitude and longitude) will be assigned to each vertex of the triangulated surface. Some conditions should be satisfied to ensure the correct implementation of the method: the Euler equation must be satisfied $F + V - (E + 2) + 2H = 0$, where F, V, E and H are the numbers

1. Roughly speaking, the genus of a surface is related to the number of holes of the surface.

of triangles, vertices, edges and handles, to filter out toroidal and handled surfaces. On the other hand, the vertex triplets, describing the triangles of the surface, must be ordered such that the surface orientation will have all the facets normal having the outward direction. The whole procedure can be summarised by the following four-step strategy:

1. The identification of northern, southern poles and the related circumpolar regions is the first step.
 2. The z -coordinate of each vertex of the triangulation is found by setting the values for poles and retrieving the others as unweighed average of their neighbours z -coordinates.
 3. The azimuthal ϕ -coordinates are found following a path of steepest descent starting from a vertex of the circumpolar region at $z = +Z$ until the vertex with $z = -Z$ is reached.
 4. To produce the mapping, it is necessary to transform the z -coordinates into the latitude θ -coordinates. The Mercator's mapping method is exploited to perform this operation.
- **Global conformal parametrisation:** Gu and Yau [95] proposed a parametrisation technique that can be exploited to find the parametrisation of surfaces with non-trivial topologies, i.e., closed surface with a genus greater than zero. The adjective global is employed because this parametrisation is able to preserve the conformality everywhere and it has no boundary discontinuity. The method relies on finding the homology basis to represent the topology of the surface. Roughly speaking, the homology basis is composed of curves that can be deformed to any closed curves on the surface. The surface will be cut along the homology basis curves to obtain a topological disk, which is called the fundamental domain. Finally, the conformal gradient and its symmetric value are evaluated and combined to found the global conformal parametrisation.
 - **Shape preserving method:** the parametrisation technique proposed by Floater [96] can be applied only to open triangulated surfaces of genus 0, so it is not as general as the global conformal parametrisation strategy proposed by Gu and Yau [95]. Nevertheless, it represents a great reference for the mapping procedure [97–99] since the resulting parameters show a distribution that preserve the shape of the triangulated surface. This leads to optimal results in the surface approximation phase, as show in [92]. The goal of this technique is to find the expression of each internal node as a linear convex combination of its neighbours. In this way, it will be possible

to find the values of the (u_1, u_2) parameters of a given point as a weighted average of those related to its neighbourhood. The shape preserving method consists of the following three steps:

1. The parameters (u_1, u_2) of the boundary nodes are found through the chord length method [93], which maps the points of the boundary of a convex polygon $D \in \mathbb{R}^2$. The parameters of the nodes belonging to the boundary of the surface are collected in the arrays \mathbf{b}_1 and \mathbf{b}_2 , which are used to solve the following linear system

$$\begin{cases} \mathbf{\Lambda} \mathbf{u}_1 = \mathbf{b}_1, \\ \mathbf{\Lambda} \mathbf{u}_2 = \mathbf{b}_2, \end{cases} \quad (2.14)$$

2. The key-phase of the strategy is the evaluation of the matrix of weights $\mathbf{\Lambda}$. The components of the matrix are evaluated in order to preserve the shape of the triangulation when passing from \mathbb{R}^3 domain to \mathbb{R}^2 domain, in terms of angles and distances. For each internal node its neighbourhood is found and a local parametrisation, based on geodesic polar map, is performed. On the resulting fictive diagram, the weight of each neighbour point in relation to the internal node is evaluated, in order to fill the $\mathbf{\Lambda}$ matrix. For more details the reader is addressed to [96].
3. The parameters (u_1, u_2) of the internal nodes are evaluated by solving the linear system of Eq. (2.14).

It is noteworthy that the parametric coordinates of the boundary nodes are determined through the *chord length* method, while the matrix $\mathbf{\Lambda}$ is assessed via a two-step procedure, which constitutes the kernel of the shape preserving method (SPM) (see [96] for more details).

2.4.2 Surface fitting

Once the parameters domain is correctly defined by means of one of the above presented method, the surface fitting phase can take place, in terms of interpolation or approximation problem. This topic has been extensively investigated in the literature. For example in [93] both *interpolation* and *approximation* techniques are proposed, summarising the limits and advantages of both the strategies. The interpolation fitting techniques constrain the parametric surface to pass exactly through the TPs; despite interpolation allows obtaining a high accuracy in terms of local results,

the interpolating surface could be affected by the so-called overfitting issue and the quality of the surface between adjacent TPs could be poor. On the other hand, the approximation methods aim to capture the shape of the original surface, by minimising the maximal deviation between the TPs and their counterparts belonging to the approximating surface. Among the different approximation methods, the ones based on the least-square fitting, constrained or unconstrained, are the most exploited: for example in [93], a particular fitting strategy, suitable for a set of TPs organised in an orderly grid, is presented.

Nevertheless, when the set of TPs is the result of a scanner acquisition, their position in the space is not always organised (i.e., they are available as a set of scattered TPs), hence a more general method should be applied to fit the data set. In [100, 101], two approaches are presented to face this kind of problems. The first work presents a problem formulation wherein a particular functional $E(\mathbf{s})$ is minimised. $E(\mathbf{s})$ is defined as a weighted sum of the energy of deformation of the surface \mathbf{s} and the square of the distance between TPs and their counterparts evaluated over the approximating surface. The two components have different effects, competing to achieve a resulting surface, which passes through the TPs and is as smooth as possible. The proposed algorithm finds iteratively the best approximating surface, which is characterised by user-defined parameters that are not included in the optimisation process (e.g., the *knot vector* (KV) components, degrees of the Bernstein's polynomial if the approximating surface is represented by a B-spline entity).

On the other hand, in the work by Mao *et al.* [101], after a curve fitting of each TPs rows, a re-sampling of the curves is proposed, with the aim of producing a well-organised grid of TPs, in order to be able to implement the same approach followed in [93].

An alternative approach is proposed in [102], which relies on the least-square approximation by a tensor-product spline surface of the set of TPs conveniently parametrised through the shape preserving method. After choosing the degrees of the surface and the KV components, the sum of squared errors plus a smoothing term (i.e., the so called thin-plate spline energy term TPSE) is minimised.

2.5 Conclusion

This non-exhaustive state of the art on the three main topics related to this Ph.D. Thesis has allowed to highlight the following features:

- Several TO methods are available in the literature. The most widespread algorithms belong either to the class of density-based TO algorithms or to the one of LSMs. Each algorithm exhibits advantages and drawbacks. It is not possible to state *a priori* which method provides better results and the choice should be made by investigating the nature of the problem at hand.
- Current multi-scale TO approaches for ACMs suffer from three main limitations. The first one is related to the problem formulation, which often includes only requirements on prescribed values of the macroscopic elastic tensor components of the ACM as done in [35, 58, 61, 63, 64, 74, 75, 77, 79–83, 103]. However, in real-world engineering applications the RVE topology at the lower scale must be optimised in order to satisfy design requirements on macroscopic structural responses, like compliance, mass, strength, etc.

The second one is related to the choice of the homogenisation scheme establishing the link between the problem scales. The homogenisation procedure must be as general as possible to avoid the introduction of unnecessary simplifying hypotheses. Moreover, it must be efficient to reduce the computational time for assessing the macroscopic elasticity tensor of the ACM, as well as the gradient of the macroscopic responses with respect to the topological variable defined at the lower scale.

The third limitation is related to the integration of suitable manufacturing constraints of geometrical nature in the problem formulation. For instance, the minimum length scale requirement should be considered in order to ensure that small topological branches could be manufactured by means of the considered process. All these aspects will be addressed in Chapter 4.

- Regarding the multi-scale TO of ACMs, a special attention must be put on the problem formulation in order to integrate pertinent DRs dealing with scale transition, manufacturing aspects, anisotropy and boundary conditions (BCs) type. As it can be inferred from the works cited above, the approaches available in the literature to perform the multi-scale TO of ACMs suffer from some drawbacks. The first issue is related to the hypotheses at the basis of the homogenisation procedure. Of course, regardless of the adopted technique, the accuracy of the homogenisation method depends upon the satisfac-

tion of the following conditions: a) the ACM is obtained by distributing the RVE according to a periodical (or quasi-periodical) pattern within the macroscopic topology; b) the characteristic lengths of the problem scales must differ (at least) of about two/three order of magnitude to fulfil the well-known scale separation condition. Regarding the latter condition, in the literature, only few works integrate the scale separation condition in the problem formulation [104, 105]. As a matter of fact, in [104, 105] the macroscopic topology is the result of the assembling of the RVE topology of each macroscopic layer according to predefined periodic patterns. Conversely, when the TO is performed simultaneously at both the macroscopic scale and the RVE one, it is difficult to ensure scale separation because the characteristic length of the macroscopic topological branches could become of the same order of the characteristic length of the RVE scale (recall that the topology of the continuum at both upper and lower scales is continuously changing during the optimisation process). Therefore, a suitable constraint must be introduced in the problem formulation to fulfil the scales separation condition at each iteration of the TO. The second issue is related to the integration of suitable manufacturing constraints in the problem formulation. In particular, the minimum length scale requirement should be considered at the RVE scale to ensure that small topological branches could be manufactured by means of the considered process. Moreover, in none of the aforementioned works, mixed non-zero Neumann-Dirichlet (ND) BCs are considered and only in few of them (e.g., in [106]) the influence of the RVE anisotropic behaviour on the optimised topology at the macroscopic scale is taken into account, but a systematic analysis considering the influence of the RVE elastic symmetry groups on the macroscopic topology is still lacking. All these issues will be addressed in Chapter 5.

- As it can be deduced from the state of the art on surface reconstruction methodologies, all the the approaches are based on preliminary assumptions and parameters defined by the user: therefore, the main drawback is the lack of a general numerical strategy able to optimise all the variables involved in the definition of the approximating surface (which are the degrees of the Bernstein's polynomials, the number of KV components and values of non-trivial KV components, the control points coordinates and the associated weights when the fitting surface is described by a general NURBS entity). All these aspects will be deeply discussed in Chapter 7 where a general surface reconstruction strategy for open and closed surfaces of genus greater

than zero is presented.

Chapter 3

The SANTO algorithm

In this Chapter, the numerical framework at the basis of the developments discussed in this Thesis is presented: the SIMP And NURBS for Topology Optimisation (SANTO) algorithm, developed at the Laboratory I2M in Bordeaux [107, 108]. This algorithm presents a strategy capable to overcome some drawbacks related to the classical density-based TO strategies, e.g., the mesh-dependency of the solution and the checkerboard effect. The SANTO algorithm makes an efficient exploitation of the NURBS parametric entities to describe the pseudo-density field. This Chapter briefly recalls the main features of the NURBS-based SIMP method and of the SANTO algorithm, which are discussed in details in [109]. The Chapter is composed of two Sections: in Sec. 3.1, the NURBS formalism is introduced, while in Sec. 3.2, a detailed explanation of the SANTO structure and its main features are illustrated.

3.1 Fundamentals of non-uniform rational basis spline hyper-surfaces

A NURBS hyper-surface is a polynomial-based function, defined over a parametric space (domain), taking values in the NURBS space (co-domain). Therefore, if N is the dimension of the parametric space and M is the dimension of the NURBS space, a NURBS entity is defined as $\mathbf{h} : \mathbb{R}^N \longrightarrow \mathbb{R}^M$. The mathematical formula of a generic NURBS hyper-surface is

$$\mathbf{h}(\zeta_1, \dots, \zeta_N) = \sum_{i_1=0}^{n_1} \cdots \sum_{i_N=0}^{n_N} R_{i_1, \dots, i_N}(\zeta_1, \dots, \zeta_N) \mathbf{y}_{i_1, \dots, i_N}, \quad (3.1)$$

where $n_j + 1$ ($j = 1, \dots, N$) is the number of *control points* (CPs) along the ζ_j parametric direction, $R_{i_1, \dots, i_N}(\zeta_1, \dots, \zeta_N)$ are the piece-wise rational basis

functions, which are related to the standard NURBS blending functions $N_{i_k, p_k}(\zeta_k)$, $k = 1, \dots, N$ by means of the relationship

$$R_{i_1, \dots, i_N}(\zeta_1, \dots, \zeta_N) = \frac{\omega_{i_1, \dots, i_N} \prod_{k=1}^N N_{i_k, p_k}(\zeta_k)}{\sum_{j_1=0}^{n_1} \cdots \sum_{j_N=0}^{n_N} \left[\omega_{j_1, \dots, j_N} \prod_{k=1}^N N_{j_k, p_k}(\zeta_k) \right]}. \quad (3.2)$$

In Eqs. (3.1) and (3.2), $\mathbf{h}(\zeta_1, \dots, \zeta_N)$ is a M -dimension vector-valued rational function, $(\zeta_1, \dots, \zeta_N)$ are scalar dimensionless parameters defined in the interval $[0, 1]$, whilst $\mathbf{y}_{i_1, \dots, i_N} \in \mathbb{R}^M$ is the vector collecting the generic CP coordinates. The j -th CP coordinate ($y_{i_1, \dots, i_N}^{(j)}$) is stored in the array $\mathbf{Y}^{(j)} \in \mathbb{R}^{(n_1+1) \times \cdots \times (n_N+1)}$, whose dimensions are $(n_1 + 1) \times \cdots \times (n_N + 1)$. The explicit expression of CPs coordinates in \mathbb{R}^M is:

$$\mathbf{Y}_{i_1, \dots, i_N}^T = \{y_{i_1, \dots, i_N}^{(1)}, \dots, y_{i_1, \dots, i_N}^{(M)}\}. \quad (3.3)$$

Curves and surfaces formulæ can be easily deduced from Eq. (3.1). The CPs layout is referred to as control polygon for NURBS curves, control net for surfaces and control hyper-net otherwise [110]. The overall number of CPs constituting the hyper-net is:

$$n_{\text{CP}} := \prod_{i=1}^N (n_i + 1). \quad (3.4)$$

The generic CP does not actually belong to the NURBS entity but it affects its shape by means of its coordinates. A weight w_{i_1, \dots, i_N} is associated to the generic CP. The higher the weight w_{i_1, \dots, i_N} , the more the NURBS entity is attracted towards the CP $\mathbf{y}_{i_1, \dots, i_N}$. For each parametric direction ζ_k , $k = 1, \dots, N$, the NURBS blending functions are of degree p_k and can be defined in a recursive way as

$$N_{i_k, 0}(\zeta_k) = \begin{cases} 1, & \text{if } v_{i_k}^{(k)} \leq \zeta_k < v_{i_k+1}^{(k)}, \\ 0, & \text{otherwise,} \end{cases} \quad (3.5)$$

$$N_{i_k, q}(\zeta_k) = \frac{\zeta_k - v_{i_k}^{(k)}}{v_{i_k+q}^{(k)} - v_{i_k}^{(k)}} N_{i_k, q-1}(\zeta_k) + \frac{v_{i_k+q+1}^{(k)} - \zeta_k}{v_{i_k+q+1}^{(k)} - v_{i_k+1}^{(k)}} N_{i_k+1, q-1}(\zeta_k), \quad (3.6)$$

$$q = 1, \dots, p_k,$$

where each blending function is defined on the knot vector

$$\mathbf{v}_{(k)}^T = \underbrace{\{0, \dots, 0\}}_{p_k+1}, v_{p_k+1}^{(k)}, \dots, v_{m_k-p_k-1}^{(k)}, \underbrace{\{1, \dots, 1\}}_{p_k+1}, \quad (3.7)$$

whose dimension is $m_k + 1$, with

$$m_k = n_k + p_k + 1. \quad (3.8)$$

Each knot vector $\mathbf{v}^{(k)}$ is a non-decreasing sequence of real numbers that can be interpreted as a discrete collection of values of the related dimensionless parameter ζ_k . The NURBS blending functions are characterised by several interesting properties: the interested reader is addressed to [111] for a deeper insight into the matter. Here, only the *local support property* is recalled because it is of paramount importance for the NURBS-based SIMP method [108, 110]:

$$R_{i_1, \dots, i_N}(\zeta_1, \dots, \zeta_N) \neq 0, \quad (3.9)$$

if $(\zeta_1, \dots, \zeta_N) \in [v_{i_1}^{(1)}, v_{i_1+p_1+1}^{(1)}] \times \dots \times [v_{i_N}^{(N)}, v_{i_N+p_N+1}^{(N)}]$.

Eq. (3.9) means that each CP (and the respective weight) affects only a precise zone of the *parametric space*, which is referred to as *local support* or *influence zone*. The extent of the local support of the generic CP depends upon the number of CPs and the basis functions degree along each direction. As illustrated in Fig. 3.1, for a given degree, the higher the CPs number the smaller the local support and, similarly, for a given number of CPs, the smaller the degree, the smaller the local support.

A pictorial view of B-spline and NURBS surfaces ($N = 2, M = 3$) is provided in Fig. 3.2. In particular, the influence of the CPs and the associated weight on the shape of the surface is highlighted.

3.2 The NURBS-based SIMP method for single-scale problems

To illustrate the main concepts at the basis of the NURBS-based SIMP method, the classical problem of minimising the compliance of the structure (under homogeneous Dirichlet's boundary conditions) subject to an inequality constraint on the volume fraction is considered in the following of this chapter .

3.2.1 Design variables

The SANTO algorithm exploits the NURBS formalism and the SIMP method to perform TO analysis overcoming, thus, the classical restrictions of the SIMP method. In the framework of the NURBS-based SIMP method

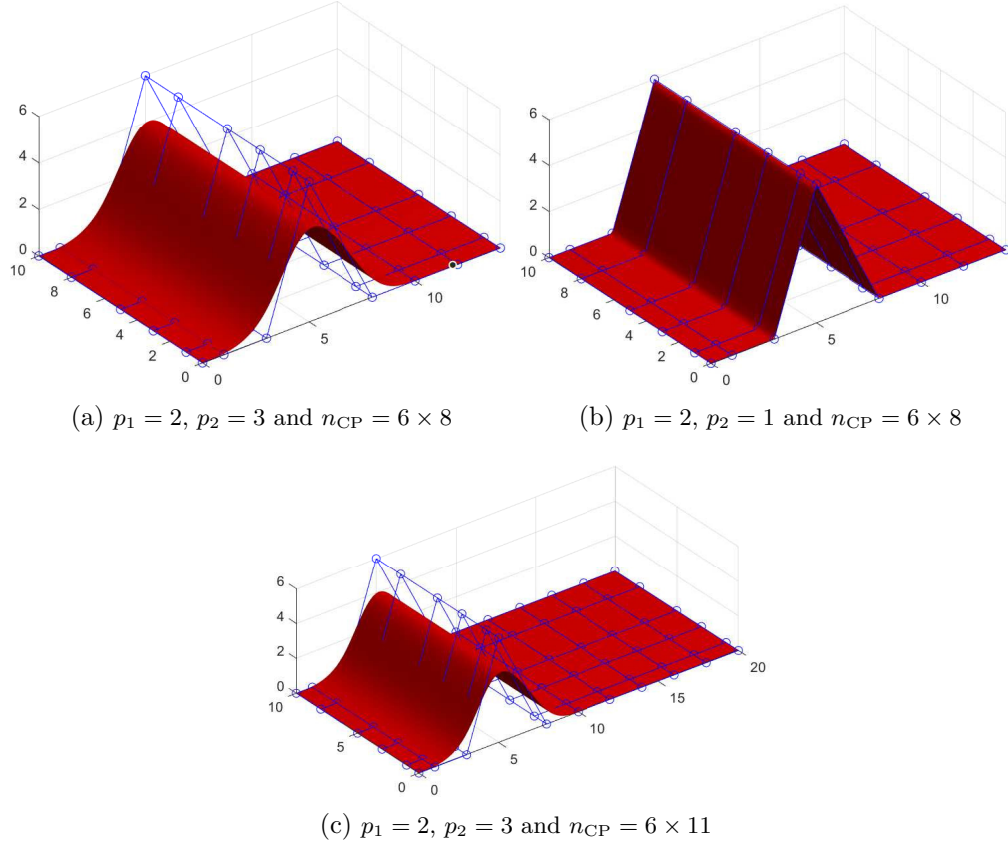


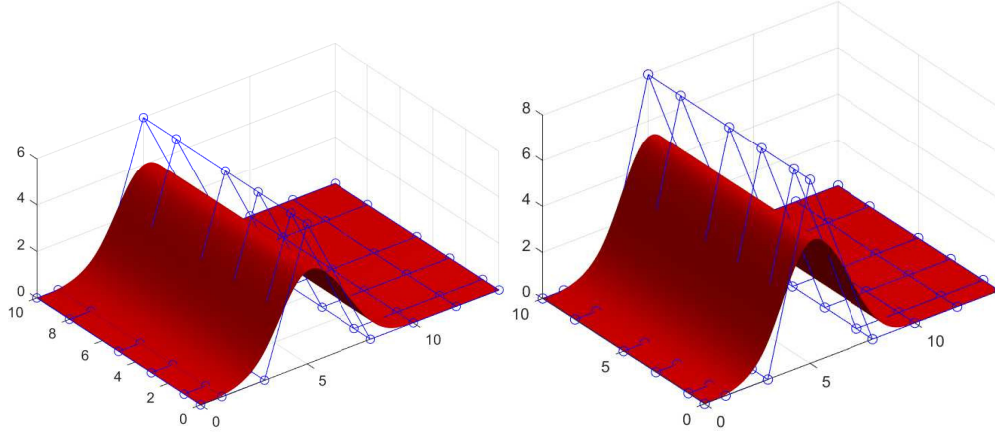
Figure 3.1 – The effect of the degree value (a)-(b), and of the CPs number (a)-(c) on the local support.

a NURBS entity of dimension $D + 1$ is used to describe a problem of dimension D . Therefore, if a 3D TO problem is considered, a 4D NURBS hyper-surface is needed to describe the part topology, whilst a 3D surface is used for 2D TO problems [108]. Without loss of generality, the formulation presented in the following of this section is limited to single-scale 3D TO problems. Consider the compact space $\mathcal{D} \subset \mathbb{R}^3$ in a Cartesian orthonormal frame $O(x_1, x_2, x_3)$:

$$\mathcal{D} := \{\mathbf{x}^T = \{x_1, x_2, x_3\} \in \mathbb{R}^3 : x_j \in [0, L_j]\}, \quad j = 1, 2, 3, \quad (3.10)$$

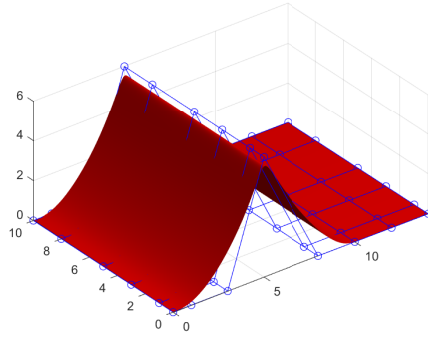
where L_j is a reference length defined along the x_j axis. The aim of TO is to search for the best distribution of a given “heterogeneous material” satisfying the requirements of the design problem.

As stated above, for 3D problems a 4D hyper-surface is employed. The first three coordinates of the NURBS entity correspond to the Cartesian



(a) B-spline surface $p_1 = 2, p_2 = 3$ and $n_{CP} = 6 \times 8$, with $\mathbf{y}_{:,4} = 6$

(b) B-spline surface $p_1 = 2, p_2 = 3$ and $n_{CP} = 6 \times 8$, with $\mathbf{y}_{:,4} = 8$



(c) NURBS surface $p_1 = 2, p_2 = 3$ and $n_{CP} = 6 \times 8$, with $\mathbf{y}_{:,4} = 6$ and $\omega_{:,4} = 6$

Figure 3.2 – The effect of the CPs value (a)-(b), and of the weights value (a)-(c) on the shape of the surface.

coordinates defining the domain, while the last coordinate corresponds to the pseudo-density field that reads:

$$\rho(\zeta_1, \zeta_2, \zeta_3) = \sum_{i_1=0}^{n_1} \sum_{i_2=0}^{n_2} \sum_{i_3=0}^{n_3} R_{i_1 i_2 i_3}(\zeta_1, \zeta_2, \zeta_3) \rho_{i_1 i_2 i_3}. \quad (3.11)$$

In Eq. (3.11), $\rho_{i_1 i_2 i_3}$ is the pseudo-density value at the generic CP, i.e., the fourth coordinate of the vector \mathbf{h} in Eq. (3.1), while $R_{i_1 i_2 i_3}$ are the rational basis functions of Eq. (3.2).

The dimensionless parameters ζ_j can be obtained as:

$$\zeta_j = \frac{x_j}{L_j}, \quad j = 1, 2, 3. \quad (3.12)$$

Among the parameters governing the shape of the NURBS entity, only the pseudo-density at CPs and the associated weights are included in the design variable vectors $\boldsymbol{\xi}_1$ and $\boldsymbol{\xi}_2$ defined as:

$$\boldsymbol{\xi}_1^T := (\rho_{000}, \dots, \rho_{n_1 n_2 n_3}), \quad \boldsymbol{\xi}_2^T := (\omega_{000}, \dots, \omega_{n_1 n_2 n_3}), \quad \boldsymbol{\xi}_1, \boldsymbol{\xi}_2 \in \mathbb{R}^{n_{\text{CP}}}, \quad (3.13)$$

accordingly, the number of design variables is, at most, $n_{\text{var}} = 2n_{\text{CP}}$.

The other parameters involved in the definition of the NURBS entity, i.e., degrees, knot-vector components and number of CPs, are set a-priori at the beginning of the TO and are not optimised: for more details the reader is addressed to [108, 110].

It is noteworthy that, since the pseudo-density field is represented by a purely geometric entity, i.e., a NURBS hyper-surface, it does not depend upon the quality of the mesh of the FE model. In particular, the pseudo-density field is “projected” over the mesh of the FE model, which is used to compute the structural responses involved in the problem formulation. This fact allows reducing the number of design variables, compared to the classic density-based TO methods, which have a number of variables equal to the number of elements constituting the mesh. On the other hand, exploiting the natural filtering capabilities of the NURBS entities, i.e., the local support property, will enable the creation of a mutual dependency among element densities, since only the elements belonging to the local support zones will be selected and taken into account to evaluate the gradient of the objective and constraints functions. Finally, as discussed in [108, 110], unlike classic density-based TO algorithms, the local support property of the NURBS blending functions allows avoiding the introduction of artificial filters to overcome numerical issues related to the well-known checkerboard effect and mesh-dependency of the optimised topology.

3.2.2 Objective function

Consider the static equilibrium of the FE model in the most general case of mixed non-zero Neumann-Dirichlet BCs:

$$\hat{\mathbf{K}} \hat{\mathbf{u}} = \hat{\mathbf{f}}, \quad \hat{\mathbf{u}}, \hat{\mathbf{f}} \in \mathbb{R}^{\hat{N}_{\text{DOF}}}, \quad \hat{\mathbf{K}} \in \mathbb{R}^{\hat{N}_{\text{DOF}} \times \hat{N}_{\text{DOF}}}, \quad (3.14)$$

where \hat{N}_{DOF} is the overall number of degrees of freedom (DOFs) before the application of BCs, $\hat{\mathbf{K}}$ is the non-reduced (singular) stiffness matrix of the FE model, while $\hat{\mathbf{f}}$ and $\hat{\mathbf{u}}$ are the non-reduced vectors of the external generalised nodal forces and displacements, respectively. Consider, now, the following definition:

Definition 3.2.1. Let $\hat{\mathfrak{M}} \in \mathbb{R}^{m \times n}$ be a generic rectangular matrix and $\mathcal{R} \subset \{i \mid 1 \leq i \leq m\}$ and $\mathcal{C} \subset \{j \mid 1 \leq j \leq n\}$ two sets of positive natural numbers. The operator $\mathfrak{M} := \mathfrak{R}(\hat{\mathfrak{M}}, \mathcal{R}, \mathcal{C})$ returns the matrix \mathfrak{M} obtained by deleting the i -th row and the j -th column from $\hat{\mathfrak{M}}$, $\forall i \in \mathcal{R}$ and $\forall j \in \mathcal{C}$. Similarly, given $\hat{\mathbf{v}} \in \mathbb{R}^n$, $\mathbf{v} := \mathfrak{R}(\hat{\mathbf{v}}, \mathcal{R})$ denotes the vector obtained by suppressing the i -th row of $\hat{\mathbf{v}}$, $\forall i \in \mathcal{R}$.

Let $\mathcal{I}_U \subset \{i \mid 1 \leq i \leq \hat{N}_{\text{DOF}}\}$ and $\mathcal{I}_{\text{BC}} \subset \{i \mid 1 \leq i \leq \hat{N}_{\text{DOF}}\}$ be two generic sets of indices such that: $\mathcal{I}_U \cap \mathcal{I}_{\text{BC}} = \emptyset$, $\#\mathcal{I}_U = N_{\text{DOF}}$, $\#\mathcal{I}_{\text{BC}} = N_{\text{BC}}$ and $N_{\text{DOF}} + N_{\text{BC}} = \hat{N}_{\text{DOF}}$ (i.e., N_{BC} is the number of DOFs where displacements are imposed, whilst N_{DOF} is the number of unknown DOFs). By applying Def. 3.2.1 to Eq. (3.14), one gets

$$\begin{bmatrix} \mathbf{K} & \mathbf{K}_{\text{BC}} \\ \mathbf{K}_{\text{BC}}^T & \tilde{\mathbf{K}} \end{bmatrix} \begin{Bmatrix} \mathbf{u} \\ \mathbf{u}_{\text{BC}} \end{Bmatrix} = \begin{Bmatrix} \mathbf{f} \\ \mathbf{r} \end{Bmatrix}, \quad (3.15)$$

with:

$$\begin{aligned} \mathbf{u} &:= \mathfrak{R}(\hat{\mathbf{u}}, \mathcal{I}_{\text{BC}}), \quad \mathbf{f} := \mathfrak{R}(\hat{\mathbf{f}}, \mathcal{I}_{\text{BC}}) \\ \mathbf{u}_{\text{BC}} &:= \mathfrak{R}(\hat{\mathbf{u}}, \mathcal{I}_U), \quad \mathbf{r} := \mathfrak{R}(\hat{\mathbf{f}}, \mathcal{I}_U), \\ \mathbf{K} &:= \mathfrak{R}(\hat{\mathbf{K}}, \mathcal{I}_{\text{BC}}, \mathcal{I}_{\text{BC}}), \quad \mathbf{K}_{\text{BC}} := \mathfrak{R}(\hat{\mathbf{K}}, \mathcal{I}_{\text{BC}}, \mathcal{I}_U), \quad \tilde{\mathbf{K}} := \mathfrak{R}(\hat{\mathbf{K}}, \mathcal{I}_U, \mathcal{I}_U), \\ \mathbf{u}, \mathbf{f} &\in \mathbb{R}^{N_{\text{DOF}}}, \quad \mathbf{u}_{\text{BC}}, \mathbf{r} \in \mathbb{R}^{N_{\text{BC}}}, \\ \mathbf{K} &\in \mathbb{R}^{N_{\text{DOF}} \times N_{\text{DOF}}}, \quad \mathbf{K}_{\text{BC}} \in \mathbb{R}^{N_{\text{DOF}} \times N_{\text{BC}}}, \quad \tilde{\mathbf{K}} \in \mathbb{R}^{N_{\text{BC}} \times N_{\text{BC}}}. \end{aligned} \quad (3.16)$$

In Eq. (3.15), \mathbf{u} and \mathbf{u}_{BC} are the unknown and imposed vectors of generalised displacements, respectively; \mathbf{f} is the vector of generalised external nodal forces, whilst \mathbf{r} is the vector of (unknown) generalised nodal reactions on the nodes where BCs on generalised displacements are imposed. \mathbf{K} , \mathbf{K}_{BC} and $\tilde{\mathbf{K}}$ are the stiffness matrices of the FE model after applying BCs.

In the context of the SIMP approach, the density field of Eq. (3.11) affects the element stiffness matrix and, accordingly, the global stiffness

matrix of the FE model as follows:

$$\begin{aligned}\hat{\mathbf{K}} &:= \sum_{e=1}^{N_e} \rho_e^\alpha \hat{\mathbf{L}}_e^T \mathbf{K}_e^0 \hat{\mathbf{L}}_e = \sum_{e=1}^{N_e} \hat{\mathbf{L}}_e^T \mathbf{K}_e \hat{\mathbf{L}}_e, \\ \mathbf{K}_e^0, \mathbf{K}_e &\in \mathbb{R}^{N_{\text{DOF}}^e \times N_{\text{DOF}}^e}, \quad \hat{\mathbf{L}}_e \in \mathbb{R}^{N_{\text{DOF}}^e \times \hat{N}_{\text{DOF}}},\end{aligned}\tag{3.17}$$

where ρ_e is the fictitious density of Eq. (3.11) computed at the centroid of the generic element e , whilst $\alpha \geq 1$ is a suitable parameter used to penalise the intermediate densities between 0 and 1, in agreement with the classic SIMP approach ($\alpha = 3$ in this study). N_e is the total number of elements and N_{DOF}^e is the number of DOFs of the generic element. In Eq. (3.17), \mathbf{K}_e^0 and \mathbf{K}_e are the non-penalised and the penalised stiffness matrices of element e , expressed in the global reference frame of the FE model, whilst $\hat{\mathbf{L}}_e$ is the connectivity matrix of element e relating the DOFs at the element-level to their counterparts at the structure-level:

$$\mathbf{u}_e = \hat{\mathbf{L}}_e \hat{\mathbf{u}},\tag{3.18}$$

where $\mathbf{u}_e \in \mathbb{R}^{N_{\text{DOF}}^e}$ is the vector of nodal displacements for element e .

The structural responses related to the design requirements considered in this study are presented in the following. The merit function is the so-called generalised compliance, introduced in [112], which is related to the total potential energy (TPE) of the continuum Π as follows:

$$\mathcal{C}(\boldsymbol{\xi}_1, \boldsymbol{\xi}_2) := -2\Pi(\boldsymbol{\xi}_1, \boldsymbol{\xi}_2),\tag{3.19}$$

where the TPE is defined as

$$\Pi(\boldsymbol{\xi}_1, \boldsymbol{\xi}_2) := \frac{1}{2} \hat{\mathbf{u}}^T \hat{\mathbf{K}} \hat{\mathbf{u}} - \mathbf{f}^T \mathbf{u}.\tag{3.20}$$

By injecting Eq. (3.15) in Eq. (3.20) and, subsequently, Eq. (3.20) in Eq. (3.19), the generalised compliance reads:

$$\mathcal{C}(\boldsymbol{\xi}_1, \boldsymbol{\xi}_2) = \mathbf{f}^T \mathbf{u} - \mathbf{u}_{\text{BC}}^T \mathbf{r}.\tag{3.21}$$

The physical meaning of the generalised compliance in the form of Eq. (3.21) is intuitively clear: a stiff structure should react to the applied loads by having small displacements and to the applied displacements by having large reaction forces.

Since the solution search is carried out through of a deterministic algorithm, the derivation of the formal expression of the gradient of the objective function with respect to the topological variables (TVs) (and of the constraint functions too) is needed to speed up the iterations. To this end, consider the following proposition.

Proposition 3.2.1. *Consider a deformable continuum subject to given external loads and displacements. If the imposed loads and displacements are independent from the pseudo-density field, the gradient of the generalised compliance reads:*

$$\frac{\partial \mathcal{C}}{\partial \xi_{i\tau}} = - \sum_{e \in \mathcal{S}_\tau} \frac{\alpha}{\rho_e} \frac{\partial \rho_e}{\partial \xi_{i\tau}} w_e, \quad i = 1, 2, \quad \tau = 1, \dots, n_{\text{CP}}. \quad (3.22)$$

where the internal work of the generic element e , i.e., w_e , is defined as

$$w_e := \mathbf{u}_e^T \mathbf{K}_e \mathbf{u}_e. \quad (3.23)$$

A proof of proposition 3.2.1 is provided in [112].

Remark 3.2.1. *In Eq. (3.22), the linear index τ has been introduced for the sake of compactness. The relation between τ and i_j , ($j = 1, 2, 3$) is:*

$$\tau := 1 + i_1 + i_2(n_1 + 1) + i_3(n_1 + 1)(n_2 + 1). \quad (3.24)$$

Moreover, in Eq. (3.22), the quantity \mathcal{S}_τ is the discretised version of the local support of Eq. (3.9), while $\frac{\partial \rho_e}{\partial \xi_{i\tau}}$ reads:

$$\frac{\partial \rho_e}{\partial \xi_{i\tau}} = \begin{cases} R_{\tau e}, & \text{if } i = 1, \\ \frac{R_{\tau e}}{\xi_{2\tau}} (\xi_{1\tau} - \rho_e), & \text{if } i = 2. \end{cases} \quad (3.25)$$

The scalar quantity $R_{\tau e}$ appearing in Eq. (3.25) is the NURBS rational basis function of Eq. (3.2) evaluated at the element centroid.

3.2.3 Constraint functions

Two further design requirements are considered in this Chapter. The first one deals with the lightness of the structure and is formulated in terms of a constraint on the overall volume of the structure V :

$$V = \sum_{e=1}^{N_e} \rho_e V_e, \quad (3.26)$$

where V_e is the volume of the generic element. By differentiating Eq. (3.26) one obtains:

$$\frac{\partial V}{\partial \xi_{i\tau}} = \sum_{e \in \mathcal{S}_\tau} V_e \frac{\partial \rho_e}{\partial \xi_{i\tau}}, \quad i = 1, 2, \quad \tau = 1, \dots, n_{\text{CP}}. \quad (3.27)$$

Therefore, the lightness requirement can be formulated as:

$$g_1(\boldsymbol{\xi}_1, \boldsymbol{\xi}_2) := \frac{V}{V_{\text{ref}}} - \gamma \leq 0, \quad (3.28)$$

where V_{ref} is a reference value of the volume, whilst γ is the imposed volume fraction.

The second requirement deals with the manufacturing constraint on the minimum thickness that can be fabricated through the selected manufacturing process. This requirement is formulated as minimum length scale (or minimum member size) constraint as:

$$g_2(\boldsymbol{\xi}_1, \boldsymbol{\xi}_2) := 1 - \frac{d_{\min}}{d_{\text{MP}}} \leq 0. \quad (3.29)$$

In Eq. (3.29), d_{\min} is the minimum length scale of the topology, while d_{MP} is the minimum dimension that can be obtained through the considered manufacturing process.

Remark 3.2.2. *As discussed in [113], the main advantage of the NURBS-based SIMP method is in the handling of the geometric constraints imposed on the TV. In particular, since the pseudo-density field describing the topology of the continuum is described by means of a NURBS hyper-surface, it is possible to properly set the integer parameters (i.e., number of CPs n_{CP} and basis functions degree p_j along each parametric direction) governing its shape to automatically satisfy the minimum length scale requirement, without introducing an explicit optimisation constraint in the problem formulation. Therefore, in the following, the manufacturing requirement of Eq. (3.29) will be controlled through this feature.*

Remark 3.2.3. *As discussed in [113], unlike the classical SIMP method, the minimum member size requirement, which can be met by properly tuning the value of the integer parameters involved in the definition of the NURBS entity does not depend upon the size of the elements composing the mesh. This means that an eventual mesh refinement has an impact only on the value of the structural responses (displacements, strains, stresses, etc.), but not on the minimum member size of the topology.*

3.2.4 Problem formulation

The TO problem is formulated in the form of a constrained non-linear programming problem (CNLPP) as follows:

$$\min_{\xi_1, \xi_2} \frac{\mathcal{C}(\xi_1, \xi_2)}{\mathcal{C}_{\text{ref}}}, \text{ subject to : } \begin{cases} \hat{\mathbf{K}}\hat{\mathbf{u}} = \hat{\mathbf{f}}, \\ g_1(\xi_1, \xi_2) \leq 0, \\ \xi_{1\tau} \in [\rho_{\min}, \rho_{\max}], \quad \xi_{2\tau} \in [\omega_{\min}, \omega_{\max}], \\ \tau = 1, \dots, n_{\text{CP}}. \end{cases} \quad (3.30)$$

In Eq. (3.30), \mathcal{C}_{ref} is the reference value of the of the generalised compliance of the structure, whilst ρ_{\min} and ρ_{\max} are lower and upper bounds of the pseudo-density at each CP, and ω_{\min} and ω_{\max} are the bounds of the weights. Of course, the lower bound of the pseudo-density must be strictly positive to prevent any singularity for the solution of the equilibrium problem. It is noteworthy that, as discussed in [112] the generalised compliance is not a positive definite functional, thus, it can take negative values. To this purpose, the reference compliance is always set equal to the absolute value of the generalised compliance of the starting solution.

3.3 The SANTO structure

The original version of the SANTO algorithm was coded in MATLAB environment [109]. In this Ph.D. Thesis, the new version coded in Python language is used. Of course, all the aspects and the new features related to multi-scale analyses presented in Chapters 4-6 have been developed and implemented only in the Python version of SANTO. The overall structure of the SANTO algorithm (for single-scale TO problems) is illustrated in Fig. 3.3 and briefly outlined in the following paragraphs.

- *Problem Setting.* In this phase the user has to set the main parameters of the problem at hand: the problem dimension, which can be 2D or 3D, the type of the parametric entity to be used, i.e., B-spline or NURBS, the integer parameters involved in the definition of the NURBS entity (i.e., CPs number and degrees), etc. Moreover, the user must set both design and non-design regions. The user must choose the type of objective function and the number and types of constraint functions, as well as the lower and upper bounds of these

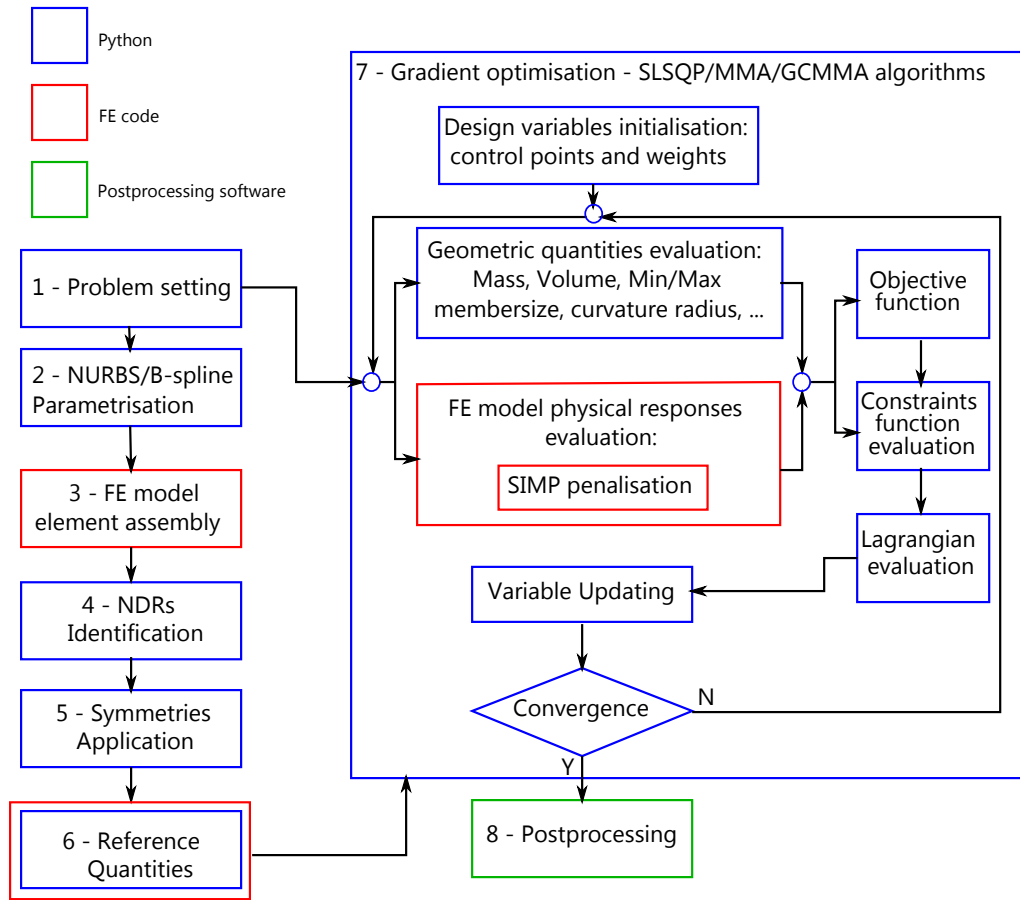


Figure 3.3 – Flow-chart of the SANTO algorithm.

latter. Finally the symmetry (mirror, translational, rotational, etc) on the geometrical entity is selected, via the activation of specific variables.

- *NURBS - B-spline parametrisation.* Once the problem setting is defined, the code automatically evaluate the NURBS continuous parameters, which are the dimensionless parameters of Eq. (3.12) and the non-trivial components of the knot-vectors of Eq. (3.7) along the different parametric directions.
- *FE model element assembly.* The user has to properly model the problem at hand in the external FE code in terms of geometry, design regions (DRs) and non-design regions (NDRs). The Python code will exploit the information about the geometrical and material features of the elements belonging to the design regions, i.e., the Cartesian coordinates of the center of gravity, the volumes, the

element connectivity, the material densities, etc.

- *NDRs identification.* Not all the zones of the structure have to be optimised and this requirement can be fulfilled by forecasting proper NDRs within the FE model at specific locations. Therefore, including all the CPs densities and the corresponding weights of the NURBS/B-spline hyper-surface (even those CPs whose local support falls within NDRs) among the design variables is useless. Hence the code automatically deactivates the CPs having an empty local support, meaning that in this region there are no active elements. The discarded CPs are set to the maximum or minimum value of the pseudo-density (depending on the location of the NDR) and they are not modified during the optimisation process.
- *Symmetries application.* Symmetries can be interpreted as variables saving from a computational standpoint. Only independent CPs densities and weights are stored in the array of design variables.
- *Reference quantities evaluation.* Geometrical and structural responses used to obtain dimensionless objective and constraint functions are assessed in this step. Of course, their definition is not unique: the external user can defined them according to the problem at hand. However, predefined strategies can be selected for the most common structural responses. For example, when the volume is considered as objective or constraint function, the reference volume is the volume of the design domain.
- *Gradient optimisation.* In the Python version of the SANTO algorithms, the user can choose among three deterministic algorithm: the sequential least squares programming (SLSQP) algorithm [114], the method of moving asymptotes (MMA) [5] and the globally-convergent method of moving asymptotes (GCMMA) [6]. Each algorithm is characterised by its own convergence criteria. For the sake of completeness, some details are here provided about the choice of the starting guess. The initial solution should be set in such a way to get a feasible point in the design domain (i.e., the set of optimisation constraints is met). However, this condition cannot be always fulfilled, especially when constraints on local structural responses (like maximum failure index, local buckling factor, etc.) are integrated in the problem formulation. Of course, the choice of a pertinent initial guess is of paramount importance and it could become a real challenge when a high number of constraints is included in the problem formulation: the higher the constraints number, the more complicated finding a feasible starting point. Once the deterministic algorithm is run, the objective function and the

optimisation constraints declared in the Problem Setting block are called from dedicated libraries. These libraries contains functions related to specific structural responses (e.g., compliance, eigenfrequencies, buckling, etc.): to assess them the user-defined FE model is invoked from Python. Conversely, the assessment of DRs of geometric nature, like volume/mass, minimum and maximum member size or the curvature radius, is done without calling the user-defined FE model. Of course, in each function, the calculation of the gradient is included. Then, the Lagrangian functional evaluation and the approximation of Hessian matrix are performed. The design variables array is updated according to the strategy implemented in the deterministic algorithm (i.e., SLSQP, MMA and GCMMA) and a convergence check is performed. This procedure is repeated until a convergence criterion is satisfied.

- *Post-processing.* After the optimisation, a threshold operation is performed on the topological descriptor, i.e., the B-spline / NURBS entity describing the pseudo-density field, to obtain the external boundary of the optimised structure. This task is straightforward in the case of a 2D problem. Hence, the external boundary can be easily extracted from a boolean intersection, carried out in a CAD software, between the final optimal surface and a plane located at a precise altitude proportional to the threshold value of the pseudo-density field. This threshold value is calculated in accordance with the satisfaction of the constraints prescribed by the user. On the other hand, in the case of a 3D problem, the boolean operation cannot be carried out in a CAD software, since the result of the optimisation is a 4D hyper-surface not compatible with standard CAD environment. Hence the threshold operation via an hyperplane should be carried out in a dedicated post-processing environment, e.g., ParaView®, from which a triangulated surface (TS) is extrapolated. The TS is embedded in a STL standard file, which is not editable in the CAD environment. The process of reconstructing the boundary surface of the optimised topology is a challenging task. This strategy is explained in detail in Chapter 7 and it consists of two fundamental steps: the parametrization of the cloud of points (derived from the STL file) and its approximation by a patch or a group of patches, wherein each patch is described through a parametric B-spline / NURBS surface.

3.4 Numerical results

For each benchmark problems considered in this section, lower and upper bounds of design variables are set as: $\rho_{\min} = 10^{-3}$, $\rho_{\max} = 1$; $\omega_{\min} = 0.5$, $\omega_{\max} = 10$.

Moreover, the non-trivial knot vectors components in Eq. (3.7) have been evenly distributed in the interval $[0, 1]$ for both 2D and 3D cases.

The effectiveness of the SANTO code is tested on 2D and 3D benchmarks. The software, coded in python language, is interfaced with the FE code ANSYS® to compute the structural responses. Moreover, the CNLPP of Eq. (3.30) has been solved through the globally convergent method of moving asymptotes (GCMMA) algorithm [6], whose parameters are listed in Tab. 3.1. For all benchmarks, the mass fraction at the macroscopic scale is $\gamma = 0.4$, while titanium is used as a bulk material with the following properties: $E = 110$ GPa, $\nu = 0.33$, $\rho = 2.8$ Kgmm⁻³. Moreover, in all benchmark problems presented in this Chapter homogeneous BCs of the Dirichlet type are taken into account, i.e., $\mathbf{u}_{BC} = \mathbf{0}$.

Table 3.1 – GCMMA algorithm parameters

Parameter	Value
<i>move</i>	0.1
<i>albfa</i>	0.1
Stop Criterion	Value
Maximum n. of function evaluations	10000
Maximum n. of iterations	$20 \times n_{\text{var}}$
Tolerance on objective function	10^{-6}
Tolerance on constraints	10^{-6}
Tolerance on input variables change	10^{-6}
Tolerance on Karush –Kuhn –Tucker norm	10^{-6}

As far as numerical tests are concerned, the following aspects are considered:

1. The influence of the NURBS entity integer parameters, i.e., blending functions degree and CPs number, on the optimised topology is investigated;
2. The influence of the geometric entity, i.e., B-spline or NURBS used to describe the pseudo-density field, on the optimised topology is studied (both 2D and 3D problems);

3. The influence of the NDR and of the minimum member size constraint (according to the methodology proposed in [113]) on the optimised topology is investigated (only for 3D problems for the sake of brevity).

Furthermore, symmetry constraints on the pseudo-density field describing the topology are imposed during optimisation: single symmetry for 2D problems (with respect to axis $x_2 = \frac{a_2}{2}$) and two planes of symmetry ($x_j = \frac{a_j}{2}$, $j = 1, 2$) for 3D problems. Of course, the presence of a symmetry constraint implies a reduction in the design variables count as follows:

$$n_{\text{var}} = \begin{cases} \prod_{i=1}^N \theta_i, & \text{for B - spline entity,} \\ 2 \prod_{i=1}^N \theta_i, & \text{for NURBS entity,} \end{cases} \quad (3.31)$$

with $N = 2$ and $N = 3$ for 2D and 3D problems, respectively, and

$$\theta_i = \begin{cases} \frac{n_i + 1}{2}, & \text{if } n_i \text{ is odd,} \\ \lfloor \frac{n_i + 1}{2} \rfloor + 1, & \text{otherwise.} \end{cases} \quad (3.32)$$

Post-processing operations are performed in ParaView[®] environment.

3.4.1 The 2D benchmark problem

In the case of 2D benchmark problem, a cantilever beam is analysed, which is a rectangle of size $a_1 = 600$ mm $a_2 = 300$ mm. The load is applied along the x_2 axis on point E, located at $(x_1 = a_1, x_2 = \frac{a_2}{2})$, as shown in Fig. 3.7, with a magnitude $F_E = 500$ N. The nodes belonging to the side AB are clamped. No NDR is considered for this benchmark.

The static FE analysis is carried out using 120×60 PLANE182 elements (with plane stress hypothesis and 4 nodes, 2 DOFs per node). The thickness of the plate is $t = 1$ mm.

Problem (3.30) is solved by employing both B-spline and NURBS surfaces. The following combinations of blending functions degrees and CPs number are considered: $p_1 = p_2 = 2, 3$ and $n_{\text{CP}} = 60 \times 30, 84 \times 42, 104 \times 52$.

The optimised topologies are shown in Figs. 3.5-3.6, whilst the mechanical responses are listed in Table 3.2.

The following remarks can be drawn from the analysis of the numerical results of the sensitivity analysis with respect to the B-spline or NURBS parameters:

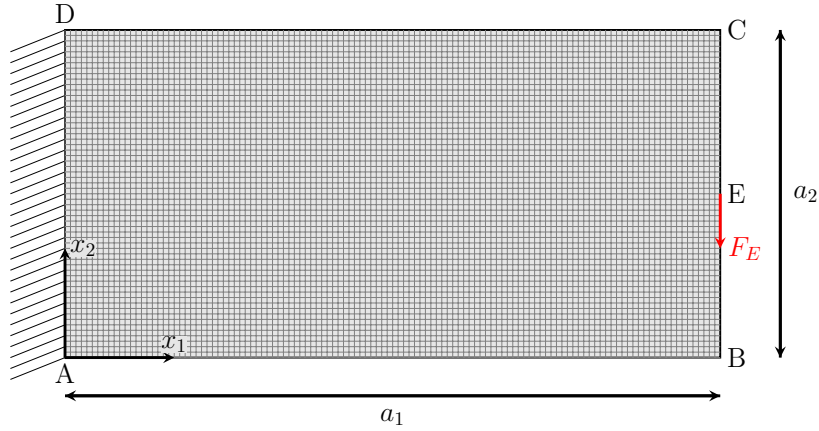


Figure 3.4 – Geometry and boundary conditions of the 2D benchmark of a cantilever beam.

Table 3.2 – 2D-BK: compliance and volume for the optimised topologies in the three configurations of B-spline/NURBS parameters.

Degree	Number of CPs	Compliance [Nmm]		Volume [mm ³]	
		B-spline	NURBS	B-spline	NURBS
$p_1 = p_2 = 2$	$n_{\text{CP}} = 1800$	197.29	182.19	71999.84	71999.95
	$n_{\text{CP}} = 3528$	187.10	178.27	71999.89	71999.82
	$n_{\text{CP}} = 5408$	186.19	177.52	71999.95	71999.92
$p_1 = p_2 = 3$	$n_{\text{CP}} = 1800$	202.46	185.24	71999.90	71999.96
	$n_{\text{CP}} = 3528$	190.79	179.56	71999.86	71999.80
	$n_{\text{CP}} = 5408$	189.47	179.66	71999.96	71999.72

1. The greater the number of CPs (for a given degree) or the smaller the degree (for a given number of CPs) the better the structural performances (in terms of compliance) of the optimised topology. The same result can be obtained in the standard SIMP algorithm by decreasing the mesh size.
2. Moreover, the increase of the number of CPs (for a given degree) and the decrease of the degree (for a given number of CPs) have an impact also on the minimum member size of the optimised topology due to local support property of Eq. (3.9), which defines the size of the influence region of the CP. Therefore, as widely discussed in [113], the integer parameters involved in the definition of the NURBS entity have a strong influence on the size of the local support and, thus, on the minimum member size, which can be properly selected

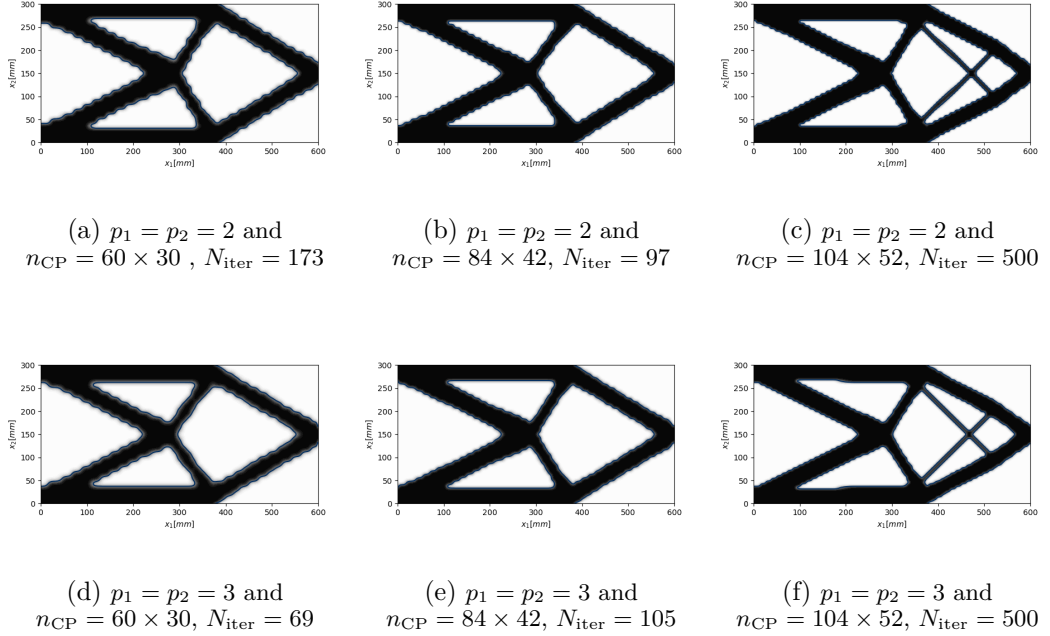


Figure 3.5 – Benchmark problem 2D-BK: influence of the degrees and CPs number on the optimised topology for B-spline solutions.

by acting directly on these parameters, without introducing an explicit constraint in the problem formulation. The interested reader is addressed to [113] for more details on this point.

- The effect of introducing the NURBS weights among the design variables is twofold. On the one hand, weights have a positive impact on the final mechanical performances of the solution (in fact the NURBS solutions show always a value of objective function lower than the one of the B-spline counterpart). On the other hand, the boundary of the topologies obtained by NURBS entities is smoother than the one of B-spline solutions having same degrees and number of CPs, see Figs. 3.5-3.6.

3.4.2 The 3D benchmark

In the case of 3D benchmark a supported structure is analysed, which is a box of size $a_1 = a_2 = a_3 = 40$ mm. As shown in Fig. 3.8, the load is

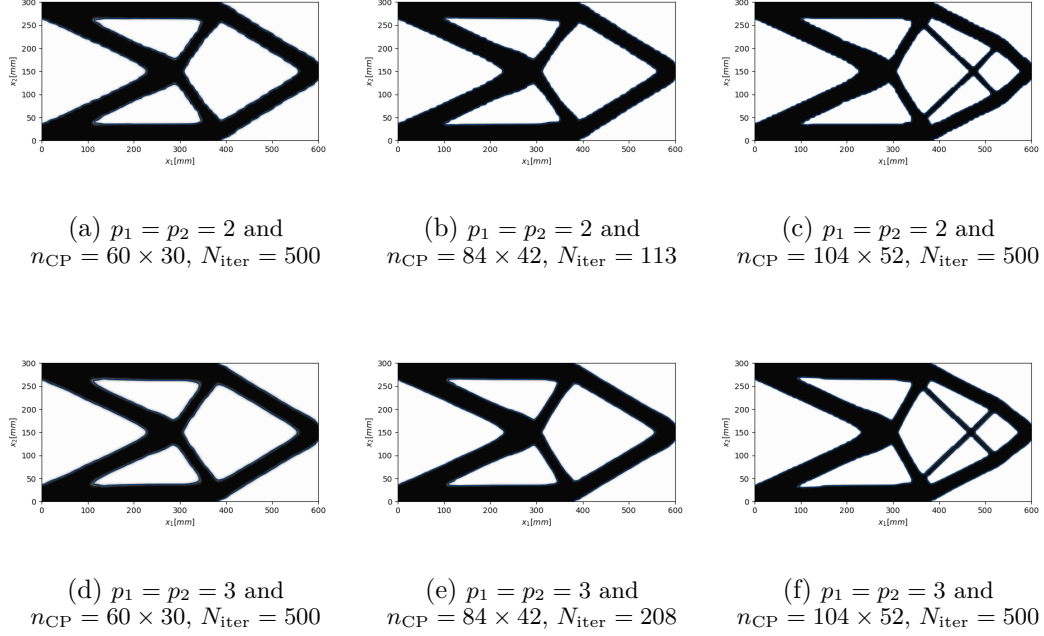


Figure 3.6 – Benchmark problem 2D-BK: influence of the degrees and CPs number on the optimised topology for NURBS solutions.

applied along the x_2 axis on point I, with a magnitude of $F_I = 20000$ N, by exploiting a MPC184 element defined between the master node I, located at $(x_1, x_2, x_3) = (20, 40, 20)$ mm, and a set of slaves nodes in the upper region of the structure, i.e., $S_I = \{(x_1, x_2, x_3) : x_1 \in [16, 24]$ mm, $x_2 = 40$ mm, $x_3 \in [16, 24]$ mm}. The nodes belonging to the four corners of the face located at $x_2 = 0$, are clamped. Five NDR are considered near to the application of the BCs and load as follows:

- $NDR_1 = \{(x_1, x_2, x_3) : x_1 \in [0, 4]$ mm, $x_2 \in [0, 4]$ mm, $x_3 \in [36, 40]$ mm}
- $NDR_2 = \{(x_1, x_2, x_3) : x_1 \in [36, 40]$ mm, $x_2 \in [0, 4]$ mm, $x_3 \in [36, 40]$ mm}
- $NDR_3 = \{(x_1, x_2, x_3) : x_1 \in [36, 40]$ mm, $x_2 \in [0, 4]$ mm, $x_3 \in [0, 4]$ mm}
- $NDR_4 = \{(x_1, x_2, x_3) : x_1 \in [0, 4]$ mm, $x_2 \in [0, 4]$ mm, $x_3 \in [0, 4]$ mm}
- $NDR_5 = \{(x_1, x_2, x_3) : x_1 \in [16, 24]$ mm, $x_2 \in [36, 40]$ mm, $x_3 \in [16, 24]$ mm}

Static FE analyses are carried out using $20 \times 20 \times 20$ SOLID185 elements

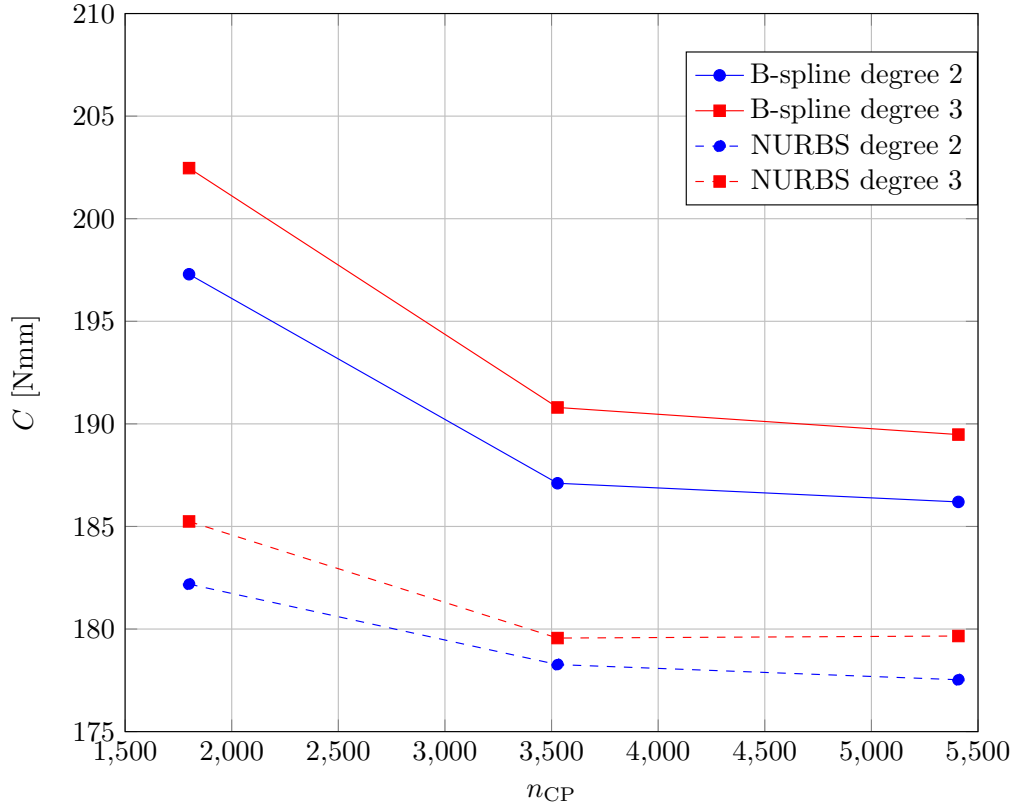


Figure 3.7 – Benchmark 2D-BK - Optimal value of the compliance vs. the number of CPs for different degrees.

(with 8 nodes and 3 DOFs per node).

Problem (5.27) is solved by employing both B-spline and NURBS hypersurfaces. Degrees and number of CPs are chosen accordingly to the results of the sensitivity analysis performed for the 2D benchmark, hence the configuration which shows the best performances in terms of compliance is used, i.e., $p_1 = p_2 = p_3 = 2$ and $n_1 = n_2 = n_3 = 17$, which corresponds to $n_{CP} = 5832$ that represents a percentage of $n_{CP}/N_e = 75\%$ of the total number of elements of the structure. This configuration of degrees and CPs ensures a minimum member size $d_{\min} = 4$ mm with a threshold value of $\rho_{th} = 0.40$ according to the methodology detailed in [113]:

The optimised topologies are shown in Fig. 3.9, whilst the mechanical responses are listed in Table 3.3.

The same remarks provided for the 2D benchmark problem can be repeated here for both B-splines and NURBS results.

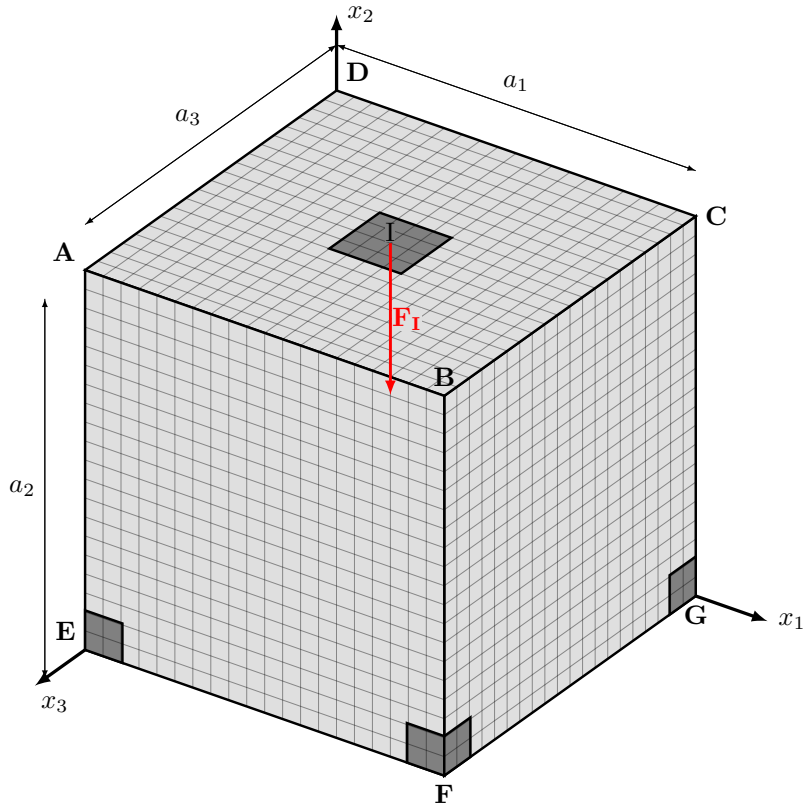


Figure 3.8 – Geometry and boundary conditions of the 3D benchmark structure.

Table 3.3 – 3D-BK: compliance and volume for the optimised topologies defined via the B-spline/NURBS entities.

Degrees and number of CPs	Compliance [Nmm]		Volume [mm ³]	
	B-spline	NURBS	B-spline	NURBS
$p_1 = p_2 = p_3 = 2, n_{CP} = 5832$	682.51	648.44	25676.75	25676.75

3.5 Conclusion

This Chapter presents the fundamentals of the NURBS-based SIMP method for single-scale problems together with some benchmark problems to show the effectiveness of the SANTO code. Numerical results obtained for single-scale 2D and 3D TO problems show that the Python version of the SANTO code provides trends of the value of the objective function versus the number of CPs and degrees consistent with the results found in



(a) B-spline with $p_1 = p_2 = p_3 = 2$ and $n_1 = n_2 = n_3 = 4$, $N_{\text{iter}} = 500$, $d_{\text{min-meas}} = 14.7$ mm



(b) NURBS with $p_1 = p_2 = p_3 = 2$ and $n_1 = n_2 = n_3 = 4$, $N_{\text{iter}} = 500$, $d_{\text{min-meas}} = 12.6$ mm

Figure 3.9 – Benchmark problem 3D-BK: influence of the degrees and CPs number on the optimised topology for (a) B-spline and (b) NURBS solutions.

[109] with the previous MATLAB version. This comparison, along with the results presented in other Ph.D. Theses [115, 116], validates the new version of the code since the same benchmark problems were tested in both the versions of SANTO obtaining an excellent agreement between results. In the following Chapters the new version of SANTO able to deal with multi-scale topology optimisation problems will be presented in details together with the new features in terms of both numerical and theoretical frameworks.

The points summarised here below provide a brief reminder about the main features of SANTO algorithm for single-scale TO problems, which represent just as many advantages of the NURBS-based SIMP method.

- Reduction of the number of design variables and implicitly defined filter zone. In Sec. 3.1 the local support property is presented as key point of the strategy in terms of variables saving and implicit filter method. In fact, a single CP affects a precise region of the fictitious density field, described by a parametric B-spline/NURBS surface/hyper-surface, which is related to a zone of the computational domain. Hence, it is not necessary to define a further filter zone, since the NURBS local support implicitly establishes a relationship among contiguous elements of the mesh of the FE model. The filter size depends on the NURBS discrete parameters, i.e., degree and number of CPs, which can be adjusted to obtain a good compromise among performances, variables saving and smoothness of the bounds. The higher the number of CPs the smaller the filter zone, and improved performances are found, but computational burden is higher in this case. When the overall number of CPs is kept constant and the degree is increased the filter size is enlarged, which implies smoother topologies but with lower performance. Moreover, the local support property imposes a length scale on the design domain, without the need of introducing explicit optimisation constraints to control this feature (unlike the classic SIMP method).
- Importance of NURBS weight. The NURBS weights have an important role in terms either of the quality of the solution (i.e., in terms of the value of the merit function) or in the smoothing of the boundary of the optimised topology.
- Results provision and consistency. The advantages of NURBS surfaces are fully exploited in terms of their CAD compatibility. When 2D problems are considered a post-processing phase can be easily implemented to obtain the optimised 2D geometry of the component boundary. Such a geometry can be stored in a standard IGS file. If 3D problems are concerned, results are provided in terms of high quality STL file, which can be reconstructed via the strategy presented in Chapter 7.
- Actual reassembled 2D-3D topologies. The TO result is totally CAD compatible in the 2D case and after the surface reconstruction for the 3D case. This fact allows for evaluating the performances of the structure on the true optimised geometry.

Chapter 4

Multi-scale topology optimisation I

Design of the representative volume element under design requirements defined at the macroscopic scale.

In this Chapter, a general framework for the multi-scale topology optimisation (TO) of lattice structures (LSs) is presented. More precisely, the goal is to find the optimal topology of the representative volume element (RVE) of the LS at the mesoscopic scale by considering design requirements defined at the macroscopic scale. The proposed method involves: Non-Uniform Rational Basis Spline (NURBS) hyper-surfaces to represent the pseudo-density field describing RVE topology, the Solid Isotropic Material with Penalisation (SIMP) approach and the strain energy-based homogenisation method (SEHM) to perform the scale transition (only weak coupling among scales is considered). Specifically, in this Chapter the following question has been addressed: what is the most efficient (in terms of computational costs) variant of the SEHM approach when coupled to a TO algorithm? In particular, a rigorous proof about the computational efficiency of the SEHM based on the elements strain energy when compared to the SEHM based on elements averaged stresses is provided. Moreover, the Dirichlet's problem properties together with the geometrical properties of the NURBS entities are exploited in deriving the analytical expression of the gradient of the macroscopic physical responses with respect to the topological variable defined at the RVE scale. To this end, the analytical formula of the gradient of the macroscopic requirements takes advantage from the local support property of the NURBS blending functions [107, 108], which establishes an implicit relationship among the pseudo-densities of adjacent elements. Thanks to

this property there is no need of introducing complicated filtering schemes, unlike the classical SIMP method.

The effectiveness of the proposed approach is tested on 2D and 3D benchmark problems. In this background, a sensitivity analysis of the optimised topology to the integer parameters, involved in the definition of the NURBS hyper-surface, is carried out. Moreover, the influence of the initial guess and of the macroscopic loading condition on the optimised topology of the RVE is also investigated.

The Chapter is organised as follows. A brief introduction on the SEHM method from a theoretical point of view in Sec. 4.1. Sec. 4.2 presents the theoretical/numerical framework of the NURBS-based SIMP method integrating multi-scale analyses. In Sec. 4.3, the effectiveness of the proposed approach is shown on 2D and 3D benchmark problems. Finally, in Sec. 4.4, the main contributions and prospects of this works are discussed.

The contents of this Chapter have been presented in the article [38].

Notation. Upper-case bold letters and symbols are used to indicate tensors (matrices), while lower-case bold letters and symbols indicate column vectors. Subscripts m and M denote quantities evaluated at RVE scale and macroscopic scale, respectively.

4.1 The strain energy homogenisation method

At the mesoscopic scale, the RVE of the LS can be interpreted, from a mechanical point of view, as an heterogeneous medium composed of two phases, i.e., the bulk material and the void. Conversely, at the macroscopic scale it can be modelled as an equivalent homogeneous anisotropic continuum whose mechanical response is described by a set of *effective* (or equivalent) material properties.

This Chapter focuses only on the elastic behaviour of the LS at the macroscopic scale, thus, the macroscopic elasticity tensor (represented as a matrix $\mathbf{C}_M \in \mathbb{R}^{6 \times 6}$ through the Voigt's notation) of the LS is determined by means of the SEHM. This technique makes use of the repetitive unit of the periodic structure to evaluate the resulting properties at the macroscopic scale. The basic assumption of the SEHM is that the strain energy of the RVE is equal to the counterpart of the corresponding “envelope volume” of the homogeneous anisotropic medium replacing the LS at the macroscopic scale. This homogenisation scheme has proven to be an efficient numerical procedure able to determine the equivalent properties of different heteroge-

neous materials characterised by complex RVE topologies [117, 118].

In order to evaluate \mathbf{C}_M , three further hypotheses have to be considered: (a) the bulk material of the LS is characterised by a linear, elastic behaviour; (b) small displacements and strains occurs when the RVE is subject to given BCs; (c) the buckling of the RVE thin topological branches (that could appear during the optimisation process) is neglected.

To assess the components of \mathbf{C}_M , the RVE is submitted to a uniform strain field ε_{mij}^0 , with $i, j = 1, 2, 3$ (tensor notation). The six independent components of the strain tensor are applied one at time by considering the following set of PBCs [119]:

$$\begin{aligned} u_{mi}(a_{m1}, x_{m2}, x_{m3}) - u_{mi}(-a_{m1}, x_{m2}, x_{m3}) &= 2a_{m1}\varepsilon_{mi1}^0, \\ u_{mi}(x_{m1}, a_{m2}, x_{m3}) - u_{mi}(x_{m1}, -a_{m2}, x_{m3}) &= 2a_{m2}\varepsilon_{mi2}^0, \\ u_{mi}(x_{m1}, x_{m2}, a_{m3}) - u_{mi}(x_{m1}, x_{m2}, -a_{m3}) &= 2a_{m3}\varepsilon_{mi3}^0, \\ \forall x_{mi} \in [-a_{mi}, a_{mi}], \quad i &= 1, 2, 3. \end{aligned} \quad (4.1)$$

In the above formula, a_{mi} is the characteristic length of the RVE along the x_{mi} axis, while u_{mi} is the component of the displacement field along the same axis. Consider now the equilibrium equation of the FE model of the RVE. In the most general case it reads:

$$\hat{\mathbf{K}}_m \hat{\mathbf{u}}_m = \hat{\mathbf{f}}_m; \quad \hat{\mathbf{u}}_m, \hat{\mathbf{f}}_m \in \mathbb{R}^{\hat{N}_{m\text{DOF}}}, \quad \hat{\mathbf{K}}_m \in \mathbb{R}^{\hat{N}_{m\text{DOF}} \times \hat{N}_{m\text{DOF}}}, \quad (4.2)$$

where $\hat{N}_{m\text{DOF}}$ is the overall number of degrees of freedom (DOFs) of the structure before the application of the BCs, while $\hat{\mathbf{K}}_m$ is the non-reduced (singular) stiffness matrix of the RVE. $\hat{\mathbf{u}}_m$ is the non-reduced vector of generalised displacements containing both imposed and unknown DOFs of the FE model and $\hat{\mathbf{f}}_m$ is the non-reduced vector of generalised nodal forces (both known and unknown quantities). The expression of the above vectors and matrix is:

$$\begin{aligned} \hat{\mathbf{K}}_m &:= \begin{bmatrix} \mathbf{K}_m & \mathbf{K}_{m\text{BC}} \\ \mathbf{K}_{m\text{BC}}^T & \tilde{\mathbf{K}}_m \end{bmatrix}, \quad \hat{\mathbf{u}}_m := \begin{Bmatrix} \mathbf{u}_m \\ \mathbf{u}_{m\text{BC}} \end{Bmatrix}, \quad \hat{\mathbf{f}}_m := \begin{Bmatrix} \mathbf{f}_m \\ \mathbf{r}_m \end{Bmatrix}, \\ \mathbf{u}_m, \mathbf{f}_m &\in \mathbb{R}^{N_{m\text{DOF}}}, \quad \mathbf{u}_{m\text{BC}}, \mathbf{r}_m \in \mathbb{R}^{N_{m\text{BC}}}, \quad \mathbf{K}_m \in \mathbb{R}^{N_{m\text{DOF}} \times N_{m\text{DOF}}}, \\ \mathbf{K}_{m\text{BC}} &\in \mathbb{R}^{N_{m\text{DOF}} \times N_{m\text{BC}}}, \quad \tilde{\mathbf{K}}_m \in \mathbb{R}^{N_{m\text{BC}} \times N_{m\text{BC}}}. \end{aligned} \quad (4.3)$$

In Eq. (4.3), $N_{m\text{DOF}}$ is the number of unknown DOFs, while $N_{m\text{BC}}$ represents the number of DOFs where BCs on generalised displacements are applied (of course $\hat{N}_{m\text{DOF}} = N_{m\text{DOF}} + N_{m\text{BC}}$). \mathbf{u}_m and $\mathbf{u}_{m\text{BC}}$ are the unknown and known vectors of generalised displacements, respectively. \mathbf{f}_m

is the vector of generalised external nodal forces, whilst \mathbf{r}_m is the vector of generalised nodal reactions where BCs on generalised displacements are imposed. \mathbf{K}_m , \mathbf{K}_{mBC} and $\tilde{\mathbf{K}}_m$ are the stiffness matrices of the FE model of the RVE after applying BCs. Inasmuch as the PBCs of Eq. (4.1) are imposed in terms of displacements and no external forces are applied to the FE model of the RVE, i.e., $\mathbf{f}_m = \mathbf{0}$, the equilibrium problem of Eq. (4.3) is of the Dirichlet's type.

The difference between the SEHM based on elements averaged stresses and the SEHM based on elements strain energy is in the post-processing of the results of the FE analyses. For both techniques, six static analyses, corresponding to the application of elementary uni-axial strain fields in Eq. (4.1), are required to uniquely assess the components of the macroscopic elasticity tensor \mathbf{C}_M of the LS.

As far as the SEHM based on elements averaged stresses is concerned, for each static analysis, the volume-averaged value of the stress vector (Voigt's notation) $\boldsymbol{\sigma}_m(\varepsilon_{m\beta}^0) \in \mathbb{R}^6$ can be easily computed and the stiffness matrix of the equivalent homogeneous material can be calculated one column at time as:

$$\mathbf{C}_{M\beta} = \frac{1}{V_{\text{RVE}}\varepsilon_{m\beta}^0} \int_{V_{\text{RVE}}} \boldsymbol{\sigma}_m(\varepsilon_{m\beta}^0) dV \approx \frac{1}{V_{\text{RVE}}\varepsilon_{m\beta}^0} \sum_{e=1}^{N_{me}} \boldsymbol{\sigma}_{me}(\varepsilon_{m\beta}^0) V_{me}, \quad (4.4)$$

$$\varepsilon_{m\beta}^0 \neq 0, \quad \varepsilon_{m\gamma}^0 = 0, \quad \beta, \gamma = 1, \dots, 6, \quad \gamma \neq \beta, \quad \mathbf{C}_{M\beta} \in \mathbb{R}^6,$$

where $\mathbf{C}_{M\beta}$ represents the β column of matrix \mathbf{C}_M . In Eq. (4.4), N_{me} is the number of elements composing the FE model of the RVE, V_{me} is the volume of the generic element, whilst $V_{\text{RVE}} = 8a_{m1}a_{m2}a_{m3}$ is the ‘‘envelope’’ volume of the 3D domain wherein the RVE is defined.

Regarding the SEHM based on elements strain energy, the work of internal forces of the RVE can be easily retrieved for each static analysis as:

$$\mathcal{C}_M := \mathbf{f}_m^T \mathbf{u}_m + \mathbf{r}_m^T \mathbf{u}_{mBC}. \quad (4.5)$$

Then, by considering both uni-axial and bi-axial strain fields in Eq. (4.1) and by imposing the equivalence between the strain energy of the equivalent homogeneous anisotropic continuum and that of the RVE of the LS, the components of matrix \mathbf{C}_M can be computed as:

$$C_{Mkk} = \frac{\mathcal{C}_M(\varepsilon_{mk}^0)}{V_{\text{RVE}}(\varepsilon_{mk}^0)^2}, \quad k = 1, \dots, 6, \quad (4.6)$$

$$C_{Mij} = \frac{\mathcal{C}_M(\varepsilon_{mi}^0, \varepsilon_{mj}^0)}{2V_{RVE}\varepsilon_{mi}^0\varepsilon_{mj}^0} - C_{Mii}\frac{\varepsilon_{mi}^0}{2\varepsilon_{mj}^0} - C_{Mjj}\frac{\varepsilon_{mj}^0}{2\varepsilon_{mi}^0}, \quad i, j = 1, \dots, 6. \quad (4.7)$$

Eq. (4.6) is used to assess the terms belonging to the main diagonal of tensor \mathbf{C}_M , whilst Eq. (4.7) allows for determining the terms outside the main diagonal. $\mathcal{C}_M(\varepsilon_{mk}^0)$ and $\mathcal{C}_M(\varepsilon_{mi}^0, \varepsilon_{mj}^0)$ represent the work of internal forces, evaluated for uni-axial and bi-axial strain fields, respectively. Of course, Eq. (4.6) must be solved before Eq. (4.7); moreover the work of internal forces of the RVE for a bi-axial strain field can be obtained from the results (displacements and forces) of the analyses wherein uni-axial strain fields are considered as follows:

$$\mathcal{C}_M(\varepsilon_{mi}^0, \varepsilon_{mj}^0) = (\mathbf{f}_{mi}^T + \mathbf{f}_{mj}^T)(\mathbf{u}_{mi} + \mathbf{u}_{mj}) + (\mathbf{r}_{mi}^T + \mathbf{r}_{mj}^T)(\mathbf{u}_{mBCi} + \mathbf{u}_{mBCj}), \quad (4.8)$$

where subscripts i and j refer to the FE analyses where uni-axial strain fields ε_{mi}^0 and ε_{mj}^0 are imposed in the PBCs of Eq. (4.1).

Finally, the density of the equivalent homogeneous anisotropic medium at the macroscopic scale is defined as:

$$\tau_M := \tau_m \frac{V_m}{V_{RVE}}, \quad (4.9)$$

where τ_m is the density of the bulk material composing the RVE, whilst V_m is the actual volume of the RVE.

Remark 4.1.1. *The material properties used in this work are expressed either in the form of engineering constants or in the form of the Cartesian components of the elasticity tensor in the material frame. In each case, the Voigt's notation employed in ANSYS software [120] is used. The passage from tensor notation to Voigt's one can be easily expressed by the following two-way relationship among indices:*

$$\{11, 22, 33, 21, 32, 31\} \Leftrightarrow \{1, 2, 3, 4, 5, 6\}. \quad (4.10)$$

4.2 The multi-scale NURBS-based SIMP method

A detailed description of the mathematical background of the NURBS-based SIMP method is available in [108, 110]. The main features of the

approach are briefly described here only for 3D multi-scale TO problems. The goal of the multi-scale TO approach presented in this study is to determine the optimum topology of the LS RVE by considering design requirements involved at both lower (i.e., microscopic or mesoscopic) and upper (macroscopic) scales. The characteristic problem scales (and the relative geometrical features) are illustrated in Fig. 4.1.

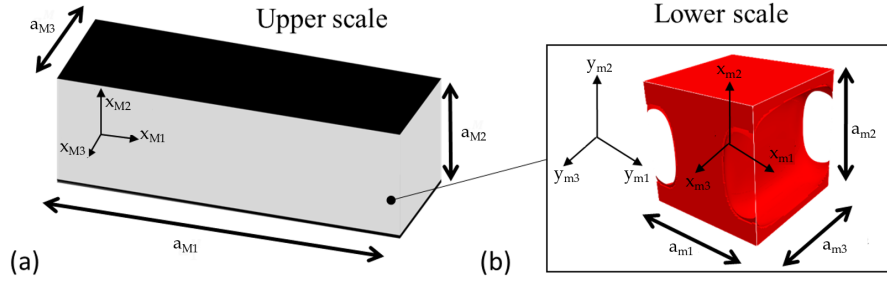


Figure 4.1 – Characteristic scales of the multi-scale topology optimisation problem: (a) the macroscopic (upper) scale of the structure and (b) the lower (i.e., mesoscopic or microscopic) scale of the lattice RVE

Consider the compact Euclidean space $\mathcal{D}_m \subset \mathbb{R}^3$ (defining the RVE domain at the lower scale) in a Cartesian orthogonal frame $O(y_{m1}, y_{m2}, y_{m3})$:

$$\mathcal{D}_m := \{\mathbf{y}_m^T = (y_{m1}, y_{m2}, y_{m3}) \in \mathbb{R}^3 : y_{mj} \in [0, 2a_{mj}], j = 1, 2, 3\}, \quad (4.11)$$

where a_j , is the characteristic length of the domain defined along x_j axis, as shown in Fig. 4.1. In the SIMP approach the *material domain* $\Omega_m \subseteq \mathcal{D}_m$ of the RVE is identified by means of the pseudo-density function $\rho(\mathbf{y}_m) \in [0, 1]$ for $\mathbf{y}_m \in \mathcal{D}_m$: $\rho(\mathbf{y}_m) = 0$ means absence of material, whilst $\rho(\mathbf{y}_m) = 1$ implies completely dense bulk material.

In the framework of the NURBS-based SIMP method, a NURBS entity of dimension $D+1$ is used to describe the topology of a problem of dimension D . Therefore, if a 3D TO problem is considered, a 4D NURBS hyper-surface is needed to describe the RVE topology. In particular, the first three coordinates of the NURBS hyper-surface correspond to the Cartesian coordinates defining the 3D domain of the lattice RVE, while the fourth coordinate corresponds to the RVE pseudo-density field and reads:

$$\rho(\zeta_{m1}, \zeta_{m2}, \zeta_{m3}) = \sum_{i_1=0}^{n_1} \sum_{i_2=0}^{n_2} \sum_{i_3=0}^{n_3} R_{i_1, i_2, i_3}(\zeta_{m1}, \zeta_{m2}, \zeta_{m3}) \rho_{i_1, i_2, i_3}. \quad (4.12)$$

In Eq. (4.12), $n_{\text{CP}} = (n_1 + 1)(n_2 + 1)(n_3 + 1)$ is the total number of CPs, while the dimensionless parameters ζ_{mj} ($j = 1, 2, 3$) can be related to the Cartesian coordinates y_{mj} of the 3D domain (see Fig. 4.1) as follows:

$$\zeta_{mj} = \frac{y_{mj}}{2a_{mj}}, \quad j = 1, 2, 3. \quad (4.13)$$

There are many parameters affecting the shape of a NURBS entity. Among them, the pseudo-density at CPs and the associated weights are identified as *design variables* and are collected in the vectors $\boldsymbol{\xi}_1$ and $\boldsymbol{\xi}_2$, respectively, defined as:

$$\boldsymbol{\xi}_1^{\text{T}} := (\rho_{0,0,0}, \dots, \rho_{n_1, n_2, n_3}), \quad \boldsymbol{\xi}_2^{\text{T}} := (\omega_{0,0,0}, \dots, \omega_{n_1, n_2, n_3}), \quad \boldsymbol{\xi}_1, \boldsymbol{\xi}_2 \in \mathbb{R}^{n_{\text{CP}}} .. \quad (4.14)$$

Accordingly, in the most general case, the overall number of design variables is $n_{\text{var}} = 2n_{\text{CP}}$.

The multi-scale TO problem presented here deals with the minimisation of the macroscopic compliance \mathcal{C}_M subject to an inequality constraint on the macroscopic mass m_M . Of course, the structure responses at the macroscopic scale are influenced by the topological variable defined at the lower scale as a result of the homogenisation process of the lattice RVE. As discussed in Section 4.1, the equilibrium of the RVE is described by Eq. (4.2) subject to the PBCs of Eq. (4.1), i.e., the RVE equilibrium problem is of Dirichlet's type. At the lower scale, the density field affects the element stiffness matrix and, accordingly, the global stiffness matrix of the FE model of the RVE as follows:

$$\hat{\mathbf{K}}_m = \sum_{e=1}^{N_{me}} \rho_e^\alpha \hat{\mathbf{L}}_{me}^{\text{T}} \mathbf{K}_{me} \hat{\mathbf{L}}_{me}, \quad \mathbf{K}_{me} \in \mathbb{R}^{N_{m\text{DOF},e} \times N_{m\text{DOF},e}}, \quad \hat{\mathbf{L}}_{me} \in \mathbb{R}^{N_{m\text{DOF},e} \times \hat{N}_{m\text{DOF}}}, \quad (4.15)$$

where ρ_e is the fictitious density of Eq. (4.12) computed at the centroid of the generic element e and N_{me} is the total number of elements composing the FE model of the RVE. $\hat{\mathbf{L}}_{me}$ is the connectivity matrix of element e (before applying the BCs), \mathbf{K}_{me} is the non-penalised element stiffness matrix expressed in the global reference frame of the model and $N_{m\text{DOF},e}$ is the number of DOFs for element e . In Eq. (4.15), $\alpha \geq 1$ is a suitable parameter that aims at penalising all the meaningless densities between 0 and 1, in agreement with the classic SIMP approach (usually $\alpha = 3$).

Conversely, the volume of the RVE is penalised as:

$$V_m = \sum_{e=1}^{N_{me}} \rho_e V_{me}, \quad (4.16)$$

where V_{me} is the volume of the generic element composing the FE model of the RVE.

At the macroscopic scale the equilibrium equation of the FE model of the structure reads:

$$\hat{\mathbf{K}}_M \hat{\mathbf{u}}_M = \hat{\mathbf{f}}_M; \quad \hat{\mathbf{u}}_M, \hat{\mathbf{f}}_M \in \mathbb{R}^{\hat{N}_{MDOF}}, \quad \hat{\mathbf{K}}_M \in \mathbb{R}^{\hat{N}_{MDOF} \times \hat{N}_{MDOF}}, \quad (4.17)$$

where \hat{N}_{MDOF} is the number of DOFs of the structure before the application of the BCs, while $\hat{\mathbf{K}}_M$ is the non-reduced stiffness matrix of the structure. $\hat{\mathbf{u}}_M$ is the non-reduced vector of generalised displacements containing both imposed and unknown DOFs of the FE model and $\hat{\mathbf{f}}_M$ is the non-reduced vector of generalised nodal forces (both known and unknown quantities). In analogy with Eq. (4.3) the following arrays can be introduced:

$$\hat{\mathbf{K}}_M := \begin{bmatrix} \mathbf{K}_M & \mathbf{K}_{MBC} \\ \mathbf{K}_{MBC}^T & \tilde{\mathbf{K}}_M \end{bmatrix}, \quad \hat{\mathbf{u}}_M := \begin{Bmatrix} \mathbf{u}_M \\ \mathbf{u}_{MBC} \end{Bmatrix}, \quad \hat{\mathbf{f}}_M := \begin{Bmatrix} \mathbf{f}_M \\ \mathbf{r}_M \end{Bmatrix}, \quad (4.18)$$

$$\mathbf{u}_M, \mathbf{f}_M \in \mathbb{R}^{N_{MDOF}}, \quad \mathbf{u}_{MBC}, \mathbf{r}_M \in \mathbb{R}^{N_{MBC}}, \quad \mathbf{K}_M \in \mathbb{R}^{N_{MDOF} \times N_{MDOF}},$$

$$\mathbf{K}_{MBC} \in \mathbb{R}^{N_{MDOF} \times N_{MBC}}, \quad \tilde{\mathbf{K}}_M \in \mathbb{R}^{N_{MBC} \times N_{MBC}},$$

whose physical meaning is the same as the counterparts defined at the lower scale, see Section 4.1. Without loss of generality, in this work only non-null external nodal forces are applied at the macroscopic scale, whilst the imposed generalised displacements are null, i.e., $\mathbf{u}_{MBC} = \mathbf{0}$. Therefore, the equilibrium equation at the macroscopic scale simplifies to:

$$\mathbf{K}_M \mathbf{u}_M = \mathbf{f}_M. \quad (4.19)$$

As stated above, the pseudo-density field, defined at the RVE scale, affects also the macroscopic responses \mathcal{C}_M and m_M through the macroscopic elasticity tensor \mathbf{C}_M and the macroscopic density τ_M of the equivalent homogeneous anisotropic material, see Eq. (4.4) (or Eqs. (4.6) and (4.7)) and Eq. (4.9), respectively. Indeed, the reduced (i.e., non-singular) stiffness matrix \mathbf{K}_M of the macroscopic FE model depends upon the tensor \mathbf{C}_M as follows:

$$\mathbf{K}_M = \sum_{e=1}^{N_{Me}} \mathbf{L}_{Me}^T \int_{V_{Me}} \mathbf{B}_{Me}^T \mathbf{C}_M \mathbf{B}_{Me} d\Omega \mathbf{L}_{Me}, \quad (4.20)$$

$$\mathbf{B}_{Me} \in \mathbb{R}^{6 \times N_{MDOF,e}}, \mathbf{L}_{Me} \in \mathbb{R}^{N_{MDOF,e} \times N_{MDOF}}.$$

In Eq. (4.20), N_{Me} is the number of elements constituting the FE model at the macroscopic scale, whilst $N_{MDOF,e}$ is the number of DOFs of the generic element. \mathbf{L}_{Me} is the connectivity matrix of element e , \mathbf{B}_{Me} is the matrix representing the product between the linear differential operator and the shape function matrices of the generic element and V_{Me} is the volume of element e .

Moreover, the mass m_M of the macroscopic FE model reads:

$$m_M = \tau_M V_M = \tau_M \sum_{e=1}^{N_{eM}} V_{Me}. \quad (4.21)$$

where V_M is the overall volume of the FE model at the macroscopic scale. Therefore, the multi-scale TO problem focusing on the minimisation of the macroscopic compliance subject to an inequality constraint on the macroscopic mass can be formulated as a constrained non-linear programming problem (CNLPP) as:

$$\min_{\xi_1, \xi_2} \frac{\mathcal{C}_M}{\mathcal{C}_{M,\text{ref}}}, \quad \text{s.t. :} \begin{cases} \mathbf{K}_M \mathbf{u}_M = \mathbf{f}_M, & \hat{\mathbf{K}}_m \hat{\mathbf{u}}_m = \hat{\mathbf{f}}_m, \\ g := \frac{m_M}{m_{M,\text{ref}}} - \gamma \leq 0, \\ \xi_{1k} \in [\rho_{m\text{min}}, \rho_{m\text{max}}], & \xi_{2k} \in [\omega_{m\text{min}}, \omega_{m\text{max}}], \\ \forall k = 1, \dots, n_{\text{CP}}. \end{cases} \quad (4.22)$$

In Eq. (4.22), $m_{M,\text{ref}}$ and $\mathcal{C}_{M,\text{ref}}$ are reference values for the mass and the compliance of the structure at the macroscopic scale, respectively, whilst γ is the imposed mass fraction. $\rho_{m\text{min}}$ and $\rho_{m\text{max}}$ are the bounds on the density at each CP. In particular, the lower bound is imposed to the density field in order to prevent any singularity for the solution of the equilibrium problem at the lower scale. $\omega_{m\text{min}}$ and $\omega_{m\text{max}}$ are suitable lower and upper bounds on weights. Moreover, in Eq. (4.22), the linear index k has been introduced for the sake of compactness. The relationship between k and i_j , ($j = 1, 2, 3$) is:

$$k := 1 + i_1 + i_2(n_1 + 1) + i_3(n_1 + 1)(n_2 + 1). \quad (4.23)$$

The other NURBS parameters (i.e., degrees, knot-vector components and number of CPs) can be identified as *design parameters*, i.e., their value is set *a-priori* at the beginning of the TO and is not optimised: the interested reader is addressed to [108] for a deeper insight in the matter.

Remark 4.2.1. *As discussed in [113], one of the main advantages of the NURBS-based SIMP method is that the minimum length-scale manufacturing requirement can be easily integrated in the optimisation process **without adding an explicit constraint function** in the CNLPP formulation of Eq. (4.22). As explained in [113], the minimum length-scale constraint can be automatically satisfied by properly setting the integer parameters involved in the definition of the NURBS hyper-surface, i.e., the number of CPs and the degrees of the blending functions along each parametric direction, i.e., n_j and p_j , respectively. A meaningful example integrating this requirement is presented in Section 4.3.2.*

The computation of the gradient of the objective function and of the constraint function with respect to the design variables ξ_1 and ξ_2 is needed to solve problem (4.22) through a suitable deterministic algorithm. The gradient of g can be immediately inferred by considering Eqs. (4.9), (4.16) and (4.21):

$$\frac{\partial g}{\partial \xi_{ik}} = \tau_m \frac{V_M}{V_{\text{RVE}}} \sum_{e \in \mathcal{S}_k} V_{mj} \frac{\partial \rho_e}{\partial \xi_{ik}}, \quad i = 1, 2, \quad k = 1, \dots, n_{\text{CP}}, \quad (4.24)$$

where \mathcal{S}_k is the discretised version of the local support of Eq. (3.9), while $\frac{\partial \rho_e}{\partial \xi_{ik}}$ reads

$$\frac{\partial \rho_e}{\partial \xi_{ik}} = \begin{cases} R_k^e, & \text{if } i = 1, \\ \frac{R_k^e}{\xi_{2k}} (\xi_{1k} - \rho_e), & \text{if } i = 2. \end{cases} \quad (4.25)$$

The scalar quantity R_k^e , appearing in Eq. (4.25), is the NURBS rational basis function of Eq. (3.2) evaluated at the element centroid.

Conversely, the gradient of \mathcal{C}_M requires a special attention. In order to derive its analytical expression, the NURBS local support property of Eq. (3.9) and the adjoint method [121] will be exploited. To this end, consider the following proposition.

Proposition 4.2.1. *Consider a deformable homogeneous anisotropic medium subject to $\mathbf{f}_M \neq \mathbf{0}$ and $\mathbf{u}_{\text{MBC}} = \mathbf{0}$. If body forces are identically*

null, the gradient of the macroscopic compliance \mathcal{C}_M with respect to the topological variable defined at the lower scale reads:

$$\frac{\partial \mathcal{C}_M}{\partial \xi_{ik}} = - \sum_{e=1}^{N_{Me}} \sum_{q=1}^6 \sum_{r=1}^6 \frac{\partial C_{Mqr}}{\partial \xi_{ik}} \varepsilon_{Meq} \varepsilon_{Mer} V_{Me}, \quad (4.26)$$

$$i = 1, 2, \quad k = 1, \dots, n_{CP},$$

with

$$\frac{\partial C_{Mqr}}{\partial \xi_{ik}} = \begin{cases} \frac{1}{V_{RVE} (\varepsilon_{mq}^0)^2} \sum_{e \in \mathcal{S}_k} \frac{\alpha}{\rho_e} \frac{\partial \rho_e}{\partial \xi_{ik}} w_{me} (\varepsilon_{mq}^0), & \text{if } q = r, \\ \frac{1}{2V_{RVE} \varepsilon_{mq}^0 \varepsilon_{mr}^0} \sum_{e \in \mathcal{S}_k} \frac{\alpha}{\rho_e} \frac{\partial \rho_e}{\partial \xi_{ik}} w_{me} (\varepsilon_{mq}^0, \varepsilon_{mr}^0) + \\ - \frac{\varepsilon_{mq}^0}{2\varepsilon_{mr}^0} \frac{\partial C_{Mqq}}{\partial \xi_{ik}} - \frac{\varepsilon_{mr}^0}{2\varepsilon_{mq}^0} \frac{\partial C_{Mrr}^M}{\partial \xi_{ik}}, & \text{if } q \neq r. \end{cases} \quad (4.27)$$

The proof of proposition 4.2.1 and the pseudo-code of the algorithm used to compute the gradient of \mathcal{C}_M are provided in Appendix A.

Remark 4.2.2. The quantity ε_{Meq} appearing in Eq. (4.26) is the generic component of the macroscopic strain vector of element e defined as

$$\varepsilon_{Me} := \mathbf{B}_{Me} \mathbf{L}_{Me} \mathbf{u}_M, \quad (4.28)$$

while the quantity w_{me} appearing in Eq. (4.27) is the work of the internal forces of the generic element of the FE model of the RVE at the lower scale.

Remark 4.2.3. As it can be inferred from Eq. (4.27), the SEHM based on elements strain energy has been used to assess the components of the macroscopic elasticity tensor of the LS. Indeed this technique reveals to be the most efficient choice (from a computational costs perspective) minimising the number of FE analyses required to assess matrix \mathbf{C}_M as well as its gradient with respect to the topological variable at the RVE scale. In particular, as discussed in Appendix A, the **SEHM based on elements strain energy needs only seven static analyses per iteration** to compute the gradient of the macroscopic compliance: at the lower scale Eq. (4.2) must be solved six times (i.e., for each elementary strain field), while at the upper scale only one analysis is needed to solve Eq. (4.19). Conversely, as discussed in Appendix B, the **SEHM based on elements averaged stresses needs, at each iteration of the optimisation process, the resolution of 43 linear systems**: seven analyses at the lower scale, i.e., one for Eq. (4.2) and six for Eq. (B.8), which must be repeated six times (for each elementary strain field), plus one analysis at the macroscopic scale to solve Eq. (4.19).

4.3 Numerical results

In this section, the effectiveness of the proposed method is tested on 2D and 3D benchmark problems. The results presented in this Section are obtained by means of the code SANTO (SIMP And NURBS for Topology Optimisation) developed at the I2M laboratory in Bordeaux [108, 110]. SANTO is coded in Python and it has been interfaced with ANSYS® software, which is used to build the FE models and assess the mechanical responses of the structure, at each pertinent scale. Moreover, the Method of Moving Asymptotes (MMA) algorithm [5] has been used to perform the solution search for CNLPP of Eq. (4.22). The parameters tuning the behaviour of the MMA algorithm as well as the user-defined convergence criteria are listed in Table 4.1.

Table 4.1 – MMA algorithm parameters

Parameter	Value
<i>move</i>	0.2
<i>albefa</i>	0.1
<i>asyntinit</i>	0.5
<i>asyincr</i>	1.2
<i>asydecr</i>	0.7
Stop Criterion	Value
Maximum n. of function evaluations	$100 \times n_{\text{var}}$
Maximum n. of iterations	10000
Tolerance on objective function	1×10^{-6}
Tolerance on constraints	1×10^{-6}
Tolerance on input variables change	10^{-6}
Tolerance on Karush–Kuhn–Tucker norm	10^{-4}

Post-processing operations are performed in ParaView® environment. As far as numerical tests are concerned, the following aspects are considered:

1. The influence of the NURBS entity integer parameters, i.e., blending functions degree and CPs number, on the RVE optimised topology is investigated (only for 2D problems);
2. The influence of the geometric entity, i.e., B-spline or NURBS used to describe the pseudo-density field of the RVE, on the optimised topology is studied (both 2D and 3D problems);
3. The influence of the starting guess on the RVE optimised topology (only for 2D problems);

4. The influence of the macroscopic loads on the optimised topology of the RVE (both 2D and 3D problems).

Lower and upper bounds of design variables are set as: $\rho_{\min} = 10^{-3}$, $\rho_{\max} = 1$; $\omega_{\min} = 0.5$, $\omega_{\max} = 10$. Moreover, the non-trivial knot vectors components in Eq. (3.7) have been evenly distributed in the interval $[0, 1]$ for both 2D and 3D cases. For all benchmarks, the mass fraction at the macroscopic scale is $\gamma = 0.4$, while an aluminium alloy is used as a bulk material of the RVE with the following properties: $E_m = 71$ GPa, $\nu_m = 0.33$, $\tau_m = 2700$ Kgm⁻³. The reference mass of the structure is defined as $m_{M,\text{ref}} = \tau_m V_m$, which corresponds to impose a unit pseudo-density field at the RVE scale in Eq. (4.16), while $\mathcal{C}_{M,\text{ref}}$ is the macroscopic compliance evaluated for the starting solution.

Furthermore, symmetry constraints on the pseudo-density field describing the RVE topology are imposed during optimisation: double symmetry for 2D problems (with respect to planes $y_{mj} = \frac{a_{mj}}{2}$, $j = 1, 2$) and three planes of symmetry ($y_{mj} = \frac{a_{mj}}{2}$, $j = 1, 2, 3$) for 3D problems in order to have an optimised topology characterised, at most, by an orthotropic behaviour. Of course, the presence of a symmetry constraints imply a reduction in the count of design variables as follows:

$$n_{\text{var}} = \begin{cases} \prod_{i=1}^N \theta_i, & \text{for B - spline entity,} \\ 2 \prod_{i=1}^N \theta_i, & \text{for NURBS entity,} \end{cases} \quad (4.29)$$

with $N = 2$ and $N = 3$ for 2D and 3D problems, respectively and

$$\theta_i = \begin{cases} \frac{n_i + 1}{2}, & \text{if } n_i \text{ is odd,} \\ \lfloor \frac{n_i + 1}{2} \rfloor + 1, & \text{otherwise.} \end{cases} \quad (4.30)$$

4.3.1 2D benchmark problem

The geometry, loads and BCs of the 2D benchmark problem (indicated as 2D-BK in the following) considered in this study are illustrated in Fig. 4.2. It is a quarter of a square plate ($a_{M1} = a_{M2} = 100$ mm) with a hole of radius $R = \frac{a_{M1}}{3}$. Uniform loads per unit length F_{M1} and F_{M2} are applied along sides AE and AB, respectively. The plate is subject to symmetric BCs on edges BC and DE. At the lower scale the RVE domain is a square of side $2a_{m1} = 2a_{m2} = 10$ mm. The RVE size has been chosen in order to have, at least, ten repetitive units along edges AB and AE.

The FE models at both upper and lower scales are made of PLANE182 elements (plane strain hypothesis, four nodes, two DOFs per node). The overall number of (quadrangular) elements composing the FE models at the macroscopic scale and at the RVE scale are $N_{Me} = 1566$ and $N_{me} = 1600$, respectively.

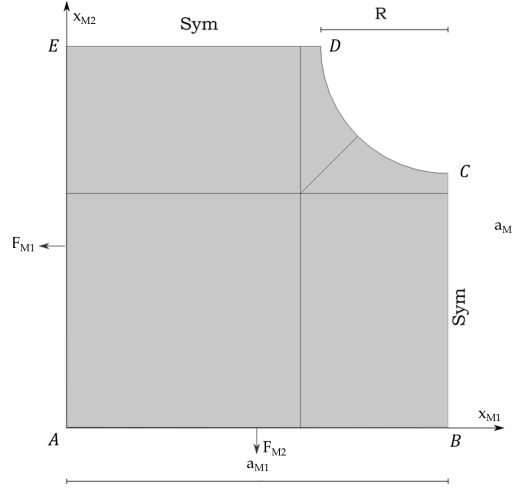


Figure 4.2 – Geometry and boundary conditions of the benchmark problem 2D-BK

4.3.1.1 Sensitivity of the RVE topology to the NURBS entity integer parameters

Problem (4.22) is solved for 2D-BK by considering the following combinations of blending functions degrees and CPs numbers: (a) $p_j = 2, 3$, ($j = 1, 2$); (b) $n_{CP} = 20 \times 20, 27 \times 27, 35 \times 35$. For this sensitivity analysis, the applied loads have been set as $F_{M1} = 0$ and $F_{M2} = 10 \text{ Nmm}^{-1}$. An initial guess characterised by a uniform density field $\rho(\zeta_{m1}, \zeta_{m2}) = \gamma$ and $\mathcal{C}_{M,\text{ref}} = 288.95 \text{ Nmm}$ has been considered for each analysis.

Results are provided in terms of macroscopic compliance \mathcal{C}_M and number of iterations N_{iter} for B-spline and NURBS entities in Figs. 4.3 and 4.4, respectively. For each solution the requirement on the mass fraction is always satisfied and the solution is located on the boundary of the feasible domain.

A synthesis of the obtained results is illustrated in Fig. 4.5 in terms of the macroscopic compliance vs. CPs number and blending functions degrees.

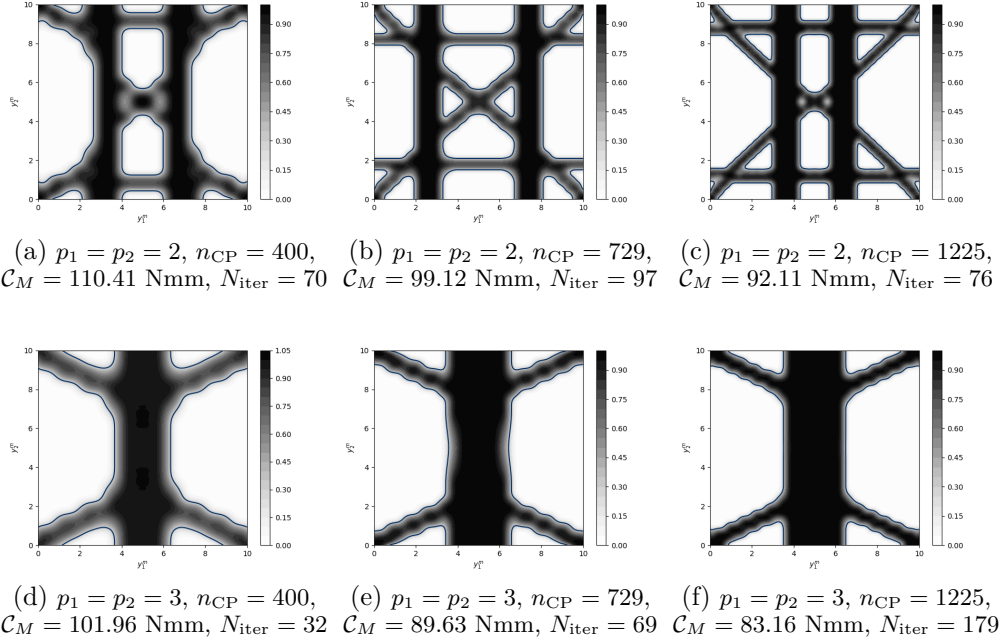


Figure 4.3 – Benchmark problem 2D-BK: sensitivity of the optimised topology to CP numbers and basis functions degrees, B-spline solutions

The following remarks can be inferred from the results of the sensitivity analysis.

1. For B-spline solutions, the greater the number of control points the smaller the objective function value. However, unlike results presented in [108, 110] for the classical problem of the compliance minimisation subject to an inequality constraint of the volume fraction involving a single scale (i.e., the macroscopic one), the bigger the degree the smaller the objective function value.
2. Conversely, for NURBS solutions, a clear trend cannot be identified, unlike results presented in [108, 110]. In particular, as a general rule one can assert that the smaller the degree (or the higher the CPs number) the smaller the objective function value in agreement with the results for single-scale problems presented in [108, 110]. However, for some combinations of CPs number and degrees, the optimised solutions do not follow this general trend: this is probably due to the strong non-convexity of the multi-scale TO problem of Eq. (4.22),

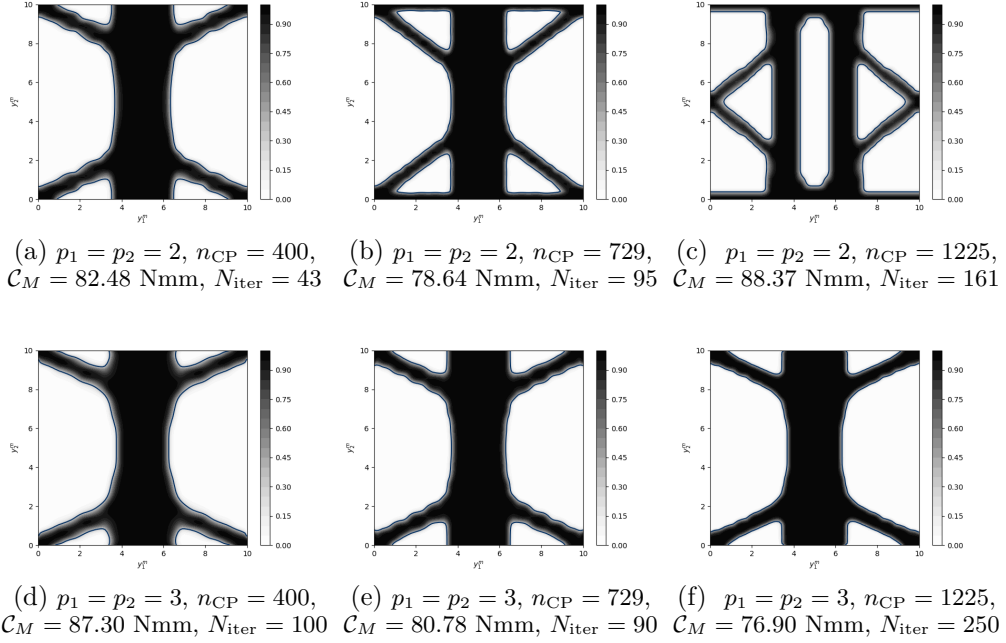


Figure 4.4 – Benchmark problem 2D-BK: sensitivity of the optimised topology to CP numbers and basis functions degrees, NURBS solutions

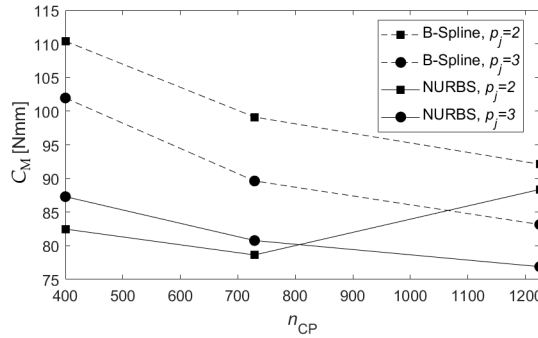


Figure 4.5 – Benchmark problem 2D-BK: compliance vs. CPs number and degrees for B-spline and NURBS solutions

which shows several local feasible minimiser as discussed in the next subsection.

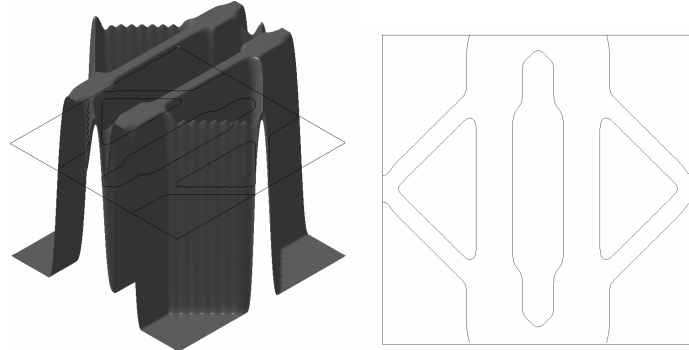
3. The CPs number and basis functions degree along each direction affect the size of the local support, see Eq. (3.9), which enforces a

minimum member size requirement in the optimised topology, as discussed in [113]. As far as this point is concerned, the same remarks as in [113] can be made: the higher the degree (or the smaller the CPs number) the greater the local support, thus each CP affects a wider region of the mesh during optimisation. Moreover, the higher the degree the smoother the topology boundary after CAD reconstruction. Conversely, small degrees (or a high CPs number) produce optimised topologies characterised by thin branches. Therefore, as a general rule, a high number of CPs and small degrees should be considered if minimum member size does not constitute a restriction for the problem at hand. High degrees and/or small CPs number should be considered otherwise.

4. Optimised topologies obtained using NURBS surfaces are characterised by values of the objective function lower than or equal to those resulting from B-spline surfaces when considering the same number of CPs and the same degrees, as shown in Fig. 4.5. In particular, from the analysis of Figs. 4.3 and 4.4, it appears that NURBS topologies have a boundary smoother than that of B-spline solutions, for each case.
5. Fig. 4.6 illustrates the outstanding advantages provided by the NURBS-based SIMP method. On the one hand, the topology is unrelated from the mesh of the FE model and it is represented by a purely geometrical entity, i.e., a 3D NURBS surface. On the other hand, the NURBS surface is a CAD-compatible entity which can be easily exported into any CAD software to rebuild in a straightforward way the boundary of the optimised 2D structure. This task can be achieved by evaluating a threshold value for the density function meeting the optimisation constraint (this operation is automatically done by the SANTO algorithm at the end of the optimisation process).

4.3.1.2 Sensitivity of the RVE topology to the initial guess

Unlike the standard CNLPP dealing with the compliance minimisation subject to a constraint on the volume fraction involving a single-scale analysis [108, 110], the CNLPP of Eq. (4.22) shows a highly non-convex behaviour. To (numerically) prove its non-convexity, the influence of the starting point on the optimised topology is discussed here. The analysis is carried out for both B-spline and NURBS solutions characterised by the following parameters: $p_1 = p_2 = 2$, $n_{CP} = 35 \times 35$. The applied loads are set as $F_{M1} = 0$ and $F_{M2} = 10 \text{ Nmm}^{-1}$.



(a) NURBS surface and cut- (b) The 2D optimised topology
ting plane

Figure 4.6 – Benchmark problem 2D-BK: CAD model of the RVE optimised topology for a NURBS surface with $p_1 = p_2 = 2$ and $n_{CP} = 1225$

For each B-spline/NURBS solution, two feasible starting points have been considered. The first one consists of a topology having one hole (where the pseudo-density is equal to ρ_{\min}) satisfying the constraint on the mass ratio and characterised by $\mathcal{C}_{M,\text{ref}} = 271.47$ Nmm. The second starting point is characterised by two holes and by a reference macroscopic compliance $\mathcal{C}_{M,\text{ref}} = 271.16$ Nmm.

Results are provided in terms of macroscopic compliance \mathcal{C}_M and number of iterations N_{iter} for B-spline and NURBS entities in Fig. 4.7. For each solution the requirement on the mass fraction is always satisfied and the solution is located on the boundary of the feasible domain.

As it can be inferred from Fig. 4.7, the choice of the initial guess has a strong impact on the optimised topology. On the one hand, for the same number of CPs and the same degrees and under the considered loads and BCs, choosing an initial guess with one hole allows finding results better (in terms of \mathcal{C}_M) than those characterising the optimised solutions shown in Figs. 4.3c and 4.4c (obtained by starting from a uniform pseudo-density field). On the other hand, for the same values of the NURBS entity integer parameters, the choice of a different starting point has a strong impact on the convergence rate of the MMA algorithm, which converges towards the nearest local (feasible) minimiser.

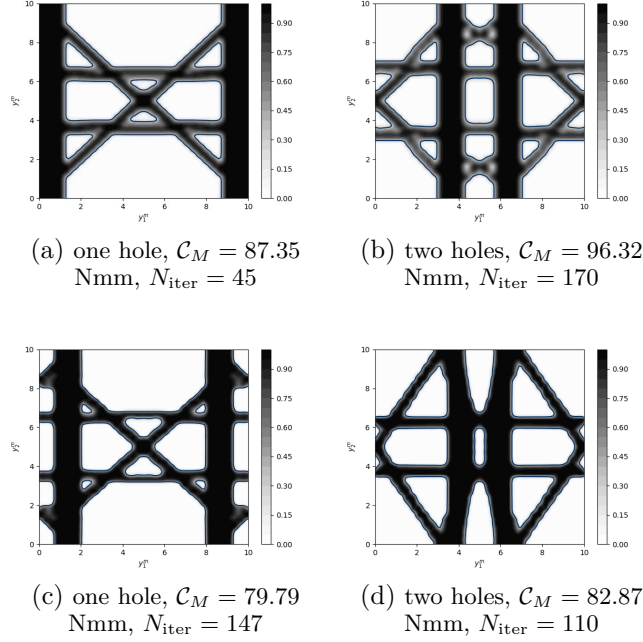


Figure 4.7 – Benchmark problem 2D-BK: influence of the initial guess on the optimised topology for (a)-(b) B-spline and (c)-(d) NURBS solutions with $p_1 = p_2 = 2$ and $n_{\text{CP}} = 1225$

4.3.1.3 Sensitivity of the RVE topology to the macroscopic loading condition

Problem (4.22) is solved for 2D-BK by considering different combinations of the applied loads: (a) $\frac{F_{M1}}{F_{M2}} = 0$ and $F_{M2} = 10 \text{ Nmm}^{-1}$ (presented in the above subsections); (b) $\frac{F_{M1}}{F_{M2}} = 0.5$ and $F_{M2} = 10 \text{ Nmm}^{-1}$; (c) $\frac{F_{M1}}{F_{M2}} = 1$ and $F_{M2} = 10 \text{ Nmm}^{-1}$; (d) $\frac{F_{M1}}{F_{M2}} \rightarrow \infty$ and $F_{M1} = 10 \text{ Nmm}^{-1}$. The goal of these analyses is to highlight the effect of the macroscopic loading condition on the optimised topology of the RVE at the lower scale.

Problem (4.22) has been solved using both B-spline and NURBS entities having degrees $p_1 = p_2 = 3$ and an overall number of CPs $n_{\text{CP}} = 35 \times 35$. An initial guess characterised by a uniform density field $\rho(\zeta_{m1}, \zeta_{m2}) = \gamma$ and $\mathcal{C}_{M,\text{ref}} = 288.95 \text{ Nmm}$ has been considered for each analysis.

The numerical results regarding the case $\frac{F_{M1}}{F_{M2}} = 0$ are illustrated in Figs. 4.3f and 4.4f. As far as the other cases are concerned, results are provided in terms of macroscopic compliance \mathcal{C}_M for B-spline and NURBS entities in Fig. 4.8. For each solution the requirement on the mass fraction is always

satisfied and the solution is located on the boundary of the feasible domain.

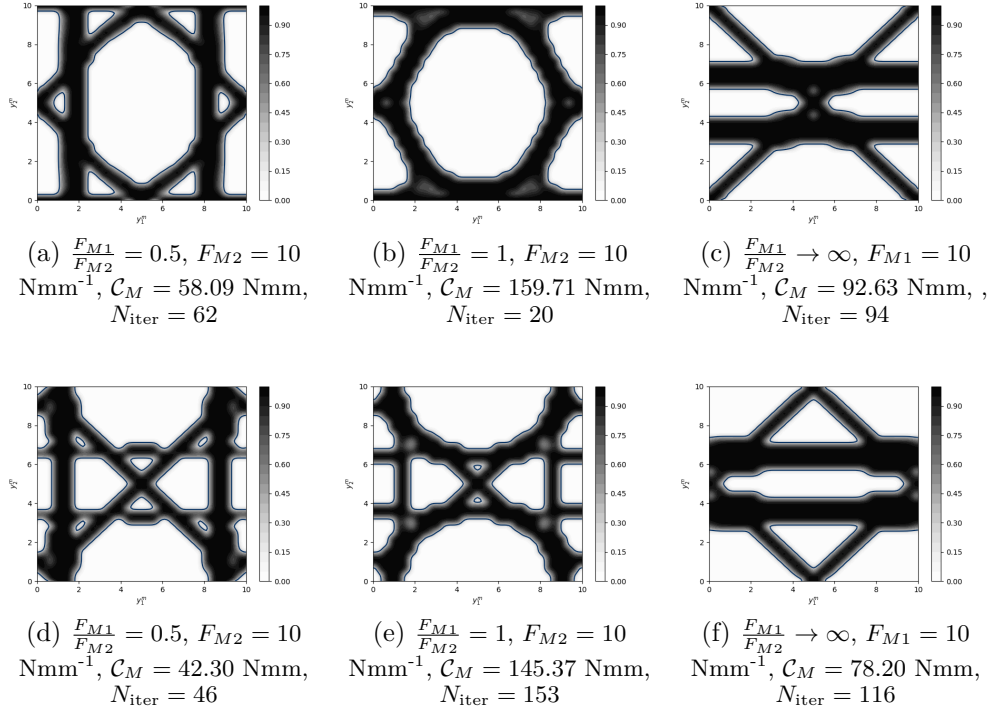


Figure 4.8 – Benchmark problem 2D-BK: influence of the macroscopic loading condition on the RVE optimised topology for (a)-(c) B-spline and (d)-(e) NURBS solutions with $p_1 = p_2 = 3$ and $n_{\text{CP}} = 1225$

As it can be inferred from Fig. 4.8, the macroscopic loading condition has a strong influence on the RVE optimised topology at the lower scale. In particular, in order to properly withstand the applied loads at the macroscopic scale and to minimise \mathcal{C}_M , the RVE topology evolves in such a way to optimise the macroscopic elastic response of the continuum. In particular, for each considered loading condition, the matrix \mathbf{C}_M related to the optimised topology is characterised by the most efficient elastic symmetry with respect to the applied loads. Indeed, the elastic constants for each topology are reported in Table 4.2. As expected, the optimised topologies of the RVE for cases $\frac{F_{M1}}{F_{M2}} = 0$ and $\frac{F_{M1}}{F_{M2}} \rightarrow \infty$ show a macroscopic orthotropic behaviour with the main orthotropy axis oriented along axis x_{M2} and x_{M1} , respectively. The macroscopic elasticity tensor of the optimised topologies of the RVE for the case $\frac{F_{M1}}{F_{M2}} = 1$ is characterised by a square symmetry, i.e.,

Table 4.2 – 2D-BK: elastic constants for the optimised topologies in the case $p_1 = p_2 = 3$, $n_{CP} = 1225$ for each loading condition

Elastic constant	$\frac{E_{M1}}{E_{M2}} = 0$		$\frac{E_{M1}}{E_{M2}} = 0.5$	
	B-spline	NURBS	B-spline	NURBS
E_{M1} [MPa]	6258.90	6487.57	5976.94	6163.72
E_{M2} [MPa]	18246.18	16515.65	15610.41	15544.38
G_{M12} [MPa]	1348.89	1411.84	2410.54	2776.16
ν_{M12}	0.29	0.27	0.44	0.48
Elastic constant	$\frac{E_{M1}}{E_{M2}} = 1$		$\frac{E_{M1}}{E_{M2}} \rightarrow \infty$	
	B-spline	NURBS	B-spline	NURBS
E_{M1} [MPa]	10214.03	8352.45	17514.38	19468.20
E_{M2} [MPa]	10273.89	8643.90	2808.68	2781.78
G_{M12} [MPa]	2365.72	2299.19	2713.64	2599.40
ν_{M12}	0.41	0.44	0.14	0.12

$E_{M1} \approx E_{M2}$ (but the RVE has not a macroscopic isotropic behaviour because $G_{M12} \neq \frac{E_{M1}}{2(1+\nu_{M12})}$) for both B-spline and NURBS solutions (although the optimised topologies are really different). It is noteworthy that the RVE topologies for the case $\frac{E_{M1}}{E_{M2}} = 0.5$ are characterised by a macroscopic orthotropic behaviour with a higher value of the Young's modulus along the x_{M2} axis. Finally, for each loading condition, NURBS solutions are characterised by a value of the merit function lower than that of the B-spline counterpart.

4.3.2 3D benchmark problem

The geometry, loads and BCs of the 3D benchmark problem (indicated as 3D-BK in the following) considered in this study are illustrated in Fig. 4.9. As shown in this figure, the optimisation domain at the macroscopic scale is a cube of side $a_{Mi} = 300$ mm ($i = 1, 2, 3$), which is meshed with SOLID185 elements (eight nodes, three DOFs per node, reduced integration): the element size is 10 mm for an overall number of $N_{Me} = 27000$ elements. Moreover, the cube is clamped at nodes A, B, C and D corresponding to the vertices of the bottom face.

As illustrated in Fig. 4.9, problem (4.22) is solved for 3D-BK by considering two load cases (LCs): in the first one (LC1) only traction loads P along x_{M2} axis are applied on nodes E, F, G, H and I belonging to the top face, whilst in the second one (LC2) shear forces P are applied on nodes

E, F, G, H (in order to generate a non-zero torque) and a traction load P is still applied on node I. The idea is to investigate the influence of the macroscopic loading condition on the optimised RVE topology at the lower scale. The value of the force applied on the generic node is $P = 300$ N.

At the lower scale the RVE domain is a cube of side $2a_{m1} = 2a_{m2} = 2a_{m3} = 10$ mm. The RVE size has been chosen in order to have, at least, 30 repetitive units along the generic axis x_{Mi} at the macroscopic scale. The RVE model has been meshed with $N_{me} = 8000$ SOLID185 elements.

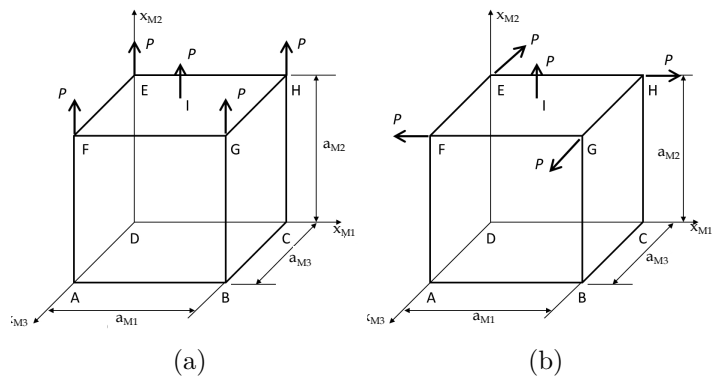


Figure 4.9 – Geometry and boundary conditions of the benchmark problem 3D-BK: (a) only axial forces are applied at the macroscopic scale, (b) axial and shear forces are applied at the macroscopic scale

For both LCs, the CNLPP of Eq. (4.22) has been enhanced by considering a constraint on the minimum length scale requirement: the minimum dimension of the optimised topology should be greater than or equal to $d_{m,\min} = 0.5$ mm. To automatically satisfy the minimum length scale requirement without introducing an explicit constraint in the problem formulation, according to the methodology presented in [113], B-spline and NURBS entities with $p_j = 3$ ($j = 1, 2, 3$) and $n_{CP} = 18 \times 18 \times 18$ are used for these analyses. Moreover, an initial guess characterised by a uniform density field $\rho(\zeta_{m1}, \zeta_{m2}, \zeta_{m3}) = \gamma$ has been selected. The reference macroscopic compliance is $\mathcal{C}_{M,\text{ref}} = 692.29$ Nmm for the first load case and $\mathcal{C}_{M,\text{ref}} = 504.94$ for the second one.

Numerical results are provided in terms of macroscopic compliance \mathcal{C}_M , number of iterations N_{iter} and measured minimum member size, i.e., $d_{m,\min-\text{meas}}$, for B-spline and NURBS entities in Fig. 4.10 (the topology illustrated in Fig. 4.10d has been cut with the plane $y_{m1} = \frac{a_{m1}}{2}$ in order to show the internal structure of the RVE). For each solution the requirement

on the mass fraction is always satisfied and the solution is located on the boundary of the feasible domain.

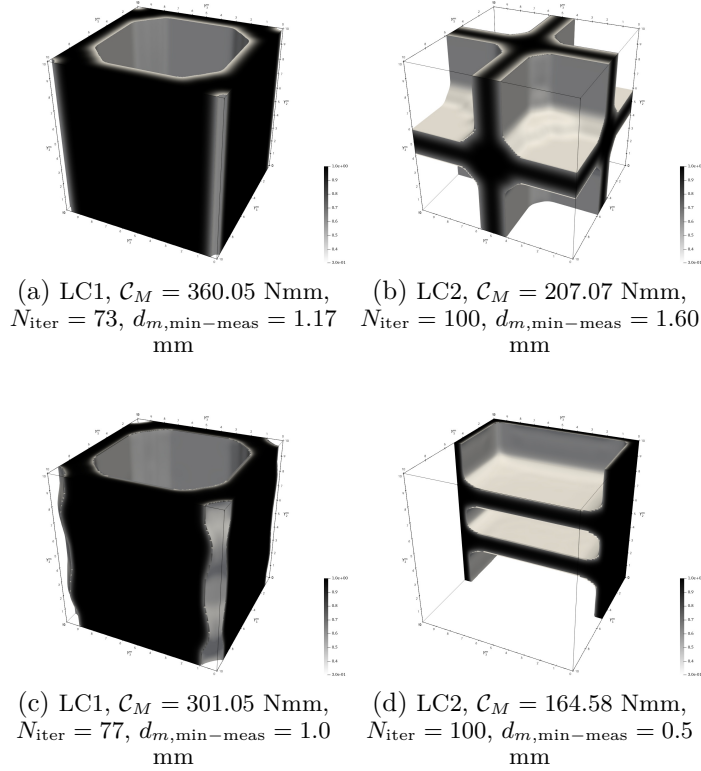


Figure 4.10 – Benchmark problem 3D-BK: influence of the loading condition at the macroscopic scale on the RVE optimised topology for (a)-(b) B-spline and (c)-(d) NURBS solutions with $p_1 = p_2 = p_3 = 3$ and $n_{\text{CP}} = 5832$

As it can be inferred from Fig. 4.10, the macroscopic loading condition has a strong influence on the RVE optimised topology at the lower scale.

Firstly, it must be pointed out that NURBS solutions show better performances than the B-spline counterparts, regardless of the considered LC. Moreover, thanks to the geometrical properties of the NURBS blending functions, the requirement on the minimum length scale is always satisfied. In particular, it is noteworthy that the minimum length scale constraint is active for the NURBS solution illustrated in Fig. 4.10d.

Secondly, in order to properly withstand the applied loads at the macroscopic scale and to minimise \mathcal{C}_M , the RVE topology evolves in such a way

to optimise the macroscopic elastic response of the continuum. As a consequence, for each LC, the matrix \mathbf{C}_M related to the optimised topology is characterised by the most efficient elastic symmetry for that case. The elastic constants for each topology are reported in Table 4.3.

Table 4.3 – 3D-BK: elastic constants for the optimised topologies in the case $p_1 = p_2 = p_3 = 3$ and $n_{CP} = 5832$ for each load case

Elastic constant	LC1		LC2	
	B-spline	NURBS	B-spline	NURBS
E_{M1} [MPa]	12375.13	13575.96	15648.95	19134.29
E_{M2} [MPa]	21792.07	25179.94	14704.77	14268.34
E_{M3} [MPa]	12375.23	13599.33	15648.95	19134.34
G_{M12} [MPa]	4895.14	5829.61	3161.04	3083.47
G_{M13} [MPa]	610.23	773.16	3466.19	5176.82
G_{M23} [MPa]	4895.17	5840.89	3161.04	3083.43
ν_{M12}	0.19	0.18	0.19	0.20
ν_{M13}	0.11	0.19	0.20	0.24
ν_{M23}	0.33	0.33	0.18	0.15

As expected, the optimised RVE topologies (B-spline and NURBS solutions) for LC1 show a macroscopic orthotropic behaviour with the main orthotropy axis aligned with the load direction, i.e., x_{M2} axis. The Young's moduli E_{M1} and E_{M3} , the shear moduli G_{M12} and G_{M23} as well as the Poisson's coefficients ν_{M12} and $\nu_{M32} = \nu_{M23} \frac{E_{M3}}{E_{M2}}$ are equal but the material does not show a transverse isotropic behaviour because $G_{M13} \neq \frac{E_{M1}}{2(\nu_{M13}+1)}$. The macroscopic elasticity tensor of B-spline and NURBS solutions for LC2 are still orthotropic, but with a value of the Young's moduli E_{M1} and E_{M3} higher than E_{M2} (which implies that the main orthotropy direction is no longer aligned with the x_{M2} axis) and with a higher value of the shear modulus G_{M13} in order to withstand shear loads (and the resulting torque).

4.4 Conclusions and prospects

In this Chapter, multi-scale TO problems of LSs have been formulated in an innovative SIMP algorithm based on NURBS entities. In particular, the proposed approach consider the topological variable defined only at the lattice RVE scale, while physical responses can be defined at each pertinent

scale of the LS, depending on the requirements of the problem at hand. The proposed approach is based on NURBS hyper-surfaces, on the standard FE method and on the SEHM involving elements strain energy to perform the scale transition.

Some features of the proposed framework need to be highlighted.

1. Three main advantages of the NURBS formalism can be clearly identified: (a) unlike the classical SIMP approach, there is no need to define a further filter zone, as the NURBS local support establishes an implicit relationship among contiguous mesh elements, (b) when compared to the classical SIMP approach, the number of design variables is reduced and (c) the CAD reconstruction phase is straightforward.
2. A sensitivity analysis of the optimised topology of the RVE to the NURBS integer parameters has been performed. Unlike the classical problem of the compliance minimisation subject to a constraint on the volume fraction stated on a single scale, when B-spline entities are employed to describe the pseudo-density field of the RVE, the greater the number of CPs (for a given degree) or the bigger the degree (for a given number of CPs) the smaller the objective function value. Conversely, when NURBS entities are used to describe the RVE topological variable, no general rules can be defined and the results seem to approximately satisfy the global trend observed in previous works (i.e., the smaller the degree or the higher the CPs number the lower the objective function value). Moreover, an excellent trade-off between computational costs and performances of the final solution can be achieved by using a CPs number equal to three-quarters of the number of mesh elements.
3. The role of NURBS weights has been assessed. In particular, by considering same number of CPs and degrees, the objective function of the NURBS solution is lower than the B-spline counterpart, and the boundary of the NURBS solution is smoother than that of the B-spline solution.
4. The influence of the initial guess has been taken into account. Particularly, multi-scale TO problems are strongly non-convex and are characterised by several local minima. Therefore, a particular care must be put in the choice of the (feasible) initial guess and multiple optimisation calculations (by using different starting points) should be performed in order to find an efficient local minimiser.
5. The macroscopic loading condition strongly influences the optimised topology of the RVE. In particular, in order to satisfy the requirements of the problem at hand and to withstand the applied loads, the RVE

topology evolves towards a configuration optimising the macroscopic elastic response of the continuum.

6. The minimum-length scale requirement is correctly taken into account, without introducing an explicit optimisation constraint, by properly setting the integer parameters of the NURBS entity.
7. The better performances, in terms of computational costs when used in the framework of multi-scale TO, of the SEHM based on elements strain energy over the SEHM based on elements averaged stresses have been rigorously proven.

As far as prospects are concerned, this work is far from being exhaustive on the topic of multi-scale analyses and LS design by means of TO. Firstly, the proposed methodology should be extended to the case of multi-scale TO problems where topological variables are defined at different scales (this aspect will be addressed in the next Chapter). To this end, in the framework of the NURBS-based SIMP method, the number of NURBS entities should be equal, at least, to the number of scales, involved into the problem formulation, wherein the definition of a topological variable makes sense. The relationships occurring among these entities (i.e., the topological variables defined at different scales) should be carefully determined in order to correctly state the optimisation problem and to satisfy the hypotheses at the basis of the SEHM.

Secondly, pertinent manufacturing requirements, related to the additive manufacturing process, should be integrated into the multi-scale TO problem formulation, especially in terms of the RVE geometrical features, e.g, overhang angle, admissible curvature, etc.

Finally, suitable failure criteria should be formulated for the homogeneous anisotropic material at the macroscopic scale and integrated in the multi-scale TO problem formulation. Furthermore, in order to identify the most critical regions at the macroscopic scale and to transfer the local stress/strain field to the lattice RVE a modified SEHM with a strong coupling between scales should be developed and integrated in the optimisation process.

Chapter 5

Multi-scale topology optimisation II

Design of architected materials by considering topological variables at different scales.

The multi-scale TO method introduced in Chapter 4, is here extended to more general multi-scale analyses involving topological variables at multiple scales. Particularly, in this Chapter the topological descriptor, i.e., the pseudo-density field, is defined at both lower scale (i.e., the scale of the RVE, which can be mesoscopic or microscopic, depending on the problem characteristic lengths) and upper scale (i.e., the macroscopic scale) of the continuum. The coupling between lower and upper scales is established by means of the SEHM, whose goal is to compute the elasticity tensor of the equivalent homogeneous anisotropic material at the upper scale. It is noteworthy that the multi-scale analysis is carried out by considering only *weak coupling*, because there is only a one-way relationship among scales (i.e., bottom-up scale transition), instead of a two-way relationship in terms of the effect of the macroscopic displacement, strain and stress fields on the lower scale responses (which are not considered in the theoretical/numerical framework presented in this Chapter). Specifically, the proposed strategy is applied to the multi-scale design of architected cellular materials (ACMs). It is noteworthy that the multi-scale TO of ACMs is formulated in the most general case by considering mixed non-zero Neumann-Dirichlet BCs and by integrating multiple design requirements (DRs) defined at different scales in the problem formulation, like the constraint on the volume fraction at both scales, the constraint on the mass fraction at the macroscopic scale, the manufacturing constraint on the minimum member size at the RVE

scale and the scale separation condition (imposed through the minimum member size at the macroscopic scale) to guarantee the validity of the results obtained through the SEHM. Moreover, the influence of the RVE elastic symmetry group on the optimised topology at both scales is analysed. The effectiveness of the proposed method is tested on 2D and 3D benchmark problems taken from the literature.

All the above aspects are investigated in this Chapter, which is organised as follows. In Sec. 5.1, the problem formulation by considering the topological descriptor at each problem scale in the SANTO framework is presented. In Sec. 5.2, numerical results obtained for different 2D and 3D benchmark problems (with the related sensitivity analyses) are presented and discussed. Finally, Sec. 5.3 ends the Chapter with meaningful conclusions and prospects.

The contents of this Chapter have been presented in the article [122].

Notation. Upper-case bold letters and symbols are used to indicate tensors (matrices), while lower-case bold letters and symbols indicate column vectors. Subscripts m and M denote quantities evaluated at RVE scale and macroscopic scale, respectively.

5.1 Multi-scale topology optimisation of ACM in the NURBS-based SIMP framework

The main goal of this Chapter consists of determining the optimised topology of the ACM at both RVE scale (or lower scale) and macroscopic scale (or upper scale). This problem can be interpreted as a design problem of a complex anisotropic medium whose goal is the concurrent optimisation of the material properties (performed through the optimisation of the RVE topology at the lower scale) and of the macroscopic topology (i.e., the way wherein the equivalent homogeneous anisotropic material is distributed at the upper scale). Of course, since the RVE topology is the same at all points of the upper scale domain, the properties of the homogenised material are uniform at the structure-level.

Unlike the approaches presented in [30–37, 39], where the goal is to obtain an RVE topology showing a given (possibly optimised) macroscopic elastic behaviour, in this study, the problem characteristic scales (i.e., the lower scale and the upper one) are weakly coupled in the sense that the DRs calculated at the macroscopic scale (and involved in the problem formulation) depend upon the topological variables defined at both scales. On

the one hand, the structural responses calculated at the lower scale, like the equivalent elastic properties of the homogeneous anisotropic material replacing the RVE at the upper scale, and the volume fraction (or the mass fraction) of the RVE depend solely upon the topological descriptor defined at the RVE scale. On the other hand, the structural responses defined at the macroscopic scale, like the compliance, the displacement field, etc. depend upon the topological descriptors defined at both scales. Of course, the dependency of the macroscopic structural responses upon the topological descriptor defined at the lower scale is implicit because the RVE topology affects the components of the macroscopic elasticity matrix \mathbf{C}_M .

The goal of the two-scale TO presented in this study is to minimise the generalised compliance of the continuum at the upper scale (under mixed non-zero BCs of the Neumann-Dirichlet type) by considering the following DRs:

1. A constraint on the volume fraction (or, equivalently, on the mass fraction) imposed on the topological descriptor defined at each scale.
2. A constraint on the minimum thickness that can be fabricated through the selected manufacturing process. This constraint is formulated as a minimum member size constraint at the RVE scale.
3. A constraint on the scale separation condition to ensure the validity of the results of the homogenisation technique in calculating equivalent elastic properties of the material at the upper scale. Since the topology of the RVE and the one of the structure are continuously changing during the optimisation process, introducing this type of constraint reveals of paramount importance to avoid the occurrence of too small topological branches at the upper scale whose size could become of the same order of magnitude of the RVE characteristic length (in such circumstances the results of the homogenisation technique are not correct). The requirement on the scale separation condition is formulated in terms of the minimum member size constraint on the topological descriptor defined at the upper scale. In particular, the smallest thickness of the topological branches occurring at the upper scale must be greater than or equal to a multiple of the characteristic length of the design domain at the lower scale.

It is noteworthy that the notion of scale separation introduced in this work is the one ensuring the validity of the results of the homogenisation process at the upper scale within a continuously changing topology. This concept should not be confused with the notion of scales coupling. The scales are separated only in terms of characteristic lengths, but they are coupled because the structural responses at the upper scale depend upon

the geometrical and material parameters defined at the lower scale. In summary, imposing the scale separation condition does not mean that the scales are uncoupled during the optimisation process.

The main features of the approach are briefly described here only for 3D multi-scale TO problems. The characteristic problem scales (and the relative geometrical features) are illustrated in Fig. 5.1.

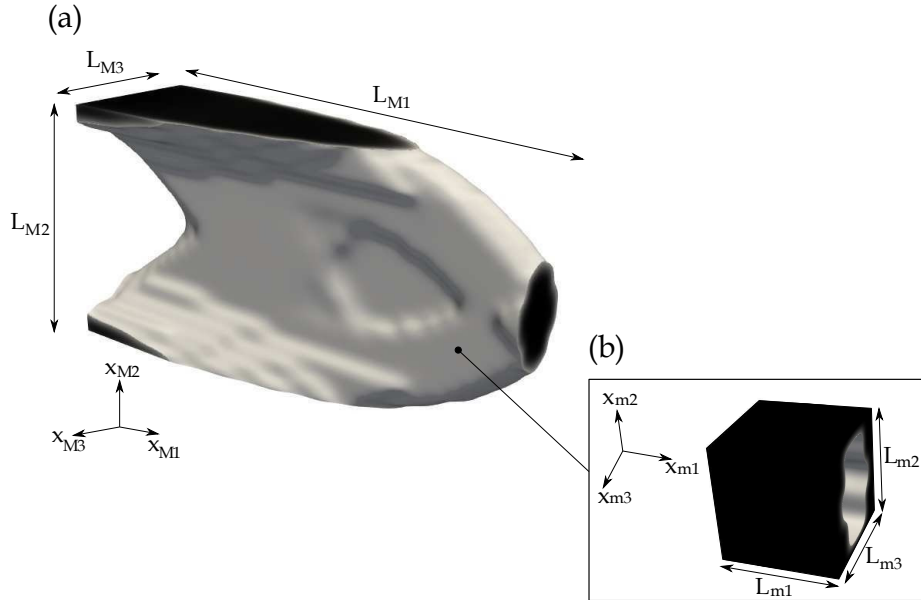


Figure 5.1 – Characteristic scales of the two-scale topology optimisation problem: (a) the upper (macroscopic) scale of the structure and (b) the lower (i.e., mesoscopic or microscopic) scale of the representative volume element of the architected cellular material

5.1.1 Design variables

Consider the compact Euclidean space $\mathcal{D}_\chi \subset \mathbb{R}^3$, defining the design domain at the generic χ -th scale ($\chi = m, M$), in a Cartesian orthogonal frame $O(x_{\chi 1}, x_{\chi 2}, x_{\chi 3})$:

$$\mathcal{D}_\chi := \{\mathbf{x}_\chi^T = (x_{\chi 1}, x_{\chi 2}, x_{\chi 3}) \in \mathbb{R}^3 : x_{\chi j} \in [0, L_{\chi j}], j = 1, 2, 3\}, \chi = m, M, \quad (5.1)$$

where $L_{\chi j}$, is the characteristic length of the domain defined along $x_{\chi j}$ axis, as shown in Fig. 5.1. In the SIMP approach the *material domain* $\Omega_\chi \subseteq \mathcal{D}_\chi$ at the generic scale is identified by means of the pseudo-density function

$\rho_\chi(\mathbf{x}_\chi) \in [0, 1]$ for $\mathbf{x}_\chi \in \mathcal{D}_\chi$: $\rho_\chi(\mathbf{x}_\chi) = 0$ means absence of material, whilst $\rho_\chi(\mathbf{x}_\chi) = 1$ implies presence of material.

In the framework of the NURBS-based SIMP method, the topological variable (at each scale) is represented by a NURBS entity. As discussed in the above Chapters, if a 3D TO problem is considered, a 4D NURBS hyper-surface is needed to describe the part topology [108]. The first three coordinates of the NURBS entity correspond to the Cartesian coordinates defining the domain, while the last coordinate corresponds to the pseudo-density field that reads:

$$\rho_\chi(\zeta_{\chi 1}, \zeta_{\chi 2}, \zeta_{\chi 3}) = \sum_{i_{\chi 1}=0}^{n_{\chi 1}} \sum_{i_{\chi 2}=0}^{n_{\chi 2}} \sum_{i_{\chi 3}=0}^{n_{\chi 3}} R_{i_{\chi 1}i_{\chi 2}i_{\chi 3}}(\zeta_{\chi 1}, \zeta_{\chi 2}, \zeta_{\chi 3}) \rho_{\chi i_{\chi 1}i_{\chi 2}i_{\chi 3}}, \quad \chi = m, M. \quad (5.2)$$

In Eq. (5.2), $\rho_{\chi i_{\chi 1}i_{\chi 2}i_{\chi 3}}$ is the pseudo-density value at the generic CP, i.e., the fourth coordinate of the vector \mathbf{h} in Eq. (3.1), while $R_{i_{\chi 1}i_{\chi 2}i_{\chi 3}}$ are the rational basis functions of Eq. (3.2).

The dimensionless parameters $\zeta_{\chi j}$ are obtained as:

$$\zeta_{\chi j} = \frac{x_{\chi j}}{L_{\chi j}}, \quad j = 1, 2, 3. \quad (5.3)$$

Among the parameters governing the shape of the NURBS entity, only the pseudo-density at CPs and the associated weights are included in the design variable vectors $\boldsymbol{\xi}_{\chi 1}$ and $\boldsymbol{\xi}_{\chi 2}$ defined as:

$$\boldsymbol{\xi}_{\chi 1}^T := (\rho_{000}, \dots, \rho_{n_{\chi 1}n_{\chi 2}n_{\chi 3}}), \quad \boldsymbol{\xi}_{\chi 2}^T := (\omega_{000}, \dots, \omega_{n_{\chi 1}n_{\chi 2}n_{\chi 3}}), \quad \boldsymbol{\xi}_{\chi 1}, \boldsymbol{\xi}_{\chi 2} \in \mathbb{R}^{n_{\chi \text{CP}}}, \quad (5.4)$$

accordingly, the number of design variables for each scale is, at most, $n_{\chi \text{var}} = 2n_{\chi \text{CP}}$, $\chi = m, M$.

The other parameters involved in the definition of the NURBS entity, i.e., degrees, knot-vector components and number of CPs, are set a-priori at the beginning of the TO and are not optimised: for more details the reader is addressed to [108, 110].

5.1.2 Objective function

At the lower scale, the stiffness matrix of the FE model of the RVE is penalised according to the following formula:

$$\hat{\mathbf{K}}_m = \sum_{e=1}^{N_{me}} \rho_{me}^\alpha (\boldsymbol{\xi}_{m1}, \boldsymbol{\xi}_{m2}) \hat{\mathbf{L}}_{me}^T \mathbf{K}_{me} \hat{\mathbf{L}}_{me}, \quad (5.5)$$

where ρ_{me} is the fictitious density of Eq. (5.2) computed at the centroid of the generic element e and N_{me} is the total number of elements composing the FE model of the RVE. $\hat{\mathbf{L}}_{me} \in \mathbb{R}^{N_{m\text{DOF}}^e \times \hat{N}_{m\text{DOF}}}$ is the connectivity matrix of element e (whose number of DOFs is $N_{m\text{DOF}}^e$), whilst $\mathbf{K}_{me} \in \mathbb{R}^{N_{m\text{DOF}}^e \times N_{m\text{DOF}}^e}$ is the non-penalised element stiffness matrix expressed in the global reference frame of the model. In Eq. (5.5), $\alpha \geq 1$ is a suitable parameter that aims at penalising all the meaningless densities between 0 and 1: in agreement with the classic SIMP approach this parameter has been set as $\alpha = 3$.

The pseudo-density function defined at the RVE scale affects also the structural responses of the continuum at the macroscopic scale, via the elasticity tensor \mathbf{C}_M , as indicated in Eqs. (4.6) and (4.7). Of course, the elasticity tensor of the equivalent homogeneous anisotropic material, replacing the true RVE architecture at the macroscopic scale, is involved in the definition of the global stiffness matrix of the FE model at the macroscopic scale $\hat{\mathbf{K}}_M$. Accordingly, matrix $\hat{\mathbf{K}}_M$ depends upon the pseudo-density fields defined at both scales as follows:

$$\hat{\mathbf{K}}_M := \sum_{e=1}^{N_{Me}} \rho_{Me}^\alpha (\boldsymbol{\xi}_{M1}, \boldsymbol{\xi}_{M2}) \hat{\mathbf{L}}_{Me}^T \int_{\Omega_{Me}} \mathbf{B}_{Me}^T \mathbf{C}_M (\boldsymbol{\xi}_{m1}, \boldsymbol{\xi}_{m2}) \mathbf{B}_{Me} d\Omega \hat{\mathbf{L}}_{Me}, \quad (5.6)$$

where N_{Me} is the number of elements constituting the FE model at the macroscopic scale, ρ_{Me}^α is the penalised fictitious density of Eq. (5.2) computed at the centroid of the generic element e of the FE model at macroscopic scale, $\hat{\mathbf{L}}_{Me} \in \mathbb{R}^{N_{M\text{DOF}}^e \times \hat{N}_{M\text{DOF}}}$ is the connectivity matrix of element e (whose number of DOFs is $N_{M\text{DOF}}^e$), while $\mathbf{B}_{Me} \in \mathbb{R}^{6 \times N_{M\text{DOF}}^e}$ is the matrix representing the product between the linear differential operator and the shape function matrices of the generic element.

The formulation of the equilibrium problem for a linear static analysis, considering the most general case of non-zero mixed Neumann-Dirichlet BCs reads:

$$\hat{\mathbf{K}}_M \hat{\mathbf{u}}_M = \hat{\mathbf{f}}_M, \quad \hat{\mathbf{u}}_M, \hat{\mathbf{f}}_M \in \mathbb{R}^{\hat{N}_{M\text{DOF}}}, \hat{\mathbf{K}}_M \in \mathbb{R}^{\hat{N}_{M\text{DOF}} \times \hat{N}_{M\text{DOF}}}, \quad (5.7)$$

where \hat{N}_{MDOF} is the overall number of DOFs of the FE model at the macroscopic scale, whilst $\hat{\mathbf{u}}_M$ and $\hat{\mathbf{f}}_M$ are the non-reduced vectors of generalised displacements and forces, respectively. Similarly to Eq. (4.3), the above formula can be rewritten as follows:

$$\begin{bmatrix} \mathbf{K}_M & \mathbf{K}_{\text{MBC}} \\ \mathbf{K}_{\text{MBC}}^T & \tilde{\mathbf{K}}_M \end{bmatrix} \begin{Bmatrix} \mathbf{u}_M \\ \mathbf{u}_{\text{MBC}} \end{Bmatrix} = \begin{Bmatrix} \mathbf{f}_M \\ \mathbf{r}_M \end{Bmatrix} \quad (5.8)$$

$\mathbf{u}_M, \mathbf{f}_M \in \mathbb{R}^{N_{\text{MDOF}}}$, $\mathbf{u}_{\text{MBC}}, \mathbf{r}_M \in \mathbb{R}^{N_{\text{MBC}}}$, $\mathbf{K}_M \in \mathbb{R}^{N_{\text{MDOF}} \times N_{\text{MDOF}}}$,
 $\mathbf{K}_{\text{MBC}} \in \mathbb{R}^{N_{\text{MDOF}} \times N_{\text{MBC}}}$, $\tilde{\mathbf{K}}_M \in \mathbb{R}^{N_{\text{MBC}} \times N_{\text{MBC}}}$,

where the physical meaning of the different quantities is the same as the counterparts defined at the lower scale, see Sec. 4.1.

Under mixed non-zero Neumann-Dirichlet BCs the macroscopic compliance \mathcal{C}_M is defined as [112]:

$$\mathcal{C}_M := \mathbf{f}_M^T \mathbf{u}_M - \mathbf{r}_M^T \mathbf{u}_{\text{MBC}}. \quad (5.9)$$

Inasmuch as the solution search for the multi-scale TO problem is carried out by means of a suitable deterministic algorithm, the derivation of the formal expression of the gradient of the objective function with respect to the topological variables at each scale (and of the constraint functions too) is needed to speed up the iterations. Such expressions have already been derived in previous works [38, 108, 110, 112] and are reported here below for the sake of completeness. In particular, when differentiating \mathcal{C}_M with respect to ξ_{mi} ($i = 1, 2$) one obtains:

$$\frac{\partial \mathcal{C}_M}{\partial \xi_{mik_m}} = - \sum_{e=1}^{N_{Me}} \sum_{q=1}^6 \sum_{r=1}^6 \frac{\partial C_{Mqr}}{\partial \xi_{mik_m}} \varepsilon_{Meq} \varepsilon_{Mer} V_{Me}, \quad (5.10)$$

$i = 1, 2, k_m = 1, \dots, n_{\text{mCP}},$

with

$$\frac{\partial C_{Mqr}}{\partial \xi_{mik_m}} = \begin{cases} \frac{1}{V_{\text{RVE}} (\varepsilon_{mq}^0)^2} \sum_{e \in \mathcal{S}_{mk_m}} \frac{\alpha}{\rho_{me}} \frac{\partial \rho_{me}}{\partial \xi_{mik_m}} \mathcal{W}_{me} (\varepsilon_{mq}^0), & \text{if } q = r, \\ \frac{1}{2V_{\text{RVE}} \varepsilon_{mq}^0 \varepsilon_{mr}^0} \sum_{e \in \mathcal{S}_{mk_m}} \frac{\alpha}{\rho_{me}} \frac{\partial \rho_{me}}{\partial \xi_{mik_m}} \mathcal{W}_{me} (\varepsilon_{mq}^0, \varepsilon_{mr}^0) + \\ - \frac{\varepsilon_{mq}^0}{2\varepsilon_{mr}^0} \frac{\partial C_{Mqq}}{\partial \xi_{mik_m}} - \frac{\varepsilon_{mr}^0}{2\varepsilon_{mq}^0} \frac{\partial C_{Mrr}}{\partial \xi_{mik_m}}, & \text{if } q \neq r. \end{cases} \quad (5.11)$$

In Eq. (5.10), ε_{Meq} ($q = 1, \dots, 6$) is the q -th component of the strain vector (Voigt's notation) of the generic element e of the FE model at the macroscopic scale, whilst V_{Me} is its volume. In Eq. (5.11), ε_{mq}^0 is the q -th elementary strain imposed to the RVE through the periodic BCs of Eq. (4.1) and \mathcal{W}_{me} is the work of internal forces of the generic element of the FE model of the RVE.

The gradient of the macroscopic compliance with respect to the topological variable at the upper scale reads:

$$\frac{\partial \mathcal{C}_M}{\partial \xi_{Mik_M}} = -\alpha \sum_{e \in \mathcal{S}_{Mk_M}} \frac{\mathcal{W}_{Me}}{\rho_{Me}} \frac{\partial \rho_{Me}}{\partial \xi_{Mik_M}}, \quad i = 1, 2, \quad k_M = 1, \dots, n_{MCP}, \quad (5.12)$$

where \mathcal{W}_{Me} is the internal work of the generic element of the FE model at the macroscopic scale. In Eqs. (5.10)-(5.12), the linear index k_χ ($\chi = m, M$) has been introduced for the sake of compactness. The relation between k_χ and $i_{\chi j}$, ($j = 1, 2, 3$) is:

$$k_\chi := 1 + i_{\chi 1} + i_{\chi 2}(n_{\chi 1} + 1) + i_{\chi 3}(n_{\chi 1} + 1)(n_{\chi 2} + 1), \quad \chi = m, M. \quad (5.13)$$

Moreover, in Eqs. (5.10)-(5.12), the quantity $\mathcal{S}_{\tau k_\tau}$ ($\tau = m, M$) is the discretised version of the local support of Eq. (3.9), while $\frac{\partial \rho_{\tau e}}{\partial \xi_{\tau ik_\tau}}$ reads:

$$\frac{\partial \rho_{\tau e}}{\partial \xi_{\tau ik_\tau}} = \begin{cases} R_{k_\tau e}, & \text{if } i = 1, \\ \frac{R_{k_\tau e}}{\xi_{\tau 2k_\tau}} (\xi_{\tau 1k_\tau} - \rho_{\tau e}), & \text{if } i = 2. \end{cases} \quad (5.14)$$

The scalar quantity $R_{k_\tau e}$ appearing in Eq. (5.14) is the NURBS rational basis function of Eq. (3.2) evaluated at the element centroid.

5.1.3 Constraint functions

The physical responses functions related to the design requirements considered in this study are presented in the following. The first requirement is related to the lightness of the structure. It is formulated either in terms of a constraint on the overall mass of the structure m_M or in terms of a constraint on its overall volume V_M . These quantities read:

$$V_M = \sum_{e=1}^{N_{Me}} \rho_{Me} V_{Me}, \quad (5.15)$$

$$m_M = \tau_M V_M. \quad (5.16)$$

In Eq. (5.16) τ_M is the density of the equivalent homogeneous anisotropic medium which is defined as:

$$\tau_M := \frac{\tau_m}{V_{\text{RVE}}} \sum_{e=1}^{N_{me}} \rho_{me} V_{me}, \quad (5.17)$$

where τ_m is the density of the bulk material composing the lattice RVE and V_{me} is the volume of the generic element composing the FE model of the RVE.

By differentiating V_M and m_M one obtains:

$$\begin{aligned} \frac{\partial V_M}{\partial \xi_{mik_m}} &= 0, \quad i = 1, 2, \quad k_m = 1, \dots, n_{m\text{CP}}, \\ \frac{\partial V_M}{\partial \xi_{Mik_M}} &= \sum_{e \in \mathcal{S}_{Mk_M}} V_{Me} \frac{\partial \rho_{Me}}{\partial \xi_{Mik_M}}, \quad i = 1, 2, \quad k_M = 1, \dots, n_{M\text{CP}}, \end{aligned} \quad (5.18)$$

$$\begin{aligned} \frac{\partial m_M}{\partial \xi_{mik_m}} &= \frac{\partial \tau_M}{\partial \xi_{mik_m}} V_M = \frac{\tau_m V_M}{V_{\text{RVE}}} \sum_{e \in \mathcal{S}_{mk_m}} V_{me} \frac{\partial \rho_{me}}{\partial \xi_{mik_m}}, \\ i &= 1, 2, \quad k_m = 1, \dots, n_{m\text{CP}}, \\ \frac{\partial m_M}{\partial \xi_{Mik_M}} &= \tau_M \frac{\partial V_M}{\partial \xi_{Mik_M}}, \\ i &= 1, 2, \quad k_M = 1, \dots, n_{M\text{CP}}. \end{aligned} \quad (5.19)$$

Therefore, the lightness requirement can be formulated either as:

$$g_1(\boldsymbol{\xi}_{M1}, \boldsymbol{\xi}_{M2}) := \frac{V_M}{V_{M\text{ref}}} - \gamma_{MV} \leq 0, \quad (5.20)$$

or as

$$g_2(\boldsymbol{\xi}_{M1}, \boldsymbol{\xi}_{M2}, \boldsymbol{\xi}_{m1}, \boldsymbol{\xi}_{m2}) := \frac{m_M}{m_{M\text{ref}}} - \gamma_{Mm} \leq 0, \quad (5.21)$$

In the above equations, $V_{M\text{ref}}$ and $m_{M\text{ref}}$ are the reference values of the macroscopic volume and mass, respectively, whilst γ_{MV} and γ_{Mm} are the imposed fraction for the macroscopic volume and mass, respectively. A further requirement is considered in terms of the volume fraction of the solid phase at the RVE scale. To this end, the RVE volume must be introduced as follows:

$$V_m = \sum_{e=1}^{N_{me}} \rho_{me} V_{me}, \quad (5.22)$$

whose gradient can be expressed as:

$$\begin{aligned} \frac{\partial V_m}{\partial \xi_{mik_m}} &= \sum_{e \in \mathcal{S}_{mk_m}} V_{me} \frac{\partial \rho_{me}}{\partial \xi_{mik_m}}, \quad i = 1, 2, \quad k_m = 1, \dots, n_{mCP}, \\ \frac{\partial V_m}{\partial \xi_{Mik_M}} &= 0, \quad i = 1, 2, \quad k_M = 1, \dots, n_{MCP}. \end{aligned} \quad (5.23)$$

Accordingly, the requirement on the RVE solid phase volume fraction can be expressed as:

$$g_3(\boldsymbol{\xi}_{m1}, \boldsymbol{\xi}_{m2}) := \frac{V_m}{V_{RVE}} - \gamma_{mV} \leq 0, \quad (5.24)$$

where γ_{mV} is the imposed volume fraction.

As stated in the introduction, two further requirements will be included in the problem formulation: the scale separation requirement and the manufacturing constraint on the minimum allowable dimensions at the RVE scale, which corresponds to the minimum thickness that can be fabricated through the selected manufacturing process. Both requirements are formulated as minimum length scale constraints at the respective scales. On the one hand, the scale separation requirement must be introduced to guarantee the presence of a given number of RVEs within the thinner branches of the optimised topology at the macroscopic scale: this ensures the accuracy of the results of the SEHM. On the other hand, the minimum member size constraint at the RVE scale must be introduced for manufacturing purposes. Accordingly, these requirements are formulated as:

$$g_4(\boldsymbol{\xi}_{M1}, \boldsymbol{\xi}_{M2}) := 1 - \frac{d_{M,\min}}{N_{RVE} \max_{j=1,2,3} L_{mj}} \leq 0, \quad j = 1, 2, 3, \quad (5.25)$$

$$g_5(\boldsymbol{\xi}_{m1}, \boldsymbol{\xi}_{m2}) := 1 - \frac{d_{m,\min}}{d_{MP}} \leq 0. \quad (5.26)$$

In Eqs. (5.25) and (5.26), $d_{i,\min}$ ($i = m, M$) is the minimum length scale of the topology at the i -th scale, while N_{RVE} is the number of RVEs to be foreseen within the thinner branches of the topology at the macroscopic scale in order to ensure the accuracy of the results of the SEHM, $\max_j L_{mj}$ is the characteristic length at the RVE scale and d_{MP} is the minimum dimension that can be obtained through the considered manufacturing process.

As discussed in [113], the main advantage of the NURBS-based SIMP method is in the handling of the geometric constraints imposed on the topological variable at the generic scale. In particular, since the pseudo-density

field describing the topology of the continuum, at both lower and upper scales, is described by means of a pure geometric entity, i.e., a NURBS hyper-surface, it is possible to properly set the integer parameters (number of CPs and basis functions degree along each parametric direction) governing its shape to automatically satisfy the minimum length scale requirement, without introducing an explicit optimisation constraint in the problem formulation. Therefore, in this study, the scale separation requirement of Eq. (5.25) and the manufacturing requirement of Eq. (5.26) are controlled by means of this feature.

Moreover, as discussed in [113], unlike classical density-based topology optimisation methods, in the NURBS-based SIMP method the minimum member size requirement does not depend upon the size of the elements composing the mesh, but only on the integer parameters involved in the definition of the NURBS entity. This means that an eventual mesh refinement has an impact only on the value of the structural responses (displacements, strains, stresses, etc.), but not on the minimum member size of the topology.

5.1.4 Problem formulation

The multi-scale TO problem considered in this study is formulated as a CNLPP as follows:

$$\min_{\xi_{\tau 1}, \xi_{\tau 2}} \frac{\mathcal{C}_M}{\mathcal{C}_{M\text{ref}}}, \text{ subject to : } \begin{cases} \hat{\mathbf{K}}_{\tau} \hat{\mathbf{u}}_{\tau} = \hat{\mathbf{f}}_{\tau}, \\ g_1 \leq 0 \text{ or } g_2 \leq 0, \\ g_3 \leq 0, \\ \xi_{\tau 1 k_{\tau}} \in [\rho_{\tau \text{min}}, \rho_{\tau \text{max}}], \quad \xi_{\tau 2 k_{\tau}} \in [\omega_{\tau \text{min}}, \omega_{\tau \text{max}}], \\ \tau = m, M, \quad \forall k_{\tau} = 1, \dots, n_{\tau \text{CP}}. \end{cases} \quad (5.27)$$

In Eq. (5.27), $\mathcal{C}_{M\text{ref}}$ is the reference value of the macroscopic compliance, whilst $\rho_{\tau \text{min}}$ and $\rho_{\tau \text{max}}$ are lower and upper bounds on the pseudo-density at each CP, and $\omega_{\tau \text{min}}$ and $\omega_{\tau \text{max}}$ are the bounds on the generic weight (the bounds on the design variables are introduced at each characteristic scale). It is noteworthy that the lower bound of the pseudo-density must be strictly positive to prevent any singularity for the solution of the equilibrium problem. The overall number of design variables of problem (5.27) is equal to $n_{\text{var}} = 2(n_{m\text{CP}} + n_{M\text{CP}})$.

Remark 5.1.1. *Since the generalised compliance can take negative values, $\mathcal{C}_{\mathcal{M}_{\text{ref}}}$ is set equal to the absolute value of the generalised compliance of the starting guess.*

5.2 Results

The proposed methodology is tested on both 2D and 3D problems: all calculations are carried out by means of the code SANTO. The software, coded in python language, is interfaced with the FE code ANSYS[®] to compute the mechanical responses of the structure at each scale. Moreover, the CNLPP of Eq. (5.27) has been solved through the GCMMA algorithm [6], whose parameters are listed in Tab. 5.1.

Table 5.1 – GCMMA algorithm parameters.

Parameter	Value
<i>move</i>	0.1
<i>albefa</i>	0.1
Stop Criterion	Value
Maximum n. of function evaluations	10000
Maximum n. of iterations	$20 \times n_{\text{var}}$
Tolerance on objective function	10^{-6}
Tolerance on constraints	10^{-6}
Tolerance on input variables change	10^{-6}
Tolerance on Karush –Kuhn –Tucker norm	10^{-6}

The design variables bounds of Problem (5.27) are set as follows: $\rho_{\chi_{\text{min}}} = 10^{-3}$, $\rho_{\chi_{\text{max}}} = 1$; $\omega_{\chi_{\text{min}}} = 0.5$, $\omega_{\chi_{\text{max}}} = 10$. Regarding the other continuous parameters involved in the NURBS entity definition, the non-trivial knot vectors components in Eq. (3.7) have been evenly distributed in the interval $[0, 1]$, for both 2D and 3D cases.

Furthermore, symmetry constraints on the pseudo-density field describing the RVE topology are imposed in all the numerical tests, except those wherein the effect of anisotropy is investigated: double symmetry for 2D problems (with respect to axes $x_{mj} = a_{mj}$, $j = 1, 2$) and three planes of symmetry ($x_{mj} = a_{mj}$, $j = 1, 2, 3$) for 3D problems, in order to have an optimised topology characterised, at most, by an orthotropic behaviour. Of course, the presence of symmetry axes/planes implies a reduction in the design variables count, at the χ -th scale, as follows:

$$n_{\chi\text{var}} = \begin{cases} \prod_{i=1}^N \theta_{\chi i}, & \text{for B – spline entity,} \\ 2 \prod_{i=1}^N \theta_{\chi i}, & \text{for NURBS entity,} \end{cases} \quad (5.28)$$

with $N = 2$ and $N = 3$ for 2D and 3D problems, respectively, and

$$\theta_{\chi i} = \begin{cases} \frac{n_{\chi i} + 1}{2}, & \text{if } n_{\chi i} \text{ is odd,} \\ \left\lfloor \frac{n_{\chi i} + 1}{2} \right\rfloor + 1, & \text{otherwise,} \end{cases} \quad (5.29)$$

where $\lfloor \dots \rfloor$ is the floor operator. Regarding the campaign of numerical tests, the following aspects are investigated:

1. The influence of the geometric entity, i.e., B-spline or NURBS, used to describe the TV at each scale on the optimised solution (only for 2D problems);
2. The influence of mixed BCs applied at the macroscopic scale on the optimised topology at each scale (for 2D and 3D problems);
3. The influence of the minimum member size at the RVE scale (related to the minimum printable dimension) on the optimised solution (for both 2D and 3D problems);
4. The influence of the scale separation constraint on the optimised solution (for both 2D and 3D problems);
5. The influence of the constraint type (mass or volume) imposed at the macroscopic scale on the optimised solution (only for 3D problems).

Unless explicitly stated, for all benchmarks, an aluminium alloy, characterised by $E_m = 71$ GPa, $\nu_m = 0.33$, $\tau_m = 2.8 \times 10^{-6} \frac{\text{kg}}{\text{mm}^3}$, is used as bulk material of the RVE. The reference macroscopic mass of the structure and the reference macroscopic compliance are those characterising the starting solution. Moreover, the reference volume (at the generic scale) is the volume of the overall design domain of dimension D .

5.2.1 2D Benchmark problems

The design domain of the RVE is shown in Fig. 5.2: it is a square of size $L_m = 2a_{m1} = 2a_{m2} = 3$ mm. Three static analyses are performed on the FE model of the RVE to determine the elasticity tensor of the ACM at the macroscopic scale through the SEHM discussed in Sec. 4.1. For each analysis, the periodic BCs of Eq. (4.1) are applied through constraint

equations among homologous nodes belonging to the opposite faces of the RVE, by considering elementary unit strains. The FE model of the RVE (which is the same for all 2D benchmark problems) has been coded in the Ansys automatic parametric design language and the mesh is made of $N_{me} = 2500$ PLANE182 elements (four nodes, two DOFs per node, plane stress hypothesis with unit thickness).

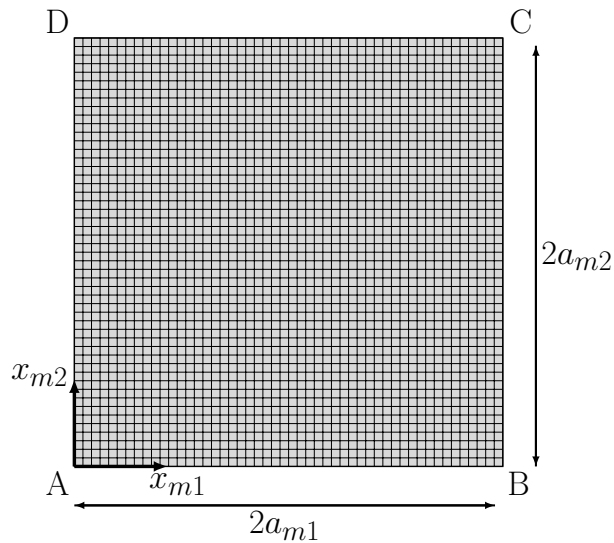


Figure 5.2 – Finite element model of the representative volume element of the architected cellular material with its characteristic size for 2D problems.

The first 2D benchmark problem (denoted as BK1-2D in the following), taken from [106], is shown in Fig. 5.3a and deals with a 2D cantilever beam. The geometrical parameters of the design domain at the macroscopic scale are: $a_{M1} = 600$ mm and $a_{M2} = 300$ mm. The set of nodes located at $x_{M1} = 0$ mm is clamped, while a point load $F_{M2} = -1$ N is applied at $(x_{M1}, x_{M2}) = (a_{M1}, a_{M2}/2)$. A static analysis is conducted on the macroscopic FE model whose mesh is made of $N_{Me} = 7200$ PLANE182 elements (plane stress hypothesis with unit thickness).

The second 2D benchmark problem (denoted as BK2-2D in the following) is characterised by the same geometrical parameters and the same mesh of BK1-2D. Also in this case the nodes located at $x_{M1} = 0$ are clamped, while the unit point force is applied at node B, as illustrated in Fig. 5.3b.

The third 2D benchmark problem (denoted as BK3-2D in the following), taken from [123] and shown in Fig. 5.4, is characterised by the same geometrical parameters and the same mesh of benchmarks BK1-2D and BK2-2D. BK3-2D is used to assess the influence of non-zero mixed Neumann-Dirichlet

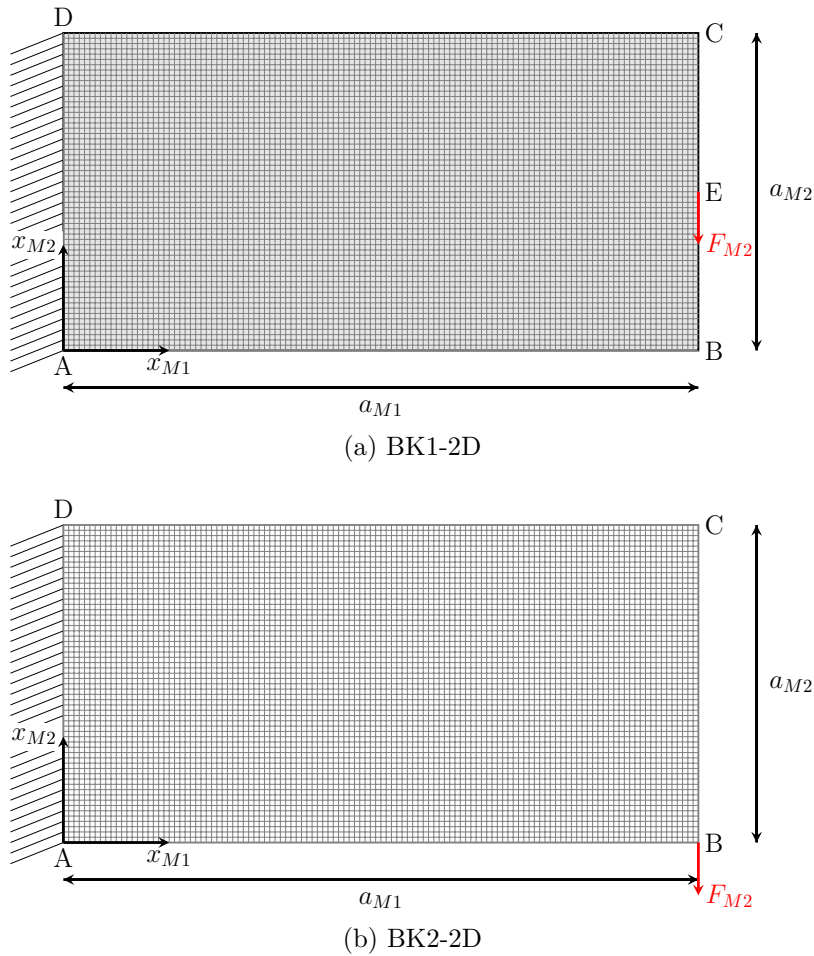


Figure 5.3 – Finite element model, geometrical parameters and applied boundary conditions of benchmark problems (a) BK1-2D and (b) BK2-2D.

BCs on the optimised topology. To this purpose, two sets of BCs are considered, as shown in Fig. 5.4. Each set of BCs corresponds to a different test case, i.e., BK3-2Da and BK3-2Db. In particular, both configurations share the following BCs: $u_{M1} = u_{M2} = 0$ at node A, $u_{M2} = 0$ at node B, $F_{M2} = -1$ N at node E (which is located at $x_{M1} = a_{M1}/2$, $x_{M2} = 0$). The difference between BK3-2Da and BK3-2Db is in the location where a variable displacement u_{M1} mm is imposed: as shown in Fig. 5.4, in the case of BK3-2Da this displacement is imposed at node B and takes value in the interval $[-0.05, 0.05]$ mm, while in the case of BK3-2Db it is imposed at node C and varies in the range $[-0.2, 0.2]$ mm.

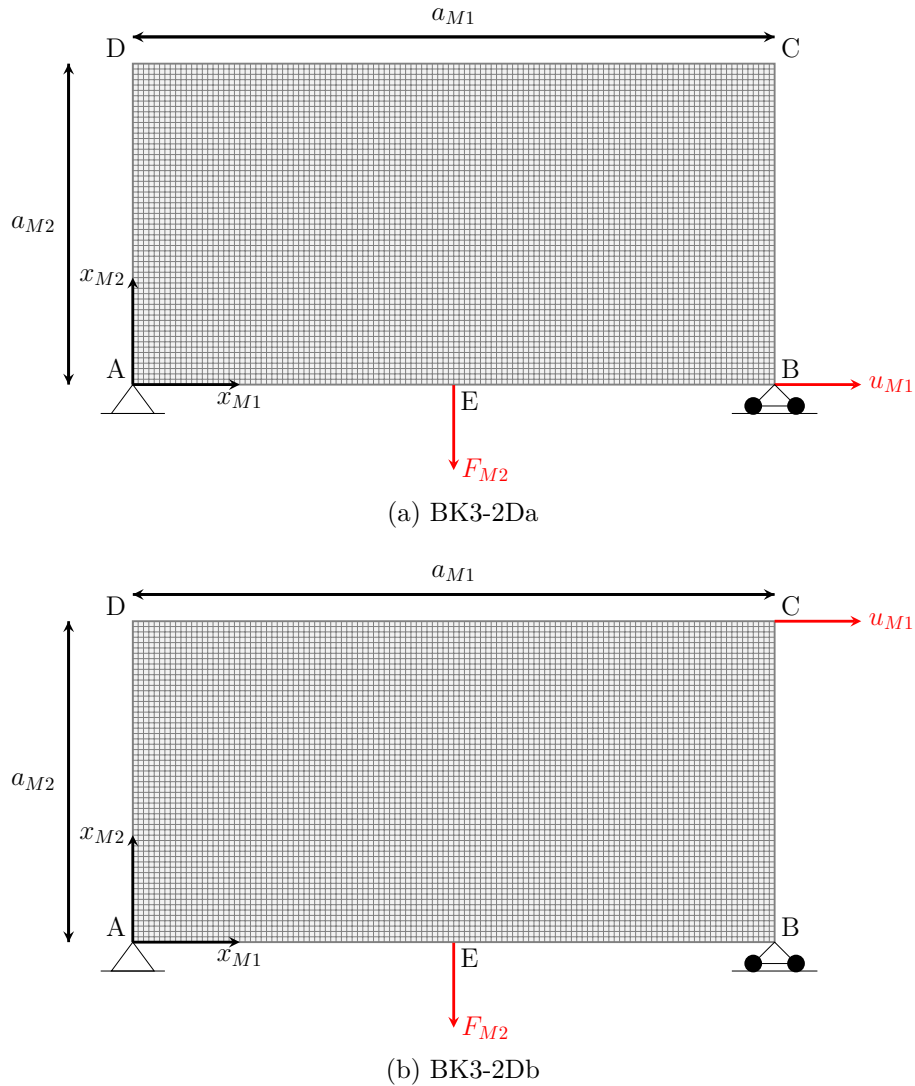


Figure 5.4 – Finite element model, geometrical parameters and applied boundary conditions of benchmark problems (a) BK3-2Da and (b) BK3-2Db.

5.2.1.1 Sensitivity of the optimised solution to the mass/volume constraint fraction

A campaign of numerical analyses is performed on BK1-2D, with the aim of showing the influence of the RVE volume fraction and of the macroscopic mass fraction on the optimised topology at both scales. The topology of the RVE is enforced to be symmetric with respect to axes $x_{mj} = a_{mj}$ ($j = 1, 2$) resulting, thus, in a ACM with an orthotropic behaviour at the macroscopic

scale. Moreover, as discussed in [58, 62], the initial guess at the RVE scale is characterised by a central hole, which is generated by setting to zero the value of the central CPs of the NURBS/B-spline entity. In particular, the number of CPs whose pseudo-density is set equal to zero is the result of an iterative process that stops when the constraint on the RVE volume fraction of Eq. (5.22) is met. The CNLPP of Eq. (5.27), for which only constraints g_2 and g_3 are included in the problem formulation, is solved by considering the following combination of blending functions degrees and CPs numbers at each scale.

At the RVE scale a B-spline surface with $n_{mCP} = 25 \times 25$ and $p_{mi} = 3$, ($i = 1, 2$) is employed. According to the methodology discussed in [113], this configuration ensures a minimum member size equal to $d_{m,\min} = 0.13$ mm within the design domain and equal to $d_{m,\min}^B = 0.12$ mm at the boundary of the domain. This value is greater than the minimum thickness that can be obtained through the direct metal laser sintering process.

At the macroscopic scale two B-spline surfaces are used: the first one has $n_{MCP} = 29 \times 15$ CPs, while the second one has $n_{MCP} = 23 \times 14$ CPs and both configurations are characterised by blending functions degrees $p_{Mi} = 3$, ($i = 1, 2$). Both solutions are characterised by a minimum length scale $d_{M\min} = 30$ mm within the domain and $d_{M,\min}^B = 6.5$ mm along its boundary, but a different number of CPs is required. In fact, as explained in [110, 113], in the post-processing phase the 3D pseudo-density descriptor, i.e., the B-spline surface, is cut by a plane placed corresponding to a given threshold value, which is $\rho_{M\text{cut}} = 0.35$ for the first surface and $\rho_{M\text{cut}} = 0.45$ for the second one (this value depends upon the constraint imposed on the mass fraction as discussed in the following). Of course, for both B-spline surfaces the minimum number of RVEs within the thinnest topological branch is equal to 10.

The optimised topologies are reported in Tabs. 5.2 and 5.3 by considering two different values of the mass fraction at the macroscopic scale, i.e., $\gamma_{Mm} = 0.35$ and $\gamma_{Mm} = 0.45$, respectively, and different values of the volume fraction of the RVE. The structural performances of the optimised topologies listed in Tabs. 5.2 and 5.3 are listed in Tab. 5.4. In this table results are provided in terms of the number of iterations to achieve convergence (N_{iter}), of the value of reference and optimised compliance as well as of the minimum member size measured at the end of the optimisation process at each scale, i.e., $\hat{d}_{\chi,\min}$ ($\chi = m, M$). The following remarks can be inferred from the analysis of these results.

Firstly, inasmuch as the constraint on the mass fraction is imposed at the macroscopic scale, and since this constraint is proportional to the product of

the volume fractions at both RVE and macroscopic scales (see Eq. (5.21)), the greater the volume fraction of the RVE the lower the volume fraction of the structure at the macroscopic scale for a given mass fraction.

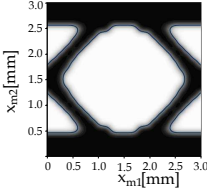
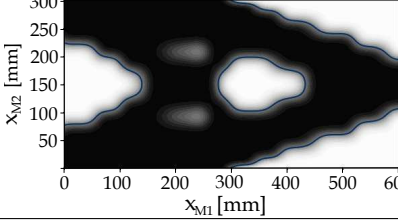
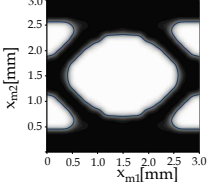
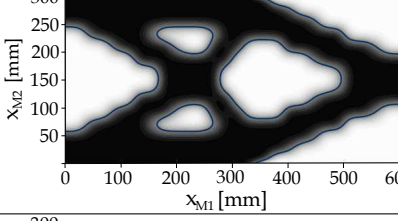
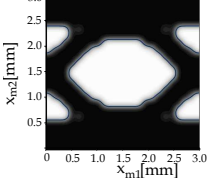
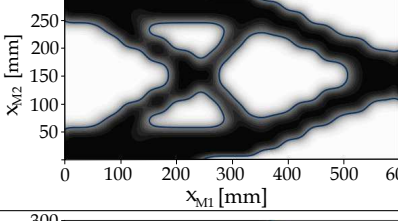
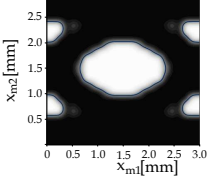
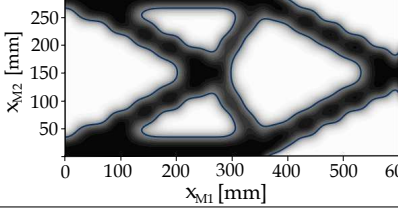
Secondly, for a given mass fraction at the macroscopic scale, the greater the volume fraction of the RVE the better the performances of the optimised solution in terms of compliance. In particular, for BK1-2D, the optimised solution is characterised by a dense isotropic material filling the whole RVE domain and by the least volume fraction at the macroscopic scale.

Finally, for each solution, the minimum length scale requirement at both the RVE scale and the macroscopic scale is systematically fulfilled thanks to the local support property of the NURBS entities, which establishes an implicit filter according to Eq. (3.9). In particular, the scale separation requirement is satisfied for both configurations of the B-spline entity. This is in agreement with the methodology presented in [113] whose aim is to set the integer parameters of the NURBS entity (i.e., number of CPs and basis functions degrees) in order to assess the lowest value of the member size achievable during the optimisation process. Of course, the minimum member size of the topology at the end of the optimisation process can be greater than this value because of the presence of further design requirements.

5.2.1.2 Sensitivity of the optimised solution to the starting guess at the lower scale

Due to the non-convexity of the CNLPP of Eq. (5.27), another sensitivity analysis is performed on BK1-2D to take into account the effect of the starting guess at the RVE scale on the optimised solution at both scales. This analysis has been conducted by considering both B-spline and NURBS entities (at each problem scale) characterised by $n_{mCP} = 25 \times 25$, $n_{MCP} = 29 \times 15$ and $p_{\chi j} = 3$ ($\chi = m, M, j = 1, 2$). These configurations are characterised by a minimum member size equal to $d_{m,\min} = 0.13$ mm $d_{M,\min} = 30$ mm, within the domain, while its value at the domain boundary is $d_{m,\min}^B = 0.12$ mm and $d_{M,\min}^B = 6.5$ mm at RVE scale and macroscopic scale, respectively. For each case, three starting guesses are considered at the RVE scale: (1) a topology with a central hole; (2) a topology with two holes generated symmetrically with respect to axis $x_{m1} = a_{m1}$; (3) a topology with four holes generated symmetrically with respect to axes $x_{mj} = a_{mj}$ ($j = 1, 2$). The generation of the holes is carried out according to the iterative process described in the above subsection in order to fulfil the design requirement on the volume fraction of the RVE. Conversely, the initial guess at the macroscopic scale is characterised by a uniform density field whose

Table 5.2 – BK1-2D: optimised topologies at both scales, when the mass fraction is set as $\gamma_{Mm} = 0.35$. Solutions obtained by employing B-spline entities, with $n_{mCP} = 25 \times 25$ and $n_{MCP} = 29 \times 15$ and $p_{\chi_i} = 3$, ($i = 1, 2$, $\chi = m, M$).

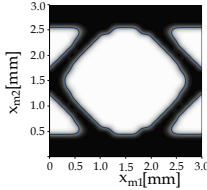
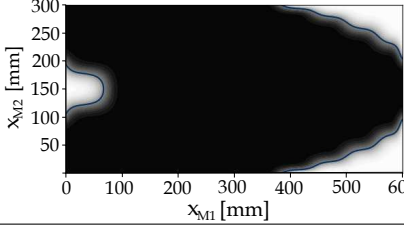
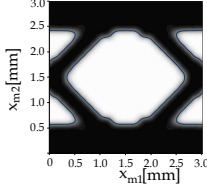
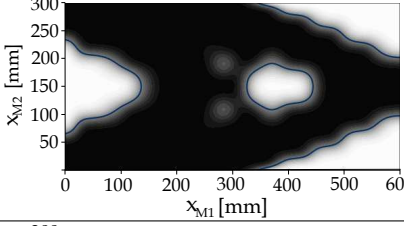
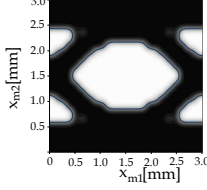
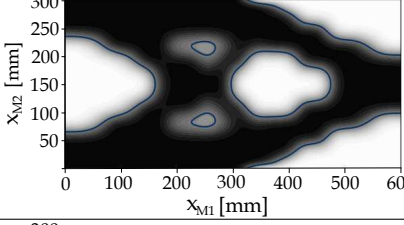
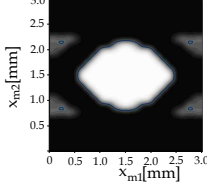
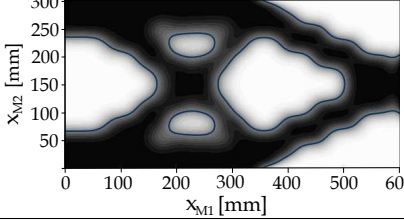
Volume/mass fractions	RVE optimised topology	Structure optimised topology	Problem number
$\gamma_{mV} = 0.5;$ $\gamma_{Mm} = 0.35$			1
$\gamma_{mV} = 0.6;$ $\gamma_{Mm} = 0.35$			2
$\gamma_{mV} = 0.7;$ $\gamma_{Mm} = 0.35$			3
$\gamma_{mV} = 0.8;$ $\gamma_{Mm} = 0.35$			4

value is determined in order to met the constraint on the macroscopic mass fraction.

For these analyses, an orthotropic behaviour of the RVE is set by imposing an orthogonal symmetry with respect to axes $x_{mj} = a_{mj}$ ($j = 1, 2$) to its topology during the optimisation process. Moreover, the volume fraction of the RVE and the mass fraction of the whole structure are set to $\gamma_{mV} = 0.6$ and $\gamma_{Mm} = 0.35$, respectively.

The optimised topologies are listed in Tabs. 5.5 and 5.6 for B-spline and NURBS solutions, respectively, whilst the related structural performances

Table 5.3 – BK1-2D: optimised topologies at both scales, when the mass fraction is set as $\gamma_{Mm} = 0.45$. Solutions obtained by employing B-spline entities, with $n_{mCP} = 25 \times 25$ and $n_{MCP} = 23 \times 14$ and $p_{\chi_i} = 3$, ($i = 1, 2$, $\chi = m, M$).

Volume/mass fractions	RVE optimised topology	Structure optimised topology	Problem number
$\gamma_{mV} = 0.5;$ $\gamma_{Mm} = 0.45$			5
$\gamma_{mV} = 0.6;$ $\gamma_{Mm} = 0.45$			6
$\gamma_{mV} = 0.7;$ $\gamma_{Mm} = 0.45$			7
$\gamma_{mV} = 0.8;$ $\gamma_{Mm} = 0.45$			8

are summarised in Tab. 5.7. From the analysis of these results some remarks can be drawn.

1. Problem (5.27) is non-convex because, for both B-spline and NURBS solutions, the optimised topologies obtained by considering an initial guess with one or two holes, at the RVE scale, correspond to equivalent local minima (the value of the macroscopic compliance is the same), although the components of the macroscopic elasticity matrix are different (this difference is more evident in the case of NURBS solutions).

Problem	$\gamma_{Mm} = 0.35$				$\gamma_{Mm} = 0.45$			
	1	2	3	4	5	6	7	8
N_{iter}	113	321	49	49	184	42	113	88
$\mathcal{C}_{M\text{ref}}(\text{Nmm})$	0.0131	0.0126	0.0130	0.0136	0.0061	0.0059	0.0060	0.0063
$\mathcal{C}_{M\text{opt}}(\text{Nmm})$	0.0034	0.0030	0.0028	0.0026	0.0026	0.0022	0.0020	0.0018
$\hat{d}_{m,\text{min}}(\text{mm})$	0.29	0.38	0.48	0.62	0.20	0.38	0.54	0.21
$\hat{d}_{M,\text{min}}(\text{mm})$	78.18	45.38	30.73	34.03	103.36	65.54	61.7	39.67
$\hat{d}_{m,\text{min}}^B(\text{mm})$	0.46	0.44	0.56	0.56	0.41	0.53	0.54	0.51
$\hat{d}_{M,\text{min}}^B(\text{mm})$	78.2	58.9	56.56	32.4	101	62.51	61.7	57.82

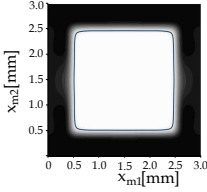
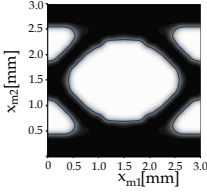
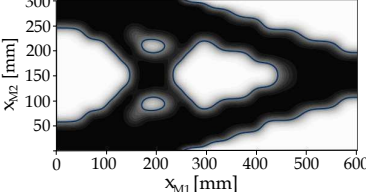
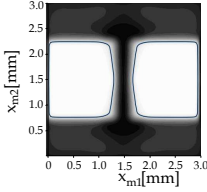
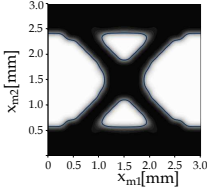
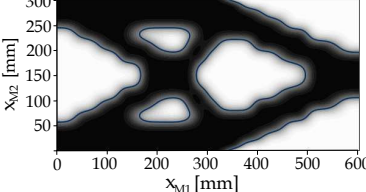
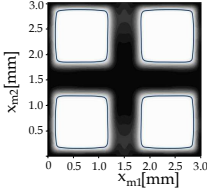
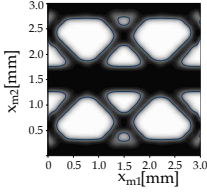
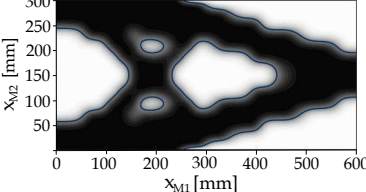
Table 5.4 – Optimisation results related to the problems listed in Tables 5.2 - 5.3 in terms of reference and optimal compliance and geometrical constraints values.

This behaviour is analogous to the one occurring when dealing with the multi-scale optimisation of composite (or anisotropic) structures [124–127] wherein different stacking sequences can correspond to the same macroscopic behaviour.

2. The optimised topologies obtained by considering a starting RVE domain with one or two holes show performances better (in terms of macroscopic compliance) than those characterising the optimised topologies obtained when considering an initial RVE domain with four holes (for both B-spline and NURBS solutions).
3. Due to the geometric properties of NURBS entities, minimum length scale requirements are always fulfilled at both scales ensuring, thus, that the optimised topologies can be actually manufactured and the results of the homogenisation process are accurate.
4. For each case, the NURBS solution outperforms the B-spline counterpart either in terms of the objective function or in terms of smoothness of the boundary of the optimised topology at both scales (in agreement with the results presented in [38, 108, 110]). This behaviour is related to the ability of NURBS entities to better approximate quadric hyper-surfaces as widely known in the CAD community.
5. It is noteworthy that B-spline solutions are characterised by transition regions larger than NURBS solutions. This is, indeed, an expected result in agreement with the results obtained for single-scale TO problems presented in [108, 110]. The reason behind the difference in the quality of the solution (in terms of the extent of the transition regions) is twofold. On the one hand, NURBS entities allow for a freedom greater than B-spline entities in describing the details of the topology. Indeed, this increased freedom is related to the number of design

variables involved in the definition of the NURBS entity (i.e., density value at each CP and the associated weight), which is higher than the one characterising the B-spline entity (only density value at each CP). This aspect has already been deeply discussed in previous works on the NURBS-based SIMP method, see [38, 108, 110]. On the other hand, when using B-spline entities as topological descriptors at both scales, it was observed that, very often, the GCMMA algorithm stops because the criterion on the tolerance on the (normalised) objective function is satisfied, which could explain the presence of the greater transition region (i.e., the algorithm converges towards a point falling in the neighbourhood of the local minimum, but not exactly towards the local minimum).

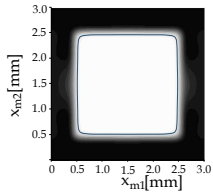
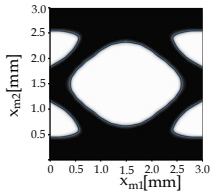
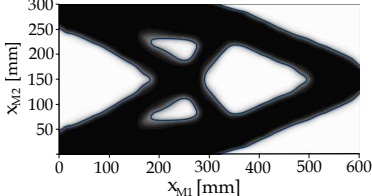
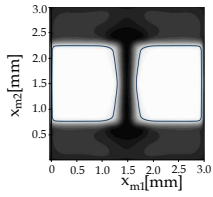
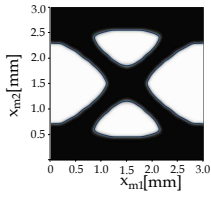
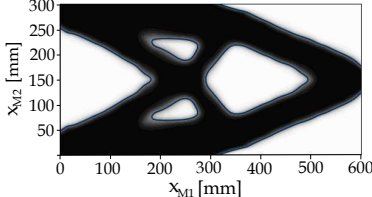
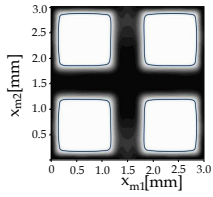
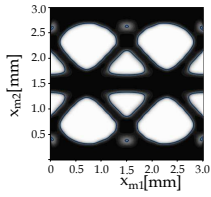
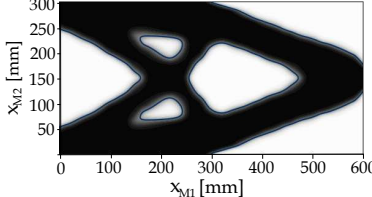
Table 5.5 – BK1-2D: optimised topologies at both scales for different starting topologies at the RVE scale. Solutions obtained by employing B-spline entities, with $n_{mCP} = 25 \times 25$ and $n_{MCP} = 29 \times 15$ and $p_{\chi_i} = 3$, ($i = 1, 2$, $\chi = m, M$).

RVE starting topology	RVE optimised topology	Structure optimised topology	Problem number
			9
$\mathbf{C}_M = \begin{bmatrix} 29658 & 5774 & 0 \\ 5774 & 9662 & 0 \\ 0 & 0 & 6246 \end{bmatrix} \text{ MPa}$			
			10
$\mathbf{C}_M = \begin{bmatrix} 29881 & 4838 & 0 \\ 4838 & 11307 & 0 \\ 0 & 0 & 5300 \end{bmatrix} \text{ MPa}$			
			11
$\mathbf{C}_M = \begin{bmatrix} 26580 & 3530 & 0 \\ 3530 & 8722 & 0 \\ 0 & 0 & 4459 \end{bmatrix} \text{ MPa}$			

5.2.1.3 Sensitivity of the optimised solution to the anisotropy of the RVE and to the macroscopic loads

The effect of the elastic symmetry group of the RVE and of the macroscopic loads is investigated on benchmark problems BK1-2D and BK2-2D. In particular, two configurations of the RVE are considered for both benchmarks.

Table 5.6 – BK1-2D: optimised topologies at both scales for different starting topologies at the RVE scale. Solutions obtained by employing NURBS entities, with $n_{mCP} = 25 \times 25$ and $n_{MCP} = 29 \times 15$ and $p_{\chi_i} = 3$, ($i = 1, 2, \chi = m, M$).

RVE starting topology	RVE optimised topology	Structure optimised topology	Problem number
			12
$\mathbf{C}_M = \begin{bmatrix} 54488 & 6043 & 0 \\ 6043 & 24056 & 0 \\ 0 & 0 & 6584 \end{bmatrix} \text{ MPa}$			
			13
$\mathbf{C}_M = \begin{bmatrix} 29881 & 4838 & 0 \\ 4838 & 11307 & 0 \\ 0 & 0 & 5300 \end{bmatrix} \text{ MPa}$			
			14
$\mathbf{C}_M = \begin{bmatrix} 26569 & 3534 & 0 \\ 3534 & 8735 & 0 \\ 0 & 0 & 4461 \end{bmatrix} \text{ MPa}$			

In the first case, the RVE is forced to show an orthotropic behaviour at the macroscopic scale by imposing two symmetry constraints (with respect to axes $x_{mj} = a_{mj}$, $j = 1, 2$) to the RVE topological variable.

In the second case, no symmetry constraint is imposed on the topological variable of the RVE, which can get an arbitrary asymmetric topology during the optimisation showing, thus, a completely anisotropic behaviour at the macroscopic scale.

Problem	B-spline solutions			NURBS solutions		
	9	10	11	12	13	14
N_{iter}	332	94	15	85	154	100
$\mathcal{C}_{M\text{ref}}(\text{Nmm})$	0.0126	0.0628	0.018	0.0126	0.0628	0.018
$\mathcal{C}_{M\text{opt}}(\text{Nmm})$	0.0030	0.0031	0.0035	0.0025	0.0025	0.0028
$\hat{d}_{m,\text{min}}(\text{Nmm})$	0.37	0.38	0.17	0.37	0.34	0.2
$\hat{d}_{M,\text{min}}(\text{Nmm})$	47.95	50.42	41.48	39.04	39.04	39.04
$\hat{d}_{m,\text{min}}^B(\text{Nmm})$	0.44	0.57	0.28	0.46	0.7	0.3
$\hat{d}_{M,\text{min}}^B(\text{Nmm})$	57	57	51.7	47.5	47.5	50

Table 5.7 – Optimisation results related to the problems listed in Tables 5.5 - 5.6 in terms of reference and optimal compliance and geometrical constraints values.

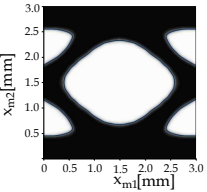
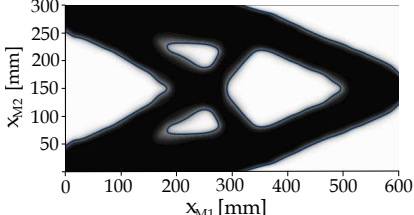
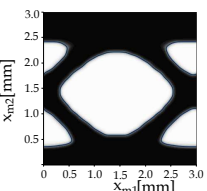
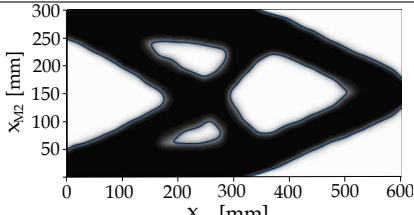
The RVE volume fraction and the macroscopic mass fraction are set to $\gamma_{mV} = 0.6$ and $\gamma_{Mm} = 0.35$, respectively, while the NURBS parameters are chosen as follows: $n_{m\text{CP}} = 25 \times 25$, $p_{mi} = 3$, ($i = 1, 2$) at the RVE scale and $n_{M\text{CP}} = 29 \times 15$, $p_{Mi} = 3$, ($i = 1, 2$) at the macroscopic one. The minimum length scale (within the domain and along its boundary) corresponding to this set of integer parameters of the NURBS surface is the same as the discussed in the previous section (for each scale). For each case, the initial guess at the RVE scale is characterised by a single hole in the centre of the RVE, while the initial topology at the macroscopic scale is uniform.

The optimised solutions for both BK1-2D and BK2-2D are reported in Tabs. 5.8 and 5.9, respectively, for both the orthotropic and the anisotropic cases. The structural performances related to these solutions are listed in Tab. 5.10. As it can be inferred from these results, the influence of the RVE behaviour, in terms of elastic symmetry type, is strictly related to the macroscopic loading conditions.

In particular, for BK1-2D the optimised topology is practically unchanged, at both scales, when passing from an orthotropic RVE to an anisotropic one. In fact, in the latter case the RVE topology converges towards a configuration characterised by (almost) a double orthogonal symmetry and by (almost) the same macroscopic behaviour and performances of the first case.

Conversely, for BK2-2D, the elastic symmetry type of the RVE has a strong influence on the optimised topology at both RVE and macroscopic scales. As it can be seen from Tab. 5.9, although the topologies of the RVE and of the structure are completely different and the macroscopic elasticity matrix has different components, both solutions show equivalent performances in

Table 5.8 – BK1-2D: optimised topologies at both scales by considering an RVE with orthotropic and anisotropic behaviour. Solutions obtained by employing NURBS entities, with $n_{mCP} = 25 \times 25$ and $n_{MCP} = 29 \times 15$ and $p_{\chi i} = 3$, ($i = 1, 2$, $\chi = m, M$).

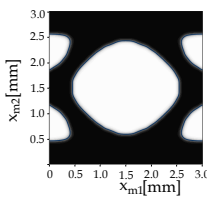
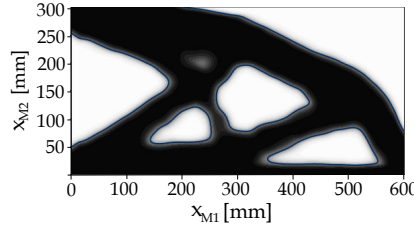
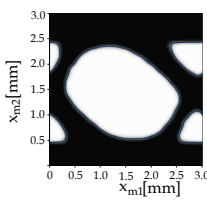
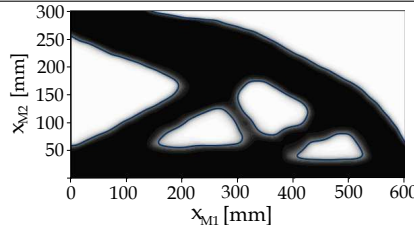
RVE optimised topology	Macroscopic optimised topology	Problem number
	 $\mathbf{C}_M = \begin{bmatrix} 29658 & 5774 & 0 \\ 5774 & 9662 & 0 \\ 0 & 0 & 6246 \end{bmatrix} \text{ MPa}$	15
	 $\mathbf{C}_M = \begin{bmatrix} 30323 & 5322 & 0.34 \\ 5322 & 9470 & 7.71 \\ 0.34 & 7.71 & 5916 \end{bmatrix} \text{ MPa}$	16

terms of the macroscopic compliance. This is a further evidence of the strong non-convexity of the CNLPP of Eq. (5.27).

5.2.1.4 Sensitivity of the optimised topology to mixed non-zero boundary conditions

The influence of mixed non-zero Neumann-Dirichlet BCs on the optimised topologies at both RVE and macroscopic scales is analysed on benchmark problems BK3-2Da and BK3-2Db. In all the analyses, no symmetry constraint is imposed to the topology at the RVE scale, which can show, eventually, an anisotropic behaviour, thus adapting its elastic response to the BCs imposed at the macroscopic scale. The RVE volume fraction and the macroscopic mass fraction are set to $\gamma_{mV} = 0.4$ and $\gamma_{Mm} = 0.2$, respectively, while the NURBS parameters are chosen as follows: $n_{mCP} = 25 \times 25$, $p_{mi} = 3$ for the lower scale and $n_{MCP} = 31 \times 17$, $p_{Mi} = 3$, ($i = 1, 2$) for

Table 5.9 – BK2-2D: optimised topologies at both scales by considering an RVE with orthotropic and anisotropic behaviour. Solutions obtained by employing NURBS entities, with $n_{mCP} = 25 \times 25$ and $n_{MCP} = 29 \times 15$ and $p_{\chi i} = 3$, ($i = 1, 2$, $\chi = m, M$).

RVE optimised topology	Structure optimised topology	Problem number
	 $\mathbf{C}_M = \begin{bmatrix} 28063 & 5906 & 0 \\ 5906 & 13093 & 0 \\ 0 & 0 & 6155 \end{bmatrix} \text{ MPa}$	17
	 $\mathbf{C}_M = \begin{bmatrix} 29016 & 5063 & -2191 \\ 5063 & 13059 & -1814 \\ -2191 & -1814 & 5390 \end{bmatrix} \text{ MPa}$	18

Problem	15	16	17	18
N_{iter}	85	237	103	254
$\mathcal{C}_{M\text{ref}}$ (Nmm)	0.0126	0.127	0.0142	0.0145
$\mathcal{C}_{M\text{opt}}$ (Nmm)	0.0025	0.0025	0.0031	0.0030
$\hat{d}_{m,\text{min}}$ (Nmm)	0.35	0.35	0.36	0.27
$\hat{d}_{M,\text{min}}$ (Nmm)	45.20	45.20	28.00	25.00
$\hat{d}_{m,\text{min}}^B$ (Nmm)	0.36	0.36	0.46	0.33
$\hat{d}_{M,\text{min}}^B$ (Nmm)	47.60	47.60	18.0	35.71

Table 5.10 – Optimisation results related to the problems listed in Tables 5.8 - 5.9 in terms of reference and optimal compliance and geometrical constraints values.

the macroscopic one. These configurations are characterised by a minimum member size (within the design domain) of $d_{m,\min} = 0.13$ mm at the RVE scale and $d_{M,\min} = 30$ mm at the macroscopic one. Conversely, the minimum member size at the boundary of the domain is equal to $d_{m,\min}^B = 0.12$ mm and $d_{M,\min}^B = 6.5$ mm at RVE scale and macroscopic scale, respectively. For each analysis, the starting guess at the lower scale is characterised by a central hole, while at the upper scale the initial topology is obtained by considering an uniform pseudo-density field. As in the other 2D test cases, the initial topologies satisfy the constraints on the RVE volume fraction and on the macroscopic mass fraction.

The influence of mixed BCs on the optimised topologies at both scales is firstly investigated on BK3-2Da: the applied horizontal displacement u_{M1} can take values in the set $[-0.05, -0.025, 0, +0.025, +0.05]$ mm. Unlike the previous analyses, the isotropic bulk material of the RVE is characterised by $E_m = 2525$ MPa, $\nu_m = 0.25$ and $\tau_m = 2.8 \times 10^{-6}$ kgmm⁻³. The optimised solutions are listed in Tab. 5.11, whilst the related structural performances are listed in Tab. 5.13. Like the single-scale optimised topologies obtained by using an isotropic material presented in [112, 123], the optimised solutions at both the RVE scale and the macroscopic scale change when varying the entity of the applied displacement. This means that the result of the concurrent optimisation of the elastic symmetry of the material (related to the RVE topology) and of the macroscopic topology strongly depends upon the intensity of the applied displacement.

A similar analysis has been conducted, by considering a single-scale optimisation and by modelling the macroscopic domain with two different bulk materials characterised by the following mechanical properties: an isotropic material with $E_M = 2525$ MPa, $\nu_m = 0.25$ and $\tau_M = 2.8 \times 10^{-6}$ kgmm⁻³ and a transversely isotropic material with $E_{M1} = 1013$ MPa, $E_{M2} = E_{M3} = 1037$ MPa, $\nu_{M12} = \nu_{M13} = 0.488$, $\nu_{M23} = 0.039$, $G_{M12} = G_{M13} = 931$ MPa, $G_{M23} = 499$ MPa and $\tau_M = 2.8 \times 10^{-7}$ kgmm⁻³. The optimised topologies are listed in Tab. 5.12, while the related structural performances are reported in Tab. 5.14. From these results one can infer that the optimised topology at the macroscopic scale is strongly influenced by the elastic symmetry group of the material even in the case of mixed BCs.

The trend of the macroscopic compliance vs. the applied displacement for the optimised topologies obtained in the case of double-scale TO optimisation and single-scale TO (for the isotropic material and the transversely isotropic material) for BK3-2Da are illustrated in Figs. 5.5 and 5.6. As it can be inferred from this results, the curve is monotonic (in the considered interval wherein u_{M1} takes value) in the case of the multi-scale TO problem,

whilst this is not the case for the single-scale TO problem (regardless the elastic symmetry of the material at the macroscopic scale).

Further analyses have been conducted on BK3-2Db, where the applied horizontal displacement u_{M1} can take values in the set $[-0.2, -0.1, -0.025, 0, +0.1, +0.2]$ mm. The properties of the bulk material at the RVE scale are the same as in the case of BK3-2Da. Also in this case the topology at both scales evolves when changing the applied displacement value u_{M1} . Tab. 5.15 reports the optimised topologies for BK3-2Da, whilst the related structural performances are reported in Tab. 5.16. The trend of the macroscopic compliance vs. the applied displacement is illustrated in Fig. 5.7. It is noteworthy that, except the case $u_{M1} = 0$, the optimised topology at both the RVE scale and the macroscopic one is completely asymmetric (thus the optimised solution is characterised by an RVE with an anisotropic behaviour). Moreover, unlike the optimised topologies resulting from the multi-scale TO in the case BK3-2Da, the trend of the macroscopic compliance vs. the applied displacement is non-monotonic.

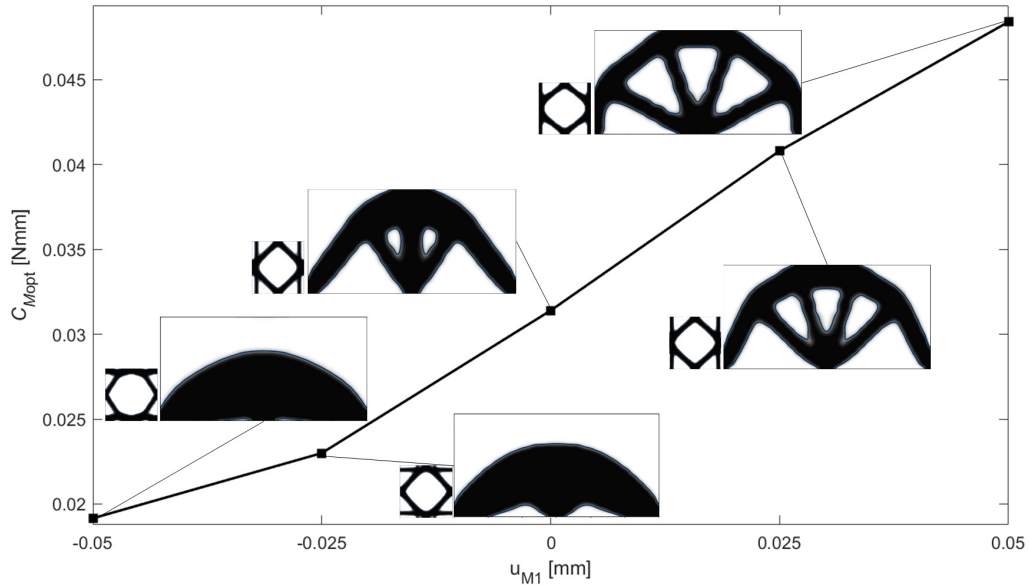


Figure 5.5 – BK3-2Da: Macroscopic compliance vs. applied displacement for optimised topologies resulting from two-scale topology optimisation. Solutions obtained by employing NURBS entities, with $n_{mCP} = 25 \times 25$ and $n_{MCP} = 31 \times 17$ and $p_{\chi i} = 3$, ($i = 1, 2$, $\chi = m, M$).

Table 5.11 – BK3-2Da: optimised topologies at both scales under mixed non-zero BCs. Solutions obtained by employing NURBS entities, with $n_{mCP} = 25 \times 25$ and $n_{MCP} = 31 \times 17$ and $p_{\chi i} = 3$, ($i = 1, 2$, $\chi = m, M$).

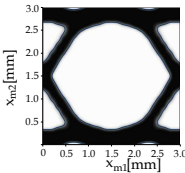
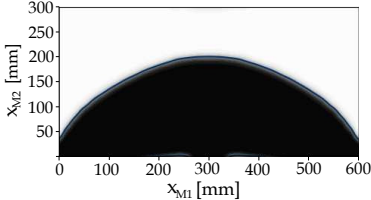
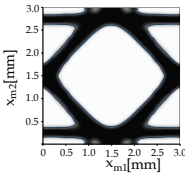
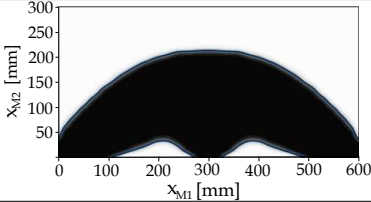
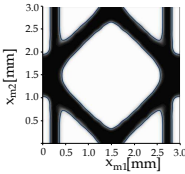
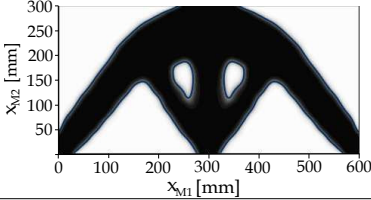
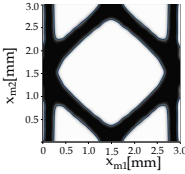
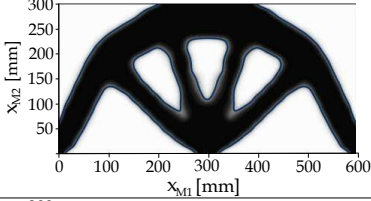
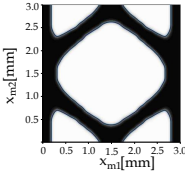
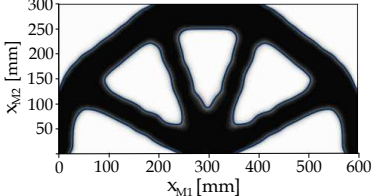
BCs	RVE optimised topology	Structure optimised topology	Problem number
$F_{M2} = -1 \text{ N},$ $u_{M1} = -0.05 \text{ mm},$			19
$F_{M2} = -1 \text{ N},$ $u_{M1} = -0.025 \text{ mm},$			20
$F_{M2} = -1 \text{ N},$ $u_{M1} = 0 \text{ mm},$			21
$F_{M2} = -1 \text{ N},$ $u_{M1} = 0.025 \text{ mm},$			22
$F_{M2} = -1 \text{ N},$ $u_{M1} = 0.05 \text{ mm},$			23

Table 5.12 – BK3-2Da: optimised topologies at the macroscopic scale under mixed non-zero BCs when the bulk material is considered isotropic or transversely isotropic. Solutions obtained by employing NURBS entities, with $n_{MCP} = 31 \times 17$ and $p_{Mi} = 3$, ($i = 1, 2$).

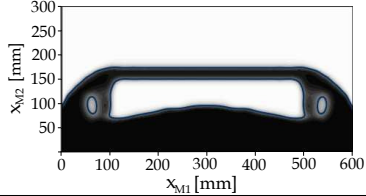
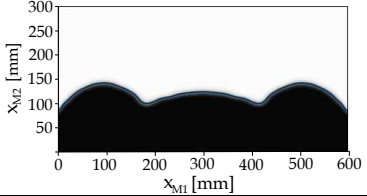
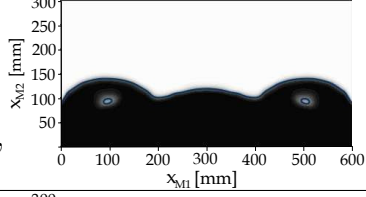
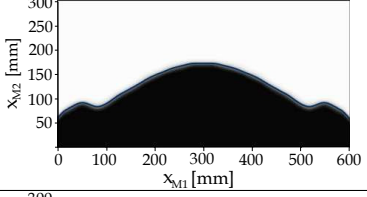
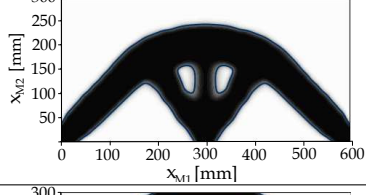
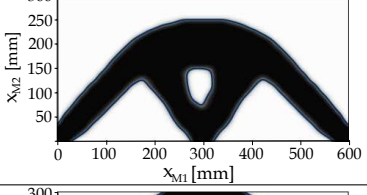
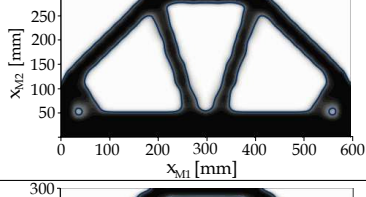
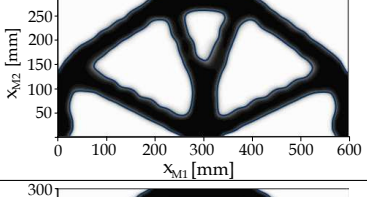
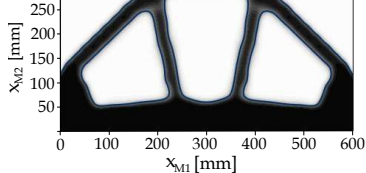
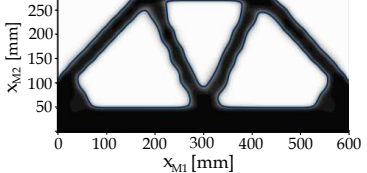
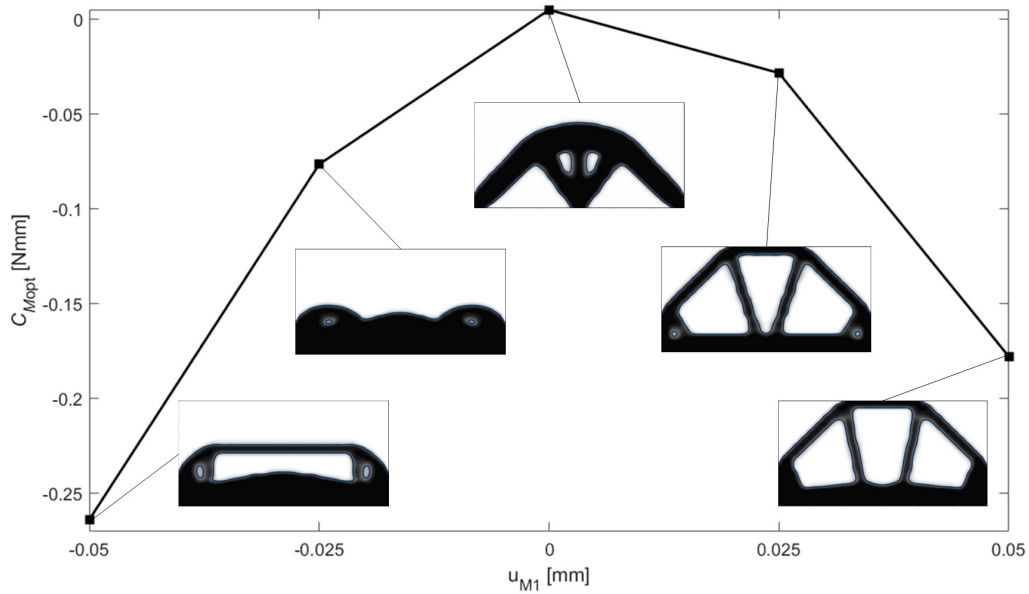
Problem number/BCs	Optimised topology (isotropy)	Optimised topology (transverse isotropy)
24 – 29 $F_{M2} = -1$ N, $u_{M1} = -0.05$ mm,		
25 – 30 $F_{M2} = -1$ N, $u_{M1} = -0.025$ mm,		
26 – 31 $F_{M2} = -1$ N, $u_{M1} = 0$ mm,		
27 – 32 $F_{M2} = -1$ N, $u_{M1} = 0.025$ mm,		
28 – 33 $F_{M2} = -1$ N, $u_{M1} = 0.05$ mm,		

Table 5.13 – Optimisation results related to the problems listed in Table 5.11 in terms of reference and optimal compliance and geometrical constraints values.

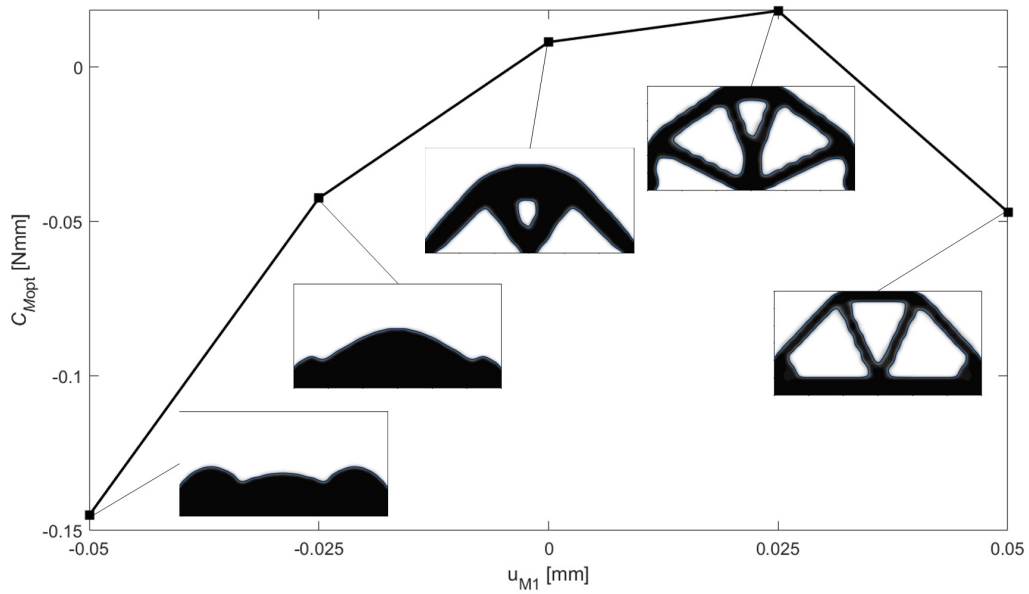
Problem	Double scale optimisation: BK3-2Da				
	19	20	21	22	23
N_{iter}	200	190	200	199	180
$\mathcal{C}_{M\text{ref}}(\text{Nmm})$	0.5682	0.5742	0.5801	0.5860	0.5919
$\mathcal{C}_{M\text{opt}}(\text{Nmm})$	0.01916	0.023	0.0314	0.0408	0.0484
$\hat{d}_{m,\text{min}}(\text{mm})$	0.27	0.22	0.2266	0.2143	0.28
$\hat{d}_{M,\text{min}}(\text{mm})$	37.4	148.68	44.8	39.26	39.02
$\hat{d}_{m,\text{min}}^B(\text{mm})$	0.20	0.33	0.3337	0.3513	0.19
$\hat{d}_{M,\text{min}}^B(\text{mm})$	37.4	36.31	30.44	59.64	23.23

Table 5.14 – Optimisation results related to the problems listed in Table 5.12 in terms of optimal compliance and geometrical constraints values.

Problem	24-29	25-30	26-31	27-32	28-33
$\mathcal{C}_{M\text{opt}}^{\text{iso}}(\text{Nmm})$	-0.2637	-0.0764	0.0050	-0.0283	-0.1778
$\mathcal{C}_{M\text{opt}}^{\text{isotr}}(\text{Nmm})$	-0.1450	-0.0424	0.0081	0.0182	-0.0469



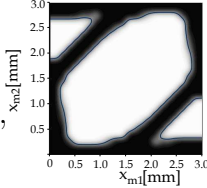
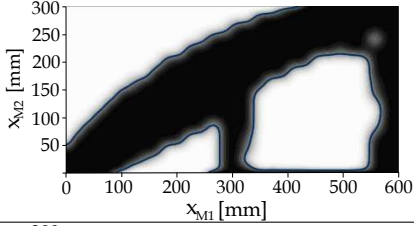
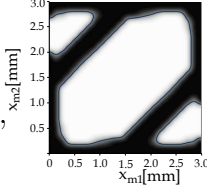
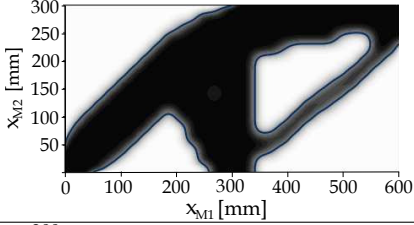
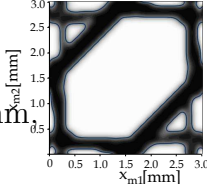
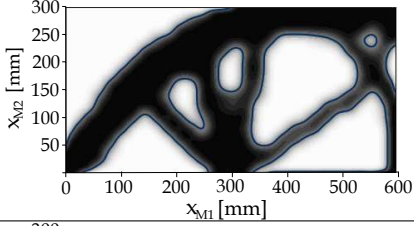
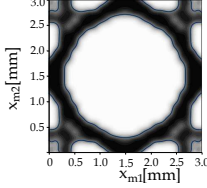
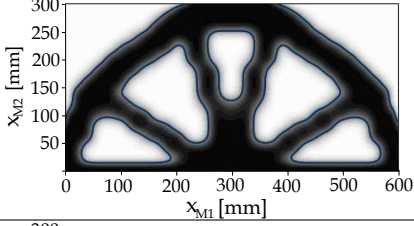
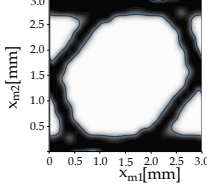
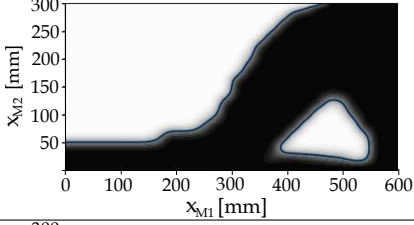
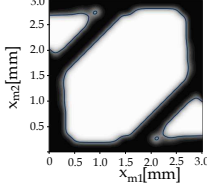
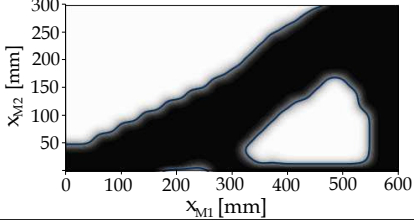
(a) isotropic material



(b) transversely isotropic material

Figure 5.6 – BK3-2Da: Macroscopic compliance vs. applied displacement for optimised topologies, resulting from single-scale topology optimisation, made of a) isotropic material and b) transversely isotropic material. Solutions obtained by employing NURBS entities, with $n_{MCP} = 31 \times 17$ and $p_{Mi} = 3$, ($i = 1, 2$).

Table 5.15 – BK3-2Db: optimised topologies at both scales under mixed non-zero BCs. Solutions obtained by employing NURBS entities, with $n_{mCP} = 25 \times 25$ and $n_{MCP} = 31 \times 17$ and $p_{\chi_i} = 3$, ($i = 1, 2$, $\chi = m, M$).

BCs	RVE optimised topology	Structure optimised topology	Problem number
$F_{M2} = -1 \text{ N},$ $u_{M1} = -0.2 \text{ mm},$			34
$F_{M2} = -1 \text{ N},$ $u_{M1} = -0.1 \text{ mm},$			35
$F_{M2} = -1 \text{ N},$ $u_{M1} = -0.025 \text{ mm},$			36
$F_{M2} = -1 \text{ N},$ $u_{M1} = 0 \text{ mm},$			37
$F_{M2} = -1 \text{ N},$ $u_{M1} = 0.1 \text{ mm},$			38
$F_{M2} = -1 \text{ N},$ $u_{M1} = 0.2 \text{ mm},$			39

Problem	Double scale optimisation: BK3-2Db					
	34	35	36	37	38	39
N_{iter}	160	160	200	51	100	163
$\mathcal{C}_{M\text{ref}}(\text{Nmm})$	0.5216	0.5633	0.5803	0.5833	0.5816	0.5582
$\mathcal{C}_{M\text{opt}}(\text{Nmm})$	-0.6459	-0.1081	0.0518	0.0763	-0.0596	-0.4973
$\hat{d}_{m,\text{min}}(\text{mm})$	0.35	0.47	0.13	0.28	0.29	0.37
$\hat{d}_{M,\text{min}}(\text{mm})$	46.55	34.50	25.35	40.97	132.18	117.73
$\hat{d}_{m,\text{min}}^B(\text{mm})$	0.32	0.21	0.23	0.20	0.29	0.28
$\hat{d}_{M,\text{min}}^B(\text{mm})$	31.94	55.16	16.62	15.44	18.08	33.8

Table 5.16 – Optimisation results related to the problems listed in Table 5.15 in terms of reference and optimal compliance and geometrical constraints values.

5.2.2 3D benchmark problems

The design domain of the RVE, shown in Fig. 5.8, is a cube of size $L_m = 2a_{m1} = 2a_{m2} = 2a_{m3} = 2.5 \text{ mm}$. Six linear static analysis are performed on the FE model of the RVE to assess the mechanical properties of the equivalent homogeneous anisotropic material via the SEHM discussed in Sec. 4.1. For each analysis, the periodic BCs of Eq. (4.1) have been applied through constraint equations among homologous nodes belonging to the opposite faces of the RVE, by considering elementary unit strains. The FE model of the RVE, which remains unchanged for all the 3D benchmark problems, is implemented in the Ansys automatic parametric design language environment with a mesh made of $N_{me} = 8000$ SOLID185 elements (8 nodes, 3 DOFs per node). For all the 3D benchmark problems, the topology of the RVE is forced to be symmetric with respect to planes $x_{mj} = a_{mj}$, ($j = 1, 2, 3$) showing, thus, an orthotropic behaviour at the macroscopic scale.

The first 3D benchmark problem (denoted as BK1-3D in the following), taken from [106] and shown in Fig. 5.9a, is the well-known 3D cantilever beam. The geometrical parameters of the design domain are: $a_{M1} = 500 \text{ mm}$, $a_{M2} = 250 \text{ mm}$ and $a_{M3} = 150 \text{ mm}$. The nodes belonging to the plane $x_{M1} = 0$ are clamped, while a vertical negative force $F_{M2} = -10 \text{ N}$ is applied to the nodes placed at $(x_{M1}, x_{M2}, x_{M3}) = (a_{M1}, a_{M2}/2 \pm e_{M\text{size}}, a_{M3}/2 \pm e_{M\text{size}})$, with $e_{M\text{size}} = 10 \text{ mm}$. A static analysis is conducted on the macroscopic FE model, discretised through $N_{Me} = 18750$ SOLID185 elements.

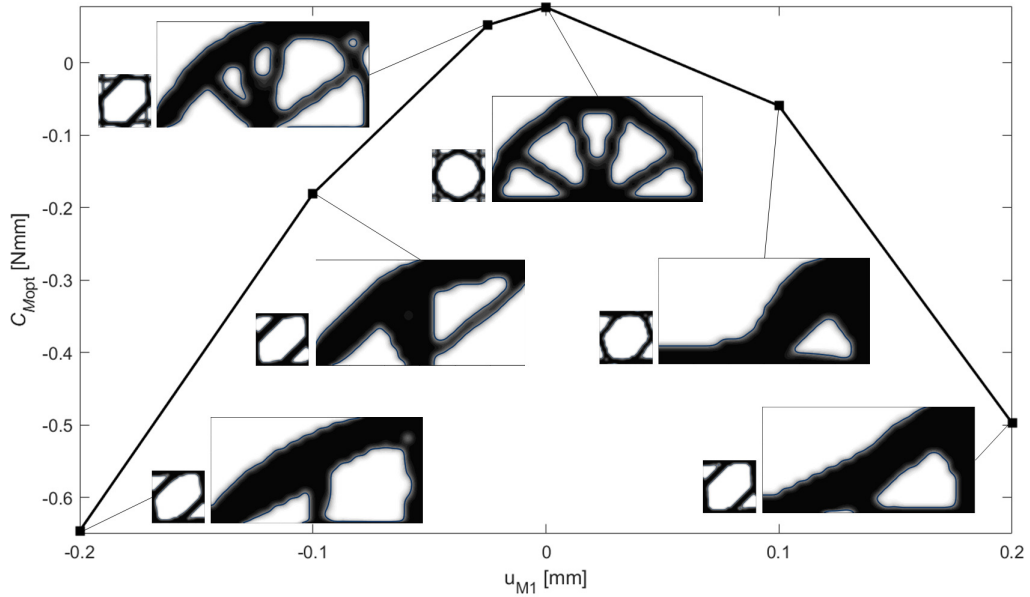


Figure 5.7 – BK3-2Db: Macroscopic compliance vs. applied displacement for optimised topologies resulting from two-scale topology optimisation. Solutions obtained by employing NURBS entities, with $n_{mCP} = 25 \times 25$ and $n_{MCP} = 31 \times 17$ and $p_{\chi i} = 3$, ($i = 1, 2$, $\chi = m, M$).

The second 3D benchmark problem (denoted as BK2-3D in the following), taken from [106] and shown in Fig. 5.9c, is a 3D supported structure of size $a_{M1} = a_{M3} = 250$ mm, $a_{M2} = 200$ mm. BK3-3D model is characterised by a mesh made of $N_{Me} = 12500$ SOLID185 elements. As shown in Fig. 5.9c, the domain is submitted to the following BCs: the nodes E, F, G, H are clamped, while a negative force $F_{M2} = -10$ N is applied to the nodes located at $(x_{M1}, x_{M2}, x_{M3}) = (a_{M1}/2 \pm e_{Msize}, a_{M2}, a_{M3}/2 \pm e_{Msize})$.

The third 3D benchmark problem (denoted as BK3-3D in the following) is the 3D Messerschmitt Bölkow Blohm beam and it is characterised by the same geometrical dimensions and mesh of BK1-3D. The nodes located at $x_{M1} \in [0, 3e_{Msize}]$, $x_{M2} = 0$ and $x_{M3} \in [0, a_{M3}]$ are connected rigidly, via MPC184 beam elements, to a master node located at $(x_{M1}, x_{M2}, x_{M3}) = (0, 0, a_{M3}/2)$, which is clamped. Moreover, nodes placed at $x_{M1} \in [a_{M1} - 3e_{Msize}, a_{M1}]$, $x_{M2} = 0$ and $x_{M3} \in [0, a_{M3}]$ are connected to the master node located at $(x_{M1}, x_{M2}, x_{M3}) = (a_{M1}, 0, a_{M3}/2)$ via MPC184 elements. To this latter a displacement u_{M1} is applied. In addition, the negative force $F_{M2} = -10$ N is applied to the master node located at $(x_{M1}, x_{M2}, x_{M3}) = (a_{M1}/2, a_{M2}, a_{M3}/2)$, which is rigidly connected via

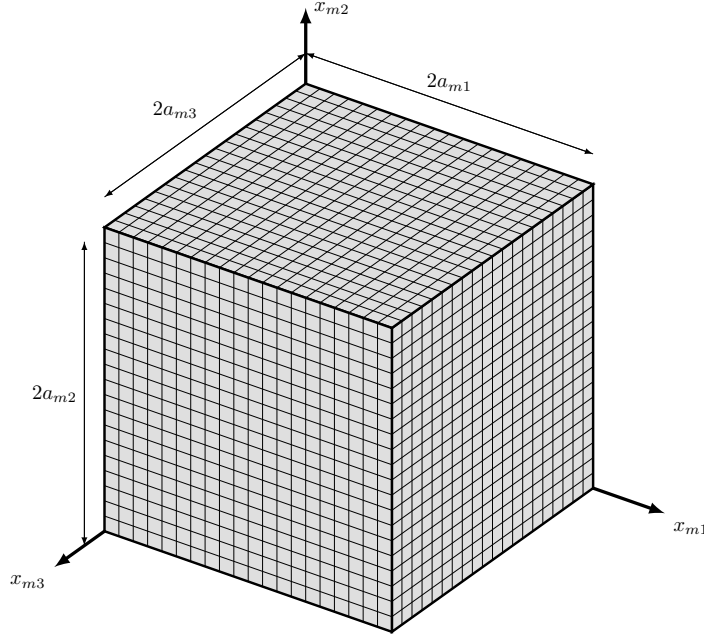


Figure 5.8 – Finite element model of the representative volume element of the architected cellular material with its characteristic size for 3D problems.

MPC184 to the nodes located at $x_{M1} = a_{M1}/2 \pm e_{Msize}$, $x_{M2} = a_{M2}$ and $x_{M3} \in [0, a_{M3}]$, as illustrated in Fig.5.9c.

5.2.2.1 Sensitivity of the optimised solution to the constraint type imposed at the macroscale

Numerical tests are performed on BK1-3D and BK2-3D, with the objective of investigating the influence of the constraint nature (i.e., macroscopic volume or mass) on the final topology at both scales. The CNLPP of Eq. (5.27), for which g_1 or g_2 and g_3 are included in the problem formulation, is solved by considering at the RVE scale a NURBS hyper-surface characterised by $n_{mCP} = 11 \times 11 \times 11$ and $p_{mi} = 3$, ($i = 1, 2, 3$), for which a minimum member size within the domain and along its boundary are $d_{m,min} = 0.13$ mm and $d_{m,min}^B = 0.12$ mm, respectively.

At the macroscopic scale two configurations of NURBS parameters are taken into account: in BK1-3D the NURBS parameters are set as: $n_{MCP} = 27 \times 15 \times 10$ and $p_{Mi} = 3$, ($i = 1, 2, 3$), while in BK2-3D they are set as $n_{MCP} = 15 \times 12 \times 15$ and $p_{Mi} = 3$, ($i = 1, 2, 3$). Both these configurations ensure a minimum member size within the domain equal to $d_{M,min} = 25$ mm, hence a minimum of 10 RVEs within the thinnest topological branch of the

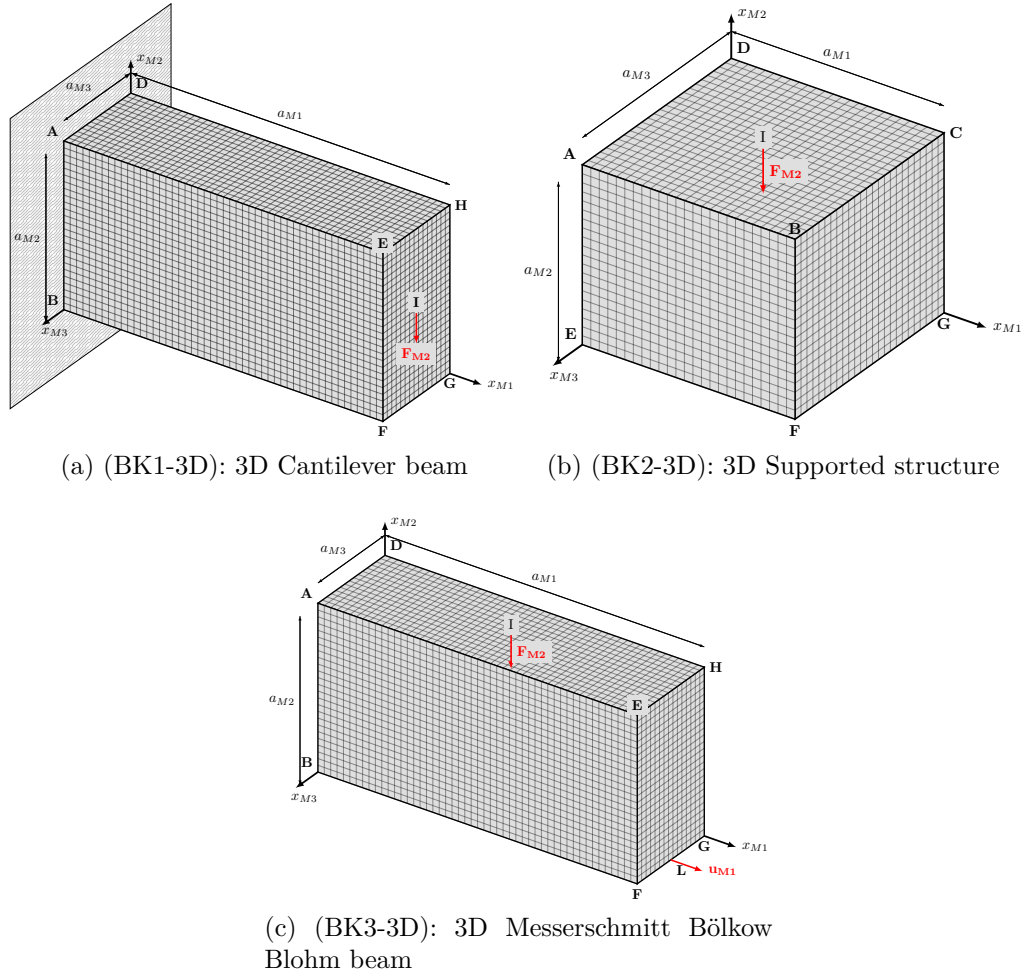


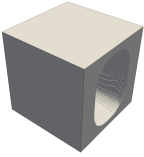
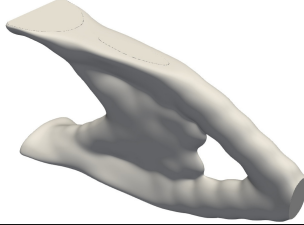
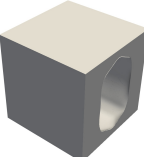
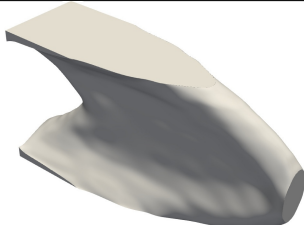
Figure 5.9 – Finite element model, geometrical parameters and applied boundary conditions of benchmark problems (a) BK1-3D, (b) BK2-3D and (c) BK3-3D.

macroscopic structure is ensured, while the minimum member size at the boundary of the design domain is $d_{M,\min}^B = 5.8$ mm.

For each analysis, the starting guess at the lower scale is characterised by a central hole, while at the upper scale the initial topology is obtained by considering an uniform pseudo-density field. Of course, the initial topologies satisfy the constraints on the RVE volume fraction and on the macroscopic mass/volume fraction.

The optimised solutions for BK1-3D and BK2-3D are reported in Tabs. 5.17 and 5.18, respectively, by considering the macroscopic volume con-

Table 5.17 – BK1-3D: optimised topologies at both scales for different macroscopic constraints. Solutions obtained by employing NURBS entities, with $n_{mCP} = 11 \times 11 \times 11$, $n_{MCP} = 27 \times 15 \times 10$ and $p_{\chi i} = 3$, ($i = 1, 2, 3$, $\chi = m, M$).

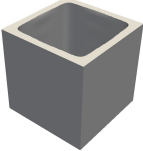
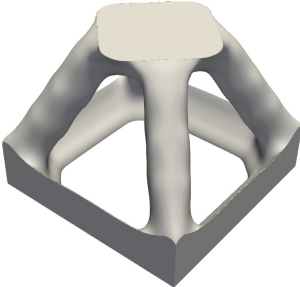
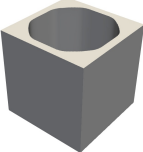
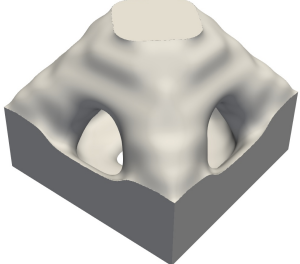
Constraints imposed	RVE optimised topology	Structure optimised topology	Problem number
$\frac{V_M}{V_{Mref}} \leq 0.2$ $\frac{V_m}{V_{mref}} \leq 0.4$ $\hat{d}_{M,\min}(\rho(\xi_M)) \geq 25 \text{ mm}$			40
$\frac{m_M}{m_{Mref}} \leq 0.2$ $\frac{V_m}{V_{mref}} \leq 0.4$ $\hat{d}_{M,\min}(\rho(\xi_M)) \geq 25 \text{ mm}$			41

straint (with volume fraction $\gamma_{MV} = 0.2$) and the macroscopic mass one (with mass fraction $\gamma_{Mm} = 0.2$). The structural performances related to the optimised topologies are reported in Tab. 5.21. The following remarks can be inferred from the analysis of these results.

Firstly, as expected, the optimised topology (at both scales) is different when considering either the constraint on the macroscopic volume fraction g_1 or the one on the macroscopic mass fraction g_2 . In particular, the solution of the CNLPP of Eq. (5.27) when integrating a constraint on the macroscopic mass fraction is characterised by a value of the objective function lower than the one characterising the solution obtained by considering constraint g_1 . This is because a macroscopic mass fraction $\gamma_{Mm} = 0.2$ corresponds to a value of the macroscopic volume fraction higher than $\gamma_{MV} = 0.2$, thus the optimised topology in this case is stiffer than the solution obtained by considering constraint g_1 . Therefore, the designer should pay attention to the problem formulation because the constraint on the macroscopic mass fraction g_2 influences the topology at both scales (unlike the constraint on the macroscopic volume fraction g_1).

Secondly, regardless of the problem formulation, the minimum length scale requirement is systematically fulfilled at both scales (for both test

Table 5.18 – BK2-3D: optimised topologies at both scales for different macroscopic constraints. Solutions obtained by employing NURBS entities, with $n_{mCP} = 11 \times 11 \times 11$, $n_{MCP} = 15 \times 12 \times 15$ and $p_{\chi_i} = 3$, ($i = 1, 2, 3$, $\chi = m, M$)

Constraints imposed	RVE optimised topology	Structure optimised topology	Problem number
$\frac{V_M}{V_{Mref}} \leq 0.2$ $\frac{V_m}{V_{mref}} \leq 0.4$ $\hat{d}_{M,\min}(\rho(\xi_M)) \geq 25 \text{ mm}$			42
$\frac{m_M}{m_{Mref}} \leq 0.2$ $\frac{V_m}{V_{mref}} \leq 0.4$ $\hat{d}_{M,\min}(\rho(\xi_M)) \geq 25 \text{ mm}$			43

cases BK1-3D and BK2-3D). In particular, when constraint g_2 is included in the CNLPP formulation, the optimised topology at the macroscopic scale is characterised by a more compact distribution of the material.

5.2.2.2 Sensitivity of the optimised solution to the scale separation requirement

The effect of the implicit scale separation constraint on the optimised topologies at both scales is analysed on BK1-3D and BK2-3D. In particular, two configurations of the macroscopic NURBS hyper-surface parameters are considered, for both benchmarks, while the same set of integer parameters is used for the topology at the RVE scale, i.e., $n_{mCP} = 11 \times 11 \times 11$ and $p_{m_i} = 3$, ($i = 1, 2, 3$), to ensure a minimum member size within the domain and along its boundary equal to $d_{m,\min} = 0.13 \text{ mm}$ and $d_{m,\min}^B = 0.12 \text{ mm}$, respectively. Therefore, for each benchmark structure, two cases are considered.

In the first case the scale separation requirement is disregarded and the NURBS integer parameters are chosen as follows: $n_{MCP} = 35 \times 25 \times 15$ and $p_{Mi} = 3$, ($i = 1, 2, 3$) for BK1-3D, $n_{MCP} = 23 \times 17 \times 23$ and $p_{Mi} = 3$, ($i = 1, 2, 3$) for BK2-3D.

In the second one, the scale separation requirement at the macroscopic scale is taken into account and the NURBS parameters are set as follows: $n_{MCP} = 27 \times 15 \times 10$ and $p_{Mi} = 3$, ($i = 1, 2, 3$) for BK1-3D; while $n_{MCP} = 15 \times 12 \times 15$ and $p_{Mi} = 3$, ($i = 1, 2, 3$) for BK2-3D. This configuration is characterised by a minimum member size inside the design domain equal to $d_{M,\min} = 25$ mm, which guarantees a minimum number of 10 RVEs along each axes within the thinnest topological branch. Moreover, the minimum member size at the boundary of the domain is $d_{M,\min}^B = 5.8$ mm.

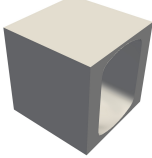
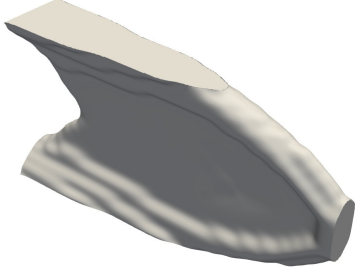
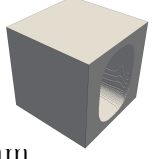
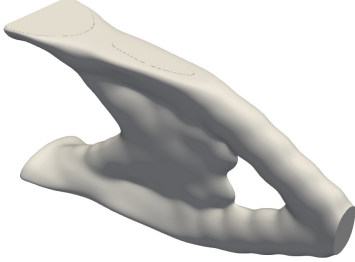
The RVE volume fraction and the macroscopic volume fraction are set to $\gamma_{mV} = 0.6$ and $\gamma_{MV} = 0.2$, respectively. Also in this case, the starting guess at the RVE scale is characterised by a central hole, while at the upper scale the initial topology is obtained by considering an uniform pseudo-density field; the initial topologies are set such that the constraints on the RVE volume fraction and on the macroscopic volume fraction are met.

As shown in Tabs. 5.19 and 5.20, the implicit constraint on the minimum member size of the macroscopic topology has an impact on the optimised topologies at both scales (the structural performances related to the optimised topologies are reported in Tab. 5.24). In terms of objective function value, for BK1-3D the optimised solution obtained without considering the scale separation requirement outperforms the optimised solution satisfying this constraint (see Tab. 5.24), the difference between the compliance of the two configurations being 7%. Conversely, for BK2-3D an unexpected result is found: the optimised topology obtained by considering the scale separation requirement outperforms the one wherein it is disregarded (the relative difference between the compliance of the two solutions is equal to 28%). This result is mainly due to the optimised topology at the RVE scale which is strongly different between the two optimised solutions reported in Tab. 5.20.

5.2.2.3 Sensitivity of the optimised topology to mixed non-zero boundary conditions

The influence of the mixed non-zero Neumann-Dirichlet BCs on the topologies at both scales is analysed on BK3-3D. In all the analyses, the topological variable at the RVE scale is characterised by the following NURBS parameters $n_{mCP} = 11 \times 11 \times 11$ and $p_{mi} = 3$, ($i = 1, 2, 3$); while the parameters characterising the topological variable at the macroscopic

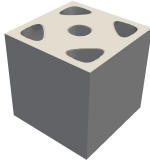
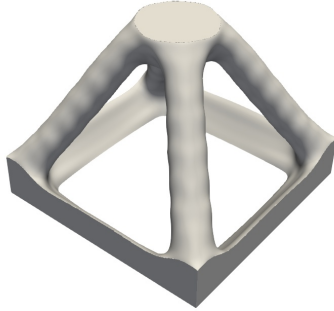
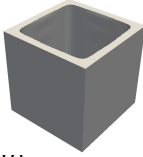
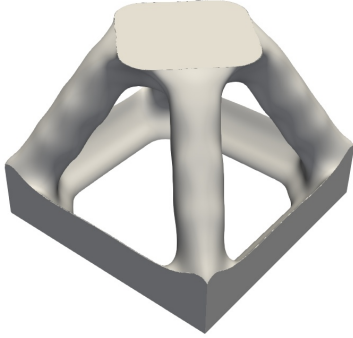
Table 5.19 – BK1-3D: influence of the scales separation requirement on the optimised topology (at both scales). Solutions obtained by employing NURBS entities, with $n_{mCP} = 11 \times 11 \times 11$, $n_{MCP} = 35 \times 25 \times 15$ (first case) or $n_{MCP} = 27 \times 15 \times 10$ (second case) and $p_{\chi i} = 3$, ($i = 1, 2, 3$, $\chi = m, M$)

Constraints imposed	RVE optimised topology	Structure optimised topology	Problem number
$\frac{V_M}{V_{Mref}} \leq 0.2,$ $\frac{V_m}{V_{mref}} \leq 0.4$			44
$\frac{V_M}{V_{Mref}} \leq 0.2,$ $\frac{V_m}{V_{mref}} \leq 0.4,$ $\hat{d}_{M,min}(\rho(\xi_M)) \geq 25 \text{ mm}$			45

scale are chosen as follows: $n_{MCP} = 27 \times 15 \times 10$ and $p_{M i} = 3$, ($i = 1, 2, 3$). These configurations ensure a minimum member size within the design domain equal to $d_{m,min} = 0.13$ mm at the RVE scale and $d_{M,min} = 25$ mm at the structure scale. On the other hand, the minimum member size at the boundary of the design domain is $d_{m,min}^B = 0.12$ mm and $d_{M,min}^B = 5.8$ mm at the RVE and structure scales, respectively. The RVE volume fraction and the macroscopic mass fraction are $\gamma_{mV} = 0.6$ and $\gamma_{Mm} = 0.35$, respectively. Moreover, the starting topology at the RVE scale is characterised by a central hole, while at the upper scale it is obtained by considering an uniform pseudo-density field; the initial solutions satisfy the constraints on the RVE volume fraction and on the macroscopic mass fraction. The material properties used in this example are $E_m = 2525$ MPa, $\nu_m = 0.25$ and $\tau_m = 2.8 \times 10^{-6}$ kgmm⁻³.

Three values of displacement u_{M1} are considered: $u_{M1} = \{-1, 0, 1\}$ mm. The optimised solutions are listed in Tab. 5.23 and the related structural performances are reported in Tab. 5.24. As expected, the RVE optimised topology is characterised by an orthotropic behaviour and, similarly to the results of the test case BK3-2Da, the optimised topology at both

Table 5.20 – BK2-3D: influence of the scales separation requirement on the optimised topology (at both scales). Solutions obtained by employing NURBS entities, with $n_{mCP} = 11 \times 11 \times 11$, $n_{MCP} = 23 \times 17 \times 23$ (first case) or $n_{MCP} = 15 \times 12 \times 15$ (second case) and $p_{\chi i} = 3$, ($i = 1, 2, 3$, $\chi = m, M$)

Constraints imposed	RVE optimised topology	Structure optimised topology	Problem number
$\frac{V_M}{V_{Mref}} \leq 0.2,$ $\frac{V_m}{V_{Mref}} \leq 0.4$			46
$\frac{V_M}{V_{Mref}} \leq 0.2,$ $\frac{V_m}{V_{mref}} \leq 0.4,$ $\hat{d}_{M,\min}(\rho(\xi_M)) \geq 25 \text{ mm}$			47

scales change when varying the entity of the applied displacement. This means that the result of the concurrent optimisation of the elastic symmetry of the material (related to the RVE topology) and of the macroscopic topology strongly depends upon the intensity of the applied displacement. Finally, the same remarks provided for benchmark problem BK3-2Da can be repeated here too.

Table 5.21 – Optimisation results related to the problems listed in Tables 5.17 - 5.18 in terms of reference and optimal compliance and geometrical constraints values.

Problem	BK1-3D: macroscopic mass/volume		BK2-3D: macroscopic mass/volume	
	40	41	42	43
N_{iter}	161	157	466	125
$\mathcal{C}_{M\text{ref}}(\text{Nmm})$	54.7654	0.4030	172.71	0.4392
$\mathcal{C}_{M\text{opt}}(\text{Nmm})$	0.1355	0.0332	0.2142	0.1061
$\hat{d}_{m,\text{min}}(\text{mm})$	0.19	0.202	0.2	0.17
$\hat{d}_{M,\text{min}}(\text{mm})$	31.16	45.51	43.14	92.3
$\hat{d}_{m,\text{min}}^B(\text{mm})$	0.2	0.2	0.2	0.17
$\hat{d}_{M,\text{min}}^B(\text{mm})$	20.2	17.5	28.7	70

Table 5.22 – Optimisation results related to the problems listed in Tables 5.19 - 5.20 in terms of reference and optimal compliance and geometrical constraints values.

Problem	BK1-3D: scale separation		BK2-3D: scale separation	
	44	45	46	47
N_{iter}	97	157	70	466
$\mathcal{C}_{M\text{ref}}(\text{Nmm})$	0.4030	0.4030	172.71	172.71
$\mathcal{C}_{M\text{opt}}(\text{Nmm})$	0.0310	0.0332	0.2746	0.2142
$\hat{d}_{m,\text{min}}(\text{mm})$	0.07	0.19	0.232	0.2
$\hat{d}_{M,\text{min}}(\text{mm})$	23.8	20.2	34.6	43.14
$\hat{d}_{m,\text{min}}^B(\text{mm})$	0.07	0.2	0.232	0.2
$\hat{d}_{M,\text{min}}^B(\text{mm})$	29	31.16	26.5	28.7

Table 5.23 – BK3-3D: optimised topologies at both scales under mixed non-zero BCs. Solutions obtained by employing NURBS hyper-surfaces, with $n_{mCP} = 11 \times 11 \times 11$, $n_{MCP} = 27 \times 15 \times 10$ and $p_{\chi i} = 3$, ($i = 1, 2, 3$, $\chi = m, M$)

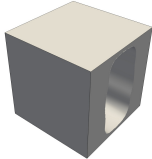
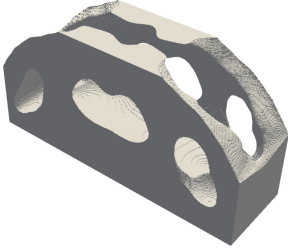
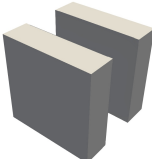
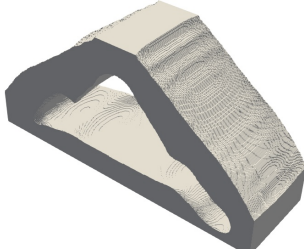
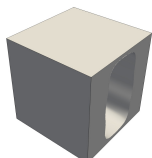
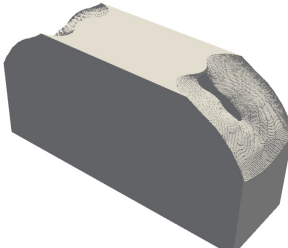
BCs	RVE optimised topology	Structure optimised topology	Problem number
$F_{M2} = -10 \text{ N}$, $u_{M1} = -1 \text{ mm}$			48
$\mathbf{C}_M = \begin{bmatrix} 43146.6 & 12692 & 3858 & 0 & 0 & 0 \\ 12692 & 39596 & 2710.7 & 0 & 0 & 0 \\ 3858 & 2710.7 & 10152.9 & 0 & 0 & 0 \\ 0 & 0 & 0 & 13178 & 0 & 0 \\ 0 & 0 & 0 & 0 & 733 & 0 \\ 0 & 0 & 0 & 0 & 0 & 3777.3 \end{bmatrix}$ MPa			
$F_{M2} = -10 \text{ N}$, $u_{M1} = 0$			49
$\mathbf{C}_M = \begin{bmatrix} 39180.9 & 11754.2 & 0.00025 & 0 & 0 & 0 \\ 11754.2 & 39180.9 & 0.00024 & 0 & 0 & 0 \\ 0.00025 & 0.00024 & 0.00057 & 0 & 0 & 0 \\ 0 & 0 & 0 & 13713.33 & 0 & 0 \\ 0 & 0 & 0 & 0 & 0.00016 & 0 \\ 0 & 0 & 0 & 0 & 0 & 0.00016 \end{bmatrix}$ MPa			
$F_{M2} = -10 \text{ N}$, $u_{M1} = 1 \text{ mm}$			50
$\mathbf{C}_M = \begin{bmatrix} 1473.90 & 358.74 & 105.1 & 0 & 0 & 0 \\ 105.1 & 1360.13 & 74.88 & 0 & 0 & 0 \\ 105.1 & 74.88 & 345.5 & 0 & 0 & 0 \\ 0 & 0 & 0 & 507.87 & 0 & 0 \\ 0 & 0 & 0 & 0 & 24.79 & 0 \\ 0 & 0 & 0 & 0 & 0 & 138.65 \end{bmatrix}$ MPa			

Table 5.24 – Optimisation results related to the problems listed in Table 5.23 in terms of reference and optimal optimal compliance and geometrical constraints values.

Problem	BK3-3D: mixed non-zero BCs		
	48	49	50
N_{iter}	97	93	98
$\mathcal{C}_{M\text{ref}}(\text{Nmm})$	-2951.98	0.0166	-2938.80.71
$\mathcal{C}_{M\text{opt}}(\text{Nmm})$	-12589.30	0.0044	-12581.59
$\hat{d}_{m,\text{min}}(\text{mm})$	0.13	0.71	0.67
$\hat{d}_{M,\text{min}}(\text{mm})$	46.6	55.2	66
$\hat{d}_{m,\text{min}}^B(\text{mm})$	0.13	0.71	0.1
$\hat{d}_{M,\text{min}}^B(\text{mm})$	20	14	11

5.3 Conclusions and prospects

In this Chapter, an approach for the concurrent optimisation of the material properties and the structure topology of ACMs has been presented. More precisely, the problem of designing ACMs is formulated as a two-scale TO problem. In this context, two topological variables have been introduced: the first one is defined at the RVE scale of the ACM (which can be the microscopic scale or the mesoscopic one, depending on the problem characteristic lengths), while the second one is defined at the macroscopic scale. A weak coupling among lower and upper scales has been considered in the problem formulation. In fact, the structural responses at the upper scale depend both on the topological descriptor defined at this scale and to the one introduced at the lower scale through the calculation of the equivalent elasticity matrix of the fictitious homogeneous material, which replaces the RVE at the upper scale. In this context, the topological variable at each scale is represented by the pseudo-density field of the SIMP method, which is described by means of a NURBS hyper-surface and the scale transition is correctly set through the SEHM based on elements strain energy. NURBS entities are efficiently exploited to derive the relationship among topological variables defined at different scales and also to determine the analytical expression of the gradient of the physical responses involved at all scales.

Some features of the proposed methodology need to be highlighted. Firstly, some advantages of the NURBS formalism can be clearly identified: (a) since the topological descriptor consists in a high-level geometric parametrisation of the pseudo-density field in the form of a NURBS en-

tity, the optimised topology does not depend upon the quality of the mesh of the finite element model, unlike the classical SIMP method; (b) unlike the classical SIMP approach, there is no need to define a further filter zone, since the NURBS local support property establishes an implicit relationship among contiguous mesh elements; (c) when compared to the classical SIMP approach, the number of design variables is reduced; (d) since the topology is described through a NURBS entity, the boundary of the topology is available at each iteration of the optimisation process, thus, the integration of constraints of geometric nature (e.g., on the local curvature of the boundary, on the local direction of the tangent vector, maximum member size, etc.) in the problem formulation and the CAD reconstruction phase of the boundary of the optimised topology become easy tasks. Of course, as in the case of the results of single-scale problems found through the NURBS-based SIMP method [108, 110], the optimised topology depends upon the NURBS integer parameters, i.e., number of control points and degrees of Bernstein's polynomials, which have a direct impact on the size of the local support of the blending functions.

Secondly, it has been shown that, depending on the problem formulation, the values of the macroscopic volume/mass fraction and of the RVE volume fraction, as expected, have a strong influence at each scale, thus a particular care must be put in the choice of the combination of such constraints to avoid "weird" topologies.

Thirdly, the influence of the RVE elastic symmetry group on the final topology, at both scales, has been considered. Results highlight that, depending on the problem at hand, forcing a pre-defined elastic symmetry (e.g., orthotropy, transverse isotropy, etc.) could not reveal a good choice because completely anisotropic solutions characterised by equivalent or better performances could exist. In analogy with the multi-scale optimisation of composite materials and structures, this is due to the non-convexity of the optimisation problem and to the existence of equivalent local minima characterised by very different properties. Fourthly, the influence of the initial guess on the optimised topologies at both scales has been taken into account. As expected, the obtained results represent a confirmation of a well-established result: under the same working hypotheses and BCs, multi-scale TO problems of ACMs are non-convex; therefore, the choice of the starting guess at the RVE scale is of paramount importance and has a strong influence on the RVE optimised topology.

Furthermore, the influence of mixed non-zero Neumann-Dirichlet BCs on the optimised solution has been investigated. The obtained results highlight that, to satisfy the requirements of the problem at hand and to withstand the applied loads, both the RVE topology and the macroscopic one evolve

towards a configuration optimising the macroscopic elastic response of the continuum, as well as the material distribution at the upper scale.

Finally, the effect of the minimum-length scale requirement at each problem scale on the optimised solutions is correctly taken into account, without the need of introducing an explicit optimisation constraint. Indeed, this requirement can be easily fulfilled by properly setting the integer parameters of the NURBS entity representing the topological variable at each scale. In particular, the technological constraint on the minimum manufacturable dimension is handled by controlling the value of the NURBS blending functions degrees and number of CPs at the lower scale, whilst the scale separation requirement is ensured by controlling the same quantities related to the NURBS entity representing the topological variable at the upper scale.

Regarding the prospects on this topic, several challenges still need to be faced. Firstly, a set of pertinent technological requirements, related to the additive manufacturing process, should be integrated into the multi-scale TO problem formulation, especially in terms of the RVE geometrical features, e.g., overhang angle, admissible curvature, etc. Secondly, in order to design ACMs against failure, a suitable homogenisation procedure with strong coupling between scales should be developed and integrated in the optimisation process. Lastly, suitable failure criteria at upper and lower scales should be derived and integrated in the multi-scale TO problem formulation for the homogeneous anisotropic material at the macroscopic scale and for the bulk material at the RVE scale.

Chapter 6

Experimental validation of the multi-scale topology optimisation method

In this Chapter, the well-known three point bending test (3PBT) benchmark problem is used to validate, experimentally, the performances of the optimised topologies resulting from both single-scale and multi-scale topology optimisation strategies relying on the NURBS-based SIMP method. As discussed in Chapters 4 and 5, the multi-scale TO makes use of: a) the NURBS entity to represent the topological descriptor at both the RVE (lower) scale and the macroscopic (upper) scale; b) the SEHM to set the link between the scales of the problem (only weak coupling among scales is considered). The results of the numerical analyses are compared with the experimental ones obtained by means of the 3PBT performed on the specimens of the optimised topologies manufactured via stereo lithography (SLA) made of rigid resin 4000, i.e., a resin with properties similar to the ones of the polyetheretherketone (PEEK).

The Chapter is organised as follows. The problem description and the general workflow, including numerical and experimental analyses, are introduced in Sec. 6.1. Sec. 6.2 presents the experimental setup used to characterise the properties of the resin composing the optimised specimens, whilst Sec. 6.3 discusses the three problem formulations considered in this work, i.e., TO at the macroscopic scale, TO at the RVE scale and TO at both scales. Sec. 6.4 illustrates the numerical results, for each problem formulation, in both 2D and 3D cases. In Sec. 6.5, the experimental validation of the optimised topologies through 3PBT is presented (with the discussion of the related experimental setup) together with the non-linear numerical analyses conducted a-posteriori on the optimised topologies to validate the

structural behaviour. Finally, Sec. 6.6 ends the Chapter with meaningful conclusions and prospects.

6.1 Problem description

The main goal of this work consists of determining the optimised topology of a structure subject to 3PBT-like loading conditions with the aim of maximising its flexural stiffness subject to design requirements on lightness and manufacturability. Specifically, three design cases (DCs) are considered. In the first case (DC1), the topological variables are defined solely at the macroscopic scale. In the second case (DC2), the topological descriptor is introduced only at the RVE scale and the loading conditions are imposed at the macroscopic scale. In the third case (DC3), the topological variables and the design requirements are defined at both lower and upper scales. Of course, in the last two design cases, since the RVE topology is the same at all points of the upper scale domain, the properties of the homogenised material are uniform at the structure-level.

It is noteworthy that in the design case DC3, which is the most general one, unlike the approaches presented in [75, 88–91], where the goal is to obtain an optimised topology at the macroscopic scale, by using a pattern of a pre-defined RVE geometry at the lower scale showing a given macroscopic elastic behaviour, in this study, all the problem characteristic scales (i.e., the lower scale and the upper one) are involved in the problem formulation by considering a weak coupling among scales, as discussed in Chapter 5. The work-flow of the approach presented in this Chapter is illustrated in Fig. 6.1. Particularly, the design strategy is articulated in the following steps:

1. The characterisation of the constitutive law of the material (i.e., the resin) composing the specimens is performed in tension and through 3PBT. From these data, the flexural Young's modulus is calculated and used (together with the Poisson's coefficient) to assess the elasticity tensor of the linear elastic material used in the TO calculations (step 2). Furthermore, the non-linear stress vs. strain curves will be used in the non-linear static analysis (step 5) conducted a-posteriori on each optimised topology.
2. The TO process in the NURBS-based SIMP framework is conducted for the three design cases discussed above: a) topological descriptor defined only at the upper scale (DC1); b) topological descriptor introduced only at the RVE scale (DC2); c) topological variables introduced at both lower and upper scales (DC3).

3. The boundary of the optimised topology is recovered at the end of the TO process by exploiting the properties of NURBS entities, as explained in [128, 129]. Unlike classical density-based TO methods, wherein the pseudo-density field is defined element-wise, the NURBS-based SIMP method makes use of a pure geometric entity to describe the pseudo-density field at each scale, thus the reconstruction of the boundary of the optimised topology becomes an easy task.
4. The optimised topologies are then converted in suitable STL files. After standard post-processing, they are manufactured through SLA process. Mass evaluation and some geometric measurements are performed to check the conformity of the specimens.
5. 3PBTs are conducted by following the procedure detailed in the ASTM norm [130]. The force vs. displacement curve is extracted as a main output of the experimental tests.
6. The boundary of the optimised topology (for each design case) is exported in the ANSYS Workbench[®] environment and a non-linear static analysis reproducing the boundary conditions (BCs) of the experimental test is performed, by considering the non-linear behaviour of the bulk material obtained at step 1. The goal is to obtain numerically the force vs. displacement curve.
7. A comparison between experimental and numerical results is performed to assess the accuracy and effectiveness of the proposed approach.

6.2 Characterisation of the bulk material properties

In order to assess the behaviour of the rigid Resin 4000 [131], i.e., the bulk material composing the specimens, traction and flexural tests have been carried out on standard samples according to ASTM norms [130, 132, 133]. The density of this resin is $\rho = 0.0014 \text{ kgm}^{-3}$ and the Poisson's coefficient is $\nu = 0.3$.

6.2.1 Tensile behaviour of rigid resin 4000

According to ASTM D638 norm [133], the tensile Young's modulus and the yield stress (tension) are measured via quasi-static tests performed at a speed equal to 1 mm/min on an INSTRON 5969 machine with a Load Cell of 50 kN.

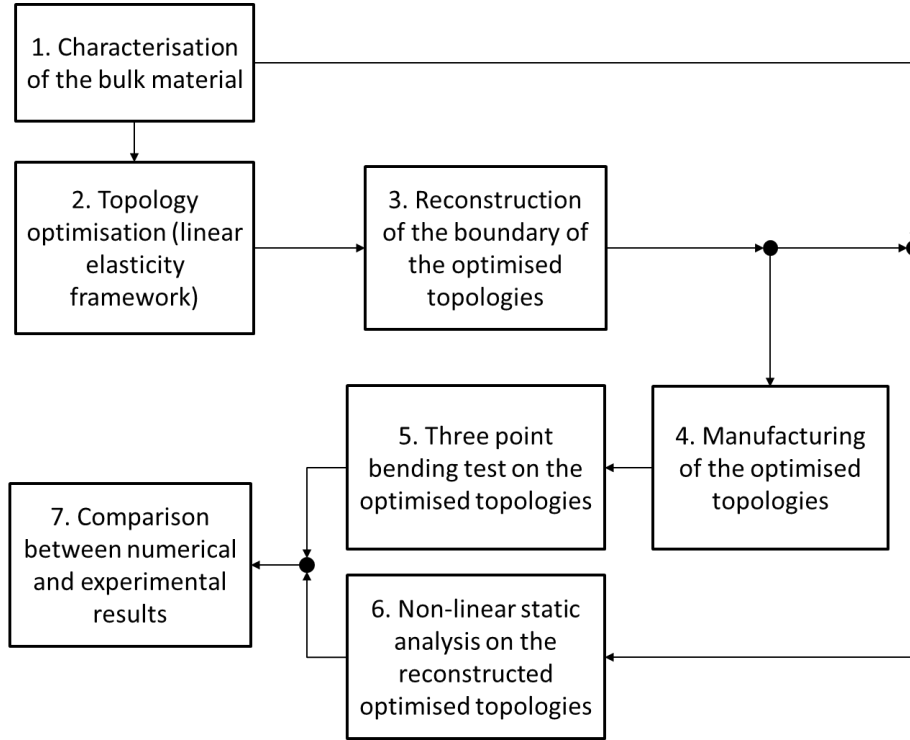


Figure 6.1 – Workflow of the design methodology for specimens subject to 3PBT-like loading conditions

One type of dog-bone sample is conceived, as shown in Fig. 6.2, and three specimens are fabricated via SLA technology. By referring to Fig. 6.2, the nominal dimensions are: $LO = 165$ mm, $WO = 19$ mm, $L = 57$ mm, $W = 13$ mm, while the actual value of W and T , measured after manufacturing the specimens, are listed in Tab. 6.1.

Table 6.1 – Actual values of W and T of the dog-bone samples.

Sample N.	W_{real} [mm]	T_{real} [mm]
1	13.06	3.28
2	13.05	3.3
3	13.01	3.29

The load profile chosen to assess yield stress and Young’s modulus is a ramp increasing from 0 mm to 5 mm during a time interval equal to $\Delta t = 350$ s. The tensile Young’s modulus is extrapolated from the initial region of the σ - ε curves obtained from the test.

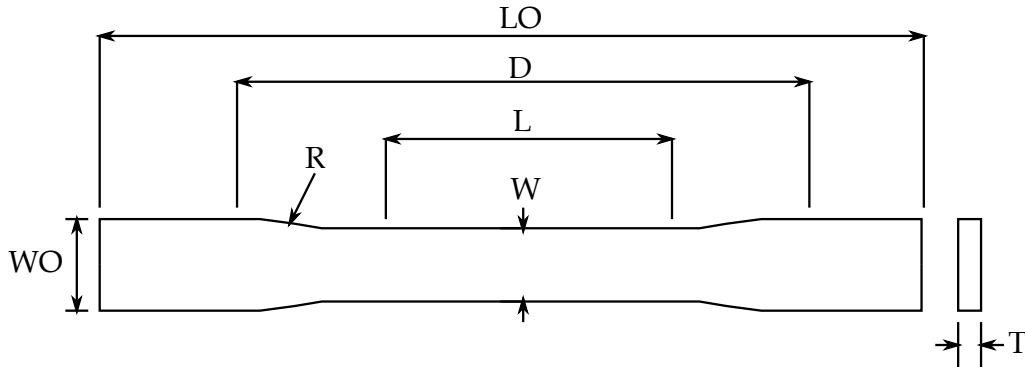


Figure 6.2 – Schematic representation of the tensile dog-bone-like specimens with the related geometric parameters.

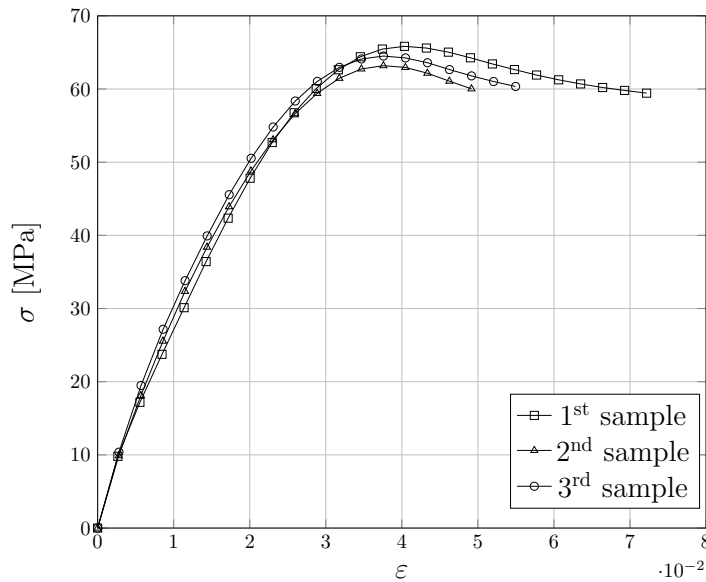


Figure 6.3 – σ - ϵ curves obtained from the tensile tests.

The curves resulting from the tensile tests are shown in Fig. 6.3 and the extrapolated results, in terms of tensile Young's modulus E_t and tensile yield stress σ_{yt} , are listed in Tab. 6.2. The resulting σ - ϵ curve used to describe the tensile behaviour of rigid resin 4000 is shown in Fig. 6.4; according to the results shown in Tab. 6.2, the tensile Young's modulus is $E_t = 3601.81$ MPa, whilst the tensile yield stress is $\sigma_{yt} = 15.80$ MPa.

Table 6.2 – Tensile yield stress σ_{yt} and tensile Young’s modulus E_t values extrapolated from the results in Fig. 6.3.

Sample N.	σ_{yt} [MPa]	E_t [MPa]
1	15.60	3536.02
2	15.74	3592.54
3	18.51	3721.93

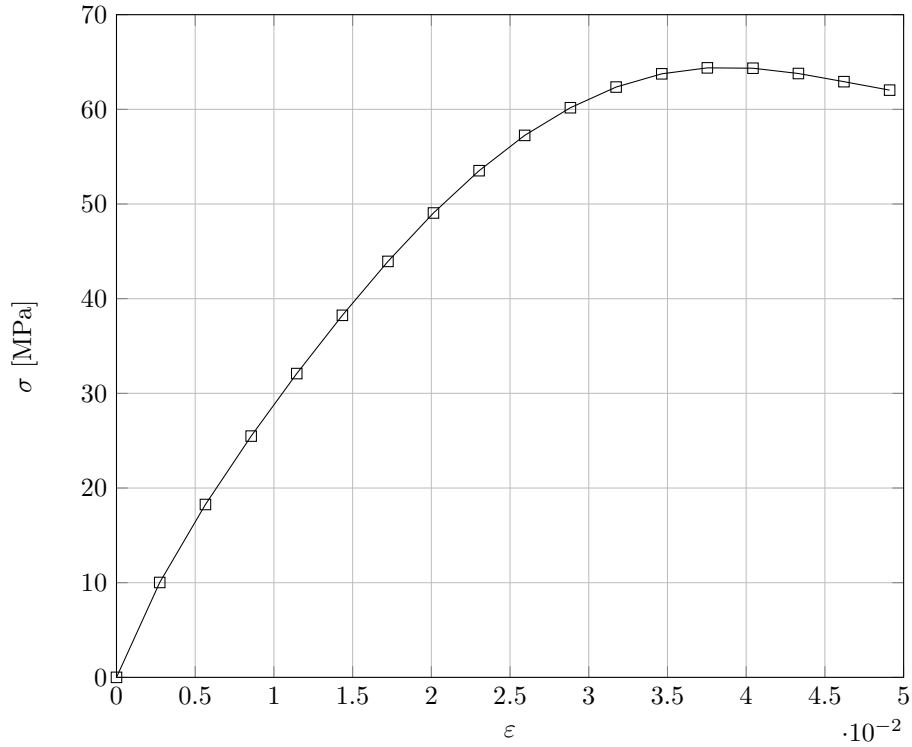


Figure 6.4 – σ - ϵ curve of the average tensile material behaviour.

6.2.2 Flexural behaviour of rigid resin 4000

To assess the flexural behaviour of the rigid resin 4000, the ASTM D790-03 norm [130] is followed. The flexural modulus has been extrapolated as a result of a 3PBT conducted via the Adamel Lhomargy DY 36 Load Cell of 100 kN by controlling the displacement with a speed equal to 1 mm/min. The schematic representation of the experimental apparatus (with the related geometric parameters) is shown in Fig. 6.5.

Three samples are used during the 3PBT. They are manufactured in the form of a parallelepiped having the following nominal dimension $96 \times$

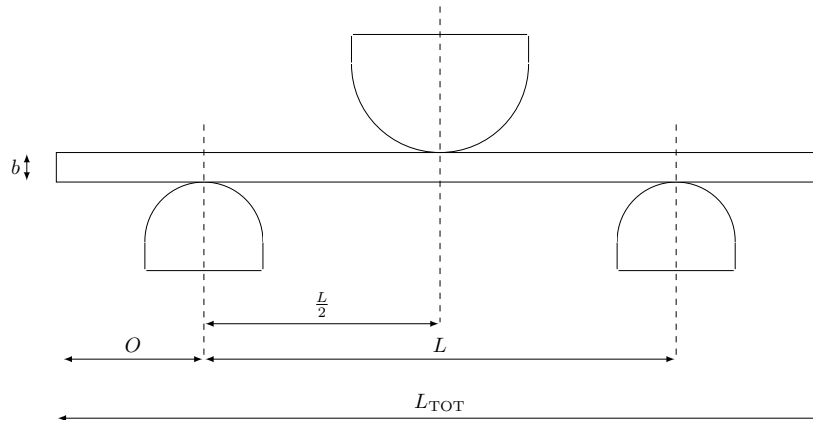


Figure 6.5 – Schematic representation of the 3PBT apparatus with the related geometric parameters

$20 \times 5 \text{ mm}^3$. The actual size of the specimens are listed in Tab. 6.3.

Table 6.3 – Actual dimensions of the samples used for 3PBT.

Sample N.	L_{TOT} [mm]	b [mm]	d [mm]
1	96.04	20.12	5.08
2	96.02	20.21	5.09
3	96.01	20.06	5.08

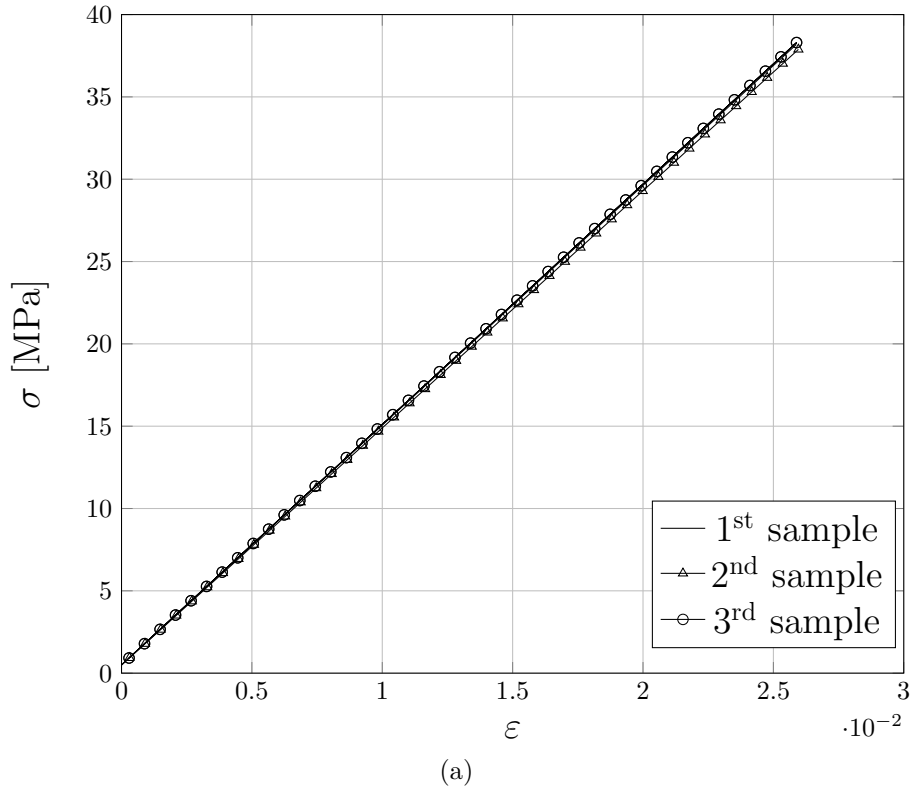
The imposed displacement varies as a ramp in the range $[0, 5.5]$ mm during a time interval equal to $\Delta t = 400$ s.

The flexural modulus E_B is extrapolated from the linear part of the σ - ε curves obtained from the test, as illustrated in Fig. 6.6. Particularly, the tangent modulus is calculated by drawing a tangent to the steepest initial straight-line portion of the load-deflection curve as

$$E_B = \frac{L^3 m}{4bd^3}, \quad (6.1)$$

where $L = 80$ mm is the support span, b is the width and d is the depth of the specimen (these geometric parameters are shown in Fig. 6.5 and their value is reported in Tab. 6.3), while m is the slope of the tangent of the load-deflection curve.

Conversely, the chord modulus may be calculated from two points selected on the load deflection curve. The selected points must be chosen according to the material specification or by customer contract. The points

Figure 6.6 – σ - ε curves obtained from 3PBT.

used for the determination of the chord modulus are reported in Tab. 6.4. The chord modulus has been calculated using the following equation:

$$E_f = \frac{\sigma_{f2} - \sigma_{f1}}{\varepsilon_{f2} - \varepsilon_{f1}}. \quad (6.2)$$

Table 6.4 – Results of the 3PBT.

Sample N.	m	σ_{f2} [MPa]	σ_{f1} [MPa]	ε_{f2}	ε_{f1}	E_B [MPa]	E_f [MPa]
1	27.20	0.49	0.45	$9.52e^{-06}$	$-4.28e^{-05}$	1323.48	1386.50
2	27.27	0.51	0.47	$1.90e^{-05}$	$-9.54e^{-06}$	1309.84	1600.91
3	27.27	0.50	0.46	$4.75e^{-06}$	$-2.85e^{-05}$	1327.44	1390.65

The resulting $\sigma - \varepsilon$ curve used to describe the flexural behaviour of rigid resin 4000 is shown in Fig. 6.7. According to the results shown in Tab. 6.4, the modulus of elasticity in bending is $E_B = 1320.20$ MPa.

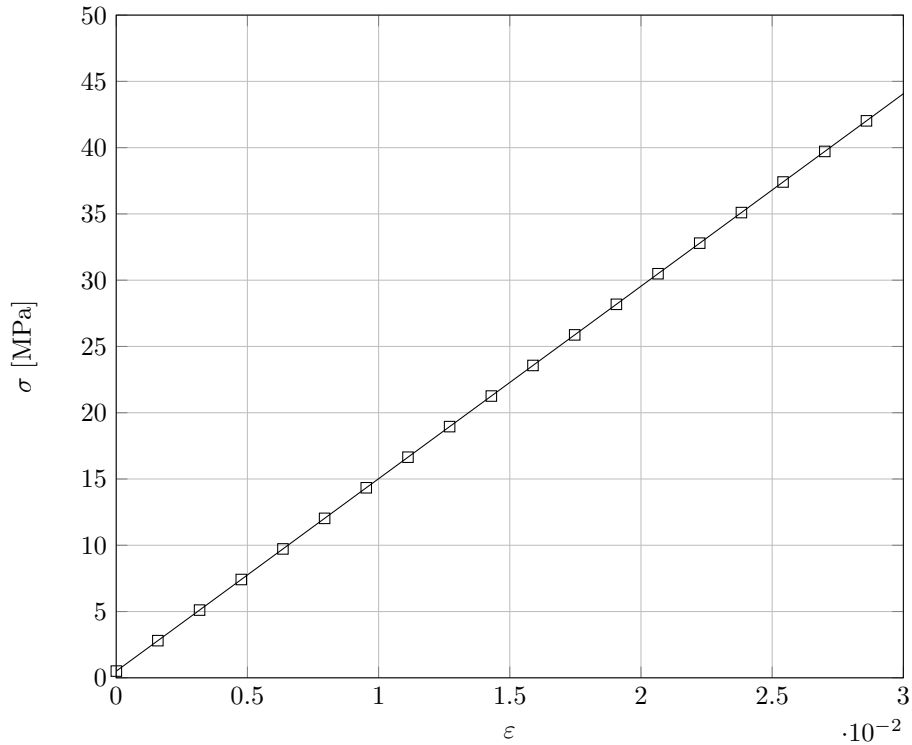


Figure 6.7 – σ - ϵ curve of the average flexural material behaviour.

6.3 Topology optimisation of 3PB-like specimen in the NURBS-based SIMP framework

As stated in Sec. 6.1, the goal of this study is to determine the optimal topology of the continuum (at each characteristic scale of the problem at hand), which minimises the generalised compliance of Eq. (5.9) by meeting the following DRs:

1. A constraint on the mass fraction imposed on the topological descriptor defined at the upper scale.
2. A constraint on the volume fraction imposed on the topological descriptor defined at the lower scale (this constraint is introduced only for design case DC3).
3. A constraint on the minimum thickness that can be fabricated through the SLA process. This constraint is formulated as a minimum member size constraint at the structure scale or at the RVE scale, depending

on the problem formulation.

4. When the topological descriptor is defined at both lower and upper scales (design case DC3), a constraint on the scale separation condition is introduced to ensure the validity of the results of the homogenisation technique in calculating equivalent elastic properties of the material at the upper scale, according to the strategy introduced in Chapter 5. Since the topology of the RVE and the one of the structure are continuously changing during the optimisation process, introducing this type of constraint is of capital importance to avoid the occurrence of too small topological branches at the upper scale whose size could become of the same order of magnitude of the RVE characteristic length (in such circumstances the results of the homogenisation technique are not correct). Specifically, the smallest thickness of the topological branches occurring at the upper scale must be greater than or equal to a multiple of the characteristic length of the design domain at the lower scale.

6.3.1 Design variables

Consider the subset $\mathcal{D}_\chi \subset \mathbb{R}^3$, defining the design domain at the generic χ -th scale ($\chi = m, M$), in a Cartesian orthogonal frame $O(x_{\chi 1}, x_{\chi 2}, x_{\chi 3})$:

$$\mathcal{D}_\chi := \{\mathbf{x}_\chi^T = (x_{\chi 1}, x_{\chi 2}, x_{\chi 3}) \in \mathbb{R}^3 : x_{\chi j} \in [0, L_{\chi j}], j = 1, 2, 3\}, \chi = m, M. \quad (6.3)$$

where $L_{\chi j}$, is the characteristic length of the domain defined along $x_{\chi j}$ axis, as illustrated in Fig. 5.1. The number and the type of design variables depend, of course, upon the characteristic scales involved in the problem at hand. Particularly, three design cases are considered in this work: a) the topological descriptor is defined only at the macroscopic scale (DC1), hence $\chi = M$; b) the topological descriptor is defined only at the RVE scale (DC2), thus $\chi = m$; c) the topological descriptor is defined at both lower and upper scales (DC3), hence $\chi = m, M$.

In the framework of the NURBS-based SIMP method, the pseudo-density function (at each scale) is represented by a NURBS entity. Specifically, for a problem of dimension D a NURBS entity of dimension $D + 1$ must be introduced: the first D coordinates are needed to describe the design domain, whilst the last coordinate represents the pseudo-density field (i.e., the topological descriptor) that reads:

$$\rho_\chi(\zeta_{\chi 1}, \zeta_{\chi 2}, \zeta_{\chi 3}) = \sum_{i_{\chi 1}=0}^{n_{\chi 1}} \sum_{i_{\chi 2}=0}^{n_{\chi 2}} \sum_{i_{\chi 3}=0}^{n_{\chi 3}} R_{i_{\chi 1} i_{\chi 2} i_{\chi 3}}(\zeta_{\chi 1}, \zeta_{\chi 2}, \zeta_{\chi 3}) \rho_{\chi i_{\chi 1} i_{\chi 2} i_{\chi 3}}, \quad \chi = m, M, \quad (6.4)$$

where $\rho_{\chi i_{\chi 1} i_{\chi 2} i_{\chi 3}}$ corresponds to the pseudo-density value at the generic CP, while $R_{i_{\chi 1} i_{\chi 2} i_{\chi 3}}$ are the rational basis functions of Eq. (3.2).

The dimensionless parameters $\zeta_{\chi j}$ are obtained as follows:

$$\zeta_{\chi j} = \frac{x_{\chi j}}{L_{\chi j}}, \quad j = 1, 2, 3. \quad (6.5)$$

Among the parameters governing the shape of the NURBS entity, only the pseudo-density at CPs and the associated weights, are included in the design variable vectors $\boldsymbol{\xi}_{\chi 1}$ and $\boldsymbol{\xi}_{\chi 2}$ defined as:

$$\boldsymbol{\xi}_{\chi 1}^T := (\rho_{000}, \dots, \rho_{n_{\chi 1} n_{\chi 2} n_{\chi 3}}), \quad \boldsymbol{\xi}_{\chi 2}^T := (\omega_{000}, \dots, \omega_{n_{\chi 1} n_{\chi 2} n_{\chi 3}}), \quad \boldsymbol{\xi}_{\chi 1}, \boldsymbol{\xi}_{\chi 2} \in \mathbb{R}^{n_{\chi \text{CP}}}, \quad (6.6)$$

accordingly, the number of design variables for each scale is, at most, $n_{\chi \text{var}} = 2n_{\chi \text{CP}}$, $\chi = m, M$.

The other parameters involved in the definition of the NURBS entity, i.e., degrees, knot-vector components and number of CPs, are set a-priori at the beginning of the TO and are not optimised.

6.3.2 Objective function and optimisation constraints

As discussed in Chapter 5, the penalisation of the global stiffness matrix of the FE model at the lower scale is performed according to Eq. (5.5). Moreover, the elasticity tensor \mathbf{C}_M of the continuum at the macroscopic scale depends upon the pseudo-density function defined at the RVE scale, as indicated in Eqs. (4.6) and (4.7). In fact, the elasticity tensor of the equivalent homogeneous anisotropic material, is involved in the definition of the global stiffness matrix of the FE model at the macroscopic scale $\hat{\mathbf{K}}_M$, hence this matrix depends upon the pseudo-density fields defined at both scales according to Eq. (5.6). Regarding the state equation at the macroscopic scale, since the 3PBT is performed by controlling the imposed

displacement, only inhomogeneous BCs of the Dirichlet's type must be considered in Eq. (5.8), i.e., $\mathbf{u}_{BC} \neq \mathbf{0}$ and $\mathbf{f} = \mathbf{0}$. Accordingly, the generalised compliance at the macroscopic scale reads:

$$\mathcal{C}_M := -\mathbf{r}_M^T \mathbf{u}_{MBC}. \quad (6.7)$$

Therefore, the generalised compliance is a non-positive definite functional in the case of the 3PBT. The design requirements considered in this study are related to the lightness of the structure, and are expressed in terms of constraints on the mass fraction at the upper scale, i.e., γ_{Mm} , and on the volume fraction of the RVE at the lower scale, i.e., γ_{mV} . The formal expressions of the mass at the macroscopic scale and of the RVE volume are given in Eqs. (5.16)-(5.22) and the corresponding design requirements are formulated in Eqs. (5.21)-(5.24). As stated above, two further requirements are included in the problem formulation. The first one deals with the scale separation condition if the topological descriptor is defined at both lower and upper scales (DC3). As discussed in Sec. 5.1.3, this requirement is introduced through a minimum length scale condition on the topological variable at the upper scale according to Eq. (5.25). Specifically, to ensure the validity of the results of the SEHM, the minimum size of the topological branches at the upper scale must be greater than or equal to a multiple of the characteristic size of the RVE at the lower scale. The second requirement is a technological constraint related to the minimum printable size and it is introduced as a minimum member size constraint at the lower scale (DC2 and DC3) or upper scale (DC1), depending on the problem formulation, according to Eq. (5.26). The formal expression of the gradient of both the objective function and the optimisation constraints with respect to the topological variables defined at each scale has already been derived in Secs. 5.1.2 and 5.1.3.

6.3.3 Problem formulation

Here below, the problem formulation is reported for the most general case, wherein the topological descriptors are introduced at both lower and upper scales. According to the formulation introduced in Chapter 5, the multi-scale TO problem is formulated as a CNLPP as follows:

$$\min_{\xi_{\tau 1}, \xi_{\tau 2}} \frac{\mathcal{C}_M}{|\mathcal{C}_{M\text{ref}}|}, \text{ subject to : } \begin{cases} \hat{\mathbf{K}}_{\tau} \hat{\mathbf{u}}_{\tau} = \hat{\mathbf{f}}_{\tau}, \\ g_1(\xi_{M1}, \xi_{M2}, \xi_{m1}, \xi_{m2}) := \frac{m_M}{m_{M\text{ref}}} - \gamma_{Mm} \leq 0, \\ g_2(\xi_{m1}, \xi_{m2}) := \frac{V_m}{V_{\text{RVE}}} - \gamma_{mV} \leq 0, \\ \xi_{\tau 1k_{\tau}} \in [\rho_{\tau\text{min}}, \rho_{\tau\text{max}}], \quad \xi_{\tau 2k_{\tau}} \in [\omega_{\tau\text{min}}, \omega_{\tau\text{max}}], \\ \tau = m, M, \quad \forall k_{\tau} = 1, \dots, n_{\tau\text{CP}}. \end{cases} \quad (6.8)$$

Of course, the number and the type of constraint functions as well as the number of design variables involved in the problem formulation depend upon the design case at hand, as discussed in Sec. 6.3.1. Particularly in Eq. (6.8), the design requirement $g_1 \leq 0$ is always active, whilst $g_2 \leq 0$ is active only when the topological descriptor is introduced at the both macroscopic scale and RVE scale (DC3). Moreover, in Eq. (6.8), $\mathcal{C}_{M\text{ref}}$ is the reference value of the macroscopic compliance, whilst $\rho_{\tau\text{min}}$ and $\rho_{\tau\text{max}}$ are lower and upper bounds on the pseudo-density at each CP, and $\omega_{\tau\text{min}}$ and $\omega_{\tau\text{max}}$ are the bounds on the generic weight (the bounds on the design variables are introduced at each characteristic scale). The overall number of design variables of problem (6.8) depends upon the design case at hand and it is equal to: a) $n_{\text{var}} = 2n_{M\text{CP}}$ for DC1; b) $n_{\text{var}} = 2n_{m\text{CP}}$ for DC2; c) $n_{\text{var}} = 2n_{m\text{CP}} + 2n_{M\text{CP}}$ for DC3.

6.4 Numerical results

The proposed methodology is tested on both 2D and 3D problems: all calculations are carried out by means of the code SANTO (SIMP and NURBS for topology optimisation). The software, coded in python language, is interfaced with the FE code ANSYS[®] to compute the mechanical responses of the structure at each scale. Moreover, the CNLPP of Eq. (6.8) has been solved through the GCMMA algorithm [6], whose parameters are listed in Tab. 6.5.

The design variables bounds are set as follows: $\rho_{\chi\text{min}} = 10^{-3}$, $\rho_{\chi\text{max}} = 1$; $\omega_{\chi\text{min}} = 0.5$, $\omega_{\chi\text{max}} = 10$, $\chi = m, M$. Regarding the other continuous parameters involved in the NURBS entity definition in the 2D and 3D cases, the non-trivial knot vectors components in Eq. (3.7) are evenly distributed in the interval $]0, 1[$.

Table 6.5 – GCMMA algorithm parameters.

Parameter	Value
<i>move</i>	0.1
<i>albefa</i>	0.1
Stop Criterion	Value
Maximum n. of function evaluations	10000
Maximum n. of iterations	$20 \times n_{\text{var}}$
Tolerance on objective function	10^{-6}
Tolerance on constraints	10^{-6}
Tolerance on input variables change	10^{-6}
Tolerance on Karush –Kuhn –Tucker norm	10^{-6}

Furthermore, symmetry constraints are imposed to the pseudo-density field describing the RVE topology: double symmetry for 2D problems (with respect to axes $x_{mj} = a_{mj}$, $j = 1, 2$) and three planes of symmetry ($x_{mj} = a_{mj}$, $j = 1, 2, 3$) for 3D problems, in order to get an optimised topology characterised, at most, by an orthotropic behaviour. The presence of symmetry axes/planes implies a reduction in the design variables count, at the χ -th scale, according to Eq. (5.28).

The main goal of the numerical tests is to investigate the influence of the problem formulation, i.e., DC1, DC2 and DC3, on the flexural stiffness of the optimised solution. For all benchmarks, the rigid resin 4000, whose physical properties are described in Sec. 6.2, is used as bulk material. Of course, all optimisation analyses are conducted under the hypothesis of small displacements and strains and by assuming a linear elastic behaviour of the rigid resin 4000 by using the flexural modulus E_B calculated in Sec. 6.2.2, a Poisson’s coefficient $\nu = 0.3$ and a density $\rho = 0.0014 \text{ kgm}^{-3}$. The reference macroscopic mass of the structure and the reference macroscopic compliance are those characterising the starting solution. Moreover, the reference volume (at the generic scale) is the volume of the overall design domain of dimension D .

6.4.1 2D results

Three different analyses are performed in 2D, corresponding to design cases DC1, DC2 and DC3 introduced in Sec. 6.1. In cases DC2 and DC3, the design domain of the RVE, illustrated in Fig. 6.8, is a square of size $L_m = 2a_{m1} = 2a_{m2} = 4 \text{ mm}$. Three static analyses are performed on the FE model of the RVE to determine the elasticity tensor of the ACM

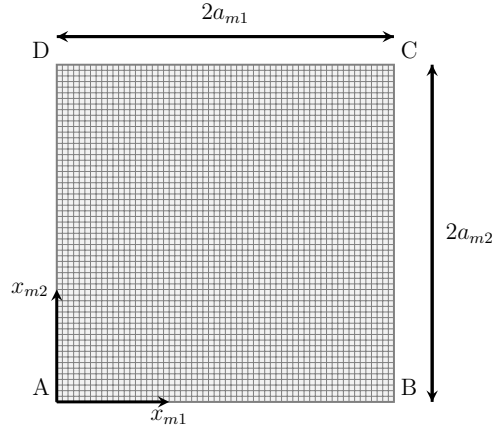


Figure 6.8 – Finite element model of the representative volume element with its characteristic size for 2D problems.

at the macroscopic scale through the SEHM discussed in Sec. 4.1. For each analysis, the periodic BCs of Eq. (4.1) are applied through constraint equations among homologous nodes belonging to the opposite faces of the RVE, by considering elementary unit strains. The FE model of the RVE (which is the same for all 2D benchmark problems) has been coded in the Ansys automatic parametric design language and the mesh is made of $N_{me} = 3600$ PLANE182 elements (four nodes, two DOFs per node, plane stress hypothesis with unit thickness).

For all the analyses the design domain at the macroscopic scale, shown in Fig. 6.9, is of rectangular shape and subject to three-point bending-like BCs. Its geometric parameters are: $a_{M1} = 100$ mm, $a_{M2} = 60$ mm, $L_S = 10$ mm and $L_N = \frac{a_{M1}}{2}$. A static analysis is conducted on the macroscopic FE model whose mesh is made of $N_{Me} = 1500$ PLANE182 elements (four nodes, two DOFs per node, plane stress hypothesis with thickness equal to 30 mm). The displacement component along x_{M2} axis is zero for the node located at $x_{M1} = L_S$, while the node located at $x_{M1} = a_{M1} - L_S$ is clamped. A vertical displacement $d_{M2} = -2$ mm is applied at $(x_{M1}, x_{M2}) = (L_N, a_{M2})$.

As stated above, when the design case DC1 is considered, only the constraint g_1 is integrated in the CNLPP of Eq. (6.8) and the mass fraction is set to $\gamma_{Mm} = 0.4$. The problem is solved by considering a NURBS surface characterised by $n_{MCP} = 50 \times 30$ CPs and blending functions degree $p_{Mi} = 3$, ($i = 1, 2$). As explained in [113], this choice corresponds to a minimum length scale $d_{Mmin} = 5$ mm. For DC1 the initial guess at the macroscopic scale is characterised by a uniform density field whose value is

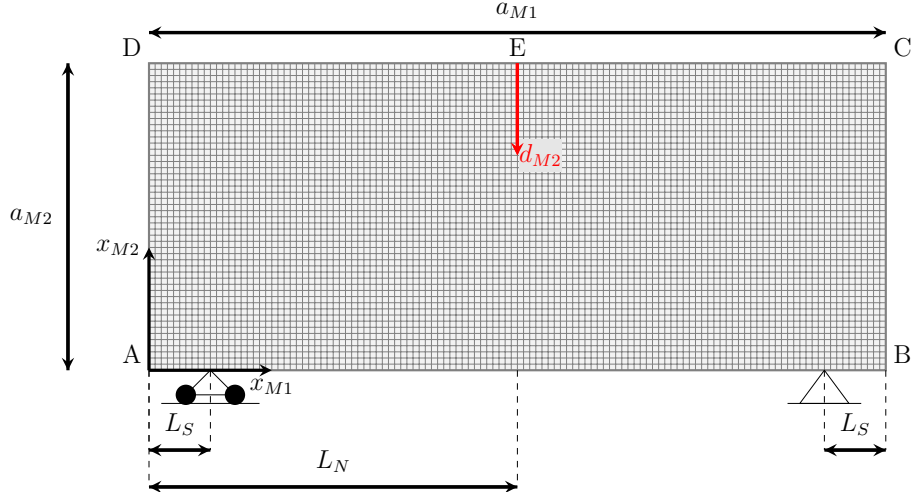


Figure 6.9 – Finite element model of the macroscopic scale problem with its characteristic size for 2D problems.

determined in order to met the constraint on the macroscopic mass fraction of Eq. (5.21).

Regarding the design case DC2, only the constraint g_1 is integrated in the CNLPP of Eq. (6.8) and the mass fraction is set to $\gamma_{Mm} = 0.4$. The problem is solved by considering a NURBS surface characterised by $n_{mCP} = 31 \times 31$ CPs and blending functions degree $p_{mi} = 3$, ($i = 1, 2$), which corresponds to a minimum length scale $d_{mmin} = 0.4$ mm at the lower scale. For DC2 the initial guess at the RVE scale is characterised by a central hole, which is generated by setting to zero the value of some CPs of the NURBS/B-spline entity. Particularly, the number of CPs whose pseudo-density is zero is the result of an iterative process that stops when the constraint on the mass fraction at the macroscopic scale of Eq. (5.21) is met.

Finally, for DC3, problem (6.8) is solved, by considering both constraints g_1 and g_2 and by using a mass fraction of $\gamma_{Mm} = 0.4$ at the upper scale and a volume fraction of $\gamma_{mV} = 0.3$ at the lower one. The NURBS surface is characterised by $n_{mCP} = 31 \times 31$ CPs at the RVE scale and by $n_{MCP} = 30 \times 10$ CPs at the macroscopic one, with the same value of blend-

Table 6.6 – Elasticity matrix of the optimised topologies illustrated in Fig. 6.10

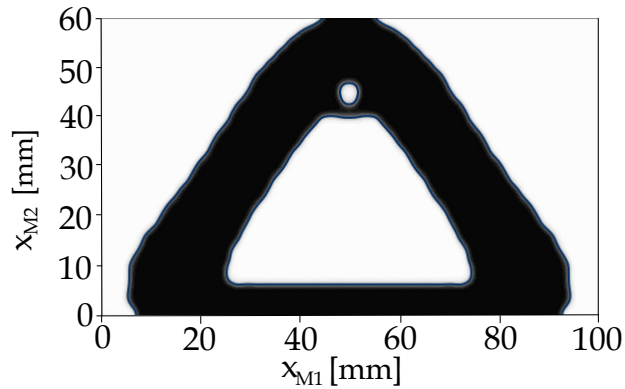
Design Case	Stiffness Matrix [MPa]
DC1	$\mathbf{C}_M = \begin{bmatrix} 5519.23 & 2365.38 & 0 \\ 2365.38 & 5519.23 & 0 \\ 0 & 0 & 1576.92 \end{bmatrix}$
DC2	$\mathbf{C}_M = \begin{bmatrix} 388.25 & 269.78 & 0 \\ 269.78 & 867.12 & 0 \\ 0 & 0 & 247.91 \end{bmatrix}$
DC3	$\mathbf{C}_M = \begin{bmatrix} 672.11 & 372.30 & 0 \\ 372.30 & 1196.43 & 0 \\ 0 & 0 & 344.07 \end{bmatrix}$

ing function degree $p_{mi} = p_{Mi} = 3$, ($i = 1, 2$). This choice corresponds to a minimum length scale of $d_{m\min} = 0.4$ mm at the lower scale and of $d_{M\min} = 20$ mm at the upper scale (in this way the number of RVEs included in the thinnest topological branch at the macroscopic scale is equal to $N_{\text{RVE}} = 5$). For DC3 the initial guess at the RVE scale is characterised by a central hole, which is generated by setting to zero the value of some CPs of the NURBS/B-spline entity. Particularly, the number of CPs whose pseudo-density is set equal to zero is the result of an iterative process that stops when the constraint on the RVE volume fraction of Eq. (5.22) is met. Conversely, the initial guess at the macroscopic scale is characterised by a uniform density field whose value is determined in order to met the constraint on the macroscopic mass fraction of Eq. (5.21).

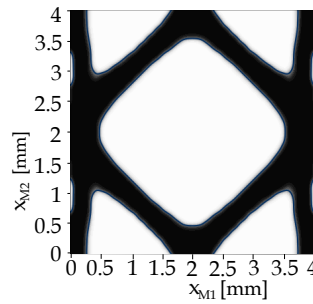
The optimised solutions are reported in Fig. 6.10: results are provided in terms of the number of iterations to achieve convergence (N_{iter}), of the value of reference and optimised compliance and mass as well as of the minimum member size measured at the end of the optimisation process, i.e., $\hat{d}_{\chi,\min}$ with ($\chi = m, M$). The macroscopic elasticity matrix related to the optimised solutions of design cases DC1, DC2 and DC3 are reported in Tab. 6.6.

From the analysis of the results, the following remarks can be inferred:

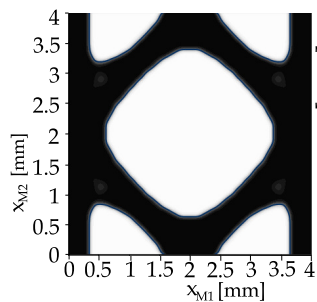
1. The optimised topology obtained when considering the design case DC1 is characterised by the highest flexural stiffness, followed by the optimised solutions of DC3 and of DC2, respectively. Particularly, this result is due to the influence of the topology at the macroscopic scale on the generalised macroscopic compliance, which is stronger than the influence of the topology at the lower scale (or, equivalently, of the



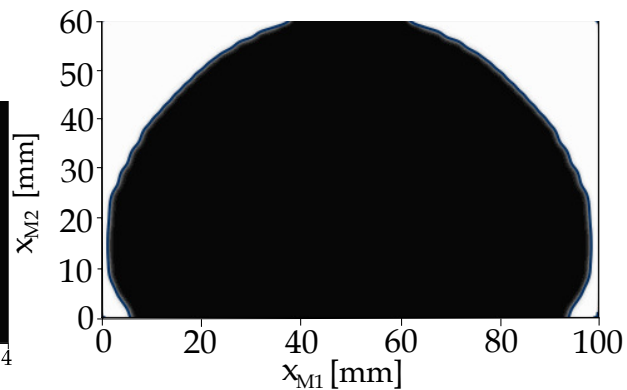
(a) $N_{iter} = 45$, $m_{Mopt} = 3.32$ kg,
 $C_{Mref} = -1983.73$ Nmm, $C_{Mopt} = -22092.65$ Nmm,
 $\hat{d}_{Mmin} = 5$ mm



(b) $N_{iter} = 107$,
 $m_{Mopt} = 3.32$ kg,
 $C_{Mref} = -901.83$ Nmm,
 $C_{Mopt} = -4582.27$ Nmm,
 $\hat{d}_{mmin} = 0.4$ mm



(c) $\hat{d}_{mmin} = 0.4$ mm



(d) $N_{iter} = 101$, $m_{Mopt} = 3.32$ kg,
 $C_{Mref} = -1529.53$ Nmm, $C_{Mopt} = -5929.39$ Nmm,
 $\hat{d}_{Mmin} = 60$ mm

Figure 6.10 – 2D test case: influence of the problem formulation on the optimised topology: a) optimised solution of DC1 (upper scale), b) optimised solution of DC2 (lower scale), c) optimised solution of DC3 (lower scale), d) optimised solution of DC3 (upper scale).

influence of the equivalent homogeneous material at the macroscopic scale) on the same quantity.

2. When considering DC2 and DC3, the optimised topology at the RVE scale shows a macroscopic orthotropic behaviour with the main orthotropy axis aligned with axis x_{2M} . This is an expected result because the displacement imposed at the macroscopic scale to simulate the BCs of the 3PBT is applied along the x_{2M} axis. Moreover, the volume fraction of the optimised topology of the RVE for DC2 is lower than the volume fraction of the optimised topology of the RVE for DC3 because, the constraint on the macroscopic mass fraction being the same among the two design cases, the RVE topology of DC2 evolves towards a configuration characterised by a lower volume fraction of the solid phase to satisfy the design requirement on lightness.
3. One can notice that, depending on the macroscopic loading conditions, it is not necessarily useful to formulate the TO problem by defining the topology descriptor at multiple scales. Specifically, for 3PBT-like BCs, an isotropic RVE (i.e., an RVE completely filled by the isotropic bulk material) reveals to be the optimal solution in terms of the behaviour of the equivalent homogeneous material used at the macroscopic scale. As expected, the same topology illustrated in Fig. 6.10 a) can be obtained in design case DC3, by suppressing the constraint on the volume fraction at the lower scale. In this case, the pseudo-density at the lower scale converges towards the unit value for all the CPs of the NURBS entity, whilst the pseudo-density field at the upper scale converges exactly towards the same configuration as DC1.
4. As discussed in [113], thanks to the local support property of the NURBS basis functions, the constraint on the minimum length scale (at both lower and upper scales) is easily satisfied for all design cases without introducing an explicit optimisation constraint in the problem formulation.

6.4.2 3D results

Analogously to the 2D case, three analyses are performed in the 3D case, corresponding to design cases DC1, DC2 and DC3. For DC2 and DC3, the design domain of the RVE, shown in Fig. 6.11, is a cube of size $L_m = 2a_{m1} = 2a_{m2} = 2a_{m3} = 4$ mm. The elasticity tensor at the macroscopic scale is assessed via six static analyses performed on the FE model of the RVE. The periodic BCs of Eq. (4.1) are applied through constraint equations

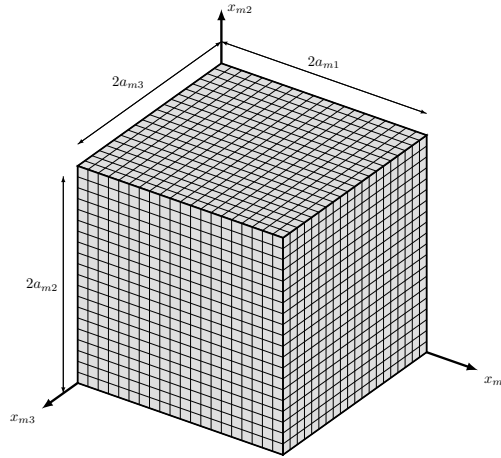


Figure 6.11 – Finite element model of the representative volume element of the with its characteristic size for 3D problems.

among homologous nodes belonging to the opposite faces of the RVE, by considering elementary unit strains, for each analysis. The FE model of the RVE (which is the same for all 3D benchmark problems) has been coded in the Ansys automatic parametric design language and the mesh is made of $N_{me} = 8000$ SOLID185 elements (8 nodes, 3 DOFs per node).

For all the analyses the macroscopic scale domain, shown in Fig. 6.12, is a parallelepiped submitted to 3PBT-like BCs. The geometrical parameters of the design domain at the macroscopic scale are: $a_{M1} = 100$ mm, $a_{M2} = 60$ mm, $a_{M3} = 30$ mm, $L_S = 10$ mm and $L_N = \frac{a_{M1}}{2}$. A static analysis is conducted on the macroscopic FE model whose mesh is made of $N_{Me} = 22500$ SOLID185 elements (8 nodes with 3 DOFs per node). The BCs are set as follows: $u_{M2} = u_{M3} = 0$ is set on the nodes located at $x_{M1} = L_S$, while $u_{M1} = u_{M2} = u_{M3} = 0$ is set on the nodes located at $x_{M1} = a_{M1} - L_S$. A vertical displacement $d_{M2} = -2$ mm is applied on nodes located at $(x_{M1}, x_{M2}) = (L_N, a_{M2})$.

Regarding DC1, only the constraint g_1 is integrated in the CNLPP of Eq. (6.8) and the mass fraction is set to $\gamma_{Mm} = 0.4$. The problem is solved by considering a NURBS surface characterised by $n_{MCP} = 25 \times 15 \times 7$ CPs and blending functions degree $p_{Mi} = 3$, ($i = 1, 2, 3$). This choice corresponds to a minimum length scale $d_{Mmin} = 5$ mm.

As far as DC2 is concerned, only the constraint g_1 is integrated in the CNLPP of Eq. (6.8) and the mass fraction is set to $\gamma_{Mm} = 0.4$. The problem is solved by considering a NURBS surface characterised by $n_{mCP} = 11 \times 11 \times 11$ CPs and blending functions degree $p_{mi} = 3$, ($i = 1, 2, 3$), which

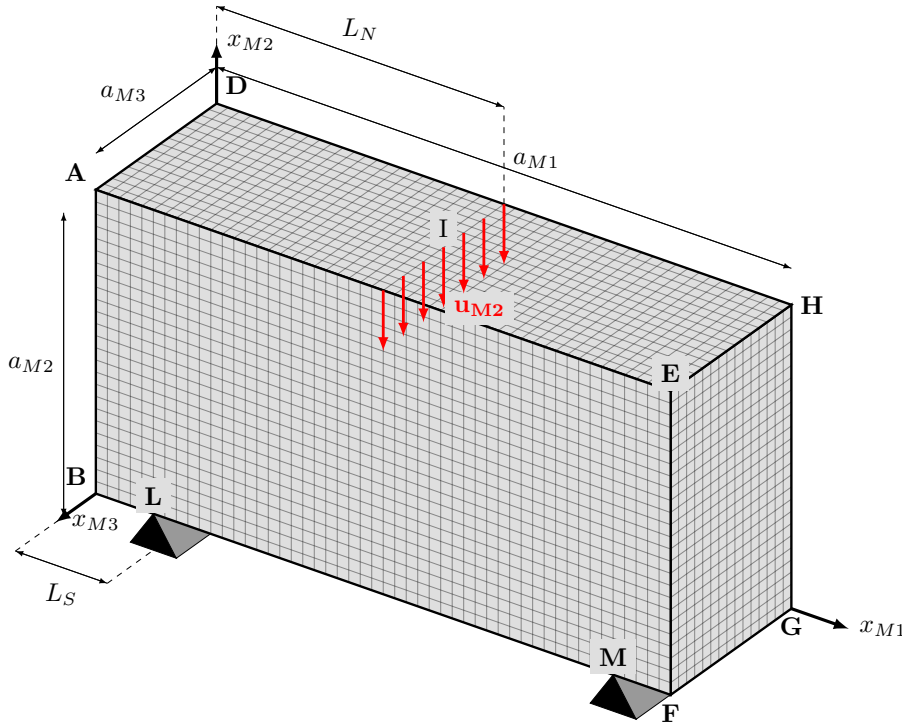


Figure 6.12 – Finite element model of the macroscopic scale with its characteristic size for 3D problems.

corresponds to a minimum length scale $d_{m\min} = 0.4$ mm within the domain.

Finally, regarding DC3, problem (6.8) is solved, by considering both constraints g_1 and g_2 and by using a mass fraction of $\gamma_{Mm} = 0.4$ at the upper scale and a volume fraction of $\gamma_{mV} = 0.3$ at the lower one. The NURBS surface is characterised by $n_{mCP} = 11 \times 11 \times 11$ CPs at the RVE scale and by $n_{MCP} = 15 \times 10 \times 5$ CPs at the macroscopic one, with the same value of blending function degree $p_{mi} = p_{Mi} = 3$, ($i = 1, 2, 3$). This choice corresponds to a minimum length scale of $d_{m\min} = 0.4$ mm at the lower scale and of $d_{M\min} = 20$ mm at the upper scale.

For each design case, the initial guess at both scales is chosen by following the same procedure used in 2D analyses.

The optimised solutions are reported in Fig. 6.13, results are provided in terms of the number of iterations to achieve convergence (N_{iter}), of the value of reference and optimised compliance and mass as well as of the minimum member size measured at the end of the optimisation process, i.e., $\hat{d}_{\chi,\min}$ with ($\chi = m, M$).

The macroscopic elasticity matrix related to the optimised solutions of

Table 6.7 – Elasticity matrix of the optimised topologies illustrated in Fig. 6.13

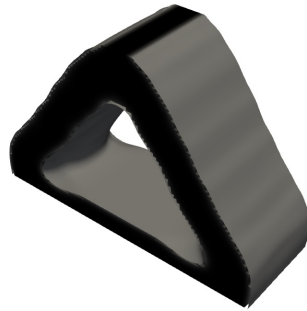
Design Case	Stiffness Matrix
DC1	$\mathbf{C}_M = \begin{bmatrix} 5519.23 & 2365.38 & 2365.38 & 0 & 0 & 0 \\ 2365.38 & 5519.23 & 2365.38 & 0 & 0 & 0 \\ 2365.38 & 2365.38 & 5519.23 & 0 & 0 & 0 \\ 0 & 0 & 0 & 1576.92 & 0 & 0 \\ 0 & 0 & 0 & 0 & 1576.92 & 0 \\ 0 & 0 & 0 & 0 & 0 & 1576.92 \end{bmatrix}$
DC2	$\mathbf{C}_M = \begin{bmatrix} 1516.15 & 454.85 & 0.044 & 0 & 0 & 0 \\ 454.85 & 1535.71 & 0.048 & 0 & 0 & 0 \\ 0.044 & 0.044 & 0.218 & 0 & 0 & 0 \\ 0 & 0 & 0 & 532.32 & 0 & 0 \\ 0 & 0 & 0 & 0 & 0.005 & 0 \\ 0 & 0 & 0 & 0 & 0 & 0.005 \end{bmatrix}$
DC3	$\mathbf{C}_M = \begin{bmatrix} 1972.03 & 591.61 & 0.041 & 0 & 0 & 0 \\ 591.61 & 1972.22 & 0.044 & 0 & 0 & 0 \\ 0.041 & 0.044 & 0.164 & 0 & 0 & 0 \\ 0 & 0 & 0 & 690.24 & 0 & 0 \\ 0 & 0 & 0 & 0 & 0.017 & 0 \\ 0 & 0 & 0 & 0 & 0 & 0.004 \end{bmatrix}$

design cases DC1, DC2 and DC3 are reported in Tab. 6.7. The same remarks done in the case of 2D analyses hold for the optimised solutions found in the 3D case.

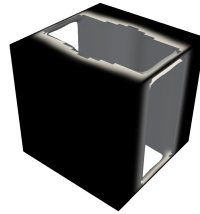
6.5 Validation of the optimised topologies through three-point bending tests

In this section, the optimised topologies found in Sec. 6.4 are validated, a posteriori, through a comparison with the results of experimental tests. For the sake of brevity, only 2D optimised solutions of design cases DC1, DC2 and DC3 are printed by means of SLA technology by extruding the related geometries. Then, the 3PBT is conducted on the optimised topologies via the Zwick-Roell machine with a load capacity of 250 kN at a speed of 0.9 mm/min.

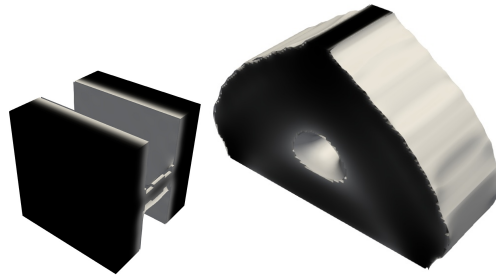
Since the optimised topology is represented by a 2D contour, a preliminary phase of reconstruction is necessary to manufacture the specimens. As



(a) $N_{\text{iter}} = 62$,
 $m_{M\text{opt}} = 99.7 \text{ kg}$,
 $\mathcal{C}_{M\text{ref}} = -1963.59 \text{ Nmm}$,
 $\mathcal{C}_{M\text{opt}} = -19922.61 \text{ Nmm}$,
 $\hat{d}_{M\text{min}} = 5 \text{ mm}$



(b) $N_{\text{iter}} = 107$,
 $m_{M\text{opt}} = 99.7 \text{ kg}$,
 $\mathcal{C}_{M\text{ref}} =$
 -799.39 Nmm ,
 $\mathcal{C}_{M\text{opt}} =$
 -9941.27 Nmm ,
 $\hat{d}_{m\text{min}} = 0.4 \text{ mm}$



(c) $\hat{d}_{m\text{min}} = 0.4 \text{ mm}$

(d) $N_{\text{iter}} = 89$,
 $m_{M\text{opt}} = 99.7 \text{ kg}$,
 $\mathcal{C}_{M\text{ref}} = -4374.75 \text{ Nmm}$,
 $\mathcal{C}_{M\text{opt}} = -12503.49 \text{ Nmm}$,
 $\hat{d}_{M\text{min}} = 20 \text{ mm}$

Figure 6.13 – 3D test case: influence of the problem formulation on the optimised topology: a) optimised solution of DC1 (upper scale), b) optimised solution of DC2 (lower scale), c) optimised solution of DC3 (lower scale), d) optimised solution of DC3 (upper scale).

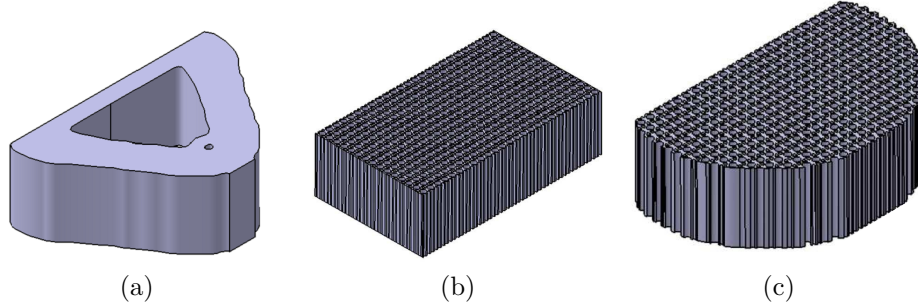


Figure 6.14 – CAD model of the optimised topology for design case (a) DC1, (b) DC2 and (c) DC3.

discussed in [128, 134], due to the use of NURBS entities to represent the topology at the lower/upper scale, the reconstruction of the boundary of the optimised topology becomes a trivial task, regardless the design case at hand. The reconstruction phase is performed via the Catia V5 software and is shown in Fig. 6.14, for each design case. Of course, when the topological descriptor is defined at both lower and upper scales (DC3), the boundary of the optimised topology is obtained by combining two operations. Firstly, the RVE topology is copied along x and y axes within the macroscopic domain (rectangular pattern). Secondly, a boolean operation is performed on the rectangular pattern, i.e., the final topology is obtained by cutting the macroscopic domain filled with the RVE topologies through the contour of the optimised topology at the macroscopic scale.

Finally, the 3D volumes are tessellated to obtain STL files and printed via Formlab 3[®], with rigid resin 4000. The manufacturing parameters chosen to print the samples are the standard ones (i.e., thickness of the layer $t_l = 0.1$ mm, thickness of the support $t_s = 2$ mm, melting thickness of the first layers $t_m = 0.3$ mm) and they are the same for all the samples. The main printing parameters related to the sample of each design case, i.e., printing time t_p , number of layers n_l , volume V_M , nominal mass m_{Mn} , actual mass m_M , are reported in Tab. 6.8, whilst the orientation and position of the samples during printing are illustrated in Fig. 6.15.

The experimental set-up of the 3PBT for each optimised sample is shown in Fig. 6.16. The machine is equipped with a dedicated support to perform the 3PBT on unconventional specimens: the loading support is placed in the middle of the top face of the sample, while two supports are placed at a distance of 80 mm on the bottom surface of the sample, providing an overhang of 10 mm.

Table 6.8 – Printing parameters of the samples for each design case.

Design case	t_p [min]	n_l	V_M [mm ³]	m_{Mn} [g]	m_M [g]
DC1	255	300	76640	106.17	102
DC2	255	300	84410	116.94	119
DC3	420	300	81630	113.08	114

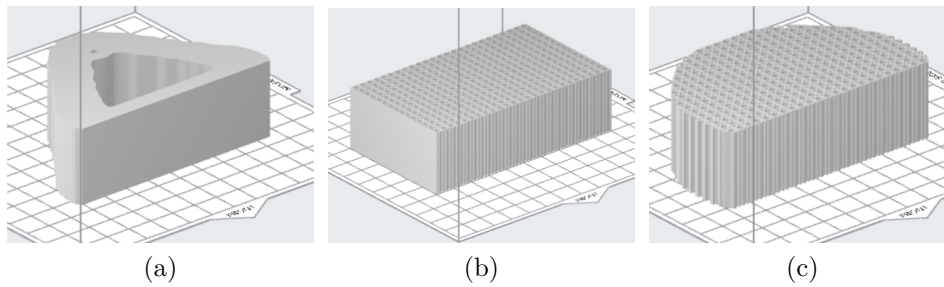


Figure 6.15 – Orientation and position of the sample during printing for design cases (a) DC1, (b) DC2 and (c) DC3

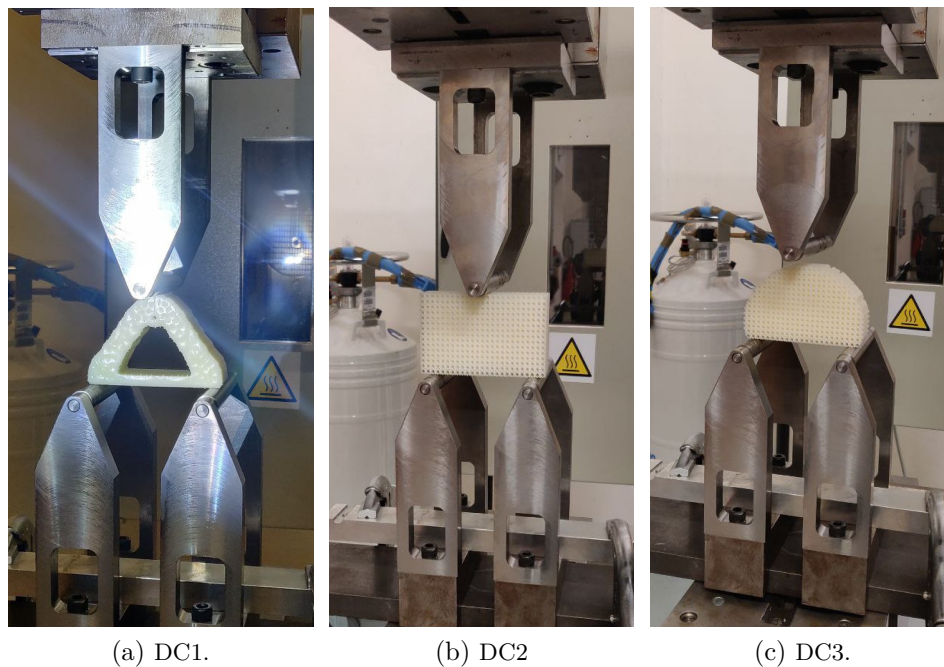


Figure 6.16 – Experimental set-up of the three-point bending test for the optimised 2D topologies for each design case.

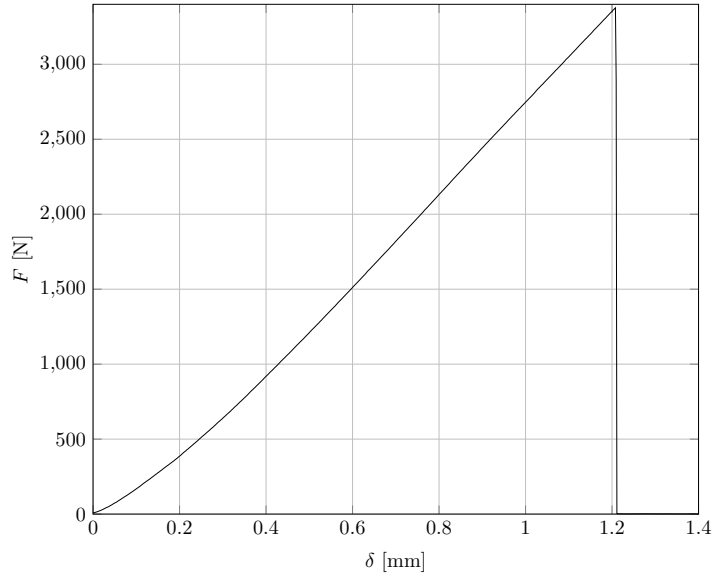


Figure 6.17 – Force vs. displacement curve obtained from three-point bending test on the optimised sample of each design case.

The experimental results are shown in Fig. 6.17 in terms of force vs. displacement curve, for each design case. One can notice that, as far as the linear part of the curves is concerned, experimental results corroborate the numerical ones discussed in Sec. 6.4, where the TO calculations are conducted assuming a linear elastic behaviour of the rigid resin 4000 and small displacements and strains. Particularly, as it can be inferred from Fig. 6.17, the flexural stiffness of the optimised topology solution of DC1 is the highest one, whilst the flexural stiffness of the optimised topology solution of DC3 is higher than the one of the counterpart solution of DC2.

To carry out a more correct comparison between numerical and experimental results, the optimised topologies, obtained after CAD reconstruction of the boundary, together with the supports of the 3PBT have been modelled in Ansys Workbench[®]. Specifically, two non-linear analyses (NLA) are carried out for each design case. In the first case (NLA1), the behaviour of the resin is modelled by considering the σ - ε curve resulting from the 3PBT conducted on the parallelepiped samples discussed in Sec. 6.2.2. In the second case (NLA2), the constitutive behaviour of the resin is modelled by exploiting the σ - ε curve of the traction tests discussed in Sec. 6.2.1. In all the analyses, the supports are modelled by using a steel with a linear elastic isotropic behaviour having a Young's modulus $E_{\text{steel}} = 200$ GPa and a Poisson's coefficient $\nu_{\text{steel}} = 0.3$.

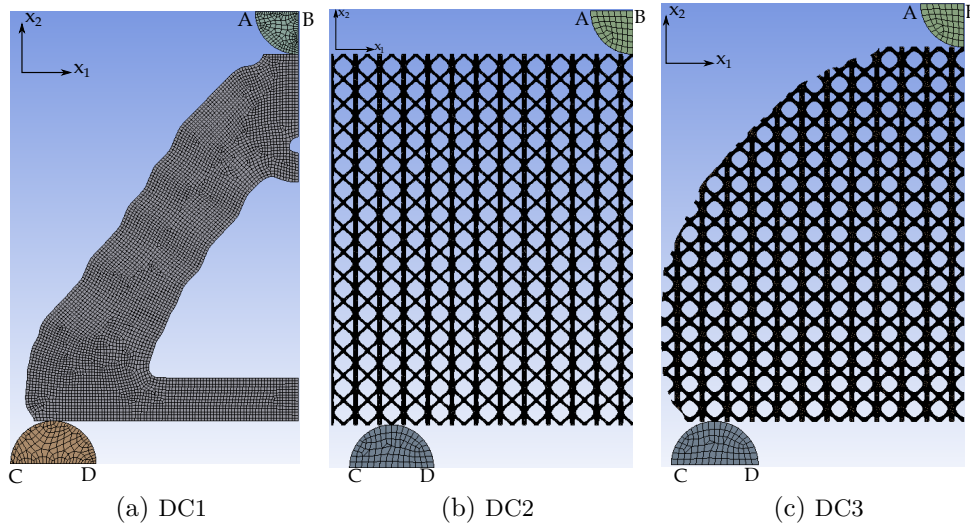


Figure 6.18 – Finite element model and boundary conditions for the non-linear analysis conducted a posteriori on the optimised samples (for each design case).

The FE model of the optimised topology (for each design case) used for non-linear analysis is shown in Fig. 6.18. In each case, PLANE182 elements (four nodes, two DOFs per node, plane stress hypothesis) with a thickness equal to 30 mm are used. Due to the symmetry of each topology, only half of the geometry is modelled. The number of elements composing the FE model is $N_e = 5200$, $N_e = 170608$ and $N_e = 154933$, for DC1, DC2 and DC3, respectively. The contact regions between the supports and the sample are modelled through CONTA171 and TARGE169 elements (2D contact elements with two nodes and two DOFs per node) for the nodes belonging to the contact region of the sample and of the support, respectively. A no separation behaviour is assigned to the contact region and the Lagrange method is used to penalise, eventually, the initial penetration. The pinball radius of the contact region is set to 0.2 mm by following the guidelines provided in [135].

By referring to Fig. 6.18, the BCs are set as follows: a) symmetry condition, i.e., $u_1 = 0$, is imposed on the nodes located on the symmetry plane; b) $u_1 = u_2 = 0$ on the nodes belonging to the segment CD; c) $u_2 = \delta = -0.5$ mm on the nodes belonging to the segment AB.

The minimum and maximum number of sub-steps for the non-linear static analysis are set to 200 and 1000, respectively.

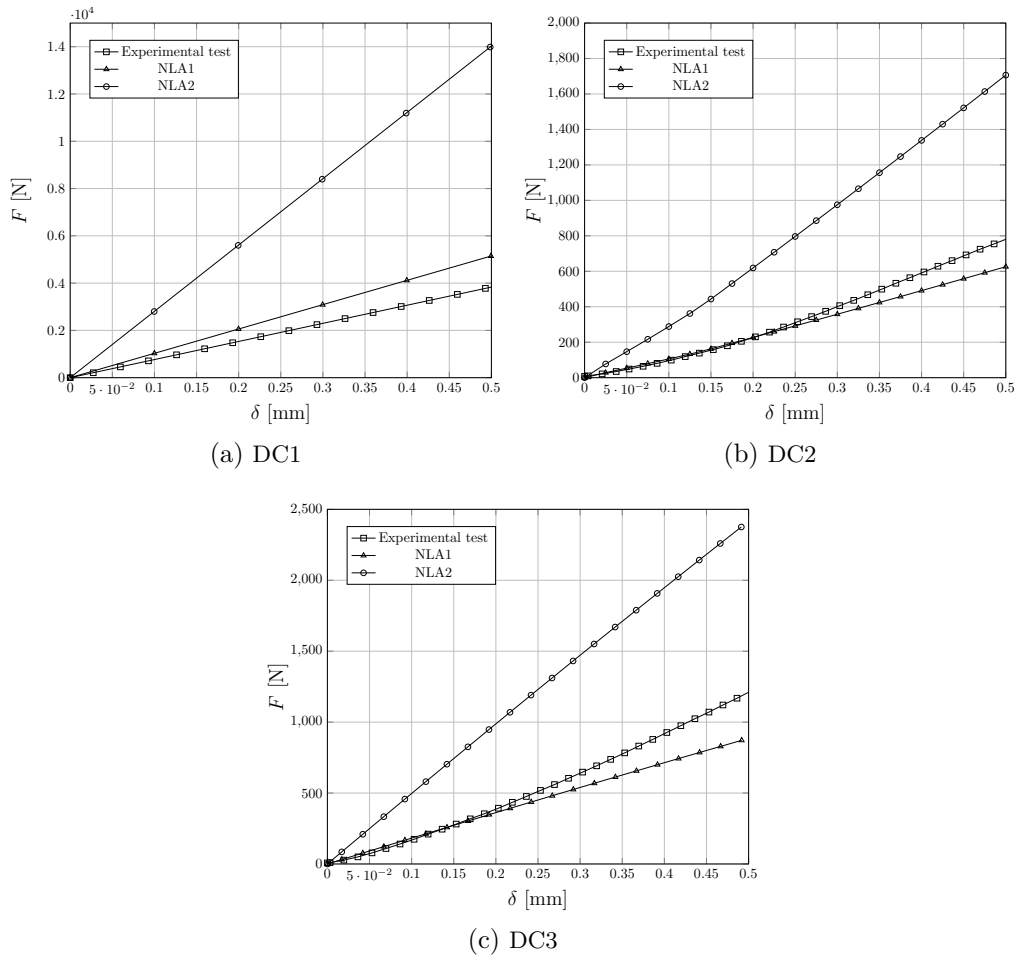


Figure 6.19 – Force vs. displacement curves for each design case by considering different material behaviours for the rigid resin 4000.

The force vs. displacement curve obtained from analyses NLA1 and NLA2 are reported in Fig. 6.19 where they are compared to the experimental counterpart, for each design case. As expected, for small displacements, the force vs. displacement curve obtained when the resin is modelled by using the flexural behaviour of Fig. 6.7 is closer to the experimental results obtained for each optimised sample.

6.6 Conclusions and prospects

In this chapter, the optimised solutions determined through the NURBS-based SIMP method, by considering different problem formula-

tions, have been validated experimentally. Particularly, three design cases are considered: in the first case, the topological descriptor is defined solely at the macroscopic scale; in the second case, the topological variable is introduced at the RVE scale; in the last case, the topological descriptor is introduced at both RVE and macroscopic scales. For each problem formulation, the goal is to maximise the flexural stiffness subject to requirements on the lightness, on the minimum member size (related to technological constraints), and, when the topological descriptor is defined simultaneously at the RVE scale and at the macroscopic one, two further requirements are considered: the scale separation condition (to ensure the validity of the results of the SEHM) and a constraint on the volume fraction of the solid phase composing the RVE. In each design case, the boundary conditions imposed at the macroscopic scale are those characterising the well-known three-point bending test: in this way, the optimised topologies obtained at the end of the process can be easily manufactured and validated experimentally. In second and third design cases, i.e., when the topological variable is defined at the RVE scale, the scale transition is ensured via the SEHM (only weak coupling among scales is considered). Indeed, the structural responses at the upper scale depend both on the topological descriptor defined at this scale and on the one introduced at the lower scale through the calculation of the equivalent elasticity matrix of the fictitious homogeneous material, which replaces the RVE at the upper scale. The optimised topologies resulting from the three design cases have been printed via SLA and validated through three-point bending test. Of course, a preliminary experimental campaign of tests has been conducted to characterise the behaviour (in traction and flexural) of the rigid resin constituting the bulk material of the optimised specimens. It is noteworthy that, although the topology optimisation has been conducted by assuming a linear elastic behaviour of the material composing the specimen and under the hypothesis of small displacements and strains, the comparison between numerical and experimental results is carried out a posteriori through non-linear finite element analysis on the reconstructed optimised topologies (i.e., after reconstruction of their boundary).

Some features of the proposed methodology need to be highlighted after a careful analysis of the numerical results.

Firstly, the best performances, in terms of flexural stiffness, are obtained in the first design case wherein the topological descriptor is introduced only at the macroscopic scale. This means that, as far as the three-point bending test is concerned, the optimised topology is characterised by an isotropic material filling the whole RVE and optimally distributed at the macroscopic scale. This is confirmed also by the results of second and third design cases,

which highlight that, to satisfy the requirements of the problem at hand and to withstand the applied loads, both the RVE topology and the macroscopic one evolve towards a configuration optimising the macroscopic elastic response of the continuum, as well as the material distribution at the upper scale, but since the lightness requirement and the constraint on the volume fraction of the solid phase are introduced, the optimised topology at the RVE scale cannot converge towards the isotropic solution. Of course, when considering the most general problem formulation, i.e., the one involving the topological descriptor at both scales, when the constraint on the volume fraction of the solid phase at the RVE scale is suppressed and only the one on the overall mass of the structure is kept, the optimised solution coincide with the one of the first design case (wherein the topological descriptor is defined solely at the upper scale).

The effect of the minimum-length scale requirement at each problem scale on the optimised solutions is correctly taken into account, without the need of introducing an explicit optimisation constraint. Indeed, this requirement can be easily fulfilled by properly setting the integer parameters of the NURBS entity representing the topological variable at each scale.

Regarding the comparison between numerical and experimental results obtained on the optimised topologies (for each design case), in terms of force vs. displacement curves, the utilisation of the non-linear constitutive law of the rigid resin as well as the modelling of the contact regions between the sample and the supports allows obtaining a good agreement between numerical and experimental curves only when the σ - ε curve describing flexural behaviour of the resin is used. Nevertheless, some discrepancies between numerical and experimental results can be observed for some values of the applied displacement. To obtain better (and more consistent) results, the complete compression-traction curve describing the true behaviour of the rigid resin should be modelled via a user-defined material routine, but this task does not fall within the scopes of the present work and could constitute a prospect of this study.

A further prospect of this work concerns the integration of the non-linear behaviour of the bulk material within the topology optimisation process, by developing also a suitable non-linear homogenisation strategy (as far as second and third design cases are concerned). Finally, suitable failure criteria at upper and lower scales should be derived and integrated into the multi-scale TO problem formulation for the homogeneous anisotropic material at the macroscopic scale and for the bulk material at the RVE scale in order to optimise not only the stiffness of the structure but also its strength.

Chapter 7

An Efficient Hybrid Optimization Strategy for Surface Reconstruction

In this Chapter, a semi-automatic surface reconstruction strategy is presented, which is able to approximate non-convex sets of target points (TPs). The strategy is split in two phases: (a) the mapping phase, making use of the shape preserving method (SPM) to get a proper parametrisation of each sub-domain composing the TPs set; (b) the fitting phase, where each patch is fitted by means of a suitable NURBS surface by considering, as design variables, all the parameters involved in its definition. The resulting algorithm is called Shape-preserving and Poly-NURBS Surface reconstruction (SPONS) algorithm. The Chapter is organised as follows. Sec. 7.1 recalls the fundamentals of the SPM. In Sec. 7.2, the surface fitting problem is formulated by considering open surfaces of genus zero. In Sec. 7.3, the problem formulation is extended to more general surfaces, i.e., to open or closed surfaces of genus greater than zero. In Secs. 7.4 and 7.5 the effectiveness of the proposed methodology is proven through some meaningful benchmarks taken from the literature and the results compared to those obtained by other methodologies. Finally, the conclusions and prospects of this work are outlined in Sec. 7.6.

The contents of this Chapter have been presented in the article [128].

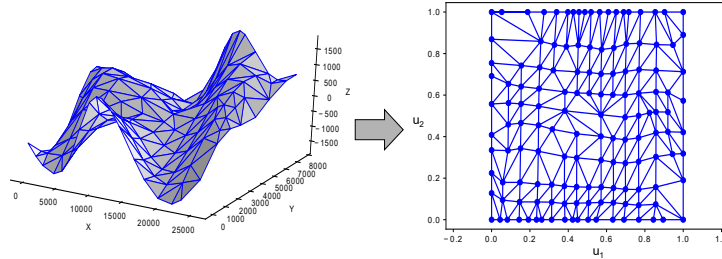


Figure 7.1 – Mapping of the triangulated surface on the parametric domain.

7.1 Fundamentals of the shape preserving method

A mapping strategy is based on the assumption that, given two surfaces with a similar topology, a bijective mapping between them can always be defined [136]. Therefore, if the surface to be mapped is represented by means of a suitable triangulation, the mapping operation is named *parametrisation* and the result of this operation is the *parametrisation domain*. The parametrisation method considered in this study is the SPM [96]. In particular, the SPM is used to find the parameters (u_1, u_2) , appearing in the definition of the NURBS surface of Eq. (3.1), and related to the TPs of the triangulated surface $S(x_i, y_i, z_i)$. The mapping operation generates an isomorphism between the triangulation P and the related graph G , as shown in Fig. 7.1. Consider the set of points (or nodes) belonging to the TS defined as $Q := \{OQ_i^T = (x_i, y_i, z_i), 1 \leq i \leq N\}$, where N is the total number of TPs. The SPM can be applied if and only if the surface tessellation $S(G, Q)$ satisfies the following requirements:

- non degenerated triangular facets F , with vertices V and edges E must compose the connectivity graph $G = G(V, E, F)$;
- the surface should be open and of genus zero, i.e., without holes.

The procedure behind the SPM is divided in three macro-phases, see [96] for more details.

1. The TPs set, included in the STL file, is split into two different subsets: the set of *internal nodes*, i.e., $Q_I := \{OQ_1, \dots, OQ_n\}$, and the set of *boundary nodes*, i.e., $Q_B := \{OQ_{n+1}, \dots, OQ_N\}$, for some $n \in [1, N[$, the latter ordered in anticlockwise sequence.
2. The boundary nodes parametrisation is performed through the *chord length* method [137], to set the known terms of the linear convex

combination system. In particular the boundary nodes are mapped on the boundary of a convex polygon $D \in [0, 1] \times [0, 1]$, i.e., a unit square, as follows:

$$\xi_{j+1}^B := \xi_j^B + \frac{\|\text{OQ}_{j+1}^B - \text{OQ}_j^B\|}{L_{\text{tot}}}, \quad j = 1, \dots, d, \quad (7.1)$$

where $L_{\text{tot}} = \sum_{j=1}^d \|\text{OQ}_{j+1}^B - \text{OQ}_j^B\|$ and $\|\cdot\|$ is the Euclidean norm in the 3D space, while ξ_j^B indicates the value of the generic dimensionless parameter (i.e., either u_1 or u_2) located on the boundary of D . In Eq. (7.1), d represents the number of boundary nodes in Q_B located on the generic edge of the unit square D .

3. Then, the generic dimensionless parameter related to each internal node ξ_i^I is expressed as a linear convex combination of its N_i neighbours, i.e., a set of ξ vertices that are located in the vicinity of ξ_i^I .

$$\xi_i^I := \sum_{j \in N_i} \lambda_{i,j} \xi_j, \quad i = 1, \dots, n, \quad \text{with:} \quad \sum_{j \in N_i} \lambda_{i,j} = 1. \quad (7.2)$$

Since the dimensionless parameters related to the boundary nodes are known, those associated to the internal nodes can be obtained by solving the following linear system:

$$\mathbf{\Lambda} \mathbf{u}_k^I = \mathbf{z}_k, \quad k = 1, 2, \quad (7.3)$$

with

$$\mathbf{z}_k := \{\lambda_{i,j} u_{k_j}^B\}, \quad i = 1, \dots, n, \quad (7.4)$$

where nodes identified by $j = n + 1, \dots, N$, represent the boundary nodes contributions. The assessment of the weights matrix $\mathbf{\Lambda}$ is performed according to a two-steps strategy, which constitutes the kernel of the SPM.

1. For each internal point OQ_i^I , the local (temporary) parametrisation of the one-ring neighbourhood (OQ_j) is computed, through a geodesic-based mapping, preserving (locally) the distance and the angles, i.e.,

$$\|\mathbf{u}_j - \mathbf{u}_i\| = \|\text{OQ}_j - \text{OQ}_i^I\|, \quad j = 1, \dots, N_i, \quad (7.5)$$

and for each triangle $[\mathbf{u}_k, \mathbf{u}_i, \mathbf{u}_j]$ in the neighbourhood of OQ_i^I

$$\begin{aligned} \text{ang}(\mathbf{u}_k, \mathbf{u}_i, \mathbf{u}_j) &= \rho \text{ang}(\text{OQ}_k, \text{OQ}_i, \text{OQ}_j), \text{ with:} \\ \rho &:= \frac{2\pi}{\theta_i}, \quad \theta_i := \sum_{k \in N_i} \text{ang}(\text{OQ}_k, \text{OQ}_i, \text{OQ}_j). \end{aligned} \quad (7.6)$$

2. The second step is to express \mathbf{u}_i as a convex combination of the neighbouring mapped points $\{\mathbf{u}_j : j \in N_i\}$. Starting from the local temporary flat map, each internal edge $\overline{\mathbf{u}_i, \mathbf{u}_k}$ is prolonged to reach the intersection with the outer convex boundary. This operation allows identifying the triangle $(\mathbf{u}_k, \mathbf{u}_r, \mathbf{u}_{r+1})$, where the barycentric coordinates are evaluated as:

$$\begin{aligned} \mu_j^k &= \frac{\text{area}(\mathbf{u}, \mathbf{u}_r, \mathbf{u}_{r+1})}{\text{area}(\mathbf{u}_k, \mathbf{u}_r, \mathbf{u}_{r+1})}, \quad \mu_j^r = \frac{\text{area}(\mathbf{u}_k, \mathbf{u}, \mathbf{u}_{r+1})}{\text{area}(\mathbf{u}_k, \mathbf{u}_r, \mathbf{u}_{r+1})}, \\ \mu_j^{r+1} &= \frac{\text{area}(\mathbf{u}_k, \mathbf{u}_r, \mathbf{u})}{\text{area}(\mathbf{u}_k, \mathbf{u}_r, \mathbf{u}_{r+1})}. \end{aligned} \quad (7.7)$$

Finally, the shape-preserving weights, appearing in matrix $\mathbf{\Lambda}$ of Eq. (7.8), are the average of the local barycentric coordinates μ_j^k .

$$\lambda_{ij} = \frac{1}{N_i} \sum_{k \in N_i} \mu_j^k. \quad (7.8)$$

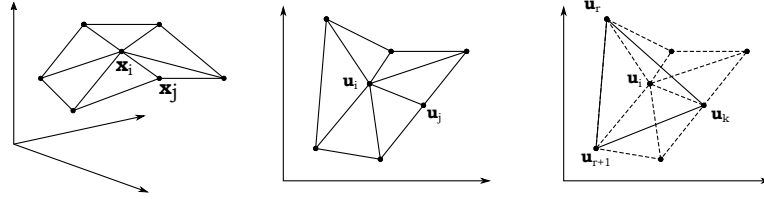


Figure 7.2 – Calculation of the weights of the SPM.

7.2 Surface Fitting of Genus zero Open Surfaces

7.2.1 Design Variables

The goal of the surface fitting problem is to find the optimum value of *all parameters* influencing the shape of a NURBS surface used to approximate

the set of TPs. Generally speaking, the set of N TPs to be approximated can be formally indicates as: $\text{OQ}_k = (x_k, y_k, z_k)$, $k = 1, \dots, N$. The approach discussed in this Sec. is very general and does not introduce neither simplifying hypotheses nor empirical rules to set the value of the parameters of the NURBS entity. In particular, all the parameters defining the NURBS surface, including the degrees and the number of CPs will be determined automatically by the proposed procedure, avoiding, thus, the use of arbitrary rules to set their value.

The variables affecting the shape of the NURBS surface are of different nature.

- *Integer variables*: the number of CPs along each parametric direction, i.e., $n_1 + 1$, $n_2 + 1$; the number of non-trivial knots along each parametric direction, i.e., $r_1 + 1$, $r_2 + 1$; the degrees of the blending functions p_1 , p_2 .
- *Continuous variables*: the non-decreasing sequence of knot vectors components $v_i^{(j)}$, $i \in [p_j + 1, m_j - p_j - 1]$, the CPs coordinates \mathbf{X}_{i_1, i_2} , the weights w_{i_1, i_2} and the set of the dimensionless parameters of the surface (u_{1_k}, u_{2_k}) , $k = 1, \dots, N$, corresponding to the set of TPs mapped on the NURBS surface.

In this work p_1 , p_2 and r_1 , r_2 are included in the vector of integer design variables

$$\zeta_1^T = \{p_1, p_2, r_1, r_2\}, \quad (7.9)$$

whilst, due to Eq. (3.8), n_j ($j = 1, 2$) is calculated as:

$$n_j = r_j + p_j. \quad (7.10)$$

Consider, now, the set of continuous parameters. As discussed in Sec. 7.1, the dimensionless parameters of the surface are provided by the SPM, so they are no longer design variables. Moreover, the optimal CPs coordinates can be found through the analytical approach proposed in [138], by minimising the following cost function f

$$\min_{\mathbf{X}_{ij}} f(\mathbf{X}_{ij}), \text{ with } f(\mathbf{X}_{ij}) := \sum_{\alpha=x,y,z} \sum_{k=1}^N [\alpha(u_{1k}, u_{2k}) - \alpha_k]^2 + \lambda J_\alpha, \quad (7.11)$$

where $\lambda \geq 0$ is a constant, whilst J_α is a smoothing term, i.e., the so-called TPSE [138], defined as

$$J_\alpha := \int_0^1 \int_0^1 \left(\frac{\partial^2 \alpha}{\partial u_1^2} \right)^2 + 2 \left(\frac{\partial^2 \alpha}{\partial u_1 \partial u_2} \right)^2 + \left(\frac{\partial^2 \alpha}{\partial u_2^2} \right)^2 du_1 du_2, \quad (7.12)$$

$$\alpha = x, y, z.$$

By introducing the following linear index

$$\begin{aligned} \tau &:= 1 + i_1 + i_2(n_1 + 1), \quad \forall i_1 = 0, \dots, n_1, \quad i_2 = 0, \dots, n_2 \Rightarrow \\ \tau &= 1, \dots, n_{\text{CP}}, \end{aligned} \quad (7.13)$$

the CPs coordinates can be grouped into the following vectors

$$\boldsymbol{\alpha}_{\text{CP}}^{\text{T}} := \{\alpha_{0,0}, \dots, \alpha_{n_1, n_2}\}, \quad \alpha = x, y, z. \quad (7.14)$$

Accordingly, the term J_α of Eq. (7.12) can be conveniently expressed in matrix form as:

$$J_\alpha = \boldsymbol{\alpha}_{\text{CP}}^{\text{T}} \mathbf{E} \boldsymbol{\alpha}_{\text{CP}}, \quad \text{with } \mathbf{E} := \mathbf{A} + 2\mathbf{B} + \mathbf{C}, \quad (7.15)$$

where matrices $\mathbf{A}, \mathbf{B}, \mathbf{C} \in \mathbb{R}^{n_{\text{CP}} \times n_{\text{CP}}}$ can be inferred from the corresponding 4D arrays, i.e.,

$$\begin{aligned} \mathbf{A}_{i,j,r,s} &:= \int_0^1 \int_0^1 \frac{\partial^2 R_{i,j}(u_1, u_2)}{\partial u_1^2} \frac{\partial^2 R_{r,s}(u_1, u_2)}{\partial u_1^2} du_1 du_2, \\ \mathbf{B}_{i,j,r,s} &:= \int_0^1 \int_0^1 \frac{\partial^2 R_{i,j}(u_1, u_2)}{\partial u_1 \partial u_2} \frac{\partial^2 R_{r,s}(u_1, u_2)}{\partial u_1 \partial u_2} du_1 du_2, \\ \mathbf{C}_{i,j,r,s} &:= \int_0^1 \int_0^1 \frac{\partial^2 R_{i,j}(u_1, u_2)}{\partial u_2^2} \frac{\partial^2 R_{r,s}(u_1, u_2)}{\partial u_2^2} du_1 du_2. \end{aligned} \quad (7.16)$$

The relationship between the 4D arrays of the above equation and the corresponding matrices can be immediately obtained by considering the linear index of Eq. (7.13):

$$\begin{aligned} \mathbf{M}_{\gamma\tau} &= \mathbf{M}_{i,j,r,s}, \quad \mathbf{M} = \mathbf{A}, \mathbf{B}, \mathbf{C}, \\ \gamma, \tau &= 1, \dots, n_{\text{CP}}; \quad i, r = 0, \dots, n_1; \quad j, s = 0, \dots, n_2. \end{aligned} \quad (7.17)$$

Of course, the local minimum of function f of Eq. (7.11) occurs when its gradient with respect to CPs coordinates $\boldsymbol{\alpha}_{\text{CP}}$ is null, i.e., $\frac{\partial f}{\partial \alpha_\tau} = 0$, $\forall \tau = 1, \dots, n_{\text{CP}}$, $\alpha = x, y, z$. By imposing this condition, one obtains the following linear system:

$$(\mathbf{G} + \lambda \mathbf{E}) \boldsymbol{\alpha}_{\text{CP}} = \mathbf{D}^{\text{T}} \mathbf{b}_\alpha, \quad \alpha = x, y, z. \quad (7.18)$$

In Eq. (7.18), $\mathbf{b}_\alpha \in \mathbb{R}^N$, $\mathbf{D} \in \mathbb{R}^{N \times n_{\text{CP}}}$ and $\mathbf{G}, \mathbf{E} \in \mathbb{R}^{n_{\text{CP}} \times n_{\text{CP}}}$. In particular, the α coordinate of the TPs are collected in vector \mathbf{b}_α :

$$\mathbf{b}_\alpha^T := \{\alpha_1, \dots, \alpha_N\}, \quad (7.19)$$

while matrices \mathbf{D} and \mathbf{G} collect the piecewise rational blending functions evaluated at the parametric coordinates (u_{1k}, u_{2k}) , $k = 1, \dots, N$ related to each TP (where u_{jk} are obtained through the SPM), i.e.,

$$\mathbf{D} := \begin{bmatrix} R_{0,0}(u_{11}, u_{21}) & \dots & R_{n_1, n_2}(u_{11}, u_{21}) \\ R_{0,0}(u_{12}, u_{22}) & \dots & R_{n_1, n_2}(u_{12}, u_{22}) \\ \vdots & \vdots & \vdots \\ R_{0,0}(u_{1N}, u_{2N}) & \dots & R_{n_1, n_2}(u_{1N}, u_{2N}) \end{bmatrix}, \quad \mathbf{G} := \mathbf{D}^T \mathbf{D}. \quad (7.20)$$

It is noteworthy that matrices \mathbf{G} and \mathbf{E} are symmetric and positive semidefinite, see [138] for more details. According to the guidelines provided in [138], the coefficient λ of Eqs. (7.11) and (7.18) has been set as follows:

$$\lambda = \frac{\|\mathbf{G}\|}{\|\mathbf{E}\|}, \quad (7.21)$$

where $\|\cdot\|$ is the l_2 norm, i.e., $\|\mathbf{M}\| = \left(\sum_{ij} M_{ij}^2\right)^{\frac{1}{2}}$.

Inasmuch as CPs coordinates are determined through Eq. (7.18), they can be excluded from the set of continuous design variables. Therefore, the rest of continuous design variables can be grouped in two different vectors:

- ζ_2 is related to the non-decreasing values of non-trivial KVs components $v_i^{(j)}$, $i \in [p_j + 1, m_j - p_j - 1]$, $j = 1, 2$;
- ζ_3 collects the values of weights w_{i_1, i_2} .

Nevertheless, since KVs are made of a non-decreasing sequence of real numbers, instead of directly using the non-trivial knots values $v_i^{(j)}$ as design variables, a more efficient choice consists in employing the following formula

$$v_i^{(j)} := \beta_i^{(j)} v_{i-1}^{(j)} + (1 - \beta_i^{(j)}) v_{i+1}^{(j)}, \quad i \in [p_j + 1, m_j - p_j - 1], \quad j = 1, 2, \quad (7.22)$$

where $\beta_i^{(j)}$ are the design variables that vary in the interval $]0, 1[$. It must be noticed that Eq. (7.22) allows avoiding the introduction of further constraint equations, during optimisation, to check if each KV is made of a non-decreasing sequence of real numbers. Therefore, the expression of vectors ζ_2 and ζ_3 reads:

$$\begin{aligned} \zeta_2^T &= \{\beta_{p_1+1}^{(1)}, \dots, \beta_{m_1-p_1-1}^{(1)}, \beta_{p_2+1}^{(2)}, \dots, \beta_{m_2-p_2-1}^{(2)}\}, \quad \zeta_2 \in \mathbb{R}^{r_1+r_2}, \\ \zeta_3^T &= \{w_{0,0}, \dots, w_{n_1, n_2}\}, \quad \zeta_3 \in \mathbb{R}^{n_{CP}}. \end{aligned} \quad (7.23)$$

According to Eqs. (7.9) and (7.23), the overall number of independent design variables (both integer and continuous) is:

$$N_{DV} = 4 + r_1 + r_2 + (r_1 + p_1 + 1)(r_2 + p_2 + 1). \quad (7.24)$$

7.2.2 Problem Formulation and Numerical Strategy

As stated beforehand, in this work, the surface fitting problem is formulated in the most general case, by integrating all independent design variables (both integer and continuous quantities) into the problem formulation. However, a quick glance to Eqs. (7.9), (7.23) and (7.24) suffices to understand that, regardless of the adopted formulation for the objective function and for the optimisation constraints, the resulting problem is defined over a domain of changing dimension. In particular, the number of design variables N_{DV} (and, thus, the problem dimension) depends upon the optimal value of the components of vector ζ_1 .

As discussed in [134, 139–144], this unconventional problem belongs to the class of optimisation problems dealing with *modular systems* belonging to different families. Roughly speaking, for a given family (or class) of modules, each module is characterised by the same design variables, which can take different values in the most general case of non-identical modules. When the goal is the simultaneous optimisation of the number of modules and of the design variables characterising each module, the resulting problem is defined over a domain of changing dimension, thus requiring a special formulation and a dedicated resolution strategy [139].

Following the approach proposed in [134, 139], in this study, a two-step optimisation process has been implemented to deal with the surface fitting problem. In this background, the general surface fitting problem is split into two sub-problems that are solved subsequently: each step of the process is characterised, hence, by a suitable problem formulation and the related optimisation algorithm.

The first optimisation step consists of the *meta-heuristic exploration phase* (MEP) and aims at finding a suitable pseudo-optimal solution. During this step only integer parameters and KV components are considered as design variables and the exploration of the domain of changing dimension is carried out by means of the ERASMUS algorithm [139]. Then, the best solution of the MEP is used as initial guess for the subsequent *deterministic optimisation phase* (DOP) whose goal is to refine the pseudo-optimal solution resulting from the MEP. During the DOP, the integer variables are kept constants, while both KVs components and weights are included among the design variables. The DOP is articulated in two steps. Firstly, solely

the KVs components are optimised, while the weights are kept constant. Secondly the KVs are kept equal to the values provided by the first step of the DOP and weights are optimised. For both steps the solution search is performed by means of the *active-set* algorithm of the MATLAB *fmincon* family, available in the MATLAB *optimization toolbox* [145]. The flow-chart of the optimisation process is illustrated in Fig. 7.3.

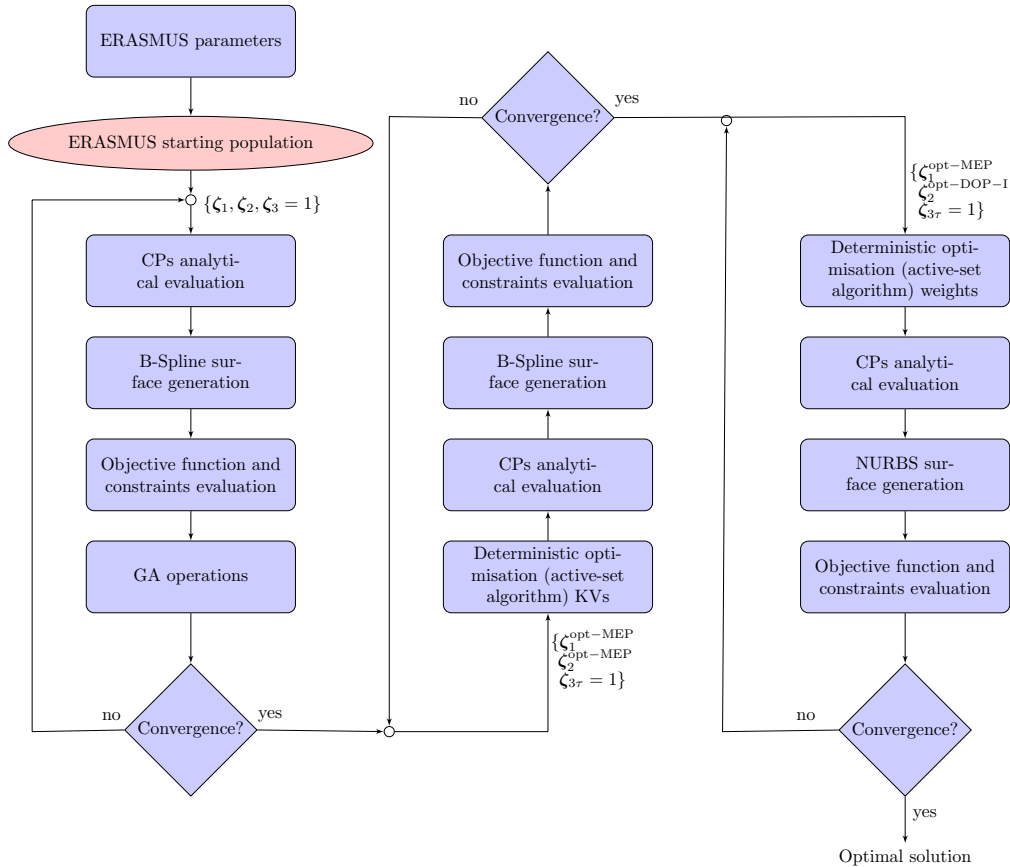


Figure 7.3 – Flowchart of the the hybrid surface fitting strategy.

7.2.2.1 The Meta-Heuristic Exploration Phase

During the MEP, only ζ_1 and ζ_2 are considered as design variables, whilst ζ_3 is set equal to a unit vector (i.e., $\zeta_{3\tau} = 1, \forall \tau = 1, \dots, n_{CP}$). According to Eqs. (3.1) and (3.2), this choice corresponds to consider a B-spline surface instead of a NURBS one. To take into account for the variable number of KV components, the objective function has been modified with respect to Eq. (7.11), i.e.,

$$\Phi(\zeta_1, \zeta_2, \zeta_3) := \begin{cases} \tilde{f}^{\frac{1}{r_1+r_2}}, & \text{if } \tilde{f} < 1, \\ \tilde{f}^{r_1+r_2}, & \text{if } \tilde{f} > 1, \end{cases} \quad (7.25)$$

with

$$\tilde{f}(\zeta_1, \zeta_2, \zeta_3) := \sum_{\alpha=x,y,z} \sum_{k=1}^N \left[\frac{\alpha(u_{1k}, u_{2k}) - \alpha_k}{L_{\max}} \right]^2 + \lambda J_\alpha K_{\max}. \quad (7.26)$$

In Eq. (7.25), the quantities L_{\max} and K_{\max} are used to get a dimensionless objective function. In particular, L_{\max} is the maximum distance between TPs, whilst K_{\max} is the maximum Gaussian curvature evaluated on the tessellation. The quantity $\frac{1}{r_1+r_2}$ (or $r_1 + r_2$, depending on the value of \tilde{f}) appears as a power of the function \tilde{f} in order to find a good balance between KVs size and accuracy of the surface approximation. In particular, thanks to the introduction of this power function, the number of the non-trivial components of the KVs is kept low during the MEP. In this way is it possible to minimise the dimensionless error estimator \tilde{f} by minimising also the number of non-trivial components of the KVs (and, thus, the number of CPs along both parametric directions). Furthermore, it is noteworthy that the role of the term J_α ($\alpha = x, y, z$) is twofold. On the one hand, it allows avoiding over-fitting by controlling the smoothness of the fitting surface. On the other hand, it allows defining a well-posed mathematical problem, because it limits the growth of the degrees p_j ($j = 1, 2$) of the blending functions during optimisation [134, 138].

As stated above, the optimal value of the CPs coordinates is the solution of the linear system of Eq. (7.18). However, for some particular combinations of degrees, number and values of KVs components (i.e., p_j , r_j and $v_i^{(j)}$, respectively) the matrix $\mathbf{G} + \lambda\mathbf{E}$ in Eq. (7.18) could possess almost null eigenvalues, so its inversion could be ill-conditioned. In order to overcome this issue, a check on the possible singularity of this matrix has to be performed to ensure the presence of dimensionless parameters u_{jk} ($j = 1, 2$, $k = 1, \dots, N$) in each knot span [137, 138]. Accordingly, a constraint on the rank of matrix $\mathbf{G} + \lambda\mathbf{E}$ must be introduced, i.e.,

$$g(\zeta_1, \zeta_2, \zeta_3) := n_{\text{CP}} - \text{rank}(\mathbf{G} + \lambda\mathbf{E}) = 0. \quad (7.27)$$

Finally, the optimisation problem for the MEP can be stated in the form

of an unconventional CNLPP as

$$\begin{aligned} & \min_{\zeta_1, \zeta_2} \Phi(\zeta_1, \zeta_2, \zeta_3), \\ & \text{subject to:} \\ & \begin{cases} g(\zeta_1, \zeta_2, \zeta_3) = 0, \\ \zeta_{1-\text{lb}} \leq \zeta_1 \leq \zeta_{1-\text{ub}}, \\ 0 < \zeta_{2k} < 1, \quad k = 1, \dots, r_1 + r_2, \\ \zeta_{3\tau} = 1, \quad \forall \tau = 1, \dots, n_{\text{CP}}, \end{cases} \end{aligned} \quad (7.28)$$

where $\zeta_{1-\text{lb}}$ and $\zeta_{1-\text{ub}}$ are suitable lower and upper bounds on the integer design variables. It is noteworthy that problem (7.28) is defined over a domain of changing dimension whose size (which corresponds to the number of design variables) is $N_{\text{DV-MEP}} = 4 + r_1 + r_2$.

The solution search for problem (7.28) is carried out by means of the ERASMUS algorithm [139]. In this context, a B-spline surface can be considered as a modular system where r_j and p_j are the design variables of the non-modular part of the system, whilst each KV represents the generic module whose variables are $\beta_i^{(j)}$, $i = p_j + 1, \dots, m_j - p_j - 1$, $j = 1, 2$. A B-spline surface is, thus, composed of two modules corresponding to the KVs.

In ERASMUS, an individual represents a candidate solution for the problem at hand. The individual's genotype of ERASMUS for problem (7.28) is illustrated in Fig. 7.4. As it can be inferred from this figure, the genotype is made of three sections. The first one is the *standard section*, which is made of two chromosomes constituted of two genes coding the integer design variables of the non-modular part of the B-spline surface, i.e., p_j, r_j , $j = 1, 2$. Second and third sections are *modular sections*. The number of chromosomes of each modular section is equal to the number of non-trivial knots r_j (coded within the standard section) and each chromosome is made of a single gene coding the variable $\beta_i^{(j)}$ related to the knot $v_i^{(j)}$ according to Eq. (7.22). Inasmuch as the value of r_j can be different for each individual, the length of the modular sections (i.e., the number of chromosomes) is not necessarily the same among the individuals belonging to the same populations. In ERASMUS, the length of the modular section is related to the concept of *species*: individuals with a different number of chromosomes belong to different species. As a consequence, when the surface fitting problem is formulated in the most general case, the ERASMUS algorithm represents a very efficient tool to perform the solution search because it allows for the *simultaneous evolution* of both species and individuals. In other words, the evolution of the population is obtained by simulating the reproduction

phase (through dedicated genetic operators) among individuals of the same species and among individuals belonging to different species. For a deeper insight in the matter, the interested reader is addressed to [139].

7.2.2.2 The Deterministic Optimisation Phase

As stated above, the DOP is split in two steps. During the first step only KVs components are considered as design variables and the pseudo-optimal solution found at the end of the MEP, i.e., $\zeta_1^{\text{opt-MEP}}$, $\zeta_2^{\text{opt-MEP}}$, is used as initial guess. In particular integer variables are kept constant and equal to $\zeta_1^{\text{opt-MEP}}$, weights take unit value as in the case of MEP, whilst only vector ζ_2 represents the design variables vector of the first step of the DOP.

The surface fitting problem is stated as a conventional CNLPP as fol-

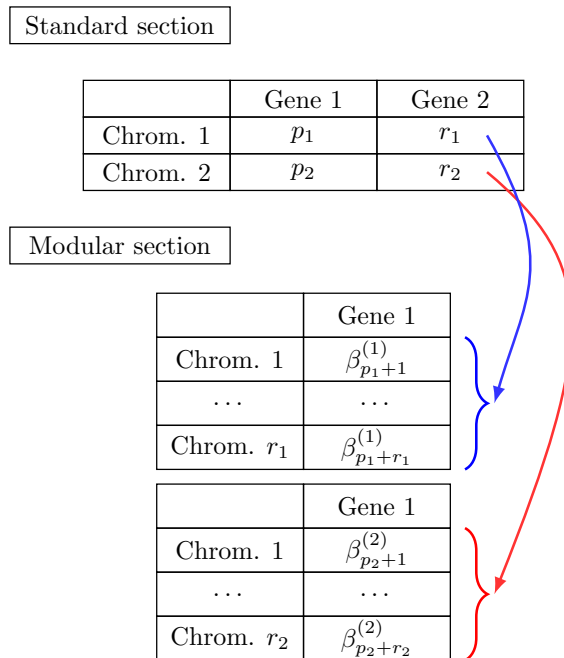


Figure 7.4 – Individual's genotype.

lows:

$$\begin{aligned} & \min_{\zeta_2} \tilde{f}(\zeta_1, \zeta_2, \zeta_3), \\ & \text{subject to:} \\ & \begin{cases} g(\zeta_1, \zeta_2, \zeta_3) = 0, \\ \zeta_1 = \zeta_1^{\text{opt-MEP}}, \\ 0 < \zeta_{2k} < 1, \quad k = 1, \dots, r_1 + r_2, \\ \zeta_{3\tau} = 1, \quad \tau = 1, \dots, n_{\text{CP}}, \end{cases} \end{aligned} \quad (7.29)$$

where \tilde{f} is defined in Eq. (7.25). In this case, the number of design variables does not change during the iterations and is equal to $N_{\text{DV-DOP-I}} = r_1 + r_2$. The optimised solution, i.e., $\zeta_2^{\text{opt-DOP-I}}$, together with the values of the $\zeta_1^{\text{opt-MEP}}$ and $\zeta_{3\tau} = 1, \forall \tau$ is used as initial guess for the second step of the DOP. In this case only NURBS weights, collected in the vector ζ_3 , are considered as design variables, the remaining quantities being equal to the optimal values provided by the previous optimisation calculations. For the second step of the DOP the CNLPP reads:

$$\begin{aligned} & \min_{\zeta_3} \tilde{f}(\zeta_1, \zeta_2, \zeta_3), \\ & \text{subject to:} \\ & \begin{cases} g(\zeta_1, \zeta_2, \zeta_3) = 0, \\ \zeta_1 = \zeta_1^{\text{opt-MEP}}, \\ \zeta_2 = \zeta_2^{\text{opt-DOP-I}}, \\ \zeta_{3-\text{lb}} \leq \zeta_3 \leq \zeta_{3-\text{ub}}, \end{cases} \end{aligned} \quad (7.30)$$

where $\zeta_{3-\text{lb}}$ and $\zeta_{3-\text{ub}}$ are lower and upper bounds on the weights. As stated above, the goal of the DOP is to reach the nearest feasible minimiser starting from the pseudo-optimal solution found at the end of the MEP. To this end, the active-set algorithm available in the MATLAB *fmincon* function [145] has been used to perform the solution search. In order to solve problems (7.29) and (7.30) by means of the active-set algorithm, the derivatives of the objective function \tilde{f} with respect to KVs components and CPs weights must be computed. The analytical expression of these derivatives is provided in Appendix C.

Remark 7.2.1. *Since the optimisation constraint $g(\zeta_1, \zeta_2, \zeta_3)$ of Eq. (7.27) is a discontinuous function related to the rank of matrix $\mathbf{G} + \lambda\mathbf{E}$, its gradient is not evaluated during the DOP. In particular a preliminary check is done before evaluating the objective function and its gradient: if constraint $g(\zeta_1, \zeta_2, \zeta_3)$ is not met, the objective function is penalised to a high value.*

7.3 General Strategy for Genus G Surfaces (Open and Closed)

The approach presented in Sec. 7.2 can be applied to open surfaces of genus $g = 0$. Nevertheless, by introducing some modifications it can be extended also to the most general case of open and closed surfaces of genus $g = G > 0$, i.e., open and closed surfaces characterised by handles and/or holes. To this purpose, a semi-automatic multi-step procedure for surface reconstruction of complex surfaces of genus greater than zero is described in this Sec..

The whole procedure is articulated in three steps. The first one is the manual segmentation (performed by the user) of the complex discrete surface available in the form of a tessellation. The goal is to split the tessellation in suitable patches meeting the requirements foreseen by SPM [96] to perform the mapping of each patch. The segmentation, as shown in Fig. 7.5, consists of partitioning the tessellation in open patches of genus $g = 0$. Furthermore, the user has to properly define the sorting of patches and, for each patch, a set of four corners, which represent the extremes of the unit square wherein each patch is mapped through the SPM. Thanks to this requirement, after carrying out the mapping phase by means of the SPM, consecutive patches will have consistent parametric (dimensionless) coordinates at adjacent (coincident) edges.

It is noteworthy that to deal with the segmentation problem of surfaces of genus greater than zero, some basic rules have been followed, in agreement with some examples presented in [146]. The main steps of the segmentation phase are:

- Identification and isolation of the protruded zones of the triangulated surface. The protrusion function on a point of the tessellation is the sum of its geodesic distances from all the other surface points; large values of this function denote that the point belongs to a protrusion.
- Generation of patches to isolate the holes and/or the handles present on the discrete surface.
- Definition of each patch as an open discrete surface, with the related set of boundary points.

A possible automation of this approach is represented by the region growing method [146], which consists of classifying each vertex of the TS with the value of the segmentation objectives and the expansion of distinct seed elements until the satisfaction of a certain termination criterion. The interested reader is addressed to [146] for a deeper insight in the matter.

The second step is the mapping phase, which is carried out for each

patch according to the SPM [96] briefly recalled in Sec. 7.1.

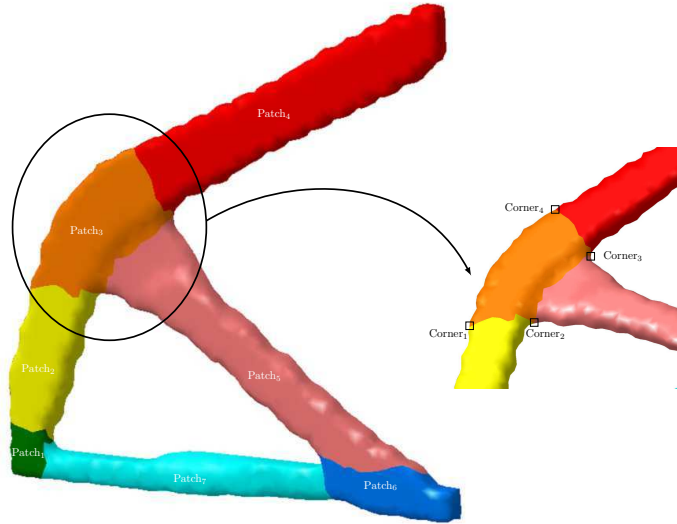


Figure 7.5 – Manual segmentation.

Then, the information obtained from these steps are exploited in the fitting phase (the third and last step of the procedure), which is performed on a set of opportunely connected NURBS surfaces (denoted as poly-NURBS entity in the following). The fitting phase is articulated in two steps. Firstly, the connectivity map between the NURBS surfaces composing the poly-NURBS entity is defined according to the user-defined patch sorting introduced in the segmentation phase. The connectivity map matrix $\mathbf{M}_{\text{conn}} \in \mathbb{R}^{n_p \times n_p}$ (n_p being the number of patches defined during the segmentation step), establishing the relationship between the NURBS surfaces fitting adjacent patches, is built as follows: the element ij is equal to the ID of the edge shared between patches i and j if they are adjacent, otherwise it is zero.

Secondly, C0 and C1 conditions are imposed between adjacent NURBS surfaces by following the order defined by the connectivity matrix \mathbf{M}_{conn} through a master-slave approach, as shown in Fig. 7.6. This operation is articulated in the following two steps.

1. C0 continuity between adjacent NURBS surfaces is ensured via the equivalence of the CPs coordinates for those CPs located on the boundary between the master patch and the surrounding slave patches.

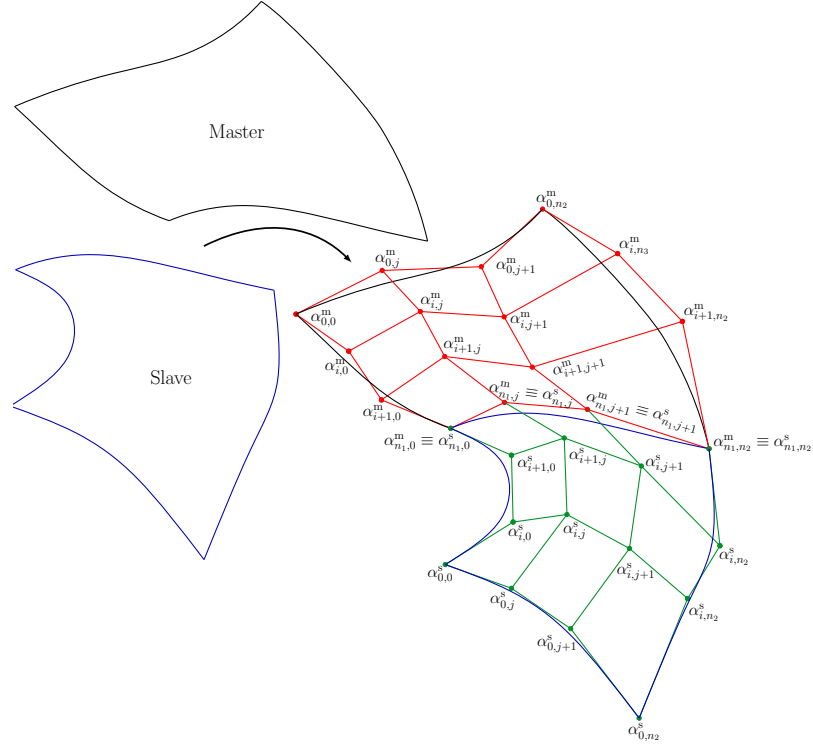


Figure 7.6 – C0 and C1 connectivity conditions.

2. By considering the notation used in Fig. 7.6, C1 continuity is imposed by forcing the collinearity of the rows of CPs located on the edges shared between consecutive patches by means of the following formula

$$\begin{cases} \alpha_{i+1,k_1}^s = 2\alpha_{i+1,k_1}^m - \alpha_{n_1,k_1}^m, & \text{with } k_1 = 0, \dots, n_2, \\ \alpha_{k_2,j+1}^s = 2\alpha_{k_2,j+1}^m - \alpha_{k_2,n_2}^m, & \text{with } k_2 = 0, \dots, n_1, \end{cases} \quad (7.31)$$

where superscripts s and m stand for slave and master patches, respectively. Once the NURBS surfaces composing the poly-NURBS entity are properly connected, problems (7.28), (7.29) and (7.30) are solved in cascade. The pseudo-code of the SPONS algorithm is detailed in Alg. 1.

It is noteworthy that, during the MEP, the connectivity between adjacent patches requires also a correct definition of the independent design variables (both integer and continuous) between patches, as shown in Fig. 7.7. In the case of the poly-NURBS entity, the overall number of independent design variables can be obtained as:

loa 1 – Genus G surface reconstruction strategy: the SPONS algorithm

1. Manual segmentation of the tessellation: creation of patches of genus 0; corners between adjacent patches must coincide.
2. \forall patch:
 - a) Perform the mapping phase according to the SPM [96].
 - b) Set the coincidence of parameters at each edge shared between adjacent patches.
3. Build the connectivity matrix \mathbf{M}_{conn} for the poly-NURBS entity to be used during the fitting phase.
4. Patches roto-translation, to align the local reference systems with the global one, to preserve the data coherence in the fitting phase.
5. Impose C0 and C1 continuity between adjacent NURBS surfaces according to Eq. (7.31).
6. Solve problems (7.28), (7.29) and (7.30) to get optimal values of the NURBS parameters. During the optimisation CPs coordinates are updated according to Eq. (7.18).

$$N_{\text{DV-MEP}} = 4n_p - 2 \sum_{k=1}^{2n_p} \sum_{l=1}^{2n_p} Z_{kl} + \sum_{k=1}^{2n_p} r_k - a_k, \quad (7.32)$$

where $\mathbf{r}, \mathbf{a} \in \mathbb{R}^{2n_p}$ and $\mathbf{Z} \in \mathbb{R}^{2n_p \times 2n_p}$ are particular arrays defined as

$$\mathbf{r}^T := \{r_1^{(1)}, \dots, r_1^{(n_p)}, r_2^{(1)}, \dots, r_2^{(n_p)}\}, \quad (7.33)$$

$$\mathbf{Z} := \frac{1}{2} (\mathbf{M} + \overline{\mathbf{M}}), \quad \mathbf{a} := \mathbf{Z}\mathbf{r}, \quad (7.34)$$

where matrices \mathbf{M} and $\overline{\mathbf{M}}$ are defined as

$$M_{kl} := \begin{cases} 1, & \text{if } \mathbf{v}_k^{(1)} = \mathbf{v}_l^{(1)}, \quad k = 1, \dots, n_p, \quad l = k, \dots, n_p, \\ 1, & \text{if } \mathbf{v}_k^{(1)} = \mathbf{v}_l^{(2)}, \quad \forall k = 1, \dots, n_p, \quad l = n_p + 1, \dots, 2n_p, \\ 1, & \text{if } \mathbf{v}_k^{(2)} = \mathbf{v}_l^{(2)}, \quad k = n_p + 1, \dots, 2n_p, \quad l = k, \dots, 2n_p, \\ 0, & \text{otherwise,} \end{cases} \quad (7.35)$$

$$M_{lk} = M_{kl},$$

$$\begin{aligned}\overline{M}_{kl} &:= M_{kl}, \quad k = 1, \dots, 2n_p, \quad l = k, \dots, 2n_p, \\ \overline{M}_{lk} &= -\overline{M}_{kl}, \quad k \neq l.\end{aligned}\tag{7.36}$$

An example of the design variables inheritance scheme among patches is illustrated in Fig. 7.7. The design variables involved in the MEP are passed automatically to the slave adjacent patches, according to one of the three following cases.

- If at the common edge master and slave patches share the parametric coordinate u_2 , the slave patch inherits the following variables $p_2^s = p_2^m$, $r_2^s = r_2^m$ and $\mathbf{v}_s^{(2)} = \mathbf{v}_m^{(2)}$.
- If at the common edge master and slave patches share the parametric coordinate u_1 , the slave patch inherits the following variables $p_1^s = p_1^m$, $r_1^s = r_1^m$ and $\mathbf{v}_s^{(1)} = \mathbf{v}_m^{(1)}$.
- If at the shared edge the parametric coordinate u_1 of the master patch is equal to the parametric coordinate u_2 of the slave patch, then the slave patch inherits the following variables $p_2^s = p_1^m$, $r_2^s = r_1^m$, $\mathbf{v}_s^{(2)} = \mathbf{v}_m^{(1)}$. Of course, labels 1 and 2 must be inverted in the converse situation, i.e., when at the shared edge the parametric coordinate u_2 of the master patch is equal to the parametric coordinate u_1 of the slave patch.

7.4 Studied Cases and Results

The effectiveness of the proposed strategy is tested on some meaningful benchmarks taken from the literature. These study cases focus on the surface reconstruction problem of both genus zero and genus $G > 0$ surfaces. In particular, six benchmark problems are illustrated and solved in this section: (BK1) the carpet-like surface, (BK2) the ear surface [147], (BK3) the face surface [148], (BK4) the thigh-bone surface [149], (BK5) a genus $g = 1$ surface, representing a region of the boundary of an optimised topology resulting from a 3D topology optimisation problem taken from [150], (BK6) the surface with genus $g = 1$ representing a Kettle [151]. The number of TPs, for the different test cases, is provided in Tab. 7.1. The design variables and their respective bounds are listed in Tab. 7.2, for each benchmark considered in this study.

The parameters tuning the behaviour of the ERASMUS algorithm, used during the MEP to solve problem (7.28), are listed in Tab. 7.3. Moreover, the handling of optimisation constraints is carried out through the automatic dynamic penalisation (ADP) technique, see [152]. The genotype of

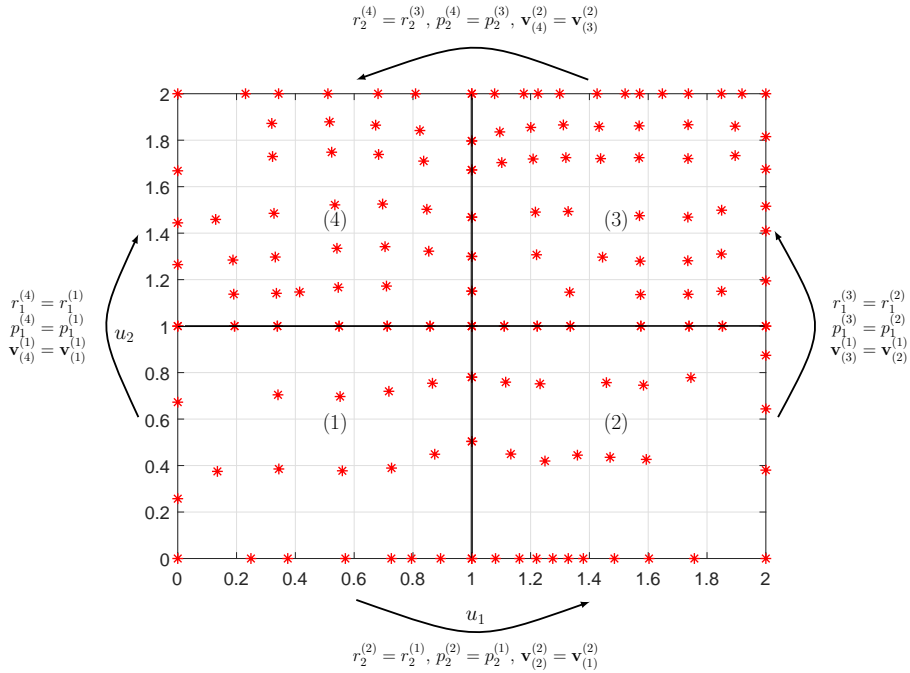


Figure 7.7 – Design variables inheritance among patches (red stars denote the parameters u_1 and u_2 resulting from the SPM for each patch).

Table 7.1 – Number of TPs for each benchmark.

	BK1	BK2	BK3	BK4				BK5, $n_p = 2$		BK5, $n_p = 4$				
patch n.	-	-	-	1	2	3	4	1	2	1	2	3	4	
N	142	5630	15276	1998	1449	4350	2169	1681	3568	1741	1243	1187	1254	
	BK6				BK7						BK8			
patch n.	1	2	3	4	1	2	3	4	5	6	1	2	3	4
N	253	1001	1160	235	748	120	648	248	654	546	1335	1536	692	584

Table 7.2 – Design variables bounds.

Benchmark	$[p_{1-lb}, p_{1-ub}]$	$[p_{2-lb}, p_{2-ub}]$	$[r_{1-lb}, r_{1-ub}]$	$[r_{2-lb}, r_{2-ub}]$	$[\beta_{lb}^{(1/2)}, \beta_{ub}^{(1/2)}]$	$[w_{i,j-lb}, w_{i,j-ub}]$
BK1			[1, 17]	[1, 17]		
BK2	[1, 6]	[1, 6]	[16, 35]	[16, 35]		
BK3			[16, 35]	[16, 35]		
BK4			[5, 20]	[5, 20]		
BK5, $n_p = 2$	[3, 5]	[3, 5]	[10, 20]	[10, 20]	[0.001, 0.999]	[1.0, 10.0]
BK5, $n_p = 4$			[5, 20]	[5, 20]		
BK6	[3, 6]	[3, 6]	[6, 20]	[6, 20]		
BK7			[6, 20]	[6, 20]		
BK8	[2, 4]	[2, 4]	[5, 15]	[5, 15]		

the individual, representing a candidate solution for problem (7.28), is illustrated in Fig. 7.4. Lower and upper bounds on the number of chromosomes

of the modular sections appearing in Tab. 7.3 are set equal to lower and upper bounds of integer variables r_i ($i = 1, 2$) reported in Tab. 7.2.

The parameters of the active-set algorithm, used during the DOP to solve problems (7.29) and (7.30), are given in Tab. 7.4. It is noteworthy that the quantity N_{DV} represents the number of design variables, which is not the same between first and second steps of the DOP.

Table 7.3 – Genetic parameters of the ERASMUS algorithm

Genetic parameters	Value
Number of populations (N_{pop})	1
Number of individuals (N_{ind})	200
Number of generations (N_{gen})	150
Crossover probability (p_{cross})	0.85
Gene mutation probability (p_{mut})	$1/N_{ind}$
Chromosomes shift probability (p_{shift})	0.5
Chromosomes number mutation probability (p_{mut-ch})	$\frac{n_{ch-ub} - n_{ch-lb}}{N_{ind}}$
Selection	Roulette-wheel
Elitism	Active

Table 7.4 – *Active-set* algorithm parameters

Parameter	Value
Solver	<i>active-set</i>
Maximum number of objective function evaluations	$100 \times N_{DV}$
Maximum number of iterations	1000
Tolerance on objective function	1×10^{-4}
Tolerance on constraints	1×10^{-4}
Tolerance on input variables change	10^{-4}
Tolerance on gradient norm of the Lagrange's function	10^{-6}

The numerical results, for each case, are collected in Tabs. 7.5 and 7.6, for MEP and DOP, respectively, whilst the computational time of each step of the fitting phase, measured on a work-station with an Intel Xeon E5-2697v2 processor (2.70–3.50 GHz) and four cores dedicated to the optimisation calculations, is listed in Tab. 7.7. For the sake of clarity, the results of the DOP reported in Tab. 7.6 are expressed in terms of normalised objective function. Regarding the first step of the DOP, the optimised solution provided by the MEP is used to normalise the merit function of Eq. (7.29). Analogously, for the second step of the DOP, i.e., Eq. (7.30), the optimal

solution of the first step of the DOP is used for normalisation purposes. Therefore, the normalised merit functions (for both steps) read:

$$\tilde{f}_{\text{DOP-I}} := \frac{\tilde{f}}{\tilde{f}_{\text{opt-MEP}}}, \quad \tilde{f}_{\text{DOP-II}} := \frac{\tilde{f}}{\tilde{f}_{\text{opt-DOP-I}}}. \quad (7.37)$$

The term \tilde{f}_{av} reported in Tab. 7.6 represents the average value of the objective function of Eq. (7.25), which can be related to the average (dimensionless) distance of the surface from the TPs. This term is defined as:

$$\tilde{f}_{\text{av}} := \frac{\sqrt{\tilde{f}}}{N}. \quad (7.38)$$

The Carpet-like surface (BK1)

The first benchmark is a genus zero open surface. The STL file of BK1 has been generated in CATIA[®] environment. The amount of TPs composing the STL file is provided in Tab. 7.1. Firstly, the mapping of the TPs cloud has been obtained via the SPM. Secondly, the surface fitting phase is performed by considering a single NURBS entity and by solving, in cascade, problems (7.28)-(7.30). The related optimal solutions are reported in Tabs. 7.5 and 7.6, while the optimal NURBS surface obtained at the end of the process, together with the related TPs cloud and the mapping resulting from the SPM, is illustrated in Fig. 7.8.

As it can be inferred from these results, during the MEP, the $N = 142$ TPs are fitted by a unique NURBS surface having $p_1 = p_2 = 5$ and only $r_1 = r_2 = 1$ non-trivial KVs components. This correspond to an overall number of CPs equal to $(n_1 + 1)(n_2 + 1) = 49$. This result is due to the formulation of the objective function Φ of Eq. (7.25), where the main purpose of the power of \tilde{f} is to limit the KVs sizes. This result is very interesting, essentially for two reasons. Firstly, the ratio of the TPs number to the CPs number is about 2.9, which implies a significant reduction in the information needed to describe such a surface with a good level of accuracy. Secondly, due to the low values of variables r_i , few design variables are involved in the subsequent DOP, which means reduced computational costs. Moreover, from the results reported in Tab. 7.6, one can infer that the optimisation steps constituting the DOP allow obtaining a strong reduction of the pseudo-optimal solution provided by the MEP. In particular, at the

Table 7.5 – MEP: numerical results.

Benchmark	p_1	p_2	r_1	r_2	n_1	n_2	Φ
BK1	5	5	1	1	6	6	0.0944
BK2	2	2	19	19	21	21	0.9635
BK3	5	5	16	16	21	21	0.9874
BK4 - patch 1	2	2	5	5	7	7	4.3974
BK4 - patch 2	2	5	5	6	7	8	
BK4 - patch 3	2	5	5	12	7	17	
BK4 - patch 4	2	5	5	6	7	11	
BK5 - patch 1	5	5	10	10	15	15	1.6776
BK5 - patch 2	5	5	10	10	15	15	
BK5 - patch 1	3	2	5	6	8	8	3.0333
BK5 - patch 2	3	3	5	5	8	8	
BK5 - patch 3	3	5	5	5	8	10	
BK5 - patch 4	3	3	5	5	8	8	
BK6 - patch 1	3	3	5	5	8	8	2.6691
BK6 - patch 2	3	3	5	5	8	8	
BK6 - patch 3	3	3	5	5	8	8	
BK6 - patch 4	3	3	5	5	8	8	
BK7 - patch 1	3	3	4	3	7	7	4.1436
BK7 - patch 2	3	3	3	6	6	9	
BK7 - patch 3	3	3	6	4	9	7	
BK7 - patch 4	3	3	4	3	7	6	
BK7 - patch 5	3	3	6	3	9	6	
BK7 - patch 6	3	3	4	6	7	9	
BK8 - patch 1	4	3	5	5	9	8	2.6481
BK8 - patch 2	4	3	5	5	9	8	
BK8 - patch 3	3	3	5	5	8	8	
BK8 - patch 4	3	3	5	5	8	8	

end of the first step of the DOP the improvement is about 91.4%, whilst at the end of the second step is about 91.6%. This means that KVs components and weights plays a key-role in the quality of the optimised NURBS surface.

The Ear Surface (BK2)

The second benchmark is a genus zero open surface of complex shape, whose projection over a plane has a non-unique solution for some points. The STL file, taken from [147], has been elaborated in CATIA[®] environment and is composed of a cloud of $N = 5630$ TPs. As in the case of BK1, also

Table 7.6 – DOP: numerical results.

Problem	$\tilde{f}_{\text{DOP-I}}$	$\tilde{f}_{\text{DOP-II}}$	\tilde{f}_{av}
BK1	0.0860	0.0844	$5.66e^{-5}$
BK2	0.9546	0.8923	$8.10e^{-5}$
BK3	0.0882	0.9596	$1.02e^{-4}$
BK4 - patch 1 BK4 - patch 2 BK4 - patch 3 BK4 - patch 4	0.3124	0.7488	$2.11e^{-4}$
BK5 - patch 1 BK5 - patch 2	0.8327	0.7595	$1.45e^{-4}$
BK5 - patch 1 BK5 - patch 2 BK5 - patch 3 BK5 - patch 4	0.0975	0.0696	$8.77e^{-6}$
BK6 - patch 1 BK6 - patch 2 BK6 - patch 3 BK6 - patch 4	0.9482	0.6303	$2.38e^{-4}$
BK7 - patch 1 BK7 - patch 2 BK7 - patch 3 BK7 - patch 4 BK7 - patch 5 BK7 - patch 6	0.7481	0.6981	$2.36e^{-4}$
BK8 - patch 1 BK8 - patch 2 BK8 - patch 3 BK8 - patch 4	0.9920	0.5558	$1.34e^{-4}$

for this example a unique NURBS surface is employed for the fitting phase. The TPs cloud, the surface parametrisation resulting from the application of the SPM and the optimal NURBS surface resulting from the optimisation process are illustrated in Fig. 7.9. As it can be inferred from the results provided in Tabs. 7.5 and 7.6, a NURBS surface with a control net made of 484 CPs is sufficient to fit the set of TPs with a good level of accuracy. Indeed, at the end of the MEP, the pseudo-optimal solution is characterised by a very good value of the merit function: the improvement due to the first step of the DOP is about 4.5%, while that of the second step (over the first

Table 7.7 – MEP and DOP: computational time [s].

Problem	MEP phase	DOP-I phase	DOP-II phase
BK1	11232	138	168
BK2	19008	186	180
BK3	14688	210	120
BK4 - patch 1	23328	222	66
BK4 - patch 2			
BK4 - patch 3			
BK4 - patch 4			
BK5 - patch 1	8640	336	150
BK5 - patch 2			
BK5 - patch 1	17280	480	78
BK5 - patch 2			
BK5 - patch 3			
BK5 - patch 4			
BK6 - patch 1	6048	300	60
BK6 - patch 2			
BK6 - patch 3			
BK6 - patch 4			
BK7 - patch 1	6912	360	120
BK7 - patch 2			
BK7 - patch 3			
BK7 - patch 4			
BK7 - patch 5			
BK7 - patch 6			
BK8 - patch 1	3456	90	60
BK8 - patch 2			
BK8 - patch 3			
BK8 - patch 4			

one) is equal to 11% (the effect of weights on the smoothness of the surface remains important). Moreover, the ratio of the TPs number to the CPs number is about 11.63, which implies a strong reduction in the information needed to describe the surface without degrading too much the accuracy. From the analysis of the results listed in Tab. 7.5 and 7.6 and from a visual inspection of Fig. 7.9, one can infer that the smoothing term of Eq. (7.12) fulfils its main purpose by controlling the value of the degrees of the final fitting surface. Of course, in this case, the size of the KVs is bigger than that of the KVs of BK1, because of the complex shape of the TPs cloud.

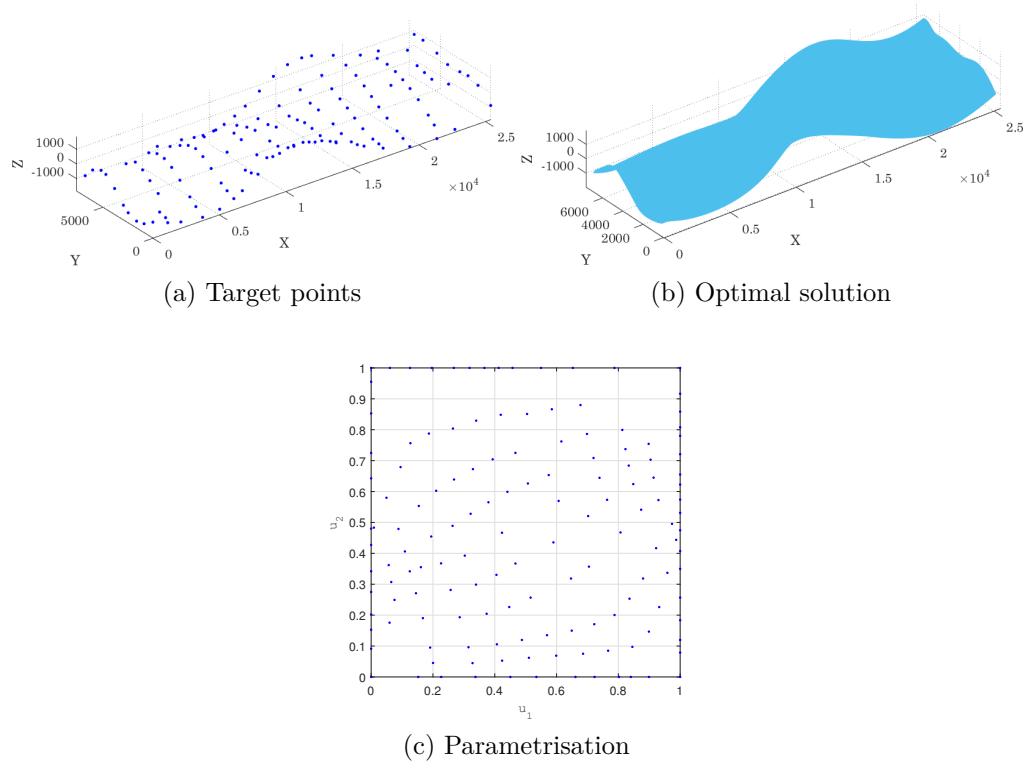


Figure 7.8 – The Carpet-like Surface (BK1)

The Face Surface (BK3)

This benchmark deals with the surface reconstruction of a genus zero open surface having the same complexity as that of BK2. The STL file, taken from [148], has been elaborated in CATIA[®] environment and is composed of a cloud of $N = 15276$ TPs. Also in this case, only one NURBS surface is employed for the fitting phase.

The TPs cloud, the surface parametrisation resulting from the application of the SPM and the optimal NURBS surface are illustrated in Fig. 7.10. As it can be inferred from the results provided in Tabs. 7.5 and 7.6, a NURBS surface with 441 CPs is sufficient to fit the set of TPs with a good level of accuracy. However, at the end of the MEP, the pseudo-optimal solution is still located far away from the local minimiser: the improvement due to the first step of the DOP is about 91%, while that of the second step (over the first one) is about 4%. Moreover, the ratio of the TPs number to the CPs number is about 34.64, which implies a strong reduction in the information needed to describe such a surface without degrading too much the accuracy.

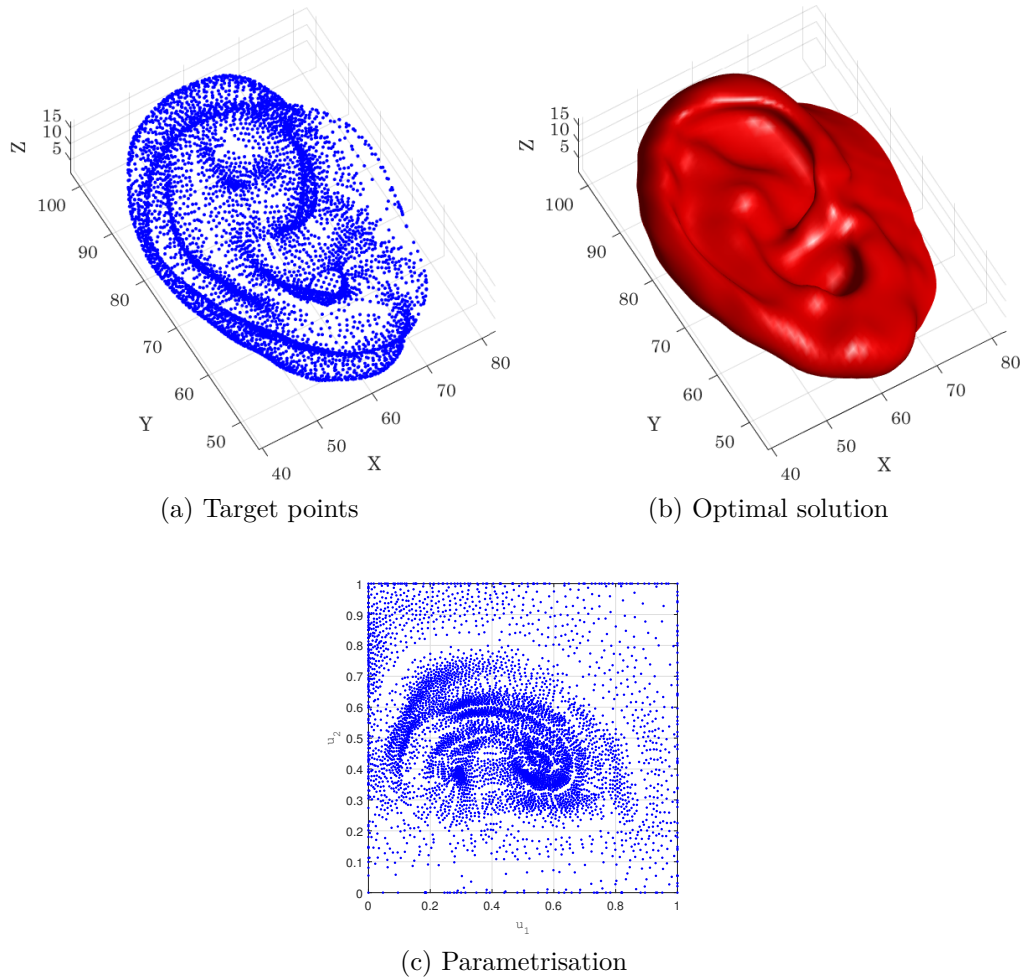


Figure 7.9 – The Ear Surface (BK2)

Regarding the effect of the smoothing term of Eq. (7.12), the same remarks as those of benchmark BK2 can be repeated here.

The Thigh-Bone Surface (BK4)

This benchmark consists of a genus zero open surface with a complex topology characterised by sub-domains having inhomogeneous shapes with protrusions and strong curvatures gradients.

To deal with the surface reconstruction of BK4, the general strategy for genus G surfaces, discussed in Sec. 7.3, has been employed. To this purpose, the STL file, taken from [149], has been elaborated in CATIA[®] environment

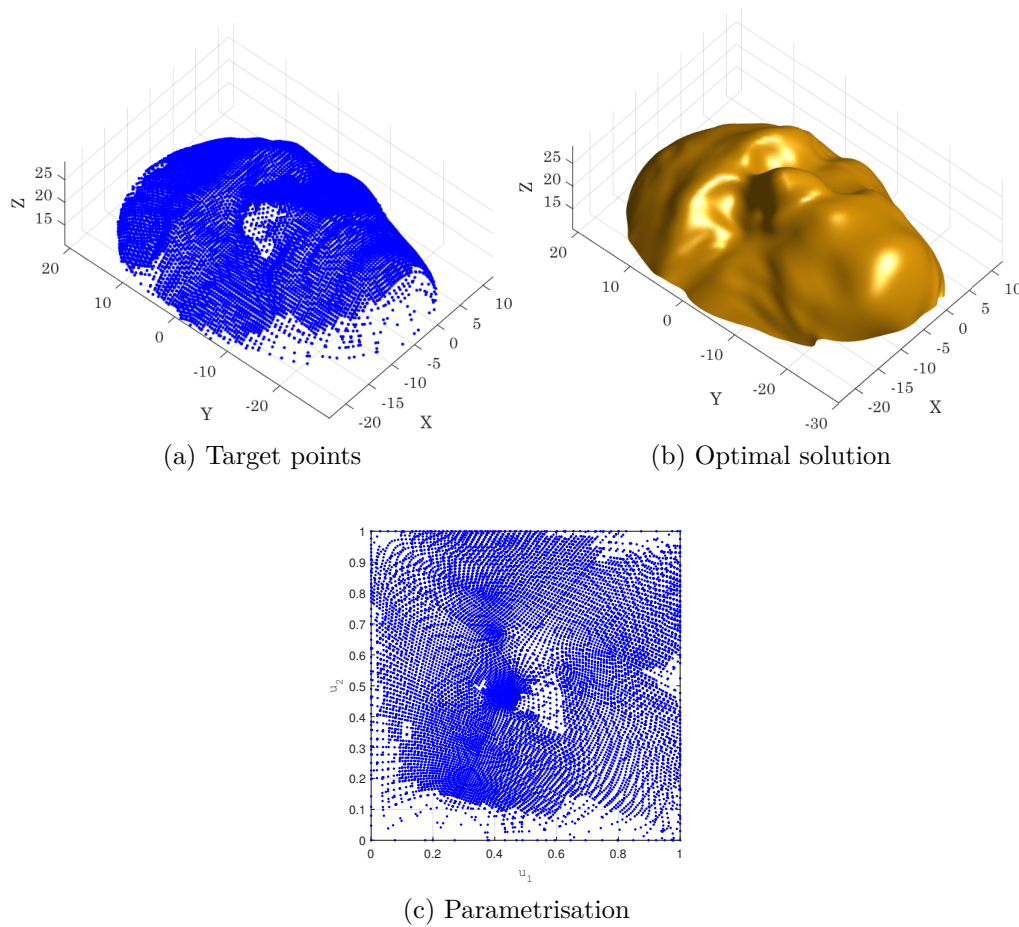


Figure 7.10 – The Face Surface (BK3)

and it has been manually split in four patches for an overall number of $N = 9966$ TPs, see Tab. 7.1. Of course, the segmentation of the tessellation is a manual step whose results depend upon the user's experience: in this case the patches have been defined in order to isolate the thigh-bone protrusion and epicondyles, in order to have sufficient information to correctly carry out the mapping phase.

The results of the SPM to get the surface parametrisation (for each patch) are illustrated in Fig. 7.11, while the TPs cloud and the optimal NURBS surfaces at the end of the MEP and of the DOP are shown in Fig. 7.12. As it can be inferred from the results provided in Tabs. 7.5 and 7.6, the pseudo-optimal solution found at the end of the MEP is located far away from the local minimiser: the improvement due to the first step of the DOP is about 69%, while that of the second step (over the first one) is about

25% (this result confirms the importance of the weights in influencing the shape of the NURBS surface for each patch). Moreover, the ratio of the TPs number to the CPs number is 18.72, 15.95, 30.21 and 22.59 for patches 1, 2, 3 and 4, respectively. As for the other benchmarks, this result implies a strong reduction in the information needed to describe such a surface by keeping a sufficient level of accuracy.

Regarding the effect of the smoothing term of Eq. (7.12), the same remarks as those of benchmarks BK2 and BK3 can be repeated here, mainly for the patches describing protrusions and epicondyles.

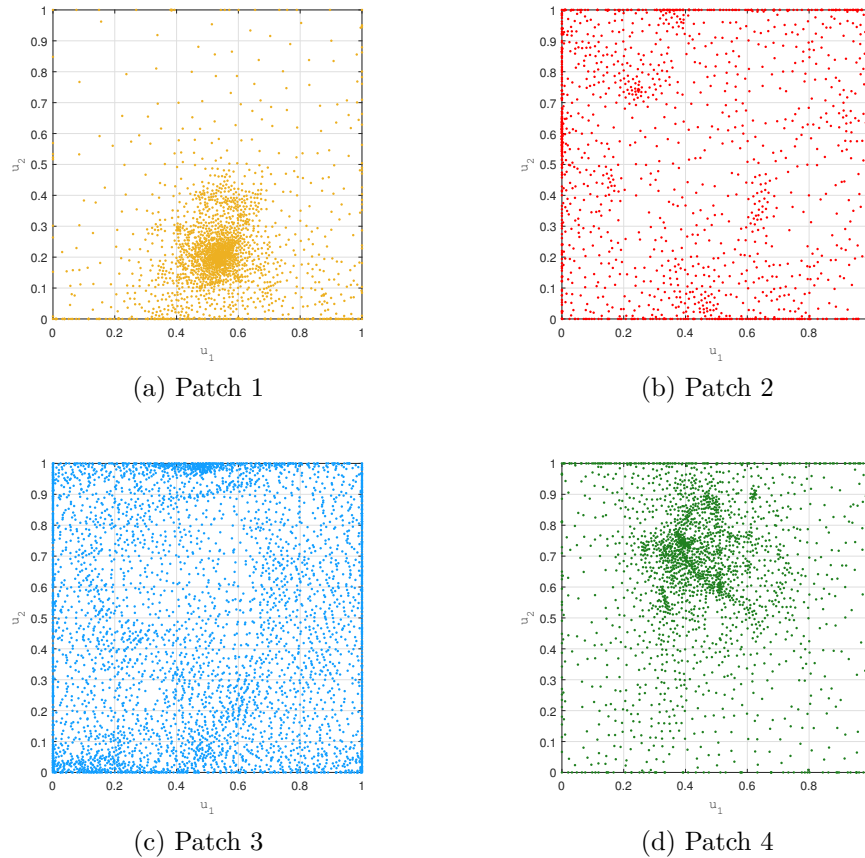


Figure 7.11 – The thigh-bone surface (BK4) - parametrisation through the SPM

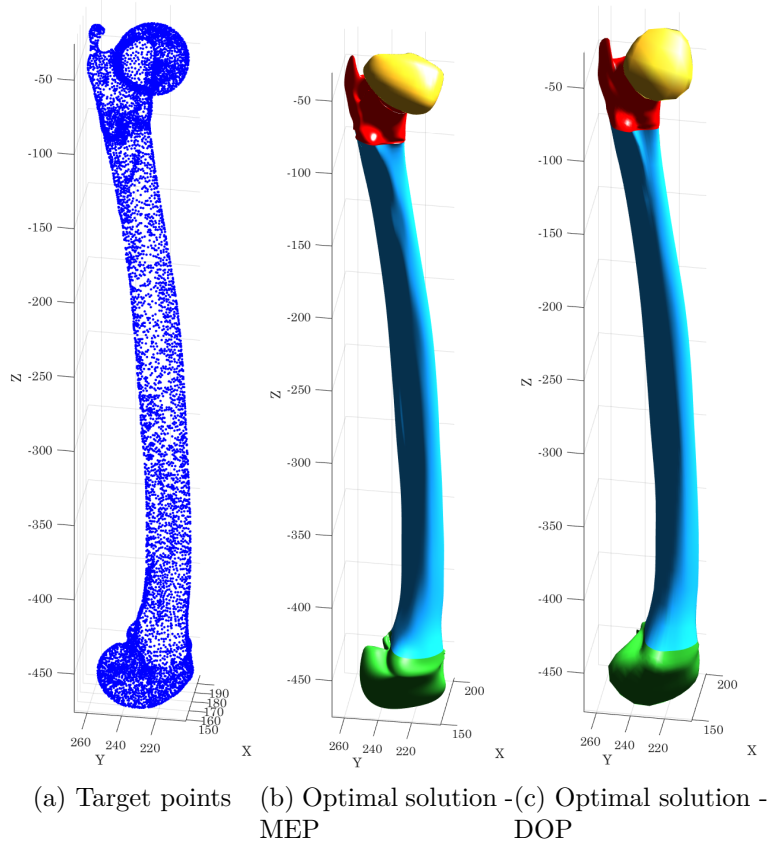


Figure 7.12 – The thigh-bone surface (BK4)

A Genus One Open Surface (BK5)

The fifth benchmark is a genus $g = 1$ open surface representing a sub-domain of the boundary of a 3D optimised topology taken from [150].

To deal with the surface reconstruction of BK5, the general strategy for genus G surfaces is considered. To this purpose, the STL file has been elaborated in CATIA[®] environment and is composed of an overall number of $N = 5425$ TPs, as indicated in Tab. 7.1. To show the influence of the number of patches on the quality of the final poly-NURBS entity fitting the TPs cloud, two cases have been considered: in the first one, the STL file has been split in $n_p = 2$ patches, whilst in the second one the number of patches is $n_p = 4$.

The results of the SPM to get the surface parametrisation (for each patch) for the cases $n_p = 2$ and $n_p = 4$ are illustrated in Figs. 7.13 and 7.14, while the TPs cloud and the optimal NURBS surfaces at the end of the MEP and

of the DOP for both cases are shown in Figs. 7.15 and 7.16, respectively. As it can be inferred from the results provided in Tabs. 7.5 and 7.6, the pseudo-optimal solution found at the end of the MEP is located far away from the local minimiser for both cases: the improvement due to the first step of the DOP is about 17% for $n_p = 2$ and about 90% for $n_p = 4$, while that of the second step (over the first one) is about 24% for $n_p = 2$ and about 93% for $n_p = 4$. This result confirms, on the one hand, the importance of the weights in influencing the shape of the NURBS surface for each patch and, on the other hand, the importance of having a sufficient number of patches to correctly approximate a given set of TPs. Moreover, the ratio of the TPs number to the CPs number is 6.57 and 13.94 for patches 1 and 2, respectively, in the case $n_p = 2$, while it is 21.49, 15.35, 11.99 and 15.48 for patches 1, 2, 3 and 4, respectively, in the case $n_p = 4$. As for the other benchmarks, this result implies a strong reduction in the information needed to describe such a surface by keeping a sufficient level of accuracy. Regarding the effect of the smoothing term of Eq. (7.12), the same remarks as those of the other benchmarks can be repeated here.

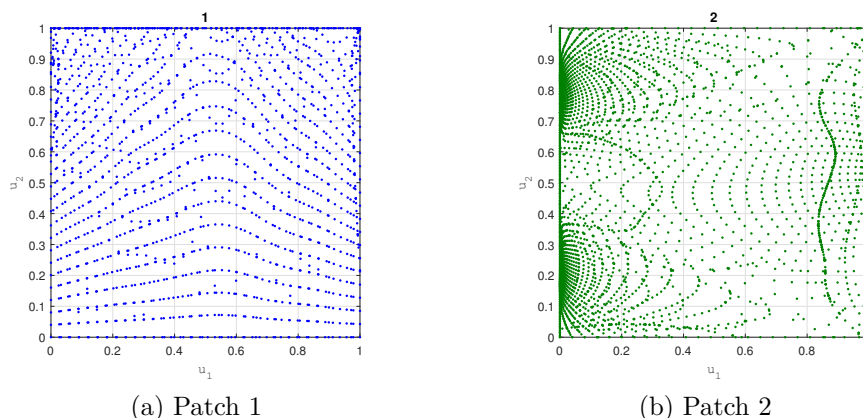


Figure 7.13 – A genus $g = 1$ open surface (BK5) - parametrisation through the SPM, case $n_p = 2$.

The Kettle Surface (BK6)

The sixth benchmark is a genus $g = 1$ open surface representing half of the model of a kettle taken from [151].

To deal with the surface reconstruction of BK6, the general strategy for genus G surfaces is considered. To this purpose, the STL file has been

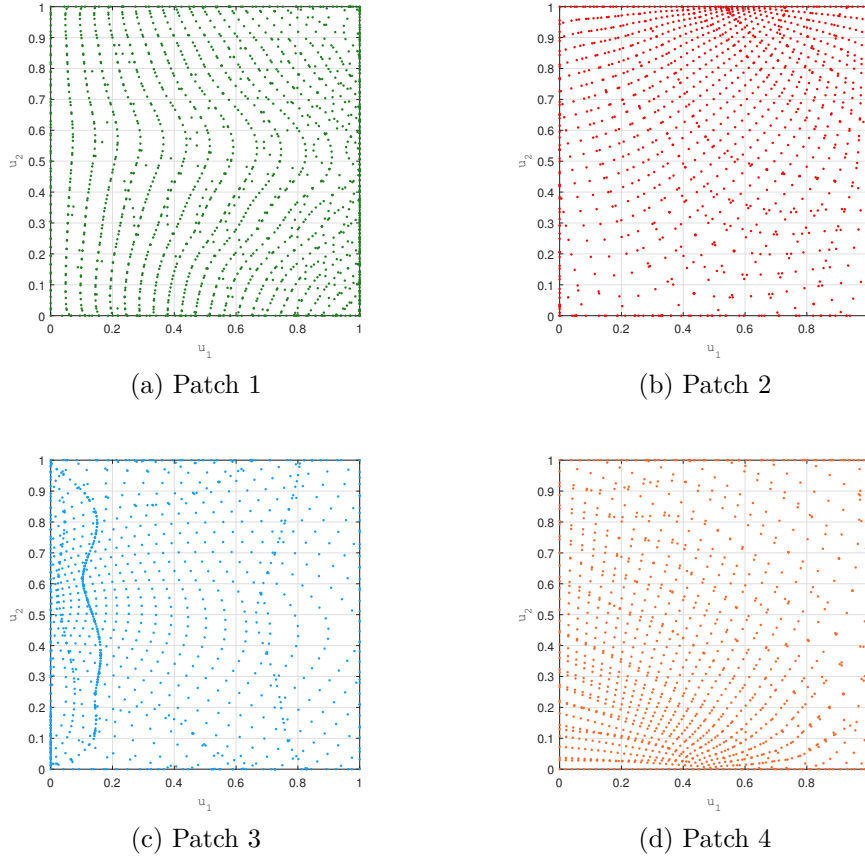


Figure 7.14 – A genus $g = 1$ open surface (BK5) - parametrization through the SPM, case $n_p = 4$.

elaborated in CATIA[®] environment and it has been manually split in four patches for an overall number of $N = 2649$ TPs, as indicated in Tab. 7.1. The results of the SPM to get the surface parametrization (for each patch) are illustrated in Fig. 7.17, while the TPs cloud and the optimal NURBS surfaces at the end of the MEP and of the DOP are shown in Fig. 7.18. As it can be inferred from the results provided in Tabs. 7.5 and 7.6, the pseudo-optimal solution found at the end of the MEP is located far away from the local minimiser: the improvement due to the first step of the DOP is about 65%, while that of the second step (over the first one) is about 34% (the influence of the weights is important also for this benchmark problem). Moreover, the ratio of the TPs number to the CPs number is 3.12, 12.36, 14.32 and 2.90 for patches 1, 2, 3 and 4, respectively. As for the other benchmarks, this result implies a strong reduction in the information

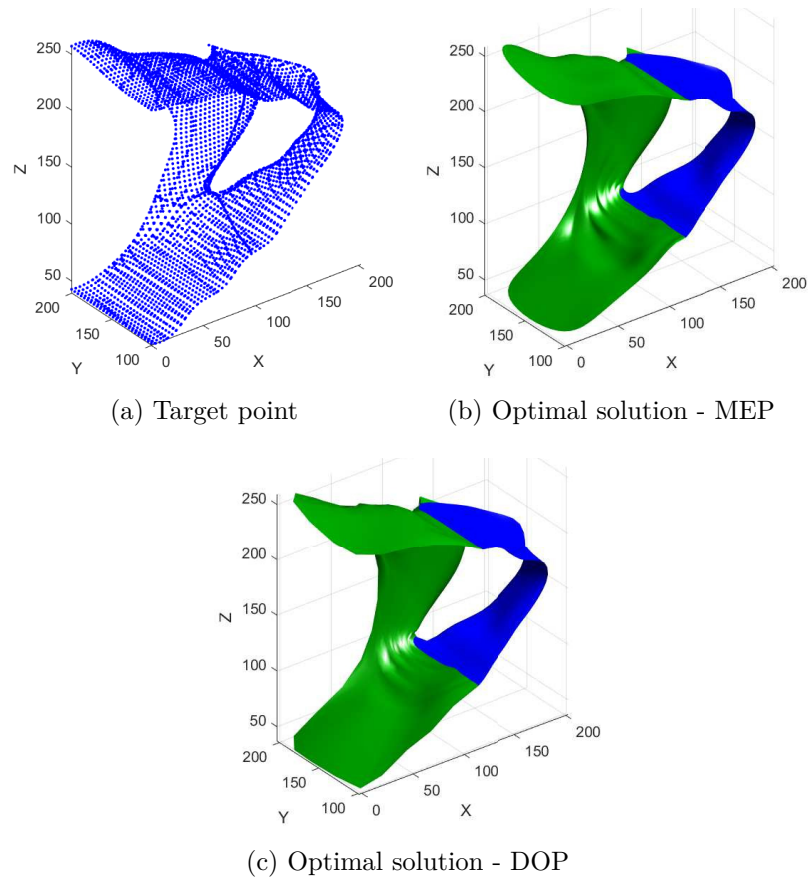


Figure 7.15 – A genus $g = 1$ open surface (BK5), case $n_p = 2$.

needed to describe this surface by keeping a sufficient level of accuracy. Regarding the effect of the smoothing term of Eq. (7.12), the same remarks as those of the other benchmarks can be repeated here.

Discussion on the Design Variables Bounds

The choice of proper bounds of design variables has a strong impact on the result of the surface fitting problem. Therefore, some remarks inherent to the definition of these bounds, reported in Tab. 7.2, are provided here below. In particular, lower and upper bounds have been established according to the following considerations.

Continuous design variables bounds are simple to set.

- From Eq. (7.22), $\beta_i^{(j)}$ is defined in the interval $]0, 1[$.
- The weights of the NURBS surface can get, *a priori*, any real value in

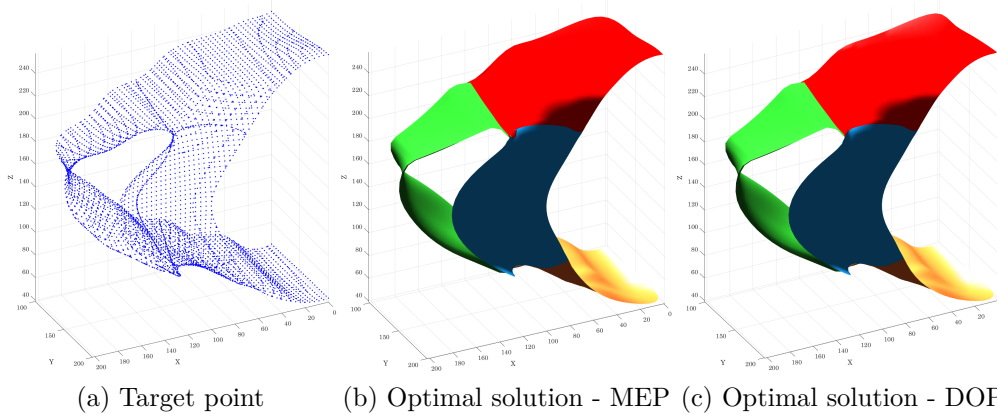


Figure 7.16 – A genus $g = 1$ open surface (BK5), case $n_p = 4$.

the range $]0, \infty[$. After a preliminary check on the first three benchmarks, it was observed that the surface shape is influenced by the ratio $w_{i,j-\text{ub}}/w_{i,j-\text{lb}}$ rather than by the value of the weight related to each CP. Moreover, the influence of weights become significant only in presence of singularities or strong curvatures gradients. Taking into account these considerations, the bounds on the weight have been set as $w_{i,j-\text{lb}} = 1$ and $w_{i,j-\text{ub}} = 10$.

The integer design variables have a strong impact on the shape of the NURBS surface and their bounds must be carefully set.

- The minimum degree is, of course, $p_{j-\text{lb}} = 1$, $j = 1, 2$. The maximum degree has been fixed in order to avoid the introduction of noise that can become important when the upper bound is not properly set. Accordingly, the maximum degree has been set to $p_{j-\text{ub}} = 6$.
- In order to establish lower and upper bounds for the number of the non-trivial KVs components r_j ($j = 1, 2$), the user should think about an ideal number of CPs tuning the shape of the approximating NURBS surface. Indeed, this problem applies also in case of standard curve/surface fitting methods (which are not capable of automatically optimise discrete parameters), where the user does not dispose of any criterion to choose a suitable number of CPs. In the framework of the proposed method, the ERASMUS algorithm is able to automatically determine the optimum number of both KVs components and degrees of the basis functions and, thus, the related optimal number of CPs $n_{\text{CP}} = (p_1 + r_1 + 1)(p_2 + r_2 + 1)$. Of course, the bounds on variables r_j can be inferred according to empirical rules (taken from practice), utilised to define a criterion for setting the

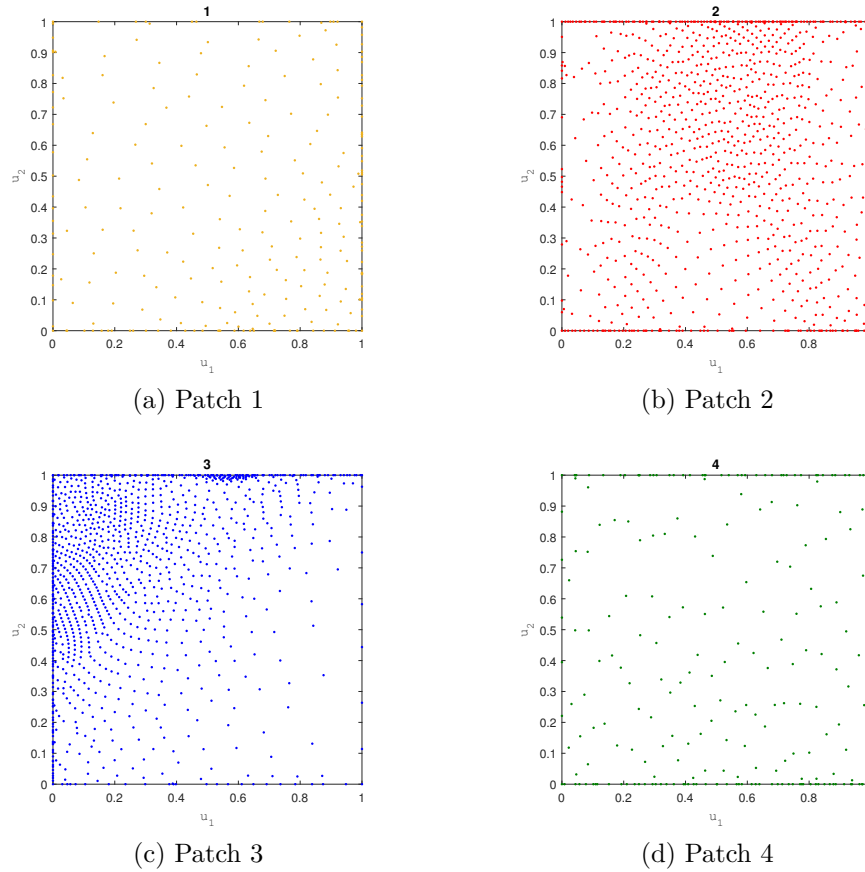


Figure 7.17 – The Kettle surface (BK6) - parametrization through the SPM

minimum and maximum number of CPs. In particular, the bounds on n_j can be set according to the following rules: (i) usually, the number of TPs should be, at least, three times the overall number of CPs; (ii) a suitable interval can be defined around this average value; in particular, the maximum number of CPs along each parametric direction must be lower than the number of TPs, whilst the minimum one should be always greater than or equal to two.

Since the proposed hybrid surface reconstruction strategy (and the related optimisation algorithms) is very efficient, it can be asserted that it is not important to choose the “right” narrow interval. When the shape of the surface is particularly complex and does not let the user guesses the size of the interval, a wider range can be set, being the GA ERASMUS able to determine automatically the optimum value of the discrete parameters. Indeed, thanks to the special features of the ERASMUS algorithm [139], it

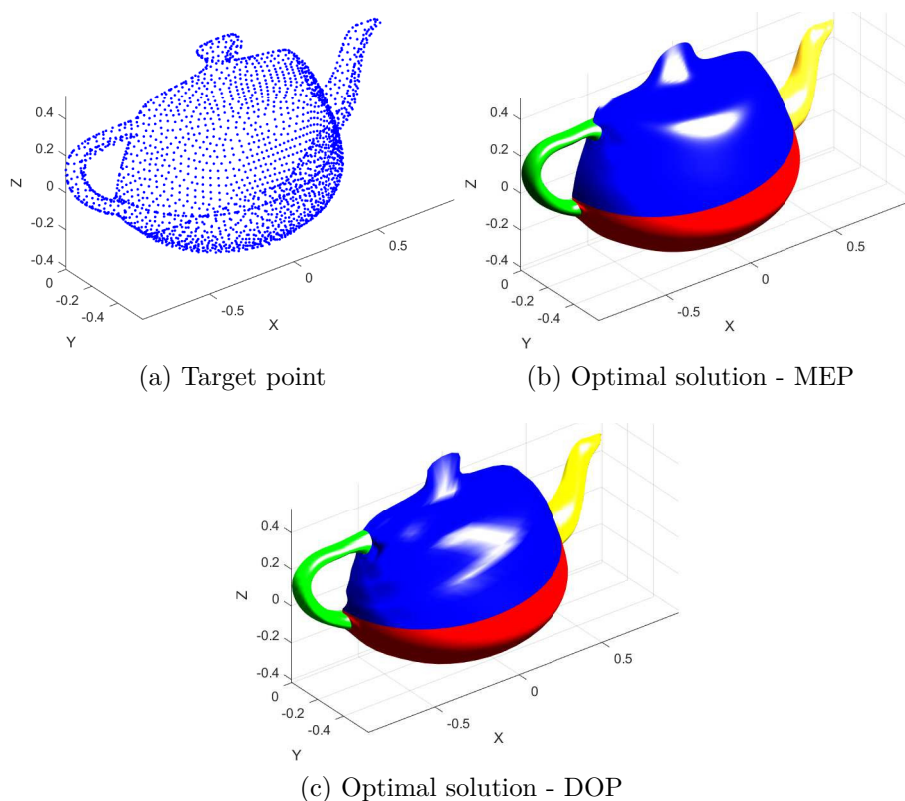


Figure 7.18 – The Kettle surface (BK6)

can be stated that the user's choice has a lower impact in the context of the proposed surface reconstruction approach when compared to classical ones.

7.5 Comparison with Surface Reconstruction Methods from the Literature

In this Section, a quantitative comparison, in terms of different fitting error estimators, between the proposed surface reconstruction method and some methods found in the literature is presented. Two benchmark problems taken from the literature are considered to this purpose: (BK7) the Fan Disk closed surface [153] and (BK8) the Club closed surface [154].

The Fan Disk Surface (BK7)

The seventh benchmark is a genus $g = 0$ closed surface representing a portion of a Fan Disk taken from [155].

To deal with the surface reconstruction of BK7, the general strategy for closed surfaces is considered. To this purpose, the STL file has been elaborated in CATIA[®] environment and it has been manually split in six patches for an overall number of $N = 2964$ TPs, as indicated in Tab. 7.1.

The results of the SPM to get the surface parametrisation (for each patch) are illustrated in Fig. 7.19, while the TPs cloud and the optimal NURBS surfaces at the end of the MEP and of the DOP are shown in Fig. 7.20. As it can be inferred from the results provided in Tabs. 7.5 and 7.6, the pseudo-optimal solution found at the end of the MEP does not fall in the neighbourhood of the local minimiser: the improvement due to the first step of the DOP is about 82%, while that of the second step (over the first one) is about 7% (in this case the influence of the weight is lower than in the case of the other benchmark problems). Moreover, the ratio of the TPs number to the CPs number is 11.69, 1.719, 9.26, 4.43, 9.34 and 6.83 for patches 1, 2, 3, 4, 5 and 6, respectively. As for the other benchmarks, this result implies a strong reduction in the information needed to describe such a surface by keeping a sufficient level of accuracy.

Regarding the effect of the smoothing term of Eq. (7.12), the same remarks as those of the other benchmarks can be repeated here. The comparison between the result provided by the proposed methodology and the one taken from [153] is reported in Tab. 7.8. The comparison is done in terms of both the maximum error (i.e., the maximum value of the distance between the points of the TPs cloud and the fitting surface) and the average error (according to Eq. (7.38)). As it can be inferred from Tab. 7.8 the proposed strategy outperforms, in terms of accuracy, the one proposed by Lavoué *et al.* [153].

The Club Surface (BK8)

The eighth benchmark is a genus $g = 0$ closed surface representing a portion of a Golf Club [156].

To deal with the surface reconstruction of BK8, the general strategy for closed surfaces is considered. To this purpose, the STL file has been elaborated in CATIA[®] environment and it has been manually split in 4 patches for an overall number of $N = 4151$ TPs, as indicated in Tab. 7.1.

The results of the SPM to get the surface parametrisation (for each patch) are illustrated in Fig. 7.21, while the TPs cloud and the optimal NURBS

Table 7.8 – Comparison of DOP results with state of the art algorithms.

Problem		Eck <i>et al.</i> [154]	Lavoué <i>et al.</i> [153]	The proposed approach
BK7	max. error.	-	1.02e-2	4.60e-3
	average error	-	-	2.36e-4
BK8	max. error	1.20e-3	-	1.58e-4
	average error	1.79e-4	-	1.34e-4

surfaces at the end of the MEP and of the DOP are shown in Fig. 7.22. As it can be inferred from the results provided in Tabs. 7.5 and 7.6, the pseudo-optimal solution found at the end of the MEP is not placed in the vicinity of the local minimiser: the improvement due to the first step of the DOP is about 63%, while that of the second step (over the first one) is about 44% (in this case the weights play a fundamental role in improving the accuracy of the fitting surface). Moreover, the ratio of the TPs number to the CPs number is 14.8, 17.07, 8.54 and 7.21 for patches 1, 2, 3 and 4, respectively. As for the other benchmarks, this result implies a strong reduction in the information needed to describe such a surface by keeping a sufficient level of accuracy.

Regarding the effect of the smoothing term of Eq. (7.12), the same remarks as those of the other benchmarks can be repeated here. Both maximum and average fitting errors are compared to those taken from [154]. As in the case of BK7, the proposed strategy outperforms the one presented in the study by Eck *et al.* [154], in terms of both global and local accuracy of the fitting surface.

7.6 Conclusions and prospects

In this Chapter, an efficient and general surface reconstruction strategy for open and closed surfaces of genus greater than or equal to zero has been presented. This strategy is, indeed, able of fitting convex and non-convex sets of TPs and is articulated into two phases: the *mapping phase* and the *fitting phase*. The proposed approach relies on the following features.

- The mapping phase makes use of the SPM method to retrieve a proper parametrisation of each sub-domain composing the TPs cloud.
- The fitting phase is formulated in the most general sense, i.e., without introducing simplifying hypotheses or rules on the set of parameters affecting the shape of the NURBS surface, which is used as a parametric entity to fit the set of TPs. To this purpose, a new expression of the objective function (taking into account for both

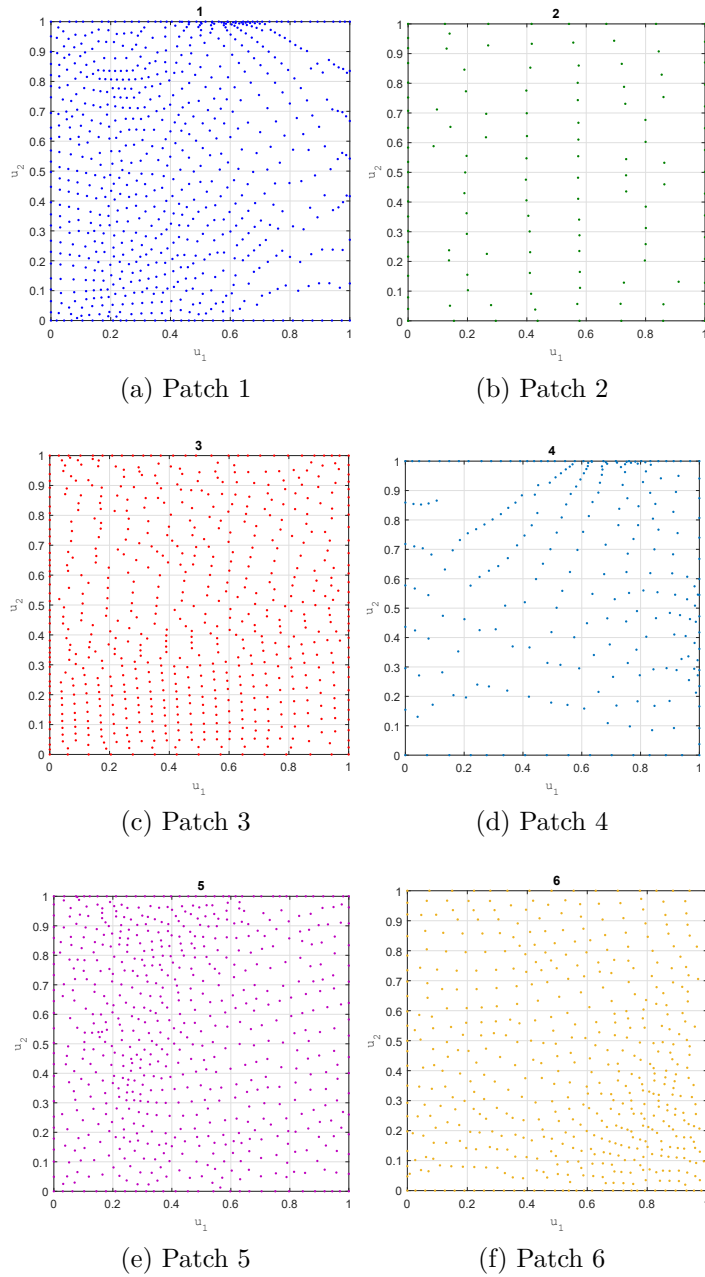


Figure 7.19 – The Fan Disk surface (BK7) - parametrisation through the SPM

integer and continuous variables tuning the shape of the NURBS entity), together with a suitable constraint on the non-singularity of the blending functions matrix, has been introduced. Moreover, the

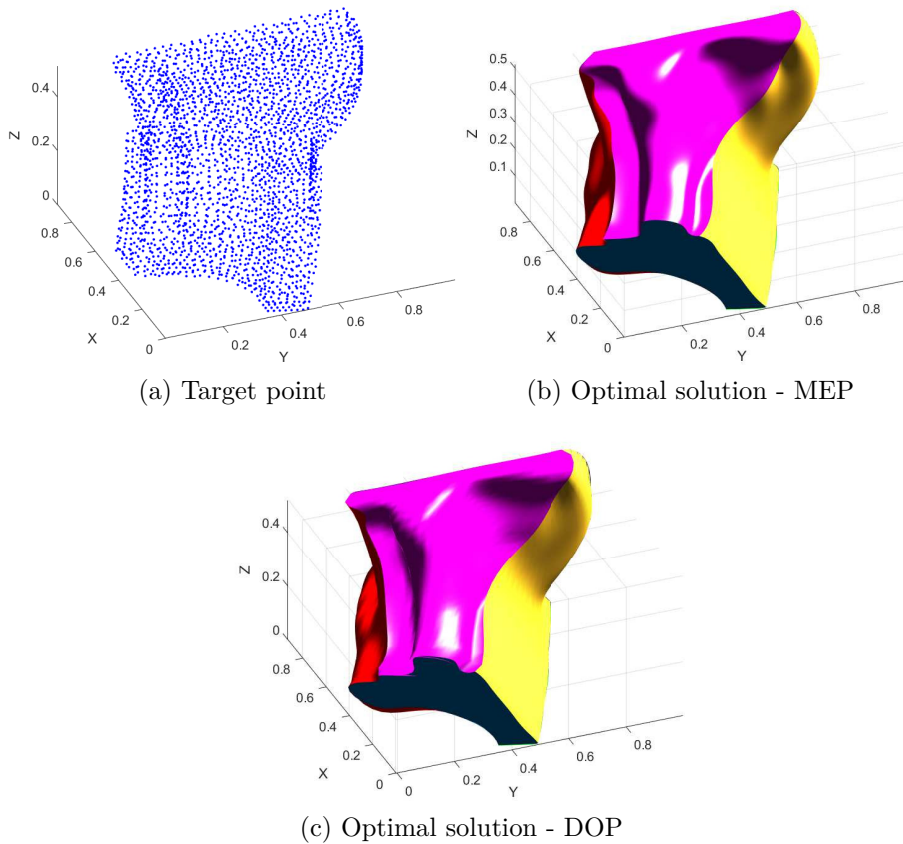


Figure 7.20 – The Fan Disk surface (BK7)

problem is stated as a special CNLPP, wherein the number of unknowns is included among the design variables. In fact, when integer parameters (i.e., degrees and number of knots along each parametric direction) are included, together with the continuous ones (i.e., the knots values and the weights), among the design variables, the resulting CNLPP is defined over a space of changing dimension, thus requiring a special optimisation algorithm to find a feasible optimal solution.

- The non-convexity of the problem and the fact that the design space has a changing dimension are the two main reasons at the basis of the use of advanced numerical strategies to solve the related CNLPP. To this purpose, the solution search for the surface fitting problem is performed by means of a hybrid optimisation tool composed by the union of the GA ERASMUS coupled to a deterministic algorithm. The optimisation strategy is split in two steps. The first one is

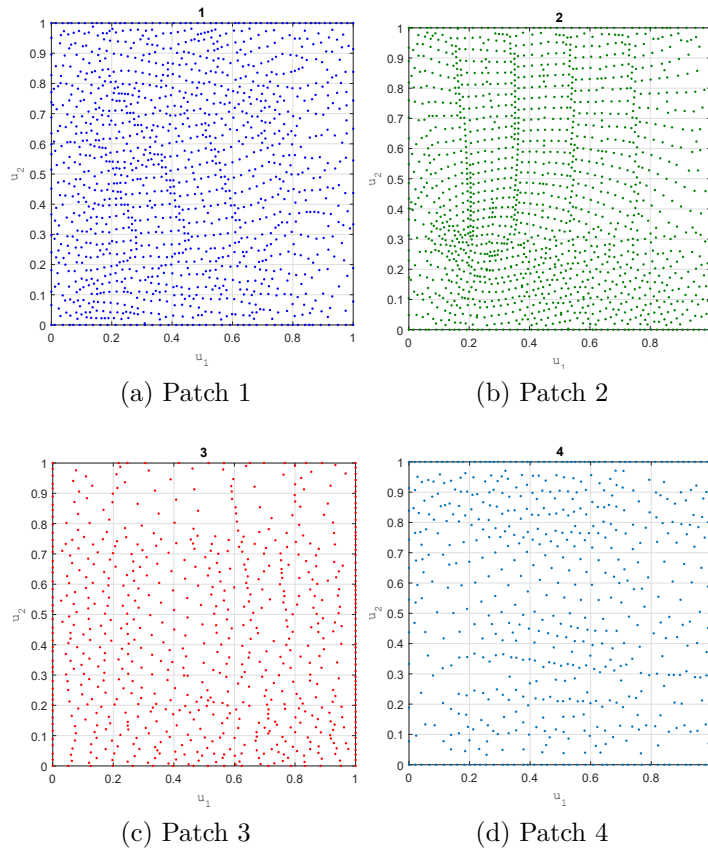


Figure 7.21 – The Club surface (BK8) - parametrisation through the SPM

the MEP, where the ERASMUS algorithm is used to determine, simultaneously, the best value of both integer and continuous design variables. Thanks to a two-level Darwinian strategy (allowing for the simultaneous evolution of species and individuals) this algorithm is able to find a solution for a CNLPP defined over a space of variable dimension (i.e., with a variable number of design variables). The aim of the MEP is to provide the starting guess for the subsequent DOP where only continuous variables are optimised, while integer ones are kept constant.

- The fitting phase (and the related CNLPP formulation) has also been generalised to the case of open and closed surfaces of genus greater than zero where an assembly of NURBS surfaces (referred to as poly-NURBS entity), properly connected, is used to fit the non-convex set of TPs.

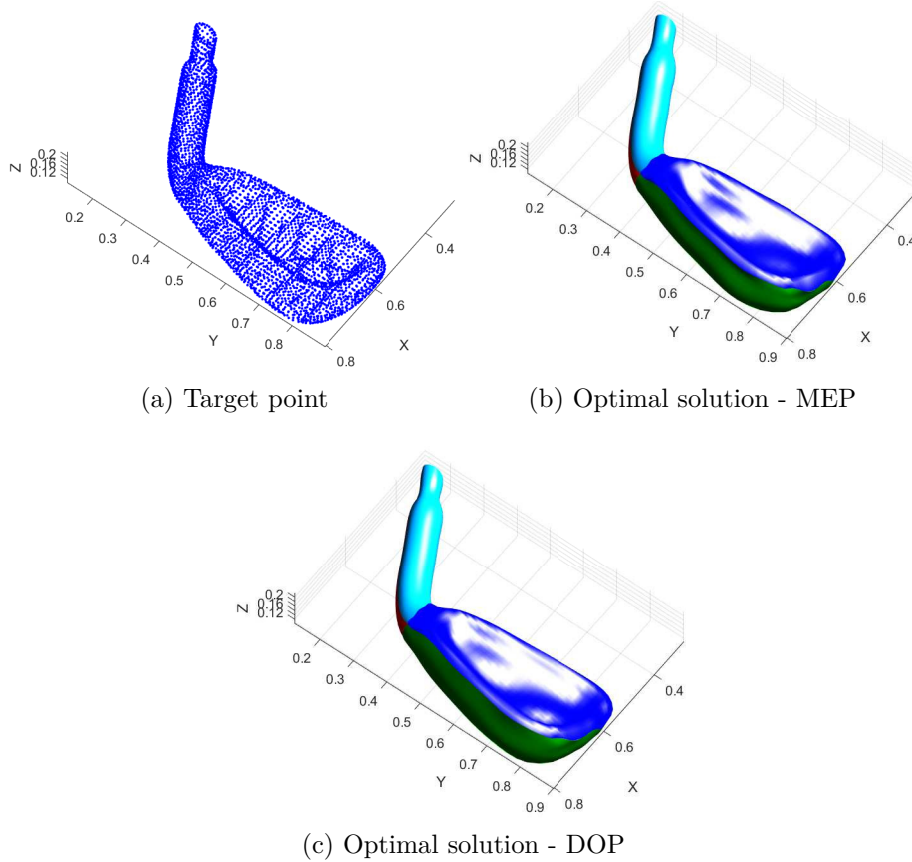


Figure 7.22 – The Club surface (BK8)

The effectiveness of the proposed approach has been tested on some meaningful benchmarks taken from the literature: the results obtained through the proposed method outperforms, in terms of accuracy, those available in the literature. Moreover, the performances of the proposed methodology are also provided in terms of computational time of the whole fitting phase. As expected, the highest amount of computational effort is related to the MEP. Conversely, the computational costs of the DOP are kept low because the gradient of the objective function has been determined in a closed form. As far as prospects of this work are concerned, two challenges still need to be faced. The first one is the development of a completely automatic segmentation strategy to define the patches splitting the tessellation. The aim of this strategy is to reduce the user's arbitrary decisions that could affect the shape of the patches (and, thus, the result of the mapping phase and the quality of the fitting surface). The second challenge consists of a

general formulation of the segmentation problem as a constrained optimisation problem. In particular, what is the best strategy to split a given tessellation? What is the optimal number of patches ensuring a correct parametrisation of the whole tessellation? What is the optimal segmentation strategy minimising the distortion and the error of the final fitting surface? Research is ongoing on the above aspects.

Chapter 8

Conclusions and prospects

A series of detailed conclusions are provided at the end of each Chapter. More wide-ranging conclusions and prospects are drawn in this last Chapter.

8.1 General conclusions

This Ph.D. has been developed in the framework of the COFFA project. The main aim of this work is a) the integration of the specificities of the multi-scale analysis in the TO optimisation framework, in particular its implementation in the software SANTO already developed in the laboratory I2M, b) the development of a semi-automatic surface reconstruction strategy to recover the boundary of the optimised topology to facilitate its integration within a CAD software.

The original version of NURBS-based SIMP method and the SANTO algorithm, presented in the Ph.D. thesis [109] and developed in Matlab[®] environment, was conceived to deal with single-scale problems for which the topological descriptor is defined solely at the scale of the structure. In the framework of the COFFA project, the aforementioned algorithm has been coded in and adapted to the Python[™] environment to enhance the performances in terms of computational time. This re-coding operation which is characterised technical and algorithmic issues, has not been detailed in this manuscript because it is not relevant from a scientific perspective. Nevertheless, the new version of the software SANTO has been validated through some of the 2D and 3D benchmark structures presented in the Ph.D. thesis by G. Costa [109] by obtaining the same results. To this purpose, a brief overview of the NURBS-based SIMP method, of the SANTO algorithm and its main standard features, is detailed in Chapter 3.

The method has been generalised to multi-scales problems with a topo-

logical descriptor defined only at the representative volume element (RVE) scale, in Chapter 4. In this case the design requirements are defined at both lower and upper scales. When dealing with this kind of problems, the first question that compulsory rise is: which is the best numerical homogenisation method to be coupled with the topology optimisation? The homogenisation method has not only to provide the equivalent elastic behaviour of the RVE at the upper scale in a time compatible with the topology optimisation process, but it has also to allow the calculation of the gradient of physical responses at the upper scale with respect to the topological variable defined at the rve scale with the less amount of operations (and, thus, by minimising the computational costs). In Chapter 4, it is shown that the strain energy homogenisation method (SEHM) based on the elements strain energy is the method that allows determining both the equivalent properties of the material and the gradient of the macroscopic structural responses with respect to the topological descriptor of the RVE with a computational effort lower than the one required to the variant of SEHM based on elements stresses.

Secondly a set of sensitivity analyses is conducted to study the influence of the initial solution and of the boundary conditions defined at the macroscopic scale on the optimal topology of the RVE: it has been highlighted that these aspects are of paramount importance in the definition of the optimal topology at the lower scale.

Similarly to previous works on the SIMP-based NURBS method, the influence of the integer parameters of the NURBS, i.e., the number of control points (CPs) and degree degrees of the Bernstein's polynomials, on the optimal topology of the RVE has been studied. It has been shown that some of the previous rules established for the topology optimisation for single-scale problems are not valid in this case. Nevertheless, one of the first advantages of the NURBS-based SIMP method, already highlighted in [109], is confirmed: it is possible to implicitly control, i.e., without adding explicit constraint in the optimisation problem, the minimum printable size by tuning the number of control points and degree of the Bernstein's polynomials used to define the NURBS entity.

In Chapter 5, the framework presented in Chapter 4 has been further generalised by considering TO problems where the topological descriptor is defined at multiple scales. This framework can be directly applied to the design of architected cellular materials (ACMs). Nevertheless, when dealing with the problem of the simultaneous optimisation of the topology at the macroscopic scale and at the RVE scale, different challenges have to be addressed. Particularly, since during the optimisation process the topological branches at the macroscopic scale can become of the same order of magni-

tude of the characteristic length of the RVE, this would make inconsistent the results provided by the SEHM, since the fundamental hypotheses of the method would not be respected. For this reason, a constraint on the scale separation has been introduced as minimum length scale on the topological variable defined at the macroscopic scale by imposing that the minimum size of the topological branches is equal to a multiple of the RVE characteristic length.

This constraint can be easily imposed by exploiting the feature of the local support of the NURBS entities and by tuning the discrete parameters, without introducing an explicit constraint in the optimisation problem. Moreover, the problem has been formulated in the most general case, by considering mixed non-zero Neumann-Dirichlet boundary conditions and by introducing the general definition of compliance proposed in [112].

In this context, it has been shown that the optimal topology at both RVE scale and macroscopic scale is strongly influenced from the BCs imposed at the macroscopic scale. Moreover, a sensitivity analysis has been conducted to show the influence of the type of the elastic symmetry of the RVE (orthotropy vs. anisotropy) on the optimal topology at both scales: depending on the applied boundary conditions at the upper scale, the optimised topology at both scales is strongly influenced by the hypotheses introduced on the RVE behaviour in terms of elastic symmetry of the equivalent material at the upper scale.

Chapter 6 presents an experimental and numerical validation of the optimal topologies found with the NURBS-based SIMP method extended to multi-scale TO problems with weak coupling discussed in Chapters 4 and 5. The experimental tests have been carried out on a structure subjected to 3PBT-like loading conditions. Three different formulations of the problem have been considered: in the first case, the topological variable is introduced only at the macroscopic scale; in the second case the topological descriptor is defined only at the RVE scale; in the third case, the topological descriptor is defined at both scales. The problem is solved considering both the 2D case and the 3D case. A series of non-linear analyses was carried out a posteriori on the optimised topologies integrating the bending behaviour of the bulk material with which the specimens are made and the specificities of the contact region between the part and the test machine supports. The results of the non-linear numerical analyses are in good agreement with the results of the experimental tests carried out on the optimised specimens and, thus, validate the effectiveness of the NURBS-based SIMP method for multi-scale TO problems. In addition, the results obtained show that, depending on the type of loads introduced to the macroscopic scale, opting for multi-scale topological optimisation is not always a good choice: in the

case of 3PBT, monolithic optimal solutions, i.e., those obtained considering the topological descriptor only at the macroscopic scale, show a bending stiffness considerably greater (with the same total mass) than that of the optimal solutions characterised by the use of architected cellular materials

Finally, Chapter 7 introduces a semi-automatic surface reconstruction strategy starting from the data available through a points cloud or STL file. On the one hand, the introduced method is based on a fast and effective parameterisation technique, i.e., the shape preserving method, which allows to transform the STL file into a two-dimensional graph defined on the unit square that is exploited to calculate the dimensionless parametric coordinates associated with each point to calculate the distance of each target point from the corresponding point belonging to the NURBS surface that constitutes the fitting surface. On the other hand, the method makes use of a general fitting strategy based on an original formulation of the problem that aims to optimise, simultaneously, the continuous and discrete variables that intervene in the definition of the NURBS surface. However, when the surface fitting problem is formulated in the most general case, including all NURBS variables in the optimisation process, the resulting CNLPP is defined on a domain of changing dimensions where the size depends on the integer parameters of the NURBS entity, i.e., the number of CPs and degrees of blending functions. In order to find a solution, a hybrid optimisation algorithm developed at the I2M laboratory has been used, which is based on an genetic algorithm (GA) allowing the simultaneous evolution of individuals and species (in this case the notion of species is associated with the dimension of the design space). In the case of surfaces of genus $G > 0$ or of particularly complex topology (e.g., characterised by protrusions and/or strong variation of local curvatures), this strategy applies to a poly-NURBS entity: in this case, the STL file is segmented manually by the user and the reconstruction strategy applies to each NURBS patch composing the poly-NURBS entity by automatically ensuring the continuity conditions between adjacent patches. The reconstruction strategy has been tested on several benchmark cases taken from the literature showing results equal or superior to those of existing strategies in commercial CAD and computer graphics software.

8.2 Prospects

The work done during this Ph.D. thesis is far from being exhaustive in the framework of the multi-scale TO problems and the development of post-processing strategies.

Particularly, research is ongoing about the development of a dedicated mathematical formalism (and of the related numerical framework) to integrate strong coupling among scales in the context of multi-scale TO problems. The idea is to make use of a dedicated global-local modelling strategy to correctly assess the strong coupling between scale, to integrate this coupling within the optimisation algorithm and to properly assess the failure phenomena appearing at the lower scale, which strongly influence the redistribution of the material, which strongly influence the redistribution of lower and upper scales.

Regarding global-local modelling -approach, a particular attention should be put on the development of failure criteria relevant to the multi-scale TO with a topological descriptor defined on multiple scales. What criteria should be applied to the most critical regions at the macroscopic scale where the continuum is modelled as an equivalent homogeneous solid? How to identify the most critical zone of interest (ZOI) and transfer the strain field to the RVE scale? How to calculate the gradients of the structural responses, at each scale, with respect to the topological descriptors introduced at the different scales in the presence of strong coupling? This problem is anything but trivial if one considers that at the macroscopic scale the ZOI changes at each iteration because the topology at the macroscopic scale evolves. Moreover, depending on the considered point, the strain field used at the RVE scale to check the local failure mechanisms is never the same and may present sudden variations, between two successive iterations.

Regarding the multi-scale TO method described in Chapter 5, it should be extended to the case of ACM composed of different RVE topologies. In this case it would be fundamental to impose constraints on the continuity of geometry at the interface between different types of RVE. How can this type of constraint be integrated into the strategy? What is the impact of such a constraint on the formulation of the problem? Is it possible to exploit the properties of NURBS to simplify this problem?

The proposed method could be used effectively in the case of multi-field problems involving design requirements of different nature (structural, thermal, etc.) in the formulation of the problem. Specifically, the strategy presented in Chapter 5 could be used to optimize the ACM used in scaffolds and/or lightweight prostheses by introducing criteria of a physical and geometric nature to stimulate the colonization of ACM by adjacent bone tissue

The multi-scale TO method discussed in Chapter 5 could be further generalized by including the orientation of the RVE among the optimisation variables defined at the macroscopic scale in order to obtain solutions with higher performance. However, the introduction of the orientation among

the optimisation variables would lead to problems when performing the reconstruction of the boundary of the ACM because, although the RVE has the same topology at each point of the structure, the latter would be distorted because of RVE orientation that evolves pointwise. Additional geometrical criteria should be introduced to take this aspect into account.

Furthermore, other constraints of geometric nature coming from additive manufacturing processes can be considered, e.g., the overhang constraint, volume of support structure, etc.

Finally, the method of surface reconstruction should be generalised by fully automating the segmentation phase of the STL in the case of surfaces of genus $G > 0$ or characterised by a significant local variation of the main curvatures. “Optimal” criteria based on the value of the local curvatures, the quality of the tessellation, etc. should be introduced to pilot the STL segmentation strategy, thus, reducing the number of arbitrary decisions made by the user.

Bibliography

- [1] M. Bendsoe and O. Sigmund. *Topology Optimization - Theory, Methods and Applications*. Springer, 2003.
- [2] O. Sigmund. A 99 line topology optimization code written in Matlab. *Structural and Multidisciplinary Optimization*, 21(2):120–127, 2001.
- [3] C.S. Jog Robert B. Haber, Martin Philip Bendsoe. *Perimeter Constrained Topology Optimization of Continuum Structures*. Springer, 1996.
- [4] Blaise Bourdin. Filters in topology optimization. *Numerical Methods in Engineering*, 50(9):2143–2158, 2001. doi: 10.1002/nme.116.
- [5] K. Svanberg. The Method of Moving Asymptotes - A new method for structural optimization. *International Journal for Numerical Methods in Engineering*, 24:359–373, 1987.
- [6] Krister Svanberg. A class of globally convergent optimization methods based on conservative convex separable approximations. *SIAM Journal on Optimization*, 12(2):555–573, jan 2002. doi: 10.1137/s1052623499362822.
- [7] O. Sigmund. A 99 line topology optimization code written in matlab. *Structural and Multidisciplinary Optimization*, 21(2):120–127, apr 2001.
- [8] Altair. Optistruct reference guide. Technical report, Altair, 2021.
- [9] Simulia Dassault. Tosca reference guide. Technical report, Dassault Systemes, 2021.
- [10] James K. Guest. Optimizing the layout of discrete objects in structures and materials: A projection-based topology optimization approach. *Computer Methods in Applied Mechanics and Engineering*, 283:330–351, jan 2015. doi: 10.1016/j.cma.2014.09.006.

- [11] Grégoire Allaire, François Jouve, and Anca-Maria Toader. Structural optimization using sensitivity analysis and a level-set method. *Journal of Computational Physics*, 194(1):363–393, feb 2004.
- [12] Grégoire Allaire and François Jouve. A level-set method for vibration and multiple loads structural optimization. *Computer Methods in Applied Mechanics and Engineering*, 194(30-33):3269–3290, aug 2005.
- [13] G. Allaire, F. Jouve, and G. Michailidis. Thickness control in structural optimization via a level set method. *Structural and Multidisciplinary Optimization*, 53(6):1349–1382, apr 2016.
- [14] Grégoire Allaire, François Jouve, and Anca-Maria Toader. Structural optimization using sensitivity analysis and a level-set method. *Journal of Computational Physics*, 194(1):363 – 393, 2004.
- [15] Takayuki Yamada, Kazuhiro Izui, Shinji Nishiwaki, and Akihiro Takezawa. A topology optimization method based on the level set method incorporating a fictitious interface energy. *Computer Methods in Applied Mechanics and Engineering*, 199(45-48):2876–2891, nov 2010. doi: 10.1016/j.cma.2010.05.013.
- [16] Kazuhisa Abe, Shunsuke Kazama, and Kazuhiro Koro. A boundary element approach for topology optimization problem using the level set method. *Communications in Numerical Methods in Engineering*, 23(5):405–416, sep 2006. doi: 10.1002/cnm.919.
- [17] Y.M. Xie and G.P. Steven. A simple evolutionary procedure for structural optimization. *Computers & Structures*, 49(5):885 – 896, 1993.
- [18] D. Chu, Y. Xie, A. Hira, and G. Steven. Evolutionary structural optimization for problems with stiffness constraints. *Finite Elements in Analysis and Design*, 21(4):239–251, 1996.
- [19] Yang X., Xie Y., Steven G., and Querin O. Topology optimization for frequencies using an evolutionary method. *Journal of Structural Engineering*, 125(12):239–251, 1999.
- [20] XY Yang, Yi Xie, Grant Steven, and Osvaldo Querin. Bidirectional evolutionary method for stiffness optimization. *AIAA Journal*, 37: 1483–1488, 1999.

- [21] Y. M. Huang, X. and Xie. Evolutionary topology optimization of continuum structures with an additional displacement constraint. *Structural and Multidisciplinary Optimization*, 40, 2009. URL <https://doi.org/10.1007/s00158-009-0382-4>.
- [22] X Huang and M Xie. Evolutionary topology optimization of continuum structures: Methods and applications. *John Wiley & Sons*, pages 121–150, 2010.
- [23] Huang X. and Xie Y. Convergent and mesh-independent solutions for the bi-directional evolutionary structural optimization method. *Finite Elements in Analysis and Design*, 43(14):1039 — 1049, 2007.
- [24] Xie Y. and Huang X. Recent developments in evolutionary structural optimization (eso) for continuum structures. *IOP Conference Series : Materials Science and Engineering*, 2010.
- [25] Tang Y., Kurtz A., and Zhao Y.F. Bidirectional evolutionary structural optimization (beso) based design method for lattice structure to be fabricated by additive manufacturing. *Computer-Aided Design*, 2015.
- [26] Fan Z., Xia L., Lai W., Xia Q., and Shi T. Evolutionary topology optimization of continuum structures with stress constraints. *Structural and Multidisciplinary Optimization*, 2019.
- [27] Da D., Xia L., Li G., and Huang X. Evolutionary topology optimization of continuum structures with smooth boundary representation. *Structural and Multidisciplinary Optimization*, 2018.
- [28] Yunlong Tang and Yaoyao Fiona Zhao. Multifunctional design of heterogeneous cellular structures. *Structural and Multidisciplinary Optimization*, 58(3):1121–1138, mar 2018. doi: 10.1007/s00158-018-1956-9.
- [29] M. Benedetti, A. du Plessis, R.O. Ritchie, M. Dallago, S.M.J. Razavi, and F. Berto. Architected cellular materials: A review on their mechanical properties towards fatigue-tolerant design and fabrication. *Materials Science and Engineering: R: Reports*, 144:100606, 2021. ISSN 0927-796X. doi: <https://doi.org/10.1016/j.mser.2021.100606>. URL <https://www.sciencedirect.com/science/article/pii/S0927796X21000012>.

- [30] Erik Andreassen and Jakob Søndergaard Jensen. Topology optimization of periodic microstructures for enhanced dynamic properties of viscoelastic composite materials. *Structural and Multidisciplinary Optimization*, 49(5):695–705, nov 2013. doi: 10.1007/s00158-013-1018-2.
- [31] Maxime Collet, Lise Noël, Matteo Bruggi, and Pierre Duysinx. Topology optimization for microstructural design under stress constraints. *Structural and Multidisciplinary Optimization*, 58(6):2677–2695, jul 2018.
- [32] Matej Borovinšek, Nejc Novak, Matej Vesenjak, Zoran Ren, and Miran Ulbin. Designing 2d auxetic structures using multi-objective topology optimization. *Materials Science and Engineering: A*, 795:139914, sep 2020. doi: 10.1016/j.msea.2020.139914.
- [33] Yongfeng Zheng, Yingjun Wang, Xiang Lu, Zhongyuan Liao, and Jinping Qu. Evolutionary topology optimization for mechanical metamaterials with auxetic property. *International Journal of Mechanical Sciences*, 179:105638, aug 2020. doi: 10.1016/j.ijmecsci.2020.105638.
- [34] Lin Cheng, Pu Zhang, Emre Biyikli, Jiayi Bai, Joshua Robbins, and Albert To. Efficient design optimization of variable-density cellular structures for additive manufacturing: theory and experimental validation. *Rapid Prototyping Journal*, 23(4):660–677, 2017.
- [35] Jie Gao, Mi Xiao, Liang Gao, Jinhui Yan, and Wentao Yan. Isogeometric topology optimization for computational design of re-entrant and chiral auxetic composites. *Computer Methods in Applied Mechanics and Engineering*, 362:112876, apr 2020. doi: 10.1016/j.cma.2020.112876.
- [36] L. Li, Z. Du, and H.A. Kim. Design of architected materials for thermoelastic macrostructures using level set method. *JOM*, 72(4):1734–1744, 2020. doi: 10.1007/s11837-020-04046-2.
- [37] M. Wallin and D.A. Tortorelli. Nonlinear homogenization for topology optimization. *Mechanics of Materials*, 145, 2020. doi: 10.1016/j.mechmat.2020.103324.
- [38] M. Montemurro, G. Bertolino, and T. Roiné. A general multi-scale topology optimisation method for lightweight lattice structures obtained through additive manufacturing technology. *Composite Structures*, 258:113360, 2021. ISSN 0263-8223. doi: https:

- [//doi.org/10.1016/j.compstruct.2020.113360](https://doi.org/10.1016/j.compstruct.2020.113360). URL <https://www.sciencedirect.com/science/article/pii/S0263822320332864>.
- [39] Yiqiang Wang, Zhen Luo, Nong Zhang, and Zhan Kang. Topological shape optimization of microstructural metamaterials using a level set method. *Computational Materials Science*, 87:178–186, 2014.
- [40] Van-Nam Hoang, Trung Pham, Duc Ho, and H. Nguyen-Xuan. Robust multiscale design of incompressible multi-materials under loading uncertainties. *Engineering with Computers*, mar 2021. doi: 10.1007/s00366-021-01372-0.
- [41] Laurent Chougrani, Jean-Philippe Perrot, Philippe Véron, and Stéphane Abed. Parts internal structure definition using non-uniform patterned lattice optimization for mass reduction in additive manufacturing. *Engineering with Computers*, 35(1):277–289, mar 2018. doi: 10.1007/s00366-018-0598-2.
- [42] Z. Wu, F. Fan, R. Xiao, and L. Yu. The substructuring-based topology optimization for maximizing the first eigenvalue of hierarchical lattice structure. *International Journal for Numerical Methods in Engineering*, 121(13):2964–2978, 2020. doi: 10.1002/nme.6342.
- [43] V.-N. Hoang, N.-L. Nguyen, P. Tran, M. Qian, and H. Nguyen-Xuan. Adaptive concurrent topology optimization of cellular composites for additive manufacturing. *JOM*, 72(6):2378–2390, 2020. doi: 10.1007/s11837-020-04158-9.
- [44] J. Jia, D. Da, C.-L. Loh, H. Zhao, S. Yin, and J. Xu. Multiscale topology optimization for non-uniform microstructures with hybrid cellular automata. *Structural and Multidisciplinary Optimization*, 62(2):757–770, 2020. doi: 10.1007/s00158-020-02533-3.
- [45] Y. Wang, D. Hu, H. Wang, T. Zhang, and H. Yan. Practical design optimization of cellular structures for additive manufacturing. *Engineering Optimization*, 52(11):1887–1902, 2020. doi: 10.1080/0305215X.2019.1696785.
- [46] P. Liu, Z. Kang, and Y. Luo. Two-scale concurrent topology optimization of lattice structures with connectable microstructures. *Additive Manufacturing*, 36:101427, 2020.
- [47] Shuzhi Xu, Jikai Liu, Jiaqi Huang, Bin Zou, and Yongsheng Ma. Multi-scale topology optimization with shell and interface layers for

- additive manufacturing. *Additive Manufacturing*, 37:101698, jan 2021. doi: 10.1016/j.addma.2020.101698.
- [48] J. Wu, W. Wang, and X. Gao. Design and optimization of conforming lattice structures. *IEEE Transactions on Visualization and Computer Graphics*, 27(1):43–56, 2021. doi: 10.1109/TVCG.2019.2938946.
- [49] D. Da and L. Xia. Design of heterogeneous mesostructures for non-separated scales and analysis of size effects. *International Journal for Numerical Methods in Engineering*, 122(5):1333–1351, 2021. doi: 10.1002/nme.6580.
- [50] Q. Li, R. Xu, J. Liu, S. Liu, and S. Zhang. Topology optimization design of multi-scale structures with alterable microstructural length-width ratios. *Composite Structures*, 230, 2019. doi: 10.1016/j.compstruct.2019.111454.
- [51] Q. Li, R. Xu, Q. Wu, and S. Liu. Topology optimization design of quasi-periodic cellular structures based on erode–dilate operators. *Computer Methods in Applied Mechanics and Engineering*, 377, 2021. doi: 10.1016/j.cma.2021.113720.
- [52] Q. Xia, H. Zong, T. Shi, and H. Liu. Optimizing cellular structures through the m-vcut level set method with microstructure mapping and high order cutting. *Composite Structures*, 261, 2021. doi: 10.1016/j.compstruct.2020.113298.
- [53] W. Kijanski and F.-J. Barthold. Two-scale shape optimisation based on numerical homogenisation techniques and variational sensitivity analysis. *Computational Mechanics*, 67(4):1021–1040, 2021. doi: 10.1007/s00466-020-01955-6.
- [54] Hao Li, Zhen Luo, Nong Zhang, Liang Gao, and Terry Brown. Integrated design of cellular composites using a level-set topology optimization method. *Computer Methods in Applied Mechanics and Engineering*, 309:453–475, 2016.
- [55] Hao Li, Zhen Luo, Liang Gao, and Qinghua Qin. Topology optimization for concurrent design of structures with multi-patch microstructures by level sets. *Computer Methods in Applied Mechanics and Engineering*, 331:536–561, 2018.

- [56] Raghavendra Sivapuram, Peter D. Dunning, and H. Alicia Kim. Simultaneous material and structural optimization by multiscale topology optimization. *Structural and Multidisciplinary Optimization*, 54(5):1267–1281, 2016.
- [57] Jikai Liu, Yufan Zheng, Rafiq Ahmad, Jinyuan Tang, and Yongsheng Ma. Minimum length scale constraints in multi-scale topology optimization for additive manufacturing. *Virtual and Physical Prototyping*, 14(3):229–241, 2019.
- [58] Jie Gao, Hao Li, Liang Gao, and Mi Xiao. Topological shape optimization of 3d micro-structured materials using energy-based homogenization method. *Advances in Engineering Software*, 116:89–102, 2018.
- [59] Weihong Zhang, Gaoming Dai, Fengwen Wang, Shiping Sun, and Hicham Bassir. Using strain energy-based prediction of effective elastic properties in topology optimization of material microstructures. *Acta Mechanica Sinica*, 23(1):77–89, 2007.
- [60] Yingjun Wang, Hang Xu, and Damiano Pasini. Multiscale isogeometric topology optimization for lattice materials. *Computer Methods in Applied Mechanics and Engineering*, 316:568–585, 2017.
- [61] James K. Guest and Jean H. Prévost. Optimizing multifunctional materials: Design of microstructures for maximized stiffness and fluid permeability. *International Journal of Solids and Structures*, 43(22-23):7028–7047, nov 2006. doi: 10.1016/j.ijsolstr.2006.03.001.
- [62] Liang Xia and Piotr Breitkopf. Concurrent topology optimization design of material and structure within FE2 nonlinear multiscale analysis framework. *Computer Methods in Applied Mechanics and Engineering*, 278:524–542, 2014.
- [63] Jie Xu, Liang Gao, Mi Xiao, Jie Gao, and Hao Li. Isogeometric topology optimization for rational design of ultra-lightweight architected materials. *International Journal of Mechanical Sciences*, 166, 2020. URL <https://doi.org/10.1016/j.ijmecsci.2019.105103>.
- [64] Yixian Du, Hanzhao Li, Zhen Luo, and Qihua Tian. Topological design optimization of lattice structures to maximize shear stiffness. *Advances in Engineering Software*, 112:211–221, oct 2017. doi: 10.1016/j.advengsoft.2017.04.011.

- [65] Liang Dong. Mechanical responses of Ti-6Al-4V cuboctahedral truss lattice structures. *Composite Structures*, 235, 2020. URL <https://doi.org/10.1016/j.compstruct.2019.111815>.
- [66] Lyes Azzouz, Yong Chen, Mauro Zarrelli, Joshua M. Pearce, Leslie Mitchell, Guogang Ren, and Marzio Grasso. Mechanical properties of 3-d printed truss-like lattice biopolymer non-stochastic structures for sandwich panels with natural fibre composite skins. *Composite Structures*, 213:220 – 230, 2019.
- [67] Yabo Liu, Zhichao Dong, Jingran Ge, Xiaohu Lin, and Jun Liang. Stiffness design of a multilayer arbitrary bcc lattice structure with face sheets. *Composite Structures*, 230, 2019. URL <https://doi.org/10.1016/j.compstruct.2019.111485>.
- [68] Chenxi Peng, Phuong Tran, H. Nguyen-Xuan, and A.J.M. Ferreira. Mechanical performance and fatigue life prediction of lattice structures: Parametric computational approach. *Composite Structures*, 235, 2020. URL <https://doi.org/10.1016/j.compstruct.2019.111821>.
- [69] Jozef Tkac, Sylwester Samborski, Katarina Monkova, and Hubert Debski. Analysis of mechanical properties of a lattice structure produced with the additive technology. *Composite Structures*, 242, 2020. URL <https://doi.org/10.1016/j.compstruct.2020.112138>.
- [70] G. Bertolino, M. Montemurro, and G. De Pasquale. Multi-scale shape optimisation of lattice structures: an evolutionary-based approach. *International Journal on Interactive Design and Manufacturing*, 13 (4):1565–1578, 2019.
- [71] K. Refai, M. Montemurro, C. Brugger, and N. Saintier. Determination of the effective elastic properties of titanium lattice structures. *Mechanics of Advanced Materials and Structures*, 2019. URL <https://doi.org/10.1080/15376494.2018.1536816>.
- [72] Grégoire Allaire, Perle Geoffroy-Donders, and Olivier Pantz. Topology optimization of modulated and oriented periodic microstructures by the homogenization method. *Computers & Mathematics with Applications*, 78(7):2197 – 2229, 2019.
- [73] Perle Geoffroy-Donders, Grégoire Allaire, and Olivier Pantz. 3-d topology optimization of modulated and oriented periodic microstructures by the homogenization method. *Journal of Computational*

- Physics*, 401, 2020. URL <https://doi.org/10.1016/j.jcp.2019.108994>.
- [74] Chuong Nguyen, Xiaoying Zhuang, Ludovic Chamoin, Xianzhong Zhao, H. Nguyen-Xuan, and Timon Rabczuk. Three-dimensional topology optimization of auxetic metamaterial using isogeometric analysis and model order reduction. *Computer Methods in Applied Mechanics and Engineering*, 371, 2020. URL <https://doi.org/10.1016/j.cma.2020.113306>.
- [75] Yan Zhang, Mi Xiao, Xiaoyu Zhang, and Liang Gao. Topological design of sandwich structures with graded cellular cores by multiscale optimization. *Computer Methods in Applied Mechanics and Engineering*, 361:112749, 2020. URL <https://doi.org/10.1016/j.cma.2019.112749>.
- [76] Renato Picelli, Raghavendra Sivapuram, Scott Townsend, and H. Alicia Kim. Stress Topology Optimisation for Architected Material Using the Level Set Method. In *Advances in Structural and Multidisciplinary Optimization*, pages 1254–1269. Springer International Publishing, 2017.
- [77] Panagiotis Vogiatzis, Shikui Chen, Xiao Wang, Tiantian Li, and Lifeng Wang. Topology optimization of multi-material negative poisson’s ratio metamaterials using a reconciled level set method. *Computer-Aided Design*, 83:15 – 32, 2017.
- [78] Ruizhen Yang and Jianbin Du. Microstructural topology optimization with respect to sound power radiation. *Structural and Multidisciplinary Optimization*, 47(2):191–206, 2012.
- [79] Yan Zhang, Mi Xiao, Hao Li, and Liang Gao. Topology optimization of material microstructures using energy-based homogenization method under specified initial material layout. *Journal of Mechanical Science and Technology*, 33(2):677–693, 2019.
- [80] Maxime Collet, Lise Noël, Matteo Bruggi, and Pierre Duysinx. Topology optimization for microstructural design under stress constraints. *Structural and Multidisciplinary Optimization*, 58(6):2677–2695, 2018.
- [81] Liang Xia and Piotr Breitkopf. Design of materials using topology optimization and energy-based homogenization approach in mat-

- lab. *Structural and Multidisciplinary Optimization*, 52(6):1229–1241, 2015.
- [82] X. Huang, A. Radman, and Y.M. Xie. Topological design of microstructures of cellular materials for maximum bulk or shear modulus. *Computational Materials Science*, 50(6):1861–1870, 2011.
- [83] Yongfeng Zheng, Yingjun Wang, Xiang Lu, Zhongyuan Liao, and Jinping Qu. Evolutionary topology optimization for mechanical metamaterials with auxetic property. *International Journal of Mechanical Sciences*, 179, 2020. URL <https://doi.org/10.1016/j.ijmecsci.2020.105638>.
- [84] Huangchao Yu, Jiaqi Huang, Bin Zou, Wen Shao, and Jikai Liu. Stress-constrained shell-lattice infill structural optimisation for additive manufacturing. *Virtual and Physical Prototyping*, 15(1):35–48, aug 2019. doi: 10.1080/17452759.2019.1647488.
- [85] Jiadong Deng, Claus B. W. Pedersen, and Wei Chen. Connected morphable components-based multiscale topology optimization. *Frontiers of Mechanical Engineering*, 14(2):129–140, jan 2019. doi: 10.1007/s11465-019-0532-3.
- [86] J. Wu, O. Sigmund, and J.P. Groen. Topology optimization of multiscale structures: a review. *Structural and Multidisciplinary Optimization*, 63(3):1455–1480, 2021. doi: 10.1007/s00158-021-02881-8.
- [87] Shashi Ranjan Mohan and Suryakumar Simhambhatla. Adopting feature resolution and material distribution constraints into topology optimisation of additive manufacturing components. *Virtual and Physical Prototyping*, 14(1):79–91, jul 2018. doi: 10.1080/17452759.2018.1501275.
- [88] R. Rashid, S.H. Masood, D. Ruan, S. Palanisamy, X. Huang, and R.A. Rahman Rashid. Topology optimisation of additively manufactured lattice beams for three-point bending test. *2018 Annual International Solid Freeform Fabrication Symposium*, 2018.
- [89] N. Korshunova, G. Alaimo, S.B. Hosseini, M. Carraturo, A. Reali, J. Niiranen, F. Auricchio, E. Rank, and S. Kollmannsberger. Bending behavior of octet-truss lattice structures: Modelling options, numerical characterization and experimental validation. *Material and Design*, 205:109693, jul 2021. doi: 10.1016/j.matdes.2021.109693.

- [90] Jingwei Zhang and Jun Yanagimoto. Topology optimization of microlattice dome with enhanced stiffness and energy absorption for additive manufacturing. *Composite Structure*, 255:112889, jan 2021. doi: 10.1016/j.compstruct.2020.112889.
- [91] Jae-Eun Kim and Keun Park. Multiscale topology optimization combining density-based optimization and lattice enhancement for additive manufacturing. *International Journal of Precision Engineering and Manufacturing-Green Technology*, 8(4):1197–1208, dec 2020. doi: 10.1007/s40684-020-00289-1.
- [92] A. Sheffer K. Hormann, B. Lévy. *Mesh Parameterization: Theory and Practice*. INRIA, August 2007.
- [93] Les Piegl and Wayne Tiller. *The NURBS book*. Springer, 1997.
- [94] Sahand Jamal Rahi and Kim Sharp. Mapping complicated surfaces onto a sphere. *International Journal of Computational Geometry & Applications*, 17(04):305–329, aug 2007.
- [95] Xianfeng Gu and Shing-Tung Yau. Global conformal surface parameterization, 2003.
- [96] Michael S. Floater. Parametrization and smooth approximation of surface triangulations. *Computer Aided Geometric Design*, 14(3):231–250, apr 1997.
- [97] Jiong Tao, Bailin Deng, and Juyong Zhang. A fast numerical solver for local barycentric coordinates. *Computer Aided Geometric Design*, 70:46–58, mar 2019.
- [98] Eden Fedida Hefetz, Edward Chien, and Ofir Weber. A subspace method for fast locally injective harmonic mapping. *Computer Graphics Forum*, 38(2):105–119, may 2019.
- [99] Haeyoung Lee, Yiyong Tong, and M. Desbrun. Geodesics-based one-to-one parameterization of 3d triangle meshes. *IEEE Multimedia*, 12(1):27–33, jan 2005.
- [100] *Surfaces from Scattered Points User’s Guide*. OpenCascade, version 7.3.0 edition, 2016.
- [101] Qing Mao, Shugui Liu, Sen Wang, and Xinhui Ma. Surface fitting for quasi scattered data from coordinate measuring systems. *Sensors*, 18(2):214, jan 2018.

- [102] Michael S. Floater. Meshless parameterization and b-spline surface approximation. In *The Mathematics of Surfaces IX*, pages 1–18. Springer London, 2000.
- [103] Shengyu Duan, Li Xi, Weibin Wen, and Daining Fang. Mechanical performance of topology-optimized 3D lattice materials manufactured via selective laser sintering. *Composite Structures*, 238, 2020. URL <https://doi.org/10.1016/j.compstruct.2020.111985>.
- [104] W. Zhang and S. Sun. Scale-related topology optimization of cellular materials and structures. *International Journal of Numerical Methods in Engineering*, 68:993–1011, 2006.
- [105] J. Alexandersen and B. S. Lazarov. Topology optimisation of manufacturable microstructural details without length scale separation using a spectral coarse basis preconditioner. *Computer Methods in Applied Mechanics and Engineering*, 290:156–182, 2015.
- [106] Jie Gao, Zhen Luo, Liang Xia, and Liang Gao. Concurrent topology optimization of multiscale composite structures in matlab. *Structural and Multidisciplinary Optimization*, 60:2621–2651, 2019.
- [107] Giulio Costa, Marco Montemurro, and Jérôme Pailhès. A 2d topology optimisation algorithm in NURBS framework with geometric constraints. *International Journal of Mechanics and Materials in Design*, 14(4):669–696, nov 2017.
- [108] Giulio Costa, Marco Montemurro, and Jérôme Pailhès. NURBS hyper-surfaces for 3d topology optimization problems. *Mechanics of Advanced Materials and Structures*, pages 1–20, may 2019.
- [109] Costa Giulio. *Design and Optimisation Methods for Structures produced by means of Additive Layer Manufacturing processes*. PhD thesis, Arts et Métiers ParisTech - Campus de Bordeaux - Institut de Mécanique et d’Ingénierie – I2M, UMR CNRS 5295, 2018.
- [110] Giulio Costa, Marco Montemurro, and Jérôme Pailhès. A 2D topology optimisation algorithm in NURBS framework with geometric constraints. *International Journal of Mechanics and Materials in Design*, 14(4):669–696, 2018.
- [111] L. Piegl and W. Tiller. *The NURBS Book*. Springer-Verlag, 2006.

- [112] M. Montemurro. On the structural stiffness maximisation of anisotropic continua under inhomogeneous neumann-dirichlet boundary conditions. *Composite Structures*, page 115289, feb 2022. doi: 10.1016/j.compstruct.2022.115289.
- [113] Giulio Costa, Marco Montemurro, and Jérôme Pailhès. Minimum length scale control in a NURBS-based SIMP method. *Computer Methods in Applied Mechanics and Engineering*, 354:963–989, 2019.
- [114] Nocedal Jorge and Wright Stephen. *Numerical Optimization*. Springer, 2006.
- [115] Roine Thibaut. *Design and Optimisation Methods for Structures produced by means of Additive Layer Manufacturing processes*. PhD thesis, Arts et Métiers ParisTech - Campus de Bordeaux - Institut de Mécanique et d'Ingénierie – I2M, UMR CNRS 5295, 2022.
- [116] Rodriguez Thibaut. *Design and Optimisation Methods for Structures produced by means of Additive Layer Manufacturing processes*. PhD thesis, Arts et Métiers ParisTech - Campus de Bordeaux - Institut de Mécanique et d'Ingénierie – I2M, UMR CNRS 5295, 2022.
- [117] Marco Delucia, Anita Catapano, Marco Montemurro, and Jérôme Pailhès. Determination of the effective thermoelastic properties of cork-based agglomerates. *Journal of Reinforced Plastics and Composites*, 38(16):760–776, 2019.
- [118] L. Cappelli, M. Montemurro, F. Dau, and L. Guillaumat. Multi-scale identification of the viscoelastic behaviour of composite materials through a non-destructive test. *Mechanics of Materials*, 2019. URL <https://doi.org/10.1016/j.mechmat.2019.103137>.
- [119] Ever J. Barbero. *Finite Element Analysis of Composite Materials Using ANSYS®*. CRC Press, dec 2013.
- [120] Help System. *Ansys® Academic Research Mechanical, Release 21.1*. ANSYS, Inc.
- [121] Ronald M. Errico. What Is an Adjoint Model? *Bulletin of the American Meteorological Society*, 78(11):2577–2592, 1997.
- [122] Giulia Bertolino and Marco Montemurro. Two-scale topology optimisation of cellular materials under mixed boundary conditions. *International Journal of Mechanical Sciences*, 216:106961, feb 2022. doi: 10.1016/j.ijmecsci.2021.106961.

- [123] Fei Niu, Shengli Xu, and Gengdong Cheng. A general formulation of structural topology optimization for maximizing structural stiffness. *Structural and Multidisciplinary Optimization*, 43(4):561–572, nov 2010. doi: 10.1007/s00158-010-0585-8.
- [124] Marco Montemurro. An extension of the polar method to the first-order shear deformation theory of laminates. *Composite Structures*, 127:328–339, sep 2015. doi: 10.1016/j.compstruct.2015.03.025.
- [125] Marco Montemurro. The polar analysis of the third-order shear deformation theory of laminates. *Composite Structures*, 131:775–789, nov 2015. doi: 10.1016/j.compstruct.2015.06.016.
- [126] Anita Catapano and Marco Montemurro. Strength optimisation of variable angle-tow composites through a laminate-level failure criterion. *Journal of Optimization Theory and Applications*, 187(3):683–706, oct 2020. doi: 10.1007/s10957-020-01750-6.
- [127] Marco Montemurro. *A contribution to the development of design strategies for the optimisation of lightweight structures*. PhD thesis, ENSAM, 12 2018.
- [128] Giulia Bertolino, Marco Montemurro, Nicolas Perry, and Franck Pourroy. An efficient hybrid optimization strategy for surface reconstruction. *Computer Graphics Forum*, 40 (6):215–241, apr 2021. doi: 10.1111/cgf.14269.
- [129] Giulio Costa, Marco Montemurro, and Jérôme Pailhès. A general hybrid optimization strategy for curve fitting in the non-uniform rational basis spline framework. *Journal of Optimization Theory and Applications*, 176(1):225–251, nov 2017.
- [130] ASTM International. *Standard Test Methods for Flexural Properties of Unreinforced and Reinforced Plastics and Electrical Insulating Materials*, 2003.
- [131] *Engineering resin - Rigid Resin 4000 - Rigid Resin 4000 Material Properties Data*. URL <https://formlabs-media.formlabs.com/datasheets/1801088-TDS-FR-0P.pdf>.
- [132] ASTM International. *Standard Test Method for Compressive Properties of Rigid Plastics*, 2016.
- [133] ASTM International. *Standard Test Method for Tensile Properties of Plastics*, 2017.

- [134] Giulio Costa, Marco Montemurro, and Jérôme Pailhès. A General Hybrid Optimization Strategy for Curve Fitting in the Non-uniform Rational Basis Spline Framework. *Journal of Optimization Theory and Applications*, 176(1):225–251, 2018.
- [135] Contact Technology Guide Help System. *ANSYS ®Academic Research Mechanical, Release 21.1*. ANSYS, Inc., November 2004.
- [136] A. Sheffer K. Hormann, B. Lévy. *Mesh Parameterization: Theory and Practice*. INRIA, August 2007.
- [137] Les Piegl and Wayne Tiller. *The NURBS book*. Springer, 1997.
- [138] Michael S. Floater. Meshless Parameterization and B-Spline Surface Approximation. In *The Mathematics of Surfaces IX*, pages 1–18. Springer London, 2000.
- [139] Marco Montemurro. *A contribution to the development of design strategies for the optimisation of lightweight structures*. Habilitation à diriger des recherches, Université de Bordeaux, France, 12 2018. URL <http://hdl.handle.net/10985/15155>.
- [140] M. Montemurro, A. Vincenti, and P. Vannucci. Design of elastic properties of laminates with minimum number of plies. *Mechanics of Composite Materials*, 48:369–390, 2012.
- [141] M. Montemurro, A. Vincenti, and P. Vannucci. A two-level procedure for the global optimum design of composite modular structures - Application to the design of an aircraft wing. Part 1: theoretical formulation. *Journal of Optimization Theory and Applications*, 155(1):1–23, 2012.
- [142] M. Montemurro, A. Vincenti, and P. Vannucci. A two-level procedure for the global optimum design of composite modular structures - Application to the design of an aircraft wing. Part 2: numerical aspects and examples. *Journal of Optimization Theory and Applications*, 155(1):24–53, 2012.
- [143] Y. Audoux, M. Montemurro, and J. Pailhès. Non-Uniform Rational Basis Spline hyper-surfaces for metamodelling. *Computer Methods in Applied Mechanics and Engineering*, 2020. URL <https://doi.org/10.1016/j.cma.2020.112918>.

- [144] Y. Audoux, M. Montemurro, and J. Pailhès. A surrogate model based on Non-Uniform Rational B-Splines hypersurfaces. *CIRP Procedia*, 70:463–468, 2018.
- [145] *Optimization Toolbox User's Guide*. The Mathworks Inc., 3 Apple Hill Drive, Natick, 2018.
- [146] Alexander Agathos, Ioannis Pratikakis, Stavros Perantonis, Nikolaos Sapidis, and Philip Azariadis. 3d mesh segmentation methodologies for CAD applications. *Computer-Aided Design and Applications*, 4 (6):827–841, jan 2007.
- [147] STL Ear. <https://pinshape.com/items/23583-3d-printed-human-ear>.
- [148] STL Face. <https://grabcad.com/>.
- [149] STL Bone. <https://www.myminifactory.com/fr/object/3d-print-human-femur-43321>.
- [150] Giulio Costa, Marco Montemurro, and Jérôme Pailhès. NURBS hyper-surfaces for 3D topology optimization problems. *Mechanics of Advanced Materials and Structures*, 2019. URL <https://doi.org/10.1080/15376494.2019.1582826>.
- [151] STL Kettle. <http://visionair.ge.imati.cnr.it/ontologies/shapes>.
- [152] Marco Montemurro, Angela Vincenti, and Paolo Vannucci. The automatic dynamic penalisation method (adp) for handling constraints with genetic algorithms. *Computer Methods in Applied Mechanics and Engineering*, 256:70 – 87, 2013.
- [153] Guillaume Lavoué, Florent Dupont, and Atilla Baskurt. Subdivision surface fitting for efficient compression and coding of 3D models. In Shipeng Li, Fernando Pereira, Heung-Yeung Shum, and Andrew G. Tescher, editors, *Visual Communications and Image Processing 2005*, volume 5960, pages 1159 – 1170. International Society for Optics and Photonics, SPIE, 2005. doi: 10.1117/12.631641. URL <https://doi.org/10.1117/12.631641>.
- [154] M. Eck and Hugues Hoppe. Automatic reconstruction of b-spline surfaces of arbitrary topological type. *Proceedings of the 23rd annual conference on Computer graphics and interactive techniques*, 1996.
- [155] STL FanDisk. <https://github.com/dcoeurjo/VolGallery/blob/master>.

- [156] STL Club. <http://hhoppe.com/proj/recon>.
- [157] Les A. Piegl and Wayne Tiller. Computing the derivative of NURBS with respect to a knot. *Computer Aided Geometric Design*, 15(9): 925–934, oct 1998.

Appendix A

Formal expression of the gradient of the work of the internal forces for multi-scale problems

The proof of Proposition 4.2.1 is given here below.

Proof. Inasmuch as body forces are identically null, the derivative of the right-hand side of Eq. (4.19) is

$$\frac{\partial \mathbf{f}_M}{\partial \xi_{ik}} = \mathbf{0}, \quad i = 1, 2, \quad k = 1, \dots, n_{CP}, \quad (\text{A.1})$$

which implies the following equality

$$\frac{\partial (\mathbf{K}_M \mathbf{u}_M)}{\partial \xi_{ik}} = \mathbf{0} \Rightarrow \frac{\partial \mathbf{u}_M}{\partial \xi_{ik}} = -(\mathbf{K}_M)^{-1} \frac{\partial \mathbf{K}_M}{\partial \xi_{ik}} \mathbf{u}_M. \quad (\text{A.2})$$

The macroscopic work of the internal forces is defined as:

$$\mathcal{C}_M := \mathbf{f}_M^T \mathbf{u}_M. \quad (\text{A.3})$$

By taking into account for Eqs. (A.1) and (A.2), the derivative of \mathcal{C}_M reads

$$\frac{\partial \mathcal{C}_M}{\partial \xi_{ik}} = \mathbf{f}_M^T \frac{\partial \mathbf{u}_M}{\partial \xi_{ik}} = -\mathbf{u}_M^T \frac{\partial \mathbf{K}_M}{\partial \xi_{ik}} \mathbf{u}_M. \quad (\text{A.4})$$

By injecting the expression of \mathbf{K}_M of Eq. (4.20) in the above formula and by considering the expression of $\boldsymbol{\varepsilon}_{Me}$ of Eq. (4.28) one gets:

$$\begin{aligned} \frac{\partial \mathcal{C}_M}{\partial \xi_{ik}} &= - \sum_{e=1}^{N_{Me}} \int_{V_{Me}} \boldsymbol{\varepsilon}_{Me}^T \frac{\partial \mathcal{C}_M}{\partial \xi_{ik}} \boldsymbol{\varepsilon}_{Me} d\Omega \\ &\approx - \sum_{e=1}^{N_{Me}} \sum_{q=1}^6 \sum_{r=1}^6 \frac{\partial C_{Mqr}}{\partial \xi_{ik}} \varepsilon_{Meq} \varepsilon_{Mer} V_{Me}. \end{aligned} \quad (\text{A.5})$$

Inasmuch as the SEHM based on elements strain energy is used in this work, the derivatives of the components C_{Mqr} of the macroscopic elasticity tensor can be easily calculated from Eqs. (4.6) and (4.7):

$$\frac{\partial C_{Mqr}}{\partial \xi_{ik}} = \begin{cases} \frac{1}{V_{\text{RVE}} (\varepsilon_{mq}^0)^2} \frac{\partial \mathcal{C}_M (\varepsilon_{mq}^0)}{\partial \xi_{ik}}, & \text{if } q = r, \\ \frac{1}{2V_{\text{RVE}} \varepsilon_{mq}^0 \varepsilon_{mr}^0} \frac{\partial \mathcal{C}_M (\varepsilon_{mq}^0, \varepsilon_{mr}^0)}{\partial \xi_{ik}} + \\ - \frac{\varepsilon_{mq}^0}{2\varepsilon_{mr}^0} \frac{\partial C_{Mqq}}{\partial \xi_{ik}} - \frac{\varepsilon_{mr}^0}{2\varepsilon_{mq}^0} \frac{\partial C_{Mrr}}{\partial \xi_{ik}}, & \text{if } q \neq r. \end{cases} \quad (\text{A.6})$$

The next passage consists of expressing the derivative of the work of the internal forces at the lower scale, i.e., $\frac{\partial \mathcal{C}_M}{\partial \xi_{ik}}$. Since Eqs. (4.2) and (4.3) hold, the work of the internal forces of the RVE can be expressed as:

$$\begin{aligned} \mathcal{C}_M &= \mathbf{f}_m^T \mathbf{u}_M + \mathbf{u}_{m\text{BC}}^T \mathbf{r}_m + \boldsymbol{\eta}^T (\mathbf{K}_m \mathbf{u}_M + \mathbf{K}_{m\text{BC}} \mathbf{u}_{m\text{BC}} - \mathbf{f}_m) + \\ &\quad + \boldsymbol{\lambda}^T (\mathbf{K}_{m\text{BC}}^T \mathbf{u}_M + \tilde{\mathbf{K}}_m \mathbf{u}_{m\text{BC}} - \mathbf{r}_m), \end{aligned} \quad (\text{A.7})$$

where $\boldsymbol{\eta}_m \in \mathbb{R}^{N_{\text{DOF}}}$ and $\boldsymbol{\lambda}_m \in \mathbb{R}^{N_{\text{BC}}}$ are two arbitrary vectors. Under the hypothesis that vectors \mathbf{f}_m and $\mathbf{u}_{m\text{BC}}$ do not depend on the topological variable, i.e.,

$$\frac{\partial \mathbf{f}_m}{\partial \xi_{ik}} = \mathbf{0}, \quad \frac{\partial \mathbf{u}_{m\text{BC}}}{\partial \xi_{ik}} = \mathbf{0}, \quad (\text{A.8})$$

the derivative of Eq. (A.7) reads:

$$\begin{aligned} \frac{\partial \mathcal{C}_M}{\partial \xi_{ik}} &= \mathbf{f}_m^T \frac{\partial \mathbf{u}_M}{\partial \xi_{ik}} + \mathbf{u}_{m\text{BC}}^T \frac{\partial \mathbf{r}_m}{\partial \xi_{ik}} + \\ &\quad + \boldsymbol{\eta}^T \left(\frac{\partial \mathbf{K}_m}{\partial \xi_{ik}} \mathbf{u}_M + \mathbf{K}_m \frac{\partial \mathbf{u}_M}{\partial \xi_{ik}} + \frac{\partial \mathbf{K}_{m\text{BC}}}{\partial \xi_{ik}} \mathbf{u}_{m\text{BC}} \right) + \\ &\quad + \boldsymbol{\lambda}^T \left(\frac{\partial \mathbf{K}_{m\text{BC}}^T}{\partial \xi_{ik}} \mathbf{u}_M + \mathbf{K}_{m\text{BC}}^T \frac{\partial \mathbf{u}_M}{\partial \xi_{ik}} + \frac{\partial \tilde{\mathbf{K}}_m}{\partial \xi_{ik}} \mathbf{u}_{m\text{BC}} - \frac{\partial \mathbf{r}_m}{\partial \xi_{ik}} \right). \end{aligned} \quad (\text{A.9})$$

In Eq. (A.9), vectors $\boldsymbol{\eta}$ and $\boldsymbol{\lambda}$ can be chosen such that the terms multiplying $\frac{\partial \mathbf{u}_M}{\partial \xi_{ik}}$ and $\frac{\partial \mathbf{r}_m}{\partial \xi_{ik}}$ vanish, i.e.,

$$\begin{aligned} \boldsymbol{\lambda} &= \mathbf{u}_{mBC}, \\ \mathbf{K}_m \boldsymbol{\eta} &= -\mathbf{f}_m - \mathbf{K}_{mBC} \boldsymbol{\lambda} = -\mathbf{f}_m - \mathbf{K}_{mBC} \mathbf{u}_{mBC} = \mathbf{K}_m \mathbf{u}_M - 2\mathbf{f}_m. \end{aligned} \quad (\text{A.10})$$

By injecting Eq. (A.10) in Eq. (A.9) one obtains:

$$\begin{aligned} \frac{\partial \mathcal{C}_M}{\partial \xi_{ik}} &= \mathbf{u}_M^T \frac{\partial \mathbf{K}_m}{\partial \xi_{ik}} \mathbf{u}_M + 2\mathbf{u}_M^T \frac{\partial \mathbf{K}_{mBC}}{\partial \xi_{ik}} \mathbf{u}_{mBC} + \mathbf{u}_{mBC}^T \frac{\partial \hat{\mathbf{K}}_m}{\partial \xi_{ik}} \mathbf{u}_{mBC} + \\ &\quad - 2\mathbf{f}_m^T (\mathbf{K}_m)^{-1} \left(\frac{\partial \mathbf{K}_m}{\partial \xi_{ik}} \mathbf{u}_M + \frac{\partial \mathbf{K}_{mBC}}{\partial \xi_{ik}} \mathbf{u}_{mBC} \right). \end{aligned} \quad (\text{A.11})$$

Inasmuch as the PBCs of Eq. (4.1) are imposed in terms of displacements and no external forces are applied to the FE model of the RVE, i.e., $\mathbf{f}_m = \mathbf{0}$, and since Eqs. (4.2) and (4.3) hold, Eq. (A.11) simplifies to:

$$\frac{\partial \mathcal{C}_M}{\partial \xi_{ik}} = \hat{\mathbf{u}}_m^T \frac{\partial \hat{\mathbf{K}}_m}{\partial \xi_{ik}} \hat{\mathbf{u}}_m. \quad (\text{A.12})$$

By considering the expression of the non-reduced stiffness matrix of the FE model of the RVE of Eq. (4.15) and by taking advantage from the local support property of Eq. (3.9), the above formula becomes:

$$\begin{aligned} \frac{\partial \mathcal{C}_M}{\partial \xi_{ik}} &= \sum_{e \in \mathcal{S}_k} \frac{\alpha}{\rho_e} \frac{\partial \rho_e}{\partial \xi_{ik}} \rho_e^\alpha \hat{\mathbf{u}}_m^T \hat{\mathbf{L}}_{me}^T \mathbf{K}_{me} \hat{\mathbf{L}}_{me} \hat{\mathbf{u}}_m \\ &= \sum_{e \in \mathcal{S}_k} \frac{\alpha}{\rho_e} \frac{\partial \rho_e}{\partial \xi_{ik}} \hat{\mathbf{u}}_m^T \hat{\mathbf{f}}_{me} = \sum_{e \in \mathcal{S}_k} \frac{\alpha}{\rho_e} \frac{\partial \rho_e}{\partial \xi_{ik}} w_{me}, \end{aligned} \quad (\text{A.13})$$

where $\hat{\mathbf{u}}_{me}, \hat{\mathbf{f}}_{me} \in \mathbb{R}^{N_{m\text{DOF},e}}$ are the generalised nodal displacements and forces of element e , while w_{me} is the work of the internal forces of element e . Finally, by injecting Eq. (A.13), evaluated for each elementary strain field, into Eq. (A.6), one can easily retrieve Eq. (4.27) and this last passage concludes the proof. \square

It is noteworthy that, when the SEHM based on elements strain energy is used, the assessment of the gradient of the macroscopic work of the internal forces requires the resolution of seven static analyses, i.e., six static analyses to get the macroscopic elasticity tensor \mathbf{C}_M , by solving Eq. (4.2) for each elementary strain field ε_{mr}^0 , ($r = 1, \dots, 6$), and one static analysis at the macroscopic scale by solving Eq. (4.19). Therefore, for each iteration of the optimisation process, Algorithm 2 is invoked to carry out all the necessary steps for computing the gradient of \mathcal{C}_M .

loa 2 – Computation of the gradient of \mathcal{C}_M .

- 1: Set $\varepsilon_{mr,0} = 0, \forall r = 1, \dots, 6$
- 2: **for** $r = 1, \dots, 6$ **do**
- 3: Set $\varepsilon_{mr,0} \neq 0$
- 4: Solve Eq. (4.2) and get $\hat{\mathbf{u}}_{me}(\varepsilon_{mr}^0), \hat{\mathbf{f}}_{me}(\varepsilon_{mr}^0), w_{me}(\varepsilon_{mr}^0), \forall e = 1, \dots, N_{Me}$
- 5: Calculate C_{Mrr} from Eq. (4.6)
- 6: Calculate $\frac{\partial C_{Mrr}}{\partial \xi_{ik}}$ from the first of Eq. (4.27)
- 7: **end for**
- 8: **for** $q = 1, \dots, 6$ **do**
- 9: **for** $r = q, \dots, 6,$ **do**
- 10: Calculate $\mathcal{C}_M(\varepsilon_{mq}^0, \varepsilon_{mr}^0)$ from Eq. (4.8)
- 11: Calculate C_{Mqr} from Eq. (4.7), set $C_{Mrq}^M = C_{qr}^M$
- 12: Calculate $w_{me}(\varepsilon_{mq}^0, \varepsilon_{mr}^0) = [\hat{\mathbf{u}}_{me}^T(\varepsilon_{mq}^0) + \hat{\mathbf{u}}_{me}^T(\varepsilon_{mr}^0)] [\hat{\mathbf{f}}_{me}(\varepsilon_{mq}^0) + \hat{\mathbf{f}}_{me}(\varepsilon_{mr}^0)],$
 $\forall e$
- 13: Calculate $\frac{\partial C_{Mqr}}{\partial \xi_{ik}}$ from the second of Eq. (4.27)
- 14: **end for**
- 15: **end for**
- 16: Solve Eq. (4.19) and get $\varepsilon_{Me}, \forall e = 1, \dots, N_{Me}$
- 17: Calculate $\frac{\partial \mathcal{C}_M}{\partial \xi_{ik}}$ from Eq. (??)

Appendix B

On the computational costs of the strain energy homogenisation method

As stated in Appendix A, the SEHM based on elements strain energy needs only seven static analyses per iteration to compute the gradient of the macroscopic work of the internal forces $\frac{\partial \mathcal{C}_M}{\partial \xi_{ik}}$. Conversely, the SEHM based on elements averaged stresses needs a higher computational effort. In order to understand this point, consider the r -th column of the macroscopic elasticity tensor of Eq. (4.4). It can be rewritten as

$$\mathbf{c}_{Mr} = \frac{1}{V_{\text{RVE}} \varepsilon_{mr}^0} \sum_{e=1}^{N_{Me}} \boldsymbol{\sigma}_{me}(\varepsilon_{mr}^0) V_{Me} + \boldsymbol{\mu}^T \left(\mathbf{K}_m \mathbf{u}_M(\varepsilon_{mr}^0) + \mathbf{K}_{m\text{BC}} \mathbf{u}_{m\text{BC}}(\varepsilon_{mr}^0) \right), \quad (\text{B.1})$$

because the second term of the right-hand side of the above formula is identically zero (recall that the equilibrium problem of the RVE is of the Dirichlet's type, i.e., $\mathbf{f}_m = \mathbf{0}$). In Eq. (B.1), $\boldsymbol{\mu} \in \mathbb{R}^{N_{m\text{DOF}} \times 6}$ is the arbitrary adjoint matrix. The derivative of Eq. (B.1) is:

$$\frac{\partial \mathbf{c}_{Mr}}{\partial \xi_{ik}} = \frac{1}{V_{\text{RVE}} \varepsilon_{mr}^0} \sum_{e=1}^{N_{Me}} \frac{\partial \boldsymbol{\sigma}_{me}}{\partial \xi_{ik}} V_{Me} + \boldsymbol{\mu}^T \left(\frac{\partial \mathbf{K}_m}{\partial \xi_{ik}} \mathbf{u}_M + \mathbf{K}_m \frac{\partial \mathbf{u}_M}{\partial \xi_{ik}} + \frac{\partial \mathbf{K}_{m\text{BC}}}{\partial \xi_{ik}} \mathbf{u}_{m\text{BC}} \right). \quad (\text{B.2})$$

The derivative of $\boldsymbol{\sigma}_{me}$ can be assessed by considering its expression:

$$\boldsymbol{\sigma}_{me} := \rho_e^\alpha \mathbf{C}_m \mathbf{B}_{me} \hat{\mathbf{L}}_{me} \hat{\mathbf{u}}_m, \quad (\text{B.3})$$

where \mathbf{C}_m is the elasticity matrix of the bulk material composing the RVE. The derivative of Eq. (B.3) reads:

$$\frac{\partial \boldsymbol{\sigma}_{me}}{\partial \xi_{ik}} = \frac{\alpha}{\rho_e} \frac{\partial \rho_e}{\partial \xi_{ik}} \boldsymbol{\sigma}_{me} + \rho_e^\alpha \mathbf{C}_m \mathbf{B}_{me} \hat{\mathbf{L}}_{me} \frac{\partial \hat{\mathbf{u}}_m}{\partial \xi_{ik}}, \quad (\text{B.4})$$

which, due to Eq. (A.8), can be simplified to:

$$\frac{\partial \boldsymbol{\sigma}_{me}}{\partial \xi_{ik}} = \frac{\alpha}{\rho_e} \frac{\partial \rho_e}{\partial \xi_{ik}} \boldsymbol{\sigma}_{me} + \rho_e^\alpha \mathbf{C}_m \mathbf{B}_{me} \mathbf{L}_{me} \frac{\partial \mathbf{u}_M}{\partial \xi_{ik}}, \quad (\text{B.5})$$

where $\mathbf{L}_{me} \in \mathbb{R}^{N_{m\text{DOF},e} \times N_{m\text{DOF}}}$ is the connectivity matrix obtained by suppressing N_{BC} columns, corresponding to the imposed displacements, from matrix $\hat{\mathbf{L}}_{me}$. By injecting Eq. (B.5) in Eq. (B.2) and by taking into account for the local support property of Eq. (3.9) one obtains:

$$\begin{aligned} \frac{\partial \mathbf{c}_{Mr}}{\partial \xi_{ik}} = & \frac{1}{V_{\text{RVE}} \varepsilon_{mr}^0} \sum_{e \in \mathcal{S}_k} \frac{\partial \rho_e}{\partial \xi_{ik}} \boldsymbol{\sigma}_{me} V_{Me} + \boldsymbol{\iota} \frac{\partial \mathbf{u}_M}{\partial \xi_{ik}} + \\ & + \boldsymbol{\mu}^T \left(\frac{\partial \mathbf{K}_m}{\partial \xi_{ik}} \mathbf{u}_M + \mathbf{K}_m \frac{\partial \mathbf{u}_M}{\partial \xi_{ik}} + \frac{\partial \mathbf{K}_{m\text{BC}}}{\partial \xi_{ik}} \mathbf{u}_{m\text{BC}} \right), \end{aligned} \quad (\text{B.6})$$

where $\boldsymbol{\iota}$ is defined as

$$\boldsymbol{\iota} := \frac{1}{V_{\text{RVE}} \varepsilon_{mr}^0} \sum_{e=1}^{N_{Me}} V_{Me} \rho_e^\alpha \mathbf{C}_m \mathbf{B}_{me} \mathbf{L}_{me}, \quad \boldsymbol{\iota} \in \mathbb{R}^{6 \times N_{m\text{DOF}}}. \quad (\text{B.7})$$

In Eq. (B.6), the matrix $\boldsymbol{\mu}$ can be chosen such that the term multiplying $\frac{\partial \mathbf{u}_M}{\partial \xi_{ik}}$ vanishes, i.e.,

$$\mathbf{K}_m \boldsymbol{\mu} = -\boldsymbol{\iota}^T, \quad (\text{B.8})$$

which corresponds to six linear systems where the unknowns are the column vectors composing the matrix $\boldsymbol{\mu}$, i.e $\boldsymbol{\mu} = \{\boldsymbol{\mu}_1, \dots, \boldsymbol{\mu}_6\}$, with $\boldsymbol{\mu}_i \in \mathbb{R}^{N_{m\text{DOF}}}$. Finally, by injecting Eq. (B.8) into Eq. (B.6), one obtains:

$$\frac{\partial \mathbf{c}_{Mr}}{\partial \xi_{ik}} = \frac{1}{V_{\text{RVE}} \varepsilon_{mr}^0} \sum_{e \in \mathcal{S}_k} \frac{\partial \rho_e}{\partial \xi_{ik}} \boldsymbol{\sigma}_{me} V_{Me} + \boldsymbol{\mu}^T \left(\frac{\partial \mathbf{K}_m}{\partial \xi_{ik}} \mathbf{u}_M + \frac{\partial \mathbf{K}_{m\text{BC}}}{\partial \xi_{ik}} \mathbf{u}_{\text{BC}} \right). \quad (\text{B.9})$$

It is noteworthy that the computation of the macroscopic work of the internal forces derivative $\frac{\partial \mathcal{C}_M}{\partial \xi_{ik}}$ when using the SEHM based on elements averaged stresses requires, at each iteration of the optimisation process, the resolution of 43 linear systems: seven analyses, consisting of Eqs. (4.2) and (B.8), for each one of the six elementary strain fields plus the macroscopic FE analysis to solve Eq. (4.19).

Appendix C

Analytical Expression of the Gradient of the Objective Function for the Surface Fitting Problem

The derivation of the analytical expression of the objective function gradient of Eq. (7.25) with respect to the continuous design variables, i.e., KVs components (ζ_2) and NURBS surface weights (ζ_3) is here presented. The gradient of \tilde{f} reads:

$$\begin{aligned} \frac{\partial \tilde{f}(\zeta_1, \zeta_2, \zeta_3)}{\partial \zeta_i} &= \\ &= \frac{1}{L_{\max}^2} \frac{\partial}{\partial \zeta_i} \left(\sum_{\alpha=x,y,z} \sum_{k=1}^N [\alpha(u_{1k}, u_{2k}) - \alpha_k]^2 \right) + \lambda K_{\max} \frac{\partial J_\alpha}{\partial \zeta_i}, \quad (\text{C.1}) \\ &i = 2, 3. \end{aligned}$$

The derivative of the first term of the right-hand side of Eq. (C.1) with respect to parameters $\beta_i^{(j)}$, which are related to the non-trivial KVs

components according to Eq. (7.22), reads:

$$\begin{aligned}
 \frac{\partial}{\partial \beta_i^{(j)}} \left(\sum_{\alpha=x,y,z} \sum_{k=1}^N [\alpha(u_{1k}, u_{2k}) - \alpha_k]^2 \right) &= \\
 &= \sum_{\alpha=x,y,z} \sum_{k=1}^N 2 [\alpha(u_{1k}, u_{2k}) - \alpha_k] \frac{\partial \alpha}{\partial \beta_i^{(j)}} = \\
 &= \sum_{\alpha=x,y,z} \sum_{k=1}^N 2 [\alpha(u_{1k}, u_{2k}) - \alpha_k] \frac{\partial \alpha}{\partial v_i^{(j)}} \frac{\partial v_i^{(j)}}{\partial \beta_i^{(j)}} = \\
 &= \sum_{\alpha=x,y,z} \sum_{k=1}^N 2 [\alpha(u_{1k}, u_{2k}) - \alpha_k] \frac{\partial \alpha}{\partial v_i^{(j)}} (v_{i-1}^{(j)} - v_{i+1}^{(j)}), \\
 & \quad i = p_j + 1, \dots, p_j + r_j, \quad j = 1, 2,
 \end{aligned} \tag{C.2}$$

where $\frac{\partial \alpha}{\partial v_i^{(j)}}$ is the expression of the B-spline surface derivatives with respect to the non-trivial KVs components, available in [157]. The analytical expression of the derivative with respect to $\beta_i^{(j)}$ of the second term of the right-hand side of Eq. (C.1) reads:

$$\begin{aligned}
 \frac{\partial J_\alpha}{\partial \beta_i^{(j)}} &= \int_0^1 \int_0^1 2 \frac{\partial^2 \alpha}{\partial u_1^2} \frac{\partial}{\partial \beta_i^{(j)}} \left(\frac{\partial^2 \alpha}{\partial u_1^2} \right) + 4 \frac{\partial^2 \alpha}{\partial u_1 \partial u_2} \frac{\partial}{\partial \beta_i^{(j)}} \left(\frac{\partial^2 \alpha}{\partial u_1 \partial u_2} \right) + \\
 &+ 2 \frac{\partial^2 \alpha}{\partial u_2^2} \frac{\partial}{\partial \beta_i^{(j)}} \left(\frac{\partial^2 \alpha}{\partial u_2^2} \right) du_1 du_2 = \int_0^1 \int_0^1 2 \frac{\partial^2 \alpha}{\partial u_1^2} \frac{\partial}{\partial v_i^{(j)}} \left(\frac{\partial^2 \alpha}{\partial u_1^2} \right) \frac{\partial v_i^{(j)}}{\partial \beta_i^{(j)}} + \\
 &+ 4 \frac{\partial^2 \alpha}{\partial u_1 \partial u_2} \frac{\partial}{\partial v_i^{(j)}} \left(\frac{\partial^2 \alpha}{\partial u_1 \partial u_2} \right) \frac{\partial v_i^{(j)}}{\partial \beta_i^{(j)}} + 2 \frac{\partial^2 \alpha}{\partial u_2^2} \frac{\partial}{\partial v_i^{(j)}} \left(\frac{\partial^2 \alpha}{\partial u_2^2} \right) \frac{\partial v_i^{(j)}}{\partial \beta_i^{(j)}} du_1 du_2,
 \end{aligned} \tag{C.3}$$

which simplifies to

$$\begin{aligned}
 \frac{\partial J_\alpha}{\partial \beta_i^{(j)}} &= \int_0^1 \int_0^1 2 \frac{\partial^2 \alpha}{\partial u_1^2} \frac{\partial}{\partial v_i^{(j)}} \left(\frac{\partial^2 \alpha}{\partial u_1^2} \right) (v_{i-1}^{(j)} - v_{i+1}^{(j)}) + \\
 &+ 4 \frac{\partial^2 \alpha}{\partial u_1 \partial u_2} \frac{\partial}{\partial v_i^{(j)}} \left(\frac{\partial^2 \alpha}{\partial u_1 \partial u_2} \right) (v_{i-1}^{(j)} - v_{i+1}^{(j)}) + \\
 &+ 2 \frac{\partial^2 \alpha}{\partial u_2^2} \frac{\partial}{\partial v_i^{(j)}} \left(\frac{\partial^2 \alpha}{\partial u_2^2} \right) (v_{i-1}^{(j)} - v_{i+1}^{(j)}) du_1 du_2,
 \end{aligned}$$

where $\frac{\partial}{\partial v_i^{(j)}} \left(\frac{\partial^2 \alpha}{\partial u_1^2} \right)$, $\frac{\partial}{\partial v_i^{(j)}} \left(\frac{\partial^2 \alpha}{\partial u_1 \partial u_2} \right)$ and $\frac{\partial}{\partial v_i^{(j)}} \left(\frac{\partial^2 \alpha}{\partial u_2^2} \right)$ are the derivatives of the second-order partial derivatives of the B-spline surface with respect

to the non-trivial KVs components. For example, in the case of the KV components along the first parametric coordinate, i.e., $v_k^{(1)}$, these derivatives read:

$$\frac{\partial}{\partial v_k^{(1)}} \left(\frac{\partial^2 \alpha}{\partial u_1^2} \right) = \sum_{i_1=0}^{n_1+1} \sum_{i_2=0}^{n_2} \frac{\partial^2 \bar{N}_{i_1, p_1}(u_1)}{\partial u_1^2} N_{i_2, p_2}(u_2) \bar{\alpha}_{i_1, i_2}, \quad (\text{C.4})$$

$$\frac{\partial}{\partial v_k^{(1)}} \left(\frac{\partial^2 \alpha}{\partial u_2^2} \right) = \sum_{i_1=0}^{n_1+1} \sum_{i_2=0}^{n_2} \bar{N}_{i_1, p_1}(u_1) \frac{\partial^2 N_{i_2, p_2}(u_2)}{\partial u_2^2} \bar{\alpha}_{i_1, i_2}. \quad (\text{C.5})$$

$$\frac{\partial}{\partial v_k^{(1)}} \left(\frac{\partial^2 \alpha}{\partial u_1 u_2} \right) = \sum_{i_1=0}^{n_1+1} \sum_{i_2=0}^{n_2} \frac{\partial \bar{N}_{i_1, p_1}(u_1)}{\partial u_1} \frac{\partial N_{i_2, p_2}(u_2)}{\partial u_2} \bar{\alpha}_{i_1, i_2}, \quad (\text{C.6})$$

In the above equations the term $\bar{N}_{i_1, p_1}(u_1)$ represents the i_1 -th basis function defined over the modified KV $\bar{\mathbf{v}}^{(1)}$, which is obtained by increasing the multiplicity of its non-trivial component $v_k^{(1)}$. Furthermore, $\bar{\alpha}_{i_1, i_2}$ is the generic component of the CPs matrix $\bar{\alpha}_{\text{CP}}$, modified to take into account for the new knot added to $\bar{\mathbf{v}}^{(1)}$ (see [157] for more details):

$$\bar{\alpha}_{i_1, i_2} = \begin{cases} 0, & i_1 = 0, \dots, k - p_1 - 1, \quad i_2 = 0, \dots, n_2, \\ \frac{\alpha_{i_1-1, i_2} - \alpha_{i_1, i_2}}{v_{i_1+p_1}^{(1)} - v_{i_1}^{(1)}}, & i_1 = k - p_1, \dots, k, \quad i_2 = 0, \dots, n_2, \\ 0, & i_1 = k + 1, \dots, n_1 + 1 \quad i_2 = 0, \dots, n_2. \end{cases} \quad (\text{C.7})$$

The derivatives with respect to the components of the KV $\mathbf{v}^{(2)}$ can be obtained by following the same passages and are not reported here for the sake of brevity.

Consider, now the gradient of the first term of the right-hand side of Eq. (C.1), which represents the distance between the NURBS surface and the TPs, with respect to the weights. Its analytical expression can be easily derived as follows:

$$\begin{aligned} \frac{\partial}{\partial w_{i_1, i_2}} \left(\sum_{\alpha=x, y, z} \sum_{k=1}^N [\alpha(u_{1k}, u_{2k}) - \alpha_k]^2 \right) &= \\ &= \sum_{\alpha=x, y, z} \sum_{k=1}^N 2 [\alpha(u_{1k}, u_{2k}) - \alpha_k] \frac{\partial \alpha}{\partial w_{i_1, i_2}} = \\ &= \sum_{\alpha=x, y, z} \sum_{k=1}^N 2 [\alpha(u_{1k}, u_{2k}) - \alpha_k] \frac{N_{i_1, p_1}(u_{1k}) N_{i_2, p_2}(u_{2k})}{W(u_{1k}, u_{2k})} \\ &\quad [\alpha_{i_1, i_2} - \alpha(u_{1k}, u_{2k})], \end{aligned} \quad (\text{C.8})$$

where the function $W(u_{1k}, u_{2k})$ is defined as

$$W(u_{1k}, u_{2k}) := \sum_{i_1=0}^{n_1} \sum_{i_2=0}^{n_2} N_{i_1, p_1}(u_{1k}) N_{i_2, p_2}(u_{2k}) w_{i_1, i_2}, \quad (\text{C.9})$$

The analytical expression of the gradient of the term J_α with respect to NURBS weight is more complicated. The first passage leads to:

$$\begin{aligned} \frac{\partial J_\alpha}{\partial w_{i,j}} &= \int_0^1 \int_0^1 2 \frac{\partial^2 \alpha}{\partial u_1^2} \frac{\partial}{\partial w_{i,j}} \left(\frac{\partial^2 \alpha}{\partial u_1^2} \right) + 4 \frac{\partial^2 \alpha}{\partial u_1 \partial u_2} \frac{\partial}{\partial w_{i_1, i_2}} \left(\frac{\partial^2 \alpha}{\partial u_1 \partial u_2} \right) + \\ &+ 2 \frac{\partial^2 \alpha}{\partial u_2^2} \frac{\partial}{\partial w_{i,j}} \left(\frac{\partial^2 \alpha}{\partial u_2^2} \right) du_1 du_2, \end{aligned} \quad (\text{C.10})$$

where the derivatives of the surface second-order partial derivatives with respect to the weights can be expressed as:

$$\begin{aligned} \frac{\partial^2}{\partial u_1^2} \left(\frac{\partial \alpha}{\partial w_{i,j}} \right) &= \frac{\partial^2 N_{i, p_1} N_{j, p_2}}{\partial u_1^2} \frac{(\alpha_{i,j} - \alpha)}{W} + \\ &- \frac{2}{W} \left[\frac{\partial \alpha}{\partial u_1} + \frac{\partial W}{\partial u_1} \frac{(\alpha_{i,j} - \alpha)}{W} \right] \left(\frac{\partial N_{i, p_1} N_{j, p_2}}{\partial u_1} - \frac{N_{i, p_1} N_{j, p_2}}{W} \frac{\partial W}{\partial u_1} \right) + \\ &- \frac{N_{i, p_1} N_{j, p_2}}{W} \left[\frac{\partial^2 \alpha}{\partial u_1^2} + \frac{\partial^2 W}{\partial u_1^2} \frac{(\alpha_{i,j} - \alpha)}{W} \right], \end{aligned} \quad (\text{C.11})$$

$$\begin{aligned} \frac{\partial^2}{\partial u_2^2} \left(\frac{\partial \alpha}{\partial w_{i,j}} \right) &= \frac{\partial^2 N_{j, p_2} N_{i, p_1}}{\partial u_2^2} \frac{(\alpha_{i,j} - \alpha)}{W} + \\ &- \frac{2}{W} \left[\frac{\partial \alpha}{\partial u_2} + \frac{\partial W}{\partial u_2} \frac{(\alpha_{i,j} - \alpha)}{W} \right] \left(\frac{\partial N_{j, p_2} N_{i, p_1}}{\partial u_2} - \frac{N_{i, p_1} N_{j, p_2}}{W} \frac{\partial W}{\partial u_2} \right) + \\ &- \frac{N_{j, p_2} N_{i, p_1}}{W} \left[\frac{\partial^2 \alpha}{\partial u_2^2} + \frac{\partial^2 W}{\partial u_2^2} \frac{(\alpha_{i,j} - \alpha)}{W} \right], \end{aligned} \quad (\text{C.12})$$

$$\begin{aligned} \frac{\partial}{\partial u_1 u_2} \left(\frac{\partial^2 \alpha}{\partial w_{i,j}} \right) &= \frac{\partial N_{i, p_1}}{\partial u_1} \frac{\partial N_{j, p_2}}{\partial u_2} \frac{(\alpha_{i, i_2} - \alpha)}{W} + \\ &- \frac{N_{i, p_1} N_{j, p_2}}{W} \left[\frac{\partial^2 \alpha}{\partial u_1 u_2} + \frac{\partial^2 W}{\partial u_1 u_2} \frac{(\alpha_{i,j} - \alpha)}{W} \right] + \\ &- \frac{\partial N_{i, p_1}}{\partial u_1} \frac{N_{j, p_2}}{W} \left[\frac{\partial \alpha}{\partial u_2} + \frac{\partial W}{\partial u_2} \frac{(\alpha_{i,j} - \alpha)}{W} \right] + \\ &- \frac{\partial N_{j, p_2}}{\partial u_2} \frac{N_{i, p_1}}{W} \left[\frac{\partial \alpha}{\partial u_1} + \frac{\partial W}{\partial u_1} \frac{(\alpha_{i,j} - \alpha)}{W} \right] + \\ &+ \frac{N_{i, p_1} N_{j, p_2}}{W^2} \left[\frac{\partial W}{\partial u_2} \frac{\partial \alpha}{\partial u_1} + \frac{\partial W}{\partial u_1} \frac{\partial \alpha}{\partial u_2} + \frac{2}{W} \frac{\partial W}{\partial u_1} \frac{\partial W}{\partial u_2} (\alpha_{i,j} - \alpha) \right]. \end{aligned} \quad (\text{C.13})$$

In the above expressions, the partial derivatives of terms $W(u_1, u_2)$ and $N_{i_j, p_j}(u_j)$, with respect to the parametric coordinates u_j , $j = 1, 2$ are computed via the Algorithms A 3.8 - A 4.4 available in [137].

Scientific production

Papers submitted to / published in international journals related to the activities presented in this Ph.D. Thesis

1. G. Bertolino, M. Montemurro. Two-scale topology optimisation of cellular materials under mixed boundary conditions. *International Journal of Mechanical Sciences*, v. 216, art. num. 106961, 2022. URL: <https://doi.org/10.1016/j.ijmecsci.2021.106961>
2. G. Bertolino, M. Montemurro, N. Perry, F. Pourroy. An Efficient Hybrid Optimization Strategy for Surface Reconstruction. *Computer Graphics Forum*, v. 40 (6), pp. 215-241, 2021. URL: <https://doi.org/10.1111/cgf.14269>
3. M. Montemurro, G. Bertolino, T. Roiné. A General Multi-Scale Topology Optimisation Method for Lightweight Lattice Structures Obtained through Additive Manufacturing Technology. *Composite Structures*, v. 258, art. num. 113360, 2021. URL: <https://doi.org/10.1016/j.compstruct.2020.113360>
4. G. Bertolino, M. Montemurro, E. Panettieri. Multi-scale topology optimisation of architected cellular materials obtained by stereolithography: analysis, design, and experiments. Virtual and physical prototyping. In preparation, 2022.

Papers submitted to / published in international journals related to the activities of this Ph.D. thesis but not presented in the manuscript

1. G. Bertolino, M. Montemurro, G. De Pasquale. Multi-scale shape optimisation of lattice structures: an evolutionary-based approach. *International Journal on Interactive Design and Manufacturing*, v. 13 (4), pp. 1565-1578, 2019. URL: <https://doi.org/10.1007/s12008-019-00580-9>
2. E. Panettieri, G. Bertolino, M. Montemurro. Hands-free printed door opener to limit the spread of Coronavirus: design through topology optimization. *Journal of Reinforced Plastics and Composites*. Under review, 2022.
3. M. Montemurro, G. Bertolino, F. Pourroy, F. Vignat, E. Panettieri. Optimised architected cellular structures obtained by electron beam melting technology: experimental and numerical approaches. *The International Journal of Advanced Manufacturing Technology*. In preparation, 2022.
4. M. Montemurro, G. Bertolino. Multi-scale topology optimisation of architected cellular materials based on a global-local modelling strategy. *Computer Methods in Applied Mechanics and Engineering*. In preparation, 2022.

International conferences with proceedings

1. G. Bertolino, M. Montemurro, N. Perry, F. Pourroy. Multi-scale topology optimisation of cellular structures by means of a pseudo-density algorithm based on NURBS hyper-surfaces. 14th World Congress on Computational Mechanics (WCCM) - ECCOMAS Congress 2020, Paris, France, 19-24 July, 2020, URL: <https://www.wccm-eccomas2020.org/frontal/docs/WCCM-XIV-ECCOMAS-2020.pdf>
2. T. Roiné, G. Bertolino, M. Montemurro, J. Pailhès. Topology optimisation of the lattice representative volume element by using a NURBS-based SIMP algorithm. 14th World Congress on Computational Mechanics (WCCM) - ECCOMAS Congress

- 2020, Paris, France, 19-24 July, 2020, URL: <https://www.wccm-eccomas2020.org/frontal/docs/WCCM-XIV-ECCOMAS-2020.pdf>
3. G. Bertolino, G. Costa, M. Montemurro, N. Perry, F. Pourroy. A general surface reconstruction method for post-processing of topology optimisation results. 2nd International Conference on Simulation for Additive Manufacturing - ECCOMAS Thematic Conference, Pavia, Italy, 11-13 September, 2019, URL: <http://congress.cimne.com/sim-am2019/frontal/doc/EbookSim-AM2019.pdf>
 4. G. De Pasquale, M. Montemurro, A. Catapano, G. Bertolino, L. Revelli. Cellular structures from additive processes: design, homogenization and experimental validation. *Structural Integrity Procedia*, v. 8, pp. 75-82, 2018. Proceedings of AIAS 2017 International Conference on Stress Analysis, Pisa, Italy, 6-9 September, 2017.
 5. M. Montemurro, G. De Pasquale, G. Bertolino. Multi-scale optimization of lattice structures for biomechanical components. 1st International Conference on Mechanics of Advanced Materials and Structures, Torino, Italy, 17-20 June 2018.

Résumé

Cette thèse porte sur l'intégration des spécificités des problèmes multi-échelle et des procédés de fabrication additive (FE), dans l'algorithme d'optimisation topologique (OT) basé sur le champ de pseudo-densité (utilisé en tant que descripteur topologique) et sur les hypersurfaces NURBS (de l'anglais *non-uniform rational basis spline*) développé au laboratoire I2M de Bordeaux. L'objectif est de faciliter le travail du concepteur lors des différentes étapes de la chaîne numérique AM, en réduisant le temps consacré à chaque étape. Pour ce faire, cette thèse aborde deux grands défis. Tout d'abord, le développement d'une stratégie de reconstruction de surface semi-automatique pour reconstruire et intégrer dans un environnement CAO la frontière de la topologie optimisée en minimisant les ressources informatiques (temps, mémoire, etc.) dédiées à cette tâche. Deuxièmement, l'intégration des spécificités des problèmes multi-échelle dans le processus d'OT. Concernant cet aspect, un cadre théorique/numérique permettant l'optimisation simultanée des descripteurs topologiques définis à plusieurs échelles a été développé. Dans ce contexte, des exigences de conception de nature différente, telles que la contrainte de fabrication sur l'épaisseur minimale imprimable, la condition de séparation d'échelle, la légèreté, la souplesse généralisée (en présence de conditions aux limites mixtes de Neumann-Dirichlet non nulles), ont été incluses dans la formulation du problème, en exploitant les propriétés du formalisme NURBS. L'efficacité de la méthode d'OT multi-échelles proposée a été testée sur des problèmes 2D et 3D tirés de la littérature et validée par les résultats d'essais.

Mots-clés : Optimisation topologique, Hypersurfaces NURBS, Analyse multi-échelle, Reconstruction de surface, Fabrication additive, Homogénéisation

Abstract

This Ph.D. thesis focuses on the integration of specificities of the multi-scale analysis and of the additive manufacturing (AM) process, into the topology optimisation (TO) algorithm based on the pseudo-density as topological descriptor and on the non-uniform rational basis spline (NURBS) hyper-surfaces developed at the I2M laboratory in Bordeaux. The goal is to facilitate the work of the designer during the different stages of the AM digital chain, by reducing the time required for each stage. Two main challenges have been faced in this Ph.D. thesis. Firstly, the development of a semi-automatic surface reconstruction strategy to recover the boundary of the optimised topology by minimising the computational resources (time, memory, etc.) dedicated to this task is proposed. Secondly, the integration of the peculiarities of multi-scale analyses in the TO process is faced. Regarding this aspect, a theoretical/numerical framework allowing the concurrent optimisation of the topological descriptors defined at multiple scales of the problem at hand has been developed. In this background design requirements of different nature, as the manufacturing constraint on the minimum member size, the scale separation condition, lightness, generalised compliance (in presence of mixed non-zero Neumann-Dirichlet boundary conditions) have been included in the problem formulation, by exploiting the properties of the NURBS formalism. The effectiveness of the proposed multi-scale TO method has been tested on both 2D and 3D benchmark structures and validated via the results of experimental tests (three-point bending tests).

Keywords: Topology optimisation, NURBS hyper-surfaces, Multi-scale analysis, Surface reconstruction, Additive manufacturing, Homogenisation